Università degli Studi di Roma "La Sapienza"

SAPIENZA
UNIVERSITÀ DI ROMA

Facoltà di Scienze Matematiche, Fisiche e Naturali

Scuola di Dottorato Vito Volterra

Dottorato in Astronomia

Thermal Noise Issue in the monolithic suspensions of the Virgo+ gravitational wave interferometer

Author

Marzia Colombini

Supervisor

Prof. Fulvio Ricci

Coordinator

Prof. Roberto Capuzzo Dolcetta

XXV ciclo 2009/2012

A.A. 2011/2012

Indice

Introduzione

Lo studio dello spettro elettromagnetico ha consentito di estendere enormemente la conoscenza dell'universo. Nel visibile le informazioni riguardanti gli oggetti astrofisici osservabili ci hanno permesso di valutare le dimensioni della nostra galassia e dell'universo circostante. Lo sviluppo di ulteriori tecnologie ha dato luogo all'indagine del cosmo a lunghezze d'onda diverse dal visibile: si è così scoperta la radiazione cosmica di fondo nella banda delle microonde e più recentemente le forti emissioni impulsive nello spettro dei raggi γ che hanno portato alla luce l'esistenza di fenomeni molto energetici. Infine, grazie alle osservazioni nella banda radio, si sono potute penetrare le nubi di polveri delle galassie distanti e vederne il centro, spesso costituito da buchi neri particolarmente massivi.

Tuttavia esistono ancora oggetti astrofisici la cui osservazione è possibile solo quando si trovano nelle vicinanze della Terra, a causa della loro bassa luminosità e delle loro ridotte dimensioni. Questi corpi celesti, che si possono formare nelle fasi finali dell'evoluzione stellare, sono buchi neri, stelle di neutroni e nane bianche; sono tra gli oggetti celesti più interessanti perchè permettono la comprensione dei processi di astrofisica delle alte energie e di fisica della materia condensata.

Per avere informazioni su questa classe di sorgenti si potrebbe utilizzare la radiazione gravitazionale. Le onde gravitazionali, previste dalla Teoria della Relatività Generale, sono emesse da tutti i corpi aventi una distribuzione di massa asimmetrica e variabile nel tempo; ma a causa della loro bassa intensità dovrebbero essere rilevabili solo nel caso in cui le masse in gioco sono dell'ordine di quelle stellari.

Nel corso degli anni si sono sviluppati diversi strumenti per la misura del segnale gravitazionale: dalle prime barre risonanti costruite nel 1960, fino agli interferometri, si continua a migliorare la sensibilità degli apparati al fine di arrivare alla rivelazione delle onde gravitazionali.

Gli interferometri attualmente in funzione sono cinque: GEO600, nato dalla collaborazione anglo-tedesca, i tre LIGO, posti in due diverse località degli Stati Uniti e infine Virgo, il rivelatore italo-francese, situato a Cascina (PI). Per come sono costruiti e per la sensibilità raggiunta, gli interferometri riuscirebbero a misurare solo i segnali gravitazionali di determinati tipi di sorgenti compresi all'interno del Gruppo Locale. Per poter aumentare il numero di sorgenti rilevabili è necessario incrementare il raggio di rivelazione degli strumenti fino all'ammasso della Vergine. Questo implica un aumento della sensibilità degli interferometri pari ad almeno un ordine di grandezza su tutta la banda di rivelazione, da qualche Hz a qualche kHz. I rivelatori in configurazione avanzata saranno in grado di rivelare alcuni eventi all'anno.

A tale scopo, sono stati progettati dei miglioramenti per Virgo, da attuare in quattro anni: la prima fase di potenziamento, appena conclusasi, prende nome di

Virgo+ e prevedeva un guadagno in sensibilità nella regione di frequenze tra $10Hz$ e $300Hz$, particolarmente interessante per la presenza di sorgenti pulsar note, come la pulsar della Crab e la pulsar della Vela. La seconda fase, attualmente in costruzione, prende nome di Advanced Virgo e partirà nella metà del 2015, completando il potenziamento della sensibilità anche alle alte frequenze (tra $300Hz$ e $10kHz$).

Al di sotto dei $10Hz$ la sensibilità di Virgo è limitata dl rumore sismico, che è invece trascurabile a frequenze più alte, grazie all'utilizzo di un complesso sistema di filtri meccanici di isolamento, chiamato superattenuatore, che sospende ogni ottica dell'interferometro. L'ultimo stadio di sospensione, che sorregge direttamente lo specchio, è chiamato payload ed è necessario per orientare lo specchio e smorzare i suoi modi interni residui.

Alle medie frequenze, tra $10Hz$ e $300Hz$, è dominante il rumore termico prodotto dal movimento microscopico casuale delle particelle che compongono un sistema in equilibrio termodinamico, movimento che si ripercuote a livello macroscopico come un'incertezza sulla posizione o sulle dimensioni del sistema stesso.

Affinchè un interferometro lavori con un basso livello di rumore termico, si richiede che le sospensioni delle masse di test abbiano un fattore di merito estremamente alto per tutti i loro modi di vibrazione nella banda di frequenze di rivelazione. In Virgo+, questa richiesta è garantita dalla presenza di una nuova sospensione realizzata con fibre di silice fusa. In essa fili, attacchi e specchi sono integralmente costituiti dallo stesso materiale in modo da formare un blocco monolitico e ridurre così il contributo dovuto alle dissipazioni interne. Inoltre, anche le prestazioni del coating degli specchi è migliorato, grazie all'uso di nuovi materiali.

Nonostante questo, dopo il montaggio delle nuove sospensioni monolitiche, si è osservato un miglioramento della curva di sensibilità più piccolo rispetto a quello previsto. In fig. 1 è riportato il confronto tra la migliore curva di sensibilità misurata in Virgo+ (in rosso) e quella di progetto (in grigio); è riportata anche la migliore curva di sensibilità misurata in Virgo (in nero) come riferimento.

La discrepanza tra la curva di sensibilità di progetto e quella misurata in Virgo+ può essere dovuta a diverse sorgenti di rumore, tra cui il rumore termico o la luce diffusa. Al fine di escludere il rumore termico come responsabile del mancato raggiungimento della sensibilità di progetto, sono state eseguite delle apposite misure sui fattori di merito delle risonanze meccaniche presenti nelle sospensioni monolitiche.

La conoscenza dei fattori di merito di un sistema ci permette di dedurre una stima del rumore termico in esso presente, definendo di un modello, sia esso analitico o numerico. Inoltre, ci permette di capire se sono presenti delle dissipazioni dovute ad un particolare componente del sistema o se ci sono degli accoppiamenti tra i diversi modi di vibrazione delle sospensioni. È fondamentale individuare tali fonti di dissipazione al fine di correggerle per la prossima fase di sviluppo di Advanced Virgo.

In questo lavoro mi sono occupata delle misure e delle analisi sui fattori di merito delle risonanze meccaniche presenti nelle sospensioni monolitiche montate in Virgo+.

Nel *primo capitolo* discuto brevemente la teoria della Relatività Generale derivando le equazioni che descrivono le onde gravitazionali. Sono quindi analizzate le loro proprietà, la loro interazione con la materia e la loro intensità. Successivamente sono riportate le principali sorgenti di onde gravitazionali rilevabili con l'interferome-

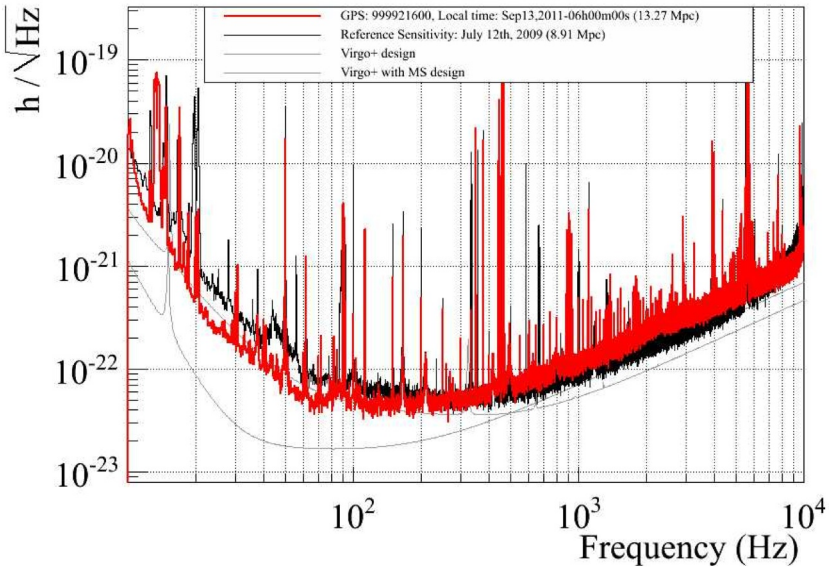

Figura 1: confronto tra la migliore curva di sensibilità misurata in Virgo+ (in rosso) e quella di progetto (in grigio); è riportata anche la migliore curva di sensibilità misurata in Virgo.

tro Virgo, ponendo particolare attenzione alle pulsar e ai sistemi binari coalescenti, rilevabili nella regione di frequenze tra $10Hz$ e $300Hz$.

Nel *secondo capitolo* è descritto come misurare le onde gravitazionali tramite uno strumento interferometrico, la configurazione base di questo rivelatore e i rumori in esso presenti. Sono discussi in dettaglio i diversi sistemi che formano l'interferometro Virgo, concludendo con la curva di sensibilità teorica e quella misurata. Successivamente sono prese in considerazione le modifiche più importanti che si ha intenzione di attuare per Advanced Virgo.

Il *terzo capitolo* verte sul rumore termico. Dopo aver affrontato la generalizzazione di questo fenomeno grazie al Teorema Fluttuazione-Dissipazione, è discusso un esempio di calcolo del rumore termico nel caso di un oscillatore semplice. Diversi modelli di dissipazione sono riportati, focalizzando la trattazione al caso della sospensione monolitica di Virgo+.

Nel *quarto capitolo* si descrive la produzione e la caratterizzazione delle fibre di silice fusa, fino all'assemblaggio di una sospensione monolitica. È trattato in dettaglio il metodo di misura dei fattori di merito e il problema dell'identificazione dei modi con un metodo basato sulla dipendenza delle frequenze dei modi dalla temperatura.

Nel *quinto capitolo* sono riportate le analisi compiute sui modi di violino delle sospensioni monolitiche. Discuto dell'anarmonicità presente e dell'andamento dei fattori di merito con la frequenza. Infine sono riportate le misure compiute appositamente su dei campioni di fibre di silice fusa al fine di individuare le sorgenti di dissipazioni presenti nel sistema di ancoraggio delle fibre all'ultimo stadio di sospensione degli specchi.

Nel *sesto capitolo* discuto come i fattori di merito misurati siano stati usati per stimare la curva di rumore termico, facendo uso di un modello analitico (per le so-

spensioni) e di un modello numerico (per le masse di test). In questo modo sarà possibile comprendere se è davvero il rumore termico il responsabile dell'alta curva di sensibilità trovata per Virgo+.

Introduction

The study of the electromagnetic spectrum allows us to greatly extend the knowledge of the universe. In the visible band, thanks to observations of astrophysical objects, we deduce dimensions of our galaxy and the nearby universe. We observe the universe also in other electromagnetic bands, as the cosmic microwave background and, more recently, thanks to gamma-ray burst detection, the most energetic events. Finally, gas and dust clouds surrounding galaxy bulges, where very massive black holes are presumably located, have been mapped thanks to radio band surveys.

Nevertheless, there are very interesting astrophysical objects which are hardly observable through electromagnetic waves, due to their low luminosity and small dimensions. Those bodies, as black holes, neutron stars and white dwarves, could arise during the last phase of massive star evolution: studying them, we can understand high energy astrophysics and highly condensed matter physics.

Gravitational radiation may help us to get informations about those classes of astrophysical sources. Gravitational waves are predicted by Einstein's general relativity theory and are emitted by every asymmetric time-variable mass-distribution. Due their very low intensity, it is possible to detect them only when the mass of the emitting body is of order of magnitude of astrophysical objects.

Many gravitational wave detectors have been developed since 1960, when the first resonant bar was tested by J. Weber. Nowadays, the most common gravitational wave detectors are interferometric antennas, which are sensitive in a large frequency band. There are five interferometers currently in use: the German-English GEO600, the three LIGO placed in two different locations in the United States, and finally Virgo, the French-Italian interferometer, placed in Cascina (Pisa). Given their sensitivity, those interferometers would detect only gravitational signals from sources, placed inside the Local Group. To increase the number of detectable sources it is necessary to expand the detection range to the Virgo cluster: that means a sensitivity increase of one order of magnitude over the whole frequency band, from few Hz to few kHz. Advanced detectors are supposed to detect few events per year.

The Virgo collaboration planned some improvements of the detector to be implemented in four years. The first upgrade phase has just ended (Virgo+) aiming to reach the final requested sensitivity in the low frequency band, between $10Hz$ and $300Hz$ where signals from known pulsars, as Crab and Vela ones are expected. The second upgrade phase, at the moment under construction, is called Advanced Virgo and it will be completed in the middle of 2015 with a sensitivity gain in the high frequency region (between $300Hz$ and $10kHz$).

Below $10Hz$, the bandwidth of Virgo is limited by the seismic noise, which is negligible at higher frequencies, thanks to a complex isolation mechanical filter system

called superattenuator which suspend each optics of the interferometer. The last stage of the suspension, which directly supports the mirror, is called payload and it is suitable equipped to orientate and control mirrors.

In the low frequency region between $10Hz$ and $300Hz$, the dominant noise source is thermal noise due to microscopic fluctuations of particles forming a physical system in thermodynamical equilibrium: they produce a macroscopic mechanical fluctuation of the interferometer mirror test mass.

In order to reduce thermal noise in an gravitational wave interferometer, we should increase quality factors of all mechanical resonances in the detection band. In Virgo+ the thermal noise reduction was achieved by means of new monolithic suspensions: the mirrors, the wires and their clamp are monolithic, made of fused silica. In such a way, the dissipation occurring the mechanical stress is concentrated and minimized. Moreover, the quality factors of the mirror coatings have been improved by using new materials.

However, after monolithic suspension mountings in Virgo+, we found an improvement smaller than the expected one. In fig. 2 the comparison between the best measured Virgo+ sensitivity curve (in red) and its design curve (in grey) is reported; it is also reported the best measured Virgo sensitivity curve (in black) as reference.

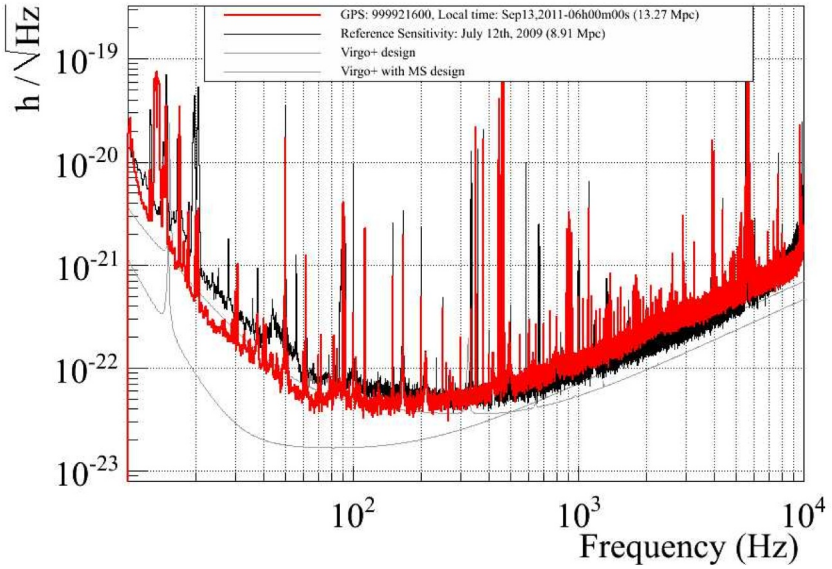

Figure 2: comparison between the best measured Virgo+ sensitivity curve (in red) and its design curve (in grey); it is also reported the best measured Virgo sensitivity curve (in black) as reference.

The observed discrepancy between the design curve and the measured one can be due to several noise sources, including thermal noise or scattered light noise. To completely exclude thermal noise as the relevant noise source causing the sensitivity gain lack, quality factor measurement campaigns were performed on every mechanical resonance of monolithic suspensions.

From quality factor measurements, it is possible to obtain a thermal noise estimation, by defining an analytical or numerical model of the physical system. Moreover,

quality factors allow us to be aware if there is any dissipation process acting on a monolithic suspension component or if there is any energy leak due to couplings between different internal modes. This study is mandatory to completely understand loss mechanisms, to improve the future suspension design and to better project Advanced Virgo suspensions.

In this work I performed measurements and analysis of mechanical resonance quality factors of Virgo+ monolithic suspensions.

In the *first chapter* I expose Einstein's general relativity theory, deriving gravitational wave equations and interaction properties. Then, I report the most common gravitational wave sources, detectable by Virgo interferometer, giving prominence to pulsars and coalescing compact binary systems, since their gravitational signal lies between $10Hz$ and $300Hz$.

In the *second chapter* I describe how it is possible to detect gravitational waves through an interferometer, focusing on its configuration and noises affecting it. I discuss with more details Virgo subsystems, including the description of the design and the measured sensitivity curves. Finally I report the most significant Advanced Virgo upgrades.

In the *third chapter* I talk about thermal noise. Starting from the fluctuation-dissipation theorem, I discuss, as an example, the thermal noise of a simple oscillator. I report also several loss mechanisms, focusing on Virgo+ monolithic suspension damping processes.

In the *fourth chapter* the monolithic suspension implementation, from the fused silica fiber production and characterization, to their clamping system and monolithic payload assembling, is reported. I describe the measurements of mechanical resonance quality factors and how it was possible to identify every resonance, thanks to their different temperature dependence.

In the *fifth chapter* the analysis on fused silica fiber violin modes is reported, enlightening their anharmonicity behavior and quality factor frequency dependence. Finally I report further measurements I performed on a single fiber suspension with a dedicated set-up, to identify possible dissipation mechanisms acting on monolithic clamping system.

The *sixth chapter* is dedicated to the estimation of Virgo+ thermal noise and the related models, analytical for suspensions and a numerical for mirror bulk. In that way we are able to predict a thermal noise curve and to understand if thermal noise is really accountable for Virgo+ sensitivity gain lack.

Chapter 1

Gravitational Waves

One of the most interesting predictions of the theory of General Relativity is the existence of the gravitational waves. The idea that a perturbation of the gravitational field should propagate as a wave is intuitive. As for electromagnetic waves, which are generated when an electric charge distribution oscillates, when a mass-energy distribution changes in time, the information about this change propagates in the form of waves.

In this chapter I introduce the basic concepts of the theory; then I show how to obtain the linearized solution of the Einstein's equations in the weak-field approximation. Finally I present the possible astronomical sources of gravitational wave.

1.1 Derivation from Einstein's Equations

General relativity is the physical theory formulated by Einstein in 1916, that generalises special relativity and Newton's law of universal gravitation, providing a unified description of gravity as a geometric property of space and time. The new idea of this theory is that space and time are merged together in a $4-$dimensional manifold. The presence of masses on this manifold causes its distortion and, on the other hand, the distortion of the $4-$dimensional space governs the dynamics of the masses on it. So, the curvature of spacetime is directly related to the energy and momentum of whatever matter and radiation are present.

The relation is specified by Einstein field equations, a system of partial differential equations [1]:

$$R_{\mu\nu} - \frac{1}{2} g_{\mu\nu} R = -\frac{8\pi G}{c^4} T_{\mu\nu} \tag{1.1}$$

where $R_{\mu\nu}$ is the Riemann tensor, connected to the covariant derivative of the metric tensor $g_{\mu\nu}$, R is the Ricci scalar, $T_{\mu\nu}$ is the stress-energy tensor, connected to the system mass-energy distribution.

Equation 1.1 is not linear; moreover any solution carries energy and momentum that modify the second member of the equation itself. So, it is difficult to find a general solution except for simple cases where there are symmetries, like in the Schwarzschild's solution.

One possible approach is to study the weak-field radiative solution, which describes waves carrying not enough energy and momentum to affect their own prop-

agation. That seems reasonable because any observable gravitational radiation is likely to be of very low intensity. In this case we can perform a linear approximation, starting from the Minkowsky metric tensor:

$$\eta_{\mu\nu} = \begin{pmatrix} -1 & 0 & 0 & 0 \\ 0 & 1 & 0 & 0 \\ 0 & 0 & 1 & 0 \\ 0 & 0 & 0 & 1 \end{pmatrix}$$

and using the perturbative method.

We write the metric solution $g_{\mu\nu}$ of Einstein's equations as a sum of two contributions:

$$g_{\mu\nu} = \eta_{\mu\nu} + h_{\mu\nu} \tag{1.2}$$

where $\eta_{\mu\nu}$ is the Minkowsky metric tensor and $h_{\mu\nu}$ is a small perturbation, which must satisfy the condition:

$$|h_{\mu\nu}| \ll 1 \tag{1.3}$$

Also the stress-energy tensor should be divided in two contributes, the unperturbed term $T^0_{\mu\nu}$ and the perturbation $T_{\mu\nu}$:

$$T^{tot}_{\mu\nu} = T^0_{\mu\nu} + T_{\mu\nu} \tag{1.4}$$

Substituting eq. 1.2 and eq. 1.4 in Einstein's equations 1.1 and considering only the first order elements, we obtain:

$$\Box h_{\mu\nu} - \left[\frac{\partial^2 h^\lambda_\nu}{\partial x^\lambda \partial x^\mu} + \frac{\partial^2 h^\lambda_\mu}{\partial x^\lambda \partial x^\nu} - \frac{\partial^2 h^\lambda_\lambda}{\partial x^\mu \partial x^\nu} \right] = -\frac{16\pi G}{c^4}(T_{\mu\nu} - \frac{1}{2} g_{\mu\nu} T^\lambda_\lambda) \tag{1.5}$$

where x^μ is the spacetime coordinate .

It is important to consider that each Einstein's equations solution is not uniquely determined: if we make a coordinate transformation, the transformed metric tensor is still a solution. That happens because it describes the same physical situation seen from a different reference frame. But, since we are working in the weak-field limit, we are entitled to make only transformations preserving the condition of eq. 1.3. So, in order to simplify eq. 1.5, it appears convenient to choose a coordinate system in which the harmonic gauge condition is satisfied:

$$g^{\mu\nu}\Gamma^\gamma_{\mu\nu} = 0$$

where $\Gamma^\gamma_{\mu\nu}$ is the Christoffel symbol, connected to the derivative of the spacetime coordinates.

So we obtain:

$$\begin{cases} \Box h_{\mu\nu} = -\frac{16\pi G}{c^4}(T_{\mu\nu} - \frac{1}{2} g_{\mu\nu} T^\lambda_\lambda) \\ \frac{\partial h^\mu_\lambda}{\partial x^\mu} = \frac{1}{2}\frac{\partial h^\gamma_\gamma}{\partial x^\lambda} \end{cases}$$

Introducing the tensor:

$$\overline{h}_{\mu\nu} \equiv h_{\mu\nu} - \frac{1}{2} g_{\mu\nu} h^\rho_\rho$$

we have:

$$\begin{cases} \Box\overline{h}_{\mu\nu} = -\frac{16\pi G}{c^4} T_{\mu\nu} \\ \frac{\partial \overline{h}^{\mu}_{\lambda}}{\partial x^{\mu}} = 0 \end{cases} \tag{1.6}$$

As in electrodynamics, the solution of eq. 1.6 can be written in terms of a retarded potential:

$$\overline{h}_{\mu\nu}(t, \vec{x}) = \frac{4G}{c^4} \int \frac{T_{\mu\nu}(t - |\vec{x} - \vec{x'}|, \vec{x'})}{|\vec{x} - \vec{x'}|} d^3x' \tag{1.7}$$

which represents the gravitational wave, calculated in the position $\vec{x}$, generated by a source described by $T_{\mu\nu}$ in the spacetime $\vec{x'}$.

Since we are in the weak-field approximation, very far from the source, $T_{\mu\nu} = 0$ holds:

$$\begin{cases} \Box\overline{h}_{\mu\nu} = 0 \\ \frac{\partial \overline{h}^{\mu}_{\lambda}}{\partial x^{\mu}} = 0 \end{cases} \tag{1.8}$$

That is the wave equation: we show that a perturbation of a flat spacetime propagates as a wave. Thanks to the double nature of the metric tensor $g_{\mu\nu}$, which indicates the spacetime shape and the gravitational potential, metric perturbations are also gravitational perturbations. The simplest solution of eq. 1.8 is a monochromatic plane wave:

$$\overline{h}_{\mu\nu} = \mathcal{R}e\left\{A_{\mu\nu} e^{ik_\gamma x^\gamma}\right\} \tag{1.9}$$

where $A_{\mu\nu}$ is the polarization tensor, connected to the wave amplitude, and k_γ is the wave vector; we are interested only in the real part of the equation.

1.2 Properties

Let us summarize the properties of gravitational waves:

- they move at the speed of light c: it is easy to see, substituting eq. 1.9 in the first equation of 1.8, that the wave vector k_γ is a null vector or a light-like vector;
- they are transversal: subtituting eq. 1.9 in the second equation of 1.8, the harmonic gauge condition, we obtain

  $$A^{\lambda}_{\alpha} k_\mu = 0$$

  i.e. the wave vector and the polarization tensor are orthogonal;
- there are only two polarization states, since the polarization tensor $A_{\mu\nu}$ is symmetric in the *transverse-traceless gauge*; for a gravitational wave propagating along the z-axis, its polarization vector is:

$$A_{\mu\nu} = \begin{pmatrix} 0 & 0 & 0 & 0 \\ 0 & A_{xx} & A_{xy} & 0 \\ 0 & A_{xy} & -A_{xx} & 0 \\ 0 & 0 & 0 & 0 \end{pmatrix}$$

The two polarizations are usually known as:

$$A_{xx} = A_+ \qquad A_{xy} = A_\times$$

the *plus* polarization and the *cross* polarization.

1.2.1 Interaction with matter

Let us study how a system of free-falling particles interact with gravitational waves. The passage of gravitational waves causes a metric perturbation, but it does not change the position of a test mass in a fixed frame. To prove that, we use the geodesic equation:

$$\frac{d^2x^\alpha}{d\tau^2} + \Gamma^\alpha_{\mu\nu}\left[\frac{dx^\mu}{d\tau}\frac{dx^\nu}{d\tau}\right] = 0 \tag{1.10}$$

where x are the spacetime coordinates, τ the proper time and $\Gamma^\alpha_{\mu\nu}$ the Christoffel symbol.

If we consider a particle at rest in the coordinate frame of the harmonic gauge, using the geodesic equation 1.10, it comes out that the particle is not affected by any acceleration.

To see the effect of the gravitational wave passage we need at least two test masses and consider their relative motion [2]. For example, we consider two particles A ad B, initially at rest, located along the x-axis of a frame: the A test mass is in the origin of the frame and the B test mass at the relative displacement $x = l_{AB}$. The distance Δl_{AB} is obtained by computing:

$$\begin{aligned}
\Delta l_{AB} &= \int |ds^2|^{1/2} \\
&= \int |g_{\mu\nu}dx^\mu dx^\nu|^{1/2} \\
&= \int_0^\epsilon |g_{xx}|^{1/2}dx \\
&\approx |g_{xx}(x=0)|^{1/2}\,\epsilon \approx [1 + \frac{1}{2}h_{xx}(x=0)]\; l_{AB}
\end{aligned} \tag{1.11}$$

where in the last equation we used the expression of the metric tensor in function of the gravitational wave amplitude. Thus, the relative displacement Δl_{AB} of the two masses oscillates periodically with the same frequency of the overpassing gravitational wave. The effect is directly proportional to the initial distance of the particles and to the wave amplitude.

We note that the effect of the gravitational wave on the spacetime metric has an intrinsic differential nature. This means that a circular-shape mass distribution is modulated at the wave frequency with opposite sign in x and in the y direction, as it is well shown in fig. 1.1.

1.2.2 Intensity

To compute the intensity of a gravitational wave we use the solution derived from the retarded potential 1.7. Using a spherical multipole expansion for the spatial

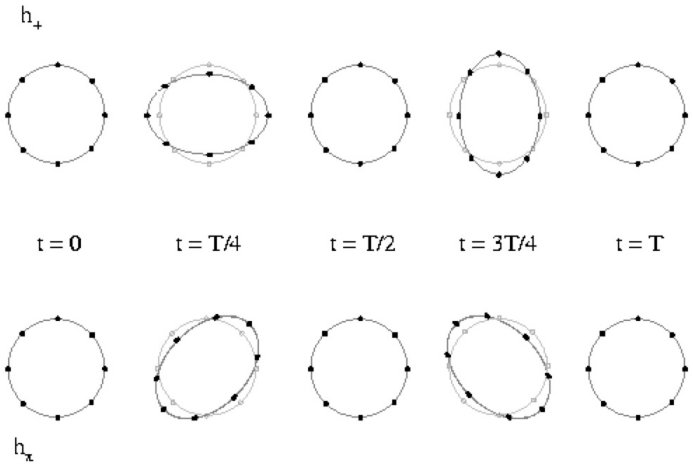

Figure 1.1: effect on a ring of particles posed on the x-y plane due to the passage of a gravitational wave coming along z axis with a plus polarization or a cross polarization. It is shown that the effect on two chosen orthogonal directions is strongly depending on the polarization of the wave.

coordinates [4] the lowest order term of this field is:

$$\bar{h}_{jk} = \frac{2G}{c^4 r}\ddot{Q}_{jk}(t - r/c) + \frac{4G}{3c^5 r}[\epsilon_{pqj}\ddot{\mathcal{S}}_{kp}(t - r/c) + \epsilon_{pqk}\ddot{\mathcal{S}}_{jp}(t - r/c)]n_q \tag{1.12}$$

where $\mathcal{S}_{jk}$ is the current quadrupole moment of the source, ϵ_{ijk} is the antisymmetric tensor and n_q is the unit vector pointing in the propagation direction. Consider that repeated down indices are summed as though a Minkowski metric η^{jk} is present.

Most gravitational wave estimates are based on this equation. When bulk mass motions dominate the dynamics, the first term describes the radiation. For example, this term gives the well-known "chirp" associated with binary inspiral (see sec. 1.3.2). It can be used to model f-mode and secular instabilities (see sec. 1.3.1). In practice, ringing waves are computed by finding solutions to the wave equation for gravitational radiation with appropriate boundary conditions. The second term in eq. 1.12 gives radiation from mass currents and it is used to calculate gravitational wave emission due to the r-mode instability (see sec. 1.3.1).

A more simplified expression of gravitational wave intensity can be found in the far field and slow motion approximation [3]:

$$\overline{h}_{\mu\nu}(t, \vec{x}) \approx \frac{G}{c^4 r}\,\ddot{Q}_{\mu\nu} \tag{1.13}$$

where r is the distance between the source and the observer ($|\vec{x}| \approx r \gg |\vec{x}'|$) and $\ddot{Q}_{\mu\nu}$ is the second derivative of the quadrupole momentum associated to the energy density $\rho(\vec{x'})$ of the source:

$$Q_{\mu\nu} = \int (3x'_\mu x'_\nu - r^2\delta_{\mu\nu})\rho(\vec{x}')d^3x'$$

The conservation of the stress-energy tensor $T^{\mu\nu}{}_{;\nu} = 0$ is equivalent to the conservation of mass and linear and angular momentum; that implies the first contribution

to the emission of gravitational waves comes from the quadrupole term[1]. So, every spherically or axially symmetric system does not emit any gravitational radiation.

To estimate the order of magnitude of the intensity, we approximate the quadrupole momentum as:

$$Q \sim \epsilon M R^2 \quad \longrightarrow \quad \ddot{Q} \sim \frac{\epsilon M R^2}{T^2}$$

where the M is the total mass of the source, R is its typical dimension, T the typical variation time of the system and ϵ is the factor measuring the asymmetry of the mass distribution.

Since the speed of the masses inside the system is $v = R/T$, we can rewrite the expression 1.13 as:

$$h \sim \frac{1}{r}\frac{GM}{c^2}\left(\frac{v}{c}\right)^2 \tag{1.14}$$

Let's consider the constant factor in front of the amplitude $G/c^2 \sim 10^{-29} m^3/s^4 kg$: it is so small that only for astronomical sources (with mass of the order of $10^{30} kg$ and/or relativistic speed $v \sim c$) we can hope to detect gravitational waves.

1.3 Sources

There are several kinds of astronomical sources of gravitational waves. We classify them on the base of frequency band:

- extremely low frequency $(10^{-18} - 10^{-13} Hz)$:
  - stochastic sources (primordial gravitational fluctuations amplified by the inflation era of the universe);
- very low frequency $(10^{-9} - 10^{-7} Hz)$:
  - stochastic sources (gravitational fluctuations due to fundamental force symmetry breaking);
- low frequency $(10^{-5} - 1\ Hz)$:
  - compact binary systems (white dwarves, neutron stars, black holes);
  - double massive black holes compact binary coalescences;
  - stochastic background (astrophysical and cosmological sources);
- high frequency $(1 - 10^4 Hz)$:
  - compact binary coalescences;
  - spinning neutron stars;
  - transient sources as stellar collapse, gamma-ray burst and supernovae;

[1] If we decompose a mass distribution in its multipole components, we have the first term proportional to M and the dipole proportional to MR. In a closed isolated system, the total mass and the linear momentum are conserved. So the terms dM/dt and $d(MR)/dt$ are null and the quadrupole term is the first non-null term.

– stochastic background, expected from string theory or inflation model.

For each kind of source it is possible to evaluate the detection rate $\dot{N}$, i.e. the number of gravitational signals which are expected to come from the source in the time unit. This rate depends either on the emitted gravitational signal and on the horizon visible from the detector [18]:

$$\dot{N} = R \cdot N_G \tag{1.15}$$

where N_G is the number of galaxies accessible from the detector and R is the rate of formation for a fixed kind of source.

The number N_G is a function of the horizon detection distance D_{hor}, dependent from the detector sensitivity:

$$N_G = \frac{4}{3}\pi \left(\frac{D_{hor}}{1Mpc}\right)^3 (2.26)^{-3}(0.0116) \tag{1.16}$$

where the correction factor 2.26 includes the average over all sky locations and orientations and the factor 0.0116 is the extrapolation density of MWEG (Milky Way Equivalent Galaxy) in space.

Formulae 1.15 and 1.16 are used in this work for reporting the calculated detection rates for the Virgo+ and Advanced Virgo gravitational wave interferometer, described in Chapter 2.

1.3.1 Neutron Stars

When a spinning neutron star is not axisymmetric, it emits continuos and monochromatic gravitational waves at twice its rotational frequency.

There are different causes which can determine the asymmetry:

1. the high spinning rate of a neutron star (up to $500Hz$) induces some equatorial bulge and flattened poles; furthermore the magnetic field could cause the star not to spin around its symmetry axis, leading to a time variation of the star quadrupole momentum;

2. the star may have some inhomogeneities in its core or crust, set up during its formation or after some convectively unstable motion;

3. the presence of an accretion disc with an angular momentum not aligned with the one of the neutron star;

4. classical and relativistic instabilities (as glitches and r-modes) in the neutron star fluid, which could cause the star to radiate energy in the form of gravitational waves.

At present there are almost 2000 neutron stars known as pulsar from their radio or x-ray emissions. However in our galaxy we expect to have at least 10^8 spinning neutron stars (most of them in binary system) that rise roughly at a rate of one every 30 years.

It is possible to evaluate the gravitational signal coming from a *known pulsar* [5]. The gravitational signal amplitude is given:

$$h_0 = \frac{16\pi^2 G}{c^4}\frac{\epsilon I_{zz} f^2}{r} \tag{1.17}$$

where I_{zz} is the moment of inertia with respect to the rotation axis z, f is the sum of the star rotation frequency and the precession frequency, r is the distance from the star and ϵ is the equatorial ellipticity, defined in terms of the principal axis of inertia:

$$\epsilon = \frac{I_{xx} - I_{yy}}{I_{zz}}$$

Replacing the physical constants in the eq. 1.17, we obtain:

$$h_0 = 4.23 \cdot 10^{-25} \left(\frac{f}{100Hz}\right)^2 \left(\frac{\epsilon}{10^{-5}}\right) \left(\frac{I_{zz}}{10^{38} kg\, m^2}\right) \left(\frac{1kpc}{r}\right)$$

The ellipticity is not known in principle, but sometimes estimated by attributing all the observed spin-down of pulsars $\dot{P}$ to the gravitational radiation; if the change in the rotational energy $E_{rot} = I_{zz}\Omega^2/2$ of a neutron star rotating with angular velocity Ω is equal to gravitational waveluminosity, the ellipticity can be written as:

$$\epsilon = 5.7 \cdot 10^{-6} \left(\frac{P}{10^{-2}s}\right)^{3/2} \left(\frac{\dot{P}}{10^{-15}}\right)^{1/2}$$

From the observation of the Crab pulsar we have $\epsilon \leq 7 \cdot 10^{-4}$; instead the maximum value allowed by standard equations of state for neutron star matter is $\epsilon \sim 5 \cdot 10^{-6}$. So, it is evident that the ellipticity estimation through gravitational wave is just an upper limit.

Thus, we can evaluate the maximum expected gravitational signal. Potentially interesting sources are within our galaxy, thus at a distance of $d \sim 10kpc$. The standard value of the moment of inertia is $I \sim 10^{38} kg\ m^2$. The maximum signal frequency is below $2kHz$. With this value, the expected gravitational signal is $h_0 \sim 5 \cdot 10^{-23}$.

The weakness of the signal and the need to integrate it over long periods (more than one year), lead to data analysis complications: in particular for the Doppler shift, due to the source-detector relative motion.

In fig. 1.2 the known pulsar spin-down limits are reported, calculated from the VSR4 data taking of Virgo+. A detection threshold based on a false alarm rate of 1% and a false dismissal rate of 10% is assumed.

For what concerns *unknown pulsars*, the aim is to find neutron stars that are electromagnetically invisible, either because their radio pulses are not beamend towards us or because they have a very low magnetic field.

Such search requires a large parameter space study, i.e. sky location, frequency and frequency derivatives; for that reason, it is computationally limited because of the large number of templates, which grow up faster than the observational time. In particular there can be limitations, as the increase of false alarm rate or the lost of

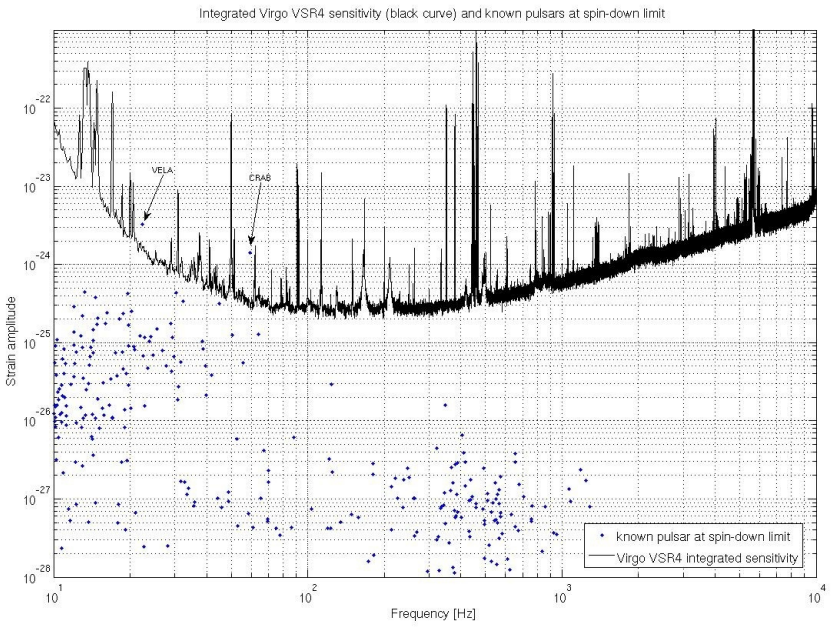

Figure 1.2: upper limits and spin-down limits for known pulsar; Virgo+ detector sensitivity curve plots the minimum detectable amplitude of the gravitational wave averaged over sky positions and pulsar orientations.

SNR by searching for a gravitational signal with a template which does not match exactly the real signal.

To partially solve that computational cost, semi-coherent methods are used. They rely on breaking up the full data sample into shorter segments of duration T_{coh}, analyzing them coherently and combining incoherently the power from the different segments. There are a number of different techniques available for performing the incoherent combination.

Typically the output of this wide-area search is a set of candidates, i.e. points in the source parameter space with values of a given statistic above a threshold. These candidates are then analyzed in a deeper way by making coincidences with another set of candidates coming from a different dataset, followed by a full coherent analysis on the surviving candidates, in order to confirm or reject them.

Glitches

Many radio pulsar exhibit glitches, events in which the source is seen to increase suddenly in the angular velocity Ω and in the spin-down rate $\dot{\Omega}$, followed by a relaxation period towards stable secular spin-down.

Glitches have been observed for the Crab, the Vela and some other pulsars. The typical intervals between these events vary from several months to years. The magnitude of the jumps in the rotation and spin-down rate are of the order $\Delta\Omega/\Omega \sim 10^{-8} - 10^{-6}$ and $\Delta\dot{\Omega}/\dot{\Omega} \sim 10^{-4} - 10^{-2}$.

Despite the large number of observational data, glitches remain an enigma from

the theoretical point of view. Some models have been developed in order to explain the nature and the characteristics of glitches [6]:

- they could be related to the existence of superfluids in the interior of neutron stars, which cause a transfer of angular momentum from a superfluid component to the rest of star (including the crust and the charged matter in the core) [7];
- the observed persistent increase in the spin-down rate, called offset, suggests that there is an increase in the spin-down torque acting on the star. This can be a consequence of variations in direction or in magnitude of the star magnetic moment. Such variations could be driven by starquakes occurring when the crust becomes less oblate, as a consequence of spin-down. Repeated starquakes (or core-quakes) can increase the angle between the rotation and magnetic axes to large values [8].

Anyway, it is possible to evaluate the available energy that may be radiated at a glitch event. For example, the Vela pulsar shows regular large glitches with a frequency change of the order of 10^{-6}. They may release an amount of energy of the order of $10^{35}J$. That energy may not be associated completely with the gravitational emission, since it depends on the detailed glitches mechanism and the source asymmestry.

Secular instabilities and r-modes

From the classical theory of Newtonian MacLaurin spheroids one finds that rotating axisymmetric fluid bodies become unstable towards non axisymmetric deformations due to a dynamical instability. The parameter which manages that instability is:

$$\beta = \frac{E_{rot}}{U_{grav}}$$

where E_{rot} is the rotational energy and U_{grav} is the star gravitational potential energy. For $\beta \geq \beta_{dyn} \equiv 0.27$, the spheroid goes unstable.

A **secular nonaxisymmetric instabilities** may set in at lower β value, i.e. $\beta \geq \beta_{sec} \equiv 0.1375$, though, due to its secular nature, has longer growth times than the dynamical instability.

Secular instabilities can be driven by two kinds of mechanism:

1. the Chandrasekhar-Friedman-Schutz instability (CFS) driven by gravitational radiation reaction [9] [10];
2. the viscosity-driven instability [11].

Chandrasekhar [12] studied the evolution of rotating incompressible newtonian stars without viscosity.

A newborn rapidly rotating highly condensed star, formed as a result of a collapse, may have a rotating configuration similar to a Jacobian ellipsoid at its dynamical stability limit: the amplitude of the emitted gravitational waves is small, because the star is nearly axisymmetric. After a cool-off phase, thanks to the emission of

gravitational waves, it is possible that the final value of β is still greater than β_{sec}, so that the development of a secular instability follows.

The evolution of a Jacobi ellipsoid as it radiates gravitationally can be determined in the standard linearized theory of gravitational wave. The rate of radiation of the angular momentum L by a mass is:

$$\frac{dL}{dt} = -\frac{32G}{5c^5}(I_{xx} - I_{yy})^2\Omega^5 \tag{1.18}$$

where I_{xx} and I_{yy} are the momentum of inertia tensor in the equatorial plane and Ω is the angular velocity. Integrating eq. 1.18, we find that during a gravitational wave emission, the angular velocity Ω of the compact star will increase (as shown in fig. 1.3) and the object will approach a point of bifurcation[2] where it becomes spheroidal and nonradiating (for istance, a MacLaurin spheroid).

But once the point of bifurcation is achieved, gravitational radiation reaction will make the configuration secularly unstable and it may proceed towards fragmentation.

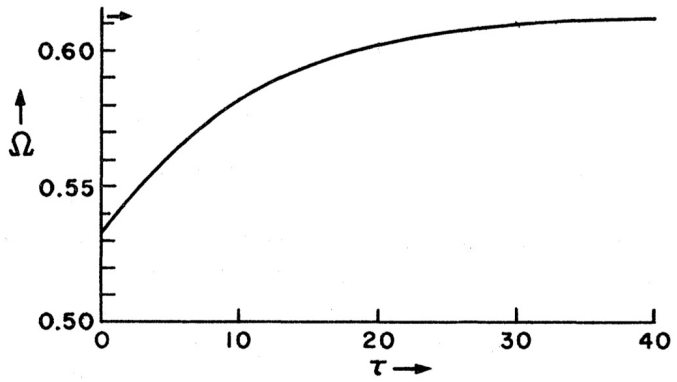

Figure 1.3: the evolution of the Jacobi ellipsoid by gravitational radiation; the angular velocity of rotation Ω in the unit $\pi G\rho$ with respect to the time τ in the unit $(25/18)(\bar{a}/R_S)^3(\bar{a}/c)$, where $\bar{a}$ is the geometric mean of the ellipsoid axes and R_S is the Schwarzschild radius.

In this phase the angular velocity Ω decreases and the final configuration is a Dedekind ellipsoid (i.e. a triaxial ellipsoid) with zero angular velocity which, obviously, does not emit gravitational radiation. As a result, the amplitude of the gravitational wave increases very rapidly at first, reaches a maximum during the fragmentation, then slowly decreases to zero again when Dedekind ellipsoid configuration is achieved (fig. 1.4).

Approximating the neutron star with a spinning bar, it is easy to estimate the amplitude of the emitted gravitational wave; it emits gravitational wave at twice its rotational frequency (due to its π-symmetry) with amplitudes $h_{bar} \propto MR^2\Omega^2/D$

[2]A bifurcation is a place or point of branching or forking into "qualitatively" or topological new types of behavior. It occurs when a small smooth change made to the parameter values (the bifurcation parameters) of a system causes a sudden change, rather than a slow and gradual evolution. Furthermore, it is a transition of a non-linear system into a realm where new laws dictate what will occur to the system.

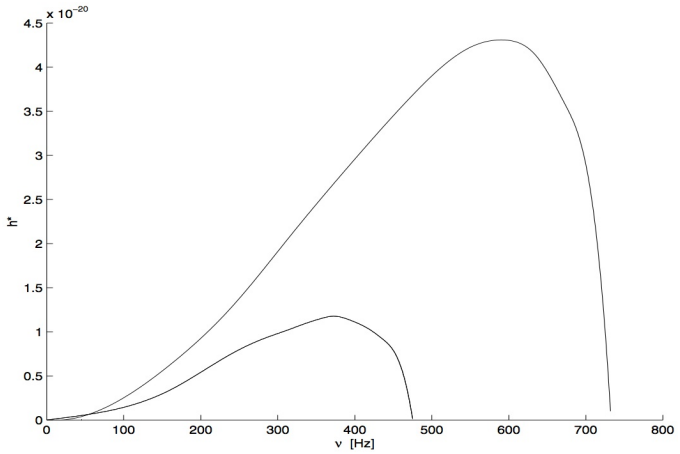

Figure 1.4: amplitude of the gravitational wave signal, as a function of the frequency, emitted by a secularly unstable neutron star, evolving from a MacLaurin spheroid toward a Dedekind ellipsoid; the upper curve corresponds to $\beta = 0.24$ and the lower one to $\beta = 0.20$, both for a star described by a polytropic equation of state with $n = 0.5$.

where M is the bar's mass, $2R$ its length, Ω its angular velocity and D the source-detector distance. Using the Newtonian quadrupole approximation, one can derive:

$$h_{bar} \approx 4.5 \cdot 10^{-21} \left(\frac{\epsilon}{0.1}\right) \left(\frac{f}{500Hz}\right)^2 \left(\frac{10kpc}{D}\right) \left(\frac{M}{0.7M_\odot}\right) \left(\frac{R}{12km}\right)^2$$

where ϵ is the ellipticity of the bar.

For what concerns the viscosity driven instability, general relativistic effects suppress it, on the contrary to what happens for the Chandrasekhar instability; so the viscosity instability can take place only for cold neutron stars described by very stiff equation of state or, for instance, during matter accretion from a companion star.

The **r-modes** are axial fluid oscillations, governed by the Coriolis force and whose coupling takes place through the current multipoles, instead of the mass multipoles (see eq. 1.12). Gravitational radiation makes a r-modes unstable if the gravitational radiation time scale is smaller, in absolute value, with respect to the viscous time scale. This condition is verified if the angular velocity of the star is greater than a critical value Ω_C depending on the star temperature (see fig. 1.5) [13].

The r-modes are described as large scale oscillating currents that approximatively move along the equipotential surfaces of the rotating star (see fig. 1.6); for this reason they are also called convective modes [14].

We can describe the MacLaurin shaped neutron star, which is a azimuthal non-axisymmetric structure, in terms of modes m with spatial structure proportional to $e^{im\phi}$, where ϕ is the azimuthal angle. At the lowest order in the angular velocity of the star Ω, the frequency of a mode of harmonic index m is:

$$\sigma_m(\Omega) = -\frac{(m-1)(m+2)}{(m+1)}\Omega$$

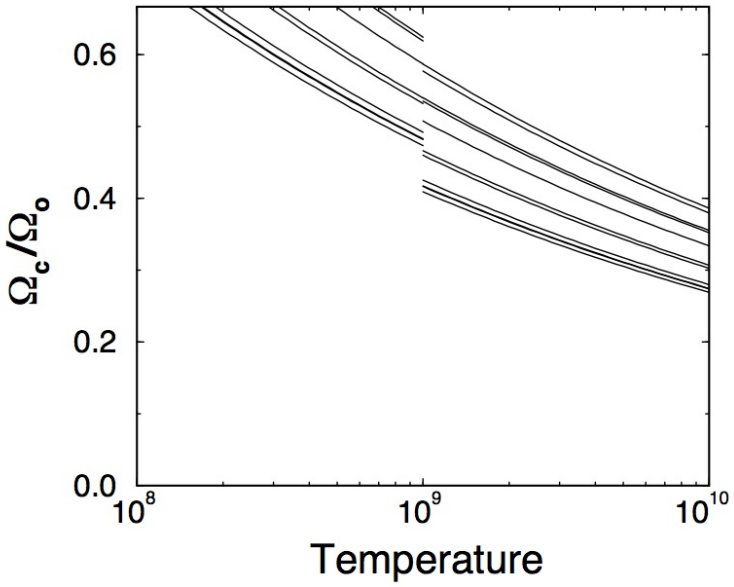

Figure 1.5: critical angular velocity Ω_C for different realistic equations of state and for a neutron star of $1.4M_\odot$ as a function of temperature; the discontinuity at $T \sim 10^9 K$ corresponds to the superfluid transition $\Omega = \sqrt{\pi G \rho}$.

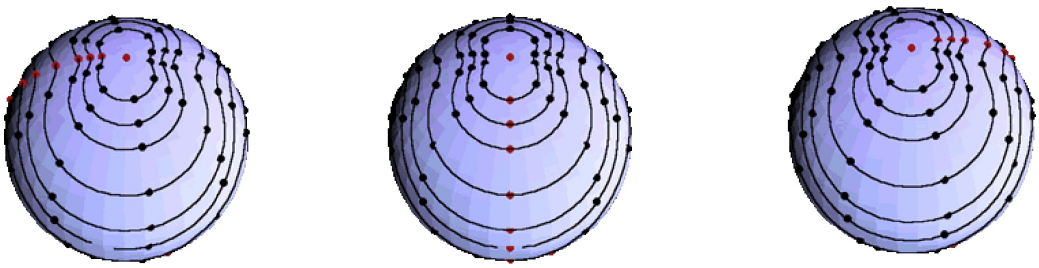

Figure 1.6: an r-mode of a rotating star, as seen by a nonrotating observer in three different sequential moments. The dots are buoys floating on the surface and moved around by the r-mode, in addition to the counterclockwise rotation of the star. The lines indicate where chains of buoys would float. The red buoys would have a fixed latitude on an unperturbed star, so the star is rotating faster than the r-mode pattern speed.

and the frequency of the emitted gravitational waves is:

$$\nu(\Omega) = -\frac{\sigma_m(\Omega)}{2\pi}$$

The amplitude of the mode is small at the beginning but then it increases, until hydrodinamic effects become important and a non-linear evolution regime is reached. The emitted gravitational wave reaches a maximum value given by:

$$h_0 \approx 4.4 \cdot 10^{-24} \left(\frac{\Omega_0}{\bar{\Omega}}\right)^3 \left(\frac{20Mpc}{r}\right) \tag{1.19}$$

where Ω_0 is the initial angular velocity of the star, $\bar{\Omega} = \sqrt{\pi G \bar{\rho}}$ and r is the distance between the source and the detector.

When the non-linear phase is reached, probably a saturation effect occurs and the mode no longer grows. At that point the excess angular momentum of the star is radiated away through gravitational radiation and the star spins down until angular velocity and temperature are suffciently small so that the crust solidifies and r-modes are completely damped. In this phase the amplitude of the emitted gravitational wave is exactly equal to eq. 1.19.

1.3.2 Compact Binary Coalescences

Inspiraling compact binaries, containing neutron stars and/or black holes, are promising sources of gravitational waves for interferometer detectors. The two compact objects steadily lose their orbital binding energy by emission of gravitational radiation; as a result, the orbital separation between them decreases, and the orbital frequency increases. Thus, the frequency of the gravitational wave signal, which equals twice the orbital frequency for the dominant harmonics, "chirps" in time (i.e. the signal becomes higher and higher pitched) until the two objects collide and merge.

The dynamics of the coalescence of the compact binary can be described in three phases (see fig. 1.7):

1. the inspiral phase, in which the star orbits contract adiabatically in hundreds of millions of years; the angular velocity increases and the separation between star decreases;

2. the merger, in which the two stars are moving at a third of the speed of light, until the collision;

3. the ring-down, when the two stars have just merged to form a super-massive object, settling down to a quiescent state.

During the **inspiral phase**, the system loses energy through gravitational wave emission. The luminosity of emitted gravitational radiation is low and the emission period is longer than orbital one: so, we can consider the process as adiabatic. The dynamics can be solved using approximation methods, as the Newtonian mechanics or, for a more detailed solution, the post-Newtonian expansion [15].

Using the Newtonian approach, the system can be described as two structureless point-particles, characterized solely by their masses m_1 and m_2, their separation a,

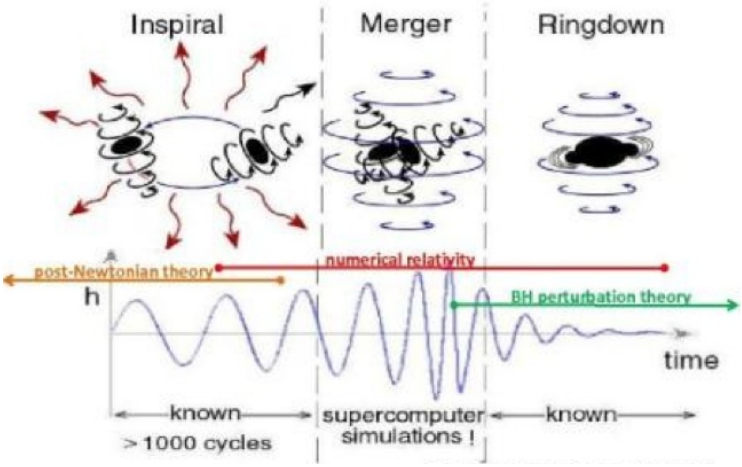

Figure 1.7: gravitational signal emitted from a compact binary system during the coalescence; the three phases are described in the text.

their orbital period P and possibly their spins; the two stars are moving on a quasi-circular orbit.

For this kind of bound system, it is easy to estimate the amplitude of gravitational signal using eq. 1.14 and the Keplerian third law [16]:

$$G(m_1 + m_2) = 4\pi \frac{a^3}{P^2} \tag{1.20}$$

Re-writing in eq. 1.20 the period with its expression in function of velocity, we obtain:

$$\left(\frac{v}{c}\right)^2 \approx \frac{G(m_1 + m_2)}{c^2 a} \tag{1.21}$$

Substituting eq. 1.21 in eq. 1.14, and after an accurate calculation for a binary star in a circular orbit (consisting in an average over the orbital period and orientation of the orbital plane) we have the gravitational signal amplitude:

$$h = \left(\frac{32}{5}\right)^{1/2} \frac{1}{r} \frac{G^{5/3}}{c^4} \frac{m_1 m_2}{(m_1 + m_2)^{1/3}} (\pi f)^{2/3} \tag{1.22}$$

where r is the detector-source distance. The emitted gravitational wave frequency is:

$$f = \frac{1}{\pi} \left(\frac{G(m_1 + m_2)}{a^3}\right)^{1/2}$$

Note that the amplitude h depends on a particular combination of masses, called *chirp mass*:

$$\mathcal{M} = \frac{(m_1 m_2)^{3/5}}{(m_1 + m_2)^{1/5}}$$

so that eq. 1.22 can be written as:

$$h \sim \frac{1}{r} \mathcal{M}^{5/3} f^{2/3}$$

The energy spectrum is:

$$\frac{dE}{df} = \frac{(\pi G)^{2/3}}{3}\mathcal{M}^{5/3} f^{-1/3}$$

It is evident that when the two stars approach, the separation a decreases and the emitted gravitational wave frequency and amplitude increase: the final signal is called *chirp* (fig. 1.8).

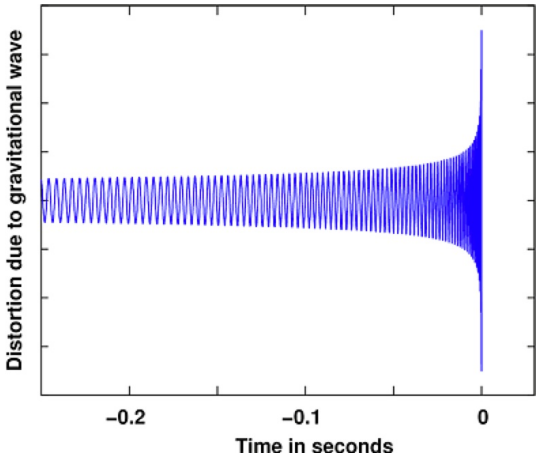

Figure 1.8: gravitational wave signal emitted from a coalescing binary system during the inspiral phase; in this case we do not take into account the spin of the stars.

If we use the post-Newtonian description to obtain the inspiral signal, the spin-orbit coupling must be taken into account. In fact, when the binary companions are spinning, the signal is modulated due to spin-orbit and spin-spin couplings. These modulations encode the parameters of sources (their masses, spins, inclination of the orbit, etc.) most of which can be extracted very accurately by matching the observed signals onto general relativistic predictions. In fig. 1.9 it is evident the deforming effects of the spin.

The inspiral phase ends when the two stars come into contact:

- if the two stars are compact objects, the contact happens when the separation is equal or less the radius of the innermost stable circular orbit ($a_{ISCO} \sim 9 \cdot 10^3 M/M_\odot m$); the gravitational signal frequency of the transition point will be:

$$f_t \approx 4kHz \left(\frac{M}{M_\odot}\right)^{-1}$$

- if one of the two stars is not a compact object, it happens when the separation is of the order of magnitude of the star dimension ($a_{dim} \sim 10^7 m$); the inspiral phase ends at frequency:

$$f_t \approx 0.1Hz \left(\frac{M}{M_\odot}\right)\left(\frac{l}{a_{dim}}\right)^{-3/2}$$

which is lower than in the previous case.

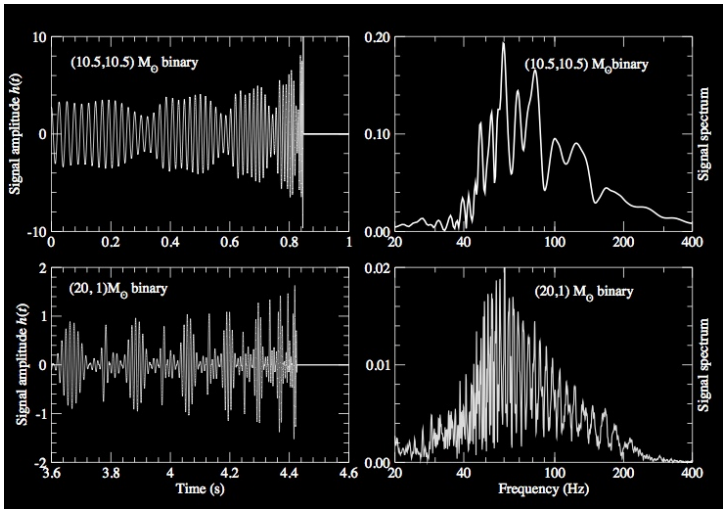

Figure 1.9: wave forms from two compact binary systems, considering spin-orbit interaction. Left panels show the time-domain waveforms, right panels show the frequency spectrum. The upper two panels show a binary composed of two equal masses; the waveform's modulation is due to interaction between the spins of the bodies and the orbital angular momentum. The lower panels show a binary composed of a neutron star and a black hole. In this case, the signal amplitude is smaller, the duration is longer due to the larger mass ratio, and the signal modulation is stronger as the spin-orbit precession of the orbital plane is greater.

Then **merger phase** begins; in this phase the orbital evolution is so rapid that adiabatic approximation previously used is not so good. The two masses go through a violent dynamical fusion that leads to a black hole on a dynamical timescale, releasing a fraction of their rest-mass energy in gravitational waves. However, a significant fraction of the stellar material could retain too much angular momentum to cross the black hole horizon promptly. This creates a temporary accretion disk around the black hole, whose formation over timescale longer than the dynamic time, can power a gamma-ray burst jet, as we can see in section 1.3.4.

The post-Newtonian approximation is not accurate when the two compact objects get close to each other. To predict the dynamics of the bodies during this phase the full non-linear structure of Einstein's equations is required, as the problem involves strong relativistic gravity and tidal deformation and disruption. The only way to solve the problem is to use numerical simulations of mergers.

Recently simulations on black hole systems have been highly successful, and analytical and phenomenological models of the merger dynamics have been developed [17]. Such progress allows to increase the accuracy and physical fidelity on gravitational signal waveform, to include a larger numbers of gravitational emission cycles before merger and to better understand the full parameter space of binary system of arbitrary spins and mass ratios.

On the contrary for neutron star binaries, the merger phase is not well understood, as it is complicated by a number of unknown physical effects, such as the equation of state and the magnetic field.

The merger signal lasts for a very short time: milliseconds, in the case of stellar mass black holes, to seconds, in the case of the heaviest systems.

During the **ring-down phase** the emitted radiation can be computed using perturbation theory and it consists of a superposition of quasi-normal modes of the compact object that forms after merger.

In the case of black holes, these modes carry a unique signature that depends only on the mass and spin angular momentum; in the case of neutron stars, it depends also on the equation of state of the supra-nuclear matter.

As in the merger phase, the signal lasts for a very short time interval: the gravitational waves are emitted in two or three cycles and they survive from milliseconds to seconds, depending on the mass of the final object. However, the superposition of different modes means that the signal can have an interesting and characteristic structure.

For what concerns detection rates, there are significant uncertainties in the astrophysical predictions for compact binary coalescences. These arise from the small sample size of observed galactic binary pulsars, from the poor constraints for predictions based on population synthesis models and from lack of confidence in a number of astrophysical parameters.

Anyway, the simplest assumption is that the coalescence rates can be assumed proportional to the stellar birth rate in the nearby galaxies: the blue luminosity traces well the star formation rate for the spiral galaxies, but ignores the contribution of older populations in elliptic galaxies.

To derive the coalescence rate R in eq. 1.15 for a double neutron star system, it is possible to use two methods:

1. extrapolation from the observed systems detected via pulsar measurements.

   This method has few free parameters, but it does suffer from a small sample of observed systems in our galaxy and the implicit assumption that these are a good representation of the total neutron star population. The difficulties on neutron star binary population reconstruction consist in the lack of knowledge about the pulsar luminosity distribution. Such distribution is described by two variables: the minimum pulsar luminosity and the negative slope of the pulsar luminosity power law. Different choice of these variables, even if still consistent with observations, could change the merger rates by an order of magnitude.

2. extrapolation from population synthesis codes.

   This method contains a number of free parameters as kick velocities, common-envelope efficiency and the companion mass distribution. Some studies choose not to use the empirical data taken from observation: in this case, flat priors are used but a small part of parameter space is explored. Other studies apply observational constrains, but in this way they are not completely independent from the estimates obtained via the first method, since the same data are used.

Even if the second method is often not complete or accurate (it gives coalescence rates which differ from the first method of two orders of magnitude), it is the only

one available for estimating coalescence rates for neutron-star/black-hole systems or double black hole systems, since they have not been observed electromagnetically.

For the double black hole binaries two different coalescence scenarios are possible:

- the isolated binary evolution scenario, which is expected to be the dominant from the double neutron star systems;
- the dynamical formation scenario, in which dynamical interaction in a dense stellar environments could play a significant role in forming the binary system.

The detection rates $\dot{N}$, calculated as in eq. 1.15, are reported in table 1.1 [18]. These values are determined assuming that all neutron stars have a mass equal to $M_{NS} = 1.4M_{\odot}$ and all black holes have mass equal to $M_{BH} = 10M_{\odot}$. Even if the neutron stars and back holes mass distribution cover a wide range of values, the uncertainties in the coalescence rates dominate errors from this simplifying assumption about component masses.

Interferometer	Source	$\dot{N}_{re} yr^{-1}$
Initial	NS-NS	0.02
	NS-BH	0.004
	BH-BH	0.007
Advanced	NS-NS	40
	NS-BH	10
	BH-BH	20

Table 1.1: detection rates for compact binary coalescence sources.

In table 1.1 there are the detection rates obtained for compact binary systems. I report only the realistic detection rate $\dot{N}_{re}$, but there are other rates which can be calculated considering different probability distributions (see [18] for more details).

The PSR1913+16 binary system

The existence of double neutron star binary system is reported by lots of observations; the most famous for gravitational wave physics is the PSR1913+16, studied by Hulse and Taylor [19]. This system represents the only indirect prove of the emission of gravitational waves.

If we consider the gravitational potential of a system, it is possible to determine the decrease of a binary system orbital period due to gravitational wave emission.

The emitted gravitational wave luminosity can be written as [3]:

$$L_{gw} = \frac{G}{5c^5} \sum_{k,n=1}^{3} \left(\frac{\partial^3 Q_{kn}(t - r/c)}{\partial t^3} \frac{\partial^3 Q_{kn}(t - r/c)}{\partial t^3} \right)$$

where Q_{kn} is the quadrupole momentum tensor and r is the detector-source distance.

Writing the quadrupole momentum for a two neutron stars binary system, we can derive the gravitational energy for time unit:

$$L_{gw} = \frac{dE_{gw}}{dt} = \frac{32G^4}{5c^5} \frac{\mu^2 M^3}{a^5} \tag{1.23}$$

where $\mu = (m_1 m_2)/(m_1 + m_2)$ is the reduced mass, M is the total mass of the system and a is the separation.

In the adiabatic approximation, the system evolves slowly and the emitted gravitational energy is equal to the variation of orbital energy:

$$\frac{dE_{orb}}{dt} + L_{gw} = 0 \tag{1.24}$$

The orbital energy can be evaluated considering a Keplerian orbit:

$$E_{orb} = -\frac{1}{2}\frac{G\mu M}{a} \tag{1.25}$$

So, substituting eq. 1.23 and eq. 1.25 in eq. 1.24:

$$-\frac{2}{3}\frac{E_{orb}}{P}\frac{dP}{dt} + \frac{32G^4}{5c^5}\frac{\mu^2 M^3}{a^5} = 0$$

we can find the orbital period variation:

$$\frac{dP}{dt} = \frac{3}{2}\frac{P}{E_{orb}}L_{gw}$$

where P is the orbit period.

After 30 years of observations the measured value is $dP/dt = (-2.4184 \pm 0.0009) \cdot 10^{-12}$ (fig. 1.10).

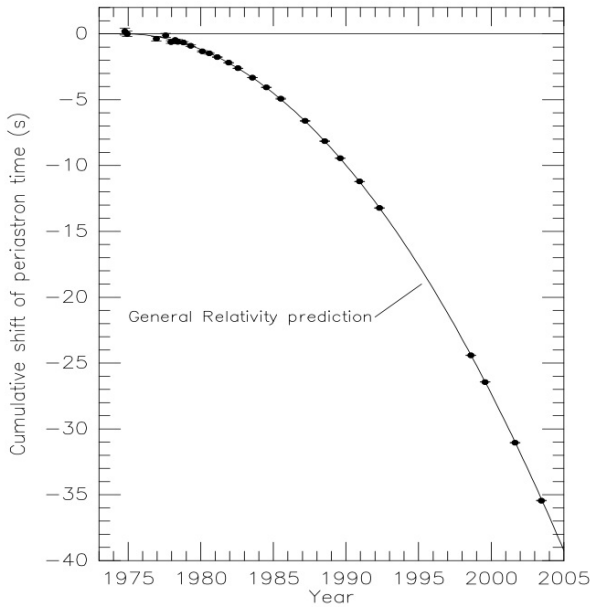

Figure 1.10: orbital decay of PSR B1913+16. The data points indicate the observed change in the epoch of periastron with date while the parabola illustrates the theoretically expected change in epoch for a system emitting gravitational radiation, according to general relativity.

1.3.3 Supernovae

During a stellar collapse with an explosion mechanism, there are the emission of gravitational waves and the formation of a neutron star or a black hole.

These stellar systems are produced by many different scenarios, but they can be loosely grouped into two categories:

- the collapse of oxygen-magnesium-neon and carbon oxygen white dwarfs pushed beyond the Chandrasekhar limit (Type I supernovae);
- the collapse of iron or oxygen-magnesium-neon stellar cores of massive stars that become too large to support themselves (Type II supernovae).

The Type II supernovae have been long studied and there are different scenarios for what concerns gravitational wave emission. In this chapter I treat in particular this kind of supernovae.

The core of massive stars ($8 - 10M_\odot \leq M \leq 100M_\odot$ at zero-age main sequence) is supported by a combination of thermal and degeneracy pressures. It it composed primarily of electron-degenerate iron-group nuclei in the final stages of their exoergic nuclear burning. When the mass is too large for these pressures to support the star core, it begins to compress and heat up. The compression leads to electron capture, neutrino emission, and ultimately, dissociation of the elements. Electron capture reduces the support from degeneracy pressure while dissociation of elements remove thermal support [20]. Let us see in detail what happens:

Collapse Once such an iron core exceeds its effective Chandrasekhar mass, it grows gravitationally unstable: collapse follows, leading to dynamical compression of the inner core material to nuclear densities.

Core bounce The nuclear equation of state stiffens, resulting in the rebound of the inner core ("core bounce").

Shock wave A hydrodynamic shock wave is launched at the outer edge of the inner core and propagates outward, colliding with the still infalling outer core. This process is one of the most energetic of the universe, releasing an energy of:

$$E \sim 3 \cdot 10^{46} \left(\frac{M}{M_\odot}\right)^2 \left(\frac{10km}{R}\right) J$$

where M is the mass of the progenitor and R its dimension. About 99% of this energy goes in neutrinos in a timescale of $\sim 100s$. About 1% is tansferred in kinetic energy of ejecta and only a 10^{-4} fraction is emitted as electromagnetic waves.

Here a problem stands: it is not clear at all why Type II supernovae explode.

In fact the shock wave quickly loses energy and stalls, because of the dissociation of heavy nuclei and the energy losses due to neutrinos that stream away from the postshock region. So, without a shock revival, it is impossible to have a supernova explosion and a compact object "quiescent" formation is inevitable.

The shock wave must be revived to plow through the stellar envelope, blow up the star, and produce a supernova explosion, leaving behind a neutron star (or even a black hole, forming via fall-back accretion). Such transfer of gravitational energy to revive the shock wave must occur sooner than $1 - 1.5s$ after the bounce (depending on progenitor star structure setting the rate of mass accretion) to produce a compact remnant as a pulsar.

The supernova explosion mechanism may involve a combination of heating of the postshock region by neutrinos, multi-dimensional hydrodynamic instabilities, proto-neutron star pulsations, magnetic fields and nuclear burning.

In literature three mechanisms are presently discussed:

1. the *neutrino mechanism* is based on postbounce neutrino energy deposition behind the stalled shock and appears to require convection and the standing-accretion-shock instability (SASI instability) to function (except for the very lowest-mass massive stars which may explode even in spherical symmetry). However, it is not yet clear how the neutrino mechanism's efficiency varies with progenitor mass and structure and what its detailed dependence on the high-density nuclear equation of state may be;

2. the *magneto-hydrodyamic (or MHD) mechanism*, probably operating only in the context of rapid progenitor rotation, depends on magnetic-field amplification during collapse and at postbounce times. It leads to explosions that develop in jet-like fashion along the axis of rotation and may also be relevant in the context of long-soft gamma-ray bursts and could be a precursor, setting the stage for a later GRB (see sec. 1.3.4);

3. the *acoustic mechanism* for core-collapse requires the excitation of large-amplitude proto-neutron star pulsations (primarily g-modes) by turbulence and SASI instability modulated accretion downstreams. These pulsations are damped by the emission of strong sound waves that steepen to shocks and deposit energy in the postshock region, eventually leading to late explosions after $1s$ from bounce. This mechanism appears to be sufficiently robust to blow up even the most massive and extended progenitors.

It is very difficult to understand what kind of mechanism leads to supernova explosion only via astronomical observations. Theoretical models and simulations can be tested using secondary observables, as ejecta morphology, compact remnant mass and proper motion or pulsar spin and magnetic field. The only messengers that could bring information about the inner core physical processes are the gravitational waves and neutrinos: both of them are produced deep inside the supernova and can travel through the universe without interactions.

Simulating gravitational collapse is a very active area of numerical astrophysics. Modeling stellar core collapse and the postbounce evolution of the supernova core is a multi-scale multi-physics problem that involves lengthscales from the extended pre-supernova stellar core (thousands of kilometers) down to small-scale turbulences in the postbounce flow (on the order of meters) and timescales from $\leq 10^{-6}s$ (the typical computational timestep) to up to $1 - 2s$ (the time for the development of a full explosion or for black hole formation to occur).

Furthermore an ideal and complete model should fully include three-dimensional hydrodynamics, general relativity, neutrino transport, realistic nuclear physics, MHD, magnetic fields and rotation. In general, some approximations can be used, as solving the hydrodynamics and radiation transports in Newtonian fashion, taking general relativity into account replacing the spherical component of the multipole decomponsition with Oppenheimer-Volkoff potential. In any case, gravitational signal can be derived using the approximation of the slow-motion weak field formalism.

We expect gravitational waves from supernovae explosion in three different phases [21]:

Bounce At core bounce, when the infalling material reaches nuclear densities and the collapse halts, the matter reaches its peak acceleration. If the collapse phase or the neutrino emission are asymmetric, either by asymmetries in the stellar structure or through rotation, this phase can lead to the strongest gravitational wave emission.

Post-bounce and Convection The convection above the proto-neutron star can also develop strong asymmetries as the convective cells merge into low-mode convection. This can lead to rapidly varying quadrupole moments in both matter and core.

Neutron Star Convection in the cooling neutron star could produce strong gravitational wave emission. Pulsations in the newly formed proto-neutron star may also produce a strong gravitational signal. But the most-studied gravitational wave source arises from bar-mode instabilities, in part because, if they develop, they may produce a gravitational signal that rivals both the bounce and convective gravitational wave signals (see sec. 1.3.1).

During the bounce phase, three different gravitational signal are identified which can be associated with distinct types of collapse or bounce dynamics (fig. 1.11):

- type I models undergo core bounce governed by the stiffening of the nuclear equation of state at nuclear density and "ring down" quickly into postbounce equilibrium. Their waveforms exhibit one pronounced large spike at bounce and then show a gradually damped ring down;

- type II models are affected significantly by rotation and undergo core bounce dominated by centrifugal forces at densities below nuclear. Their dynamics exhibits "multiple bounces", i.e. slow harmonic-oscillator-like damped bounce and re-expansion collapse cycles; this behaviour is reflected in the waveform by distinct signal peaks associated with every bounce;

- type III models are characterized by fast collapse (owing to a very soft subnuclear equation of state or very efficient electron capture), extremely small masses of the homologously collapsing inner core and low-amplitude gravitational waves and a subdominant negative spike in the waveform associated with bounce.

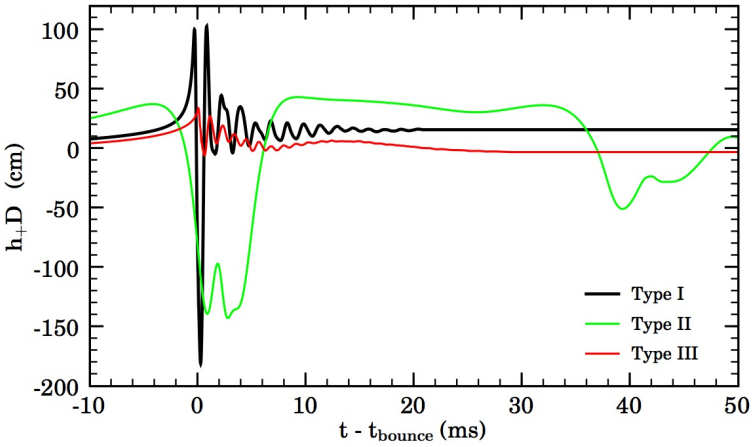

Figure 1.11: axisymmetric gravitational burst signal (h_+D in units of cm, where D is the distance of the source) as a function of time after core bounce for the three explained types.

In a typical supernova, simulations suggest that gravitational waves could extract between $10^{-11} - 10^{-7}$ of the total of available mass-energy; the frequency range of the signal would be around $100 - 1000Hz$, while the amplitude would be [22]:

$$h \sim 1.5 \cdot 10^{-21} \left(\frac{E}{10^{-7} M_\odot c^2}\right)^{1/2} \left(\frac{1ms}{T}\right)^{1/2} \left(\frac{1kHz}{f}\right) \left(\frac{10kpc}{D}\right)$$

where E is the emitted energy, T the time of emission, f the observed frequency and D the source-detector distance.

In particular for type I model supernova where the bounce is governed by a stiffening equation of state, it is possible to calculate the gravitational signal characteristics for three different iron core angular velocities [23]: the results are reported in table 1.2.

$\Omega_{core}(rad/s)$	$h_{max} \cdot 10^{-21}$	$E_{GW} \cdot 10^{-8}(M_\odot c^2)$	$f_{peak}(Hz)$
$\leq 1 - 1.5$	≤ 0.5	≤ 0.1	$700 - 800$
$1 - 2$ to $6 - 13$	$0.5 - 10$	$0.1 - 5$	$400 - 800$
$\geq 6 - 13$	$3.5 - 7.5$	$0.07 - 0.5$	$70 - 200$

Table 1.2: gravitational signal characteristics of rotating iron core collapse and core bounce based on the type I dynamics; the three distinct groups are based primarily on their precollapse central angular velocity Ω_{core}, h_{max} is the maximum gravitational wave strain amplitude (scaled to 10 kpc) at bounce, E_{GW} is the energy radiated away in gravitational waves, f_{peak} is the frequency at which the gravitational wave energy spectrum dE/df peaks.

For what concerns gravitational emission during postbounce and convective phase, these phenomena are intrinsically multi-dimensional and lead generically to time-varying mass quadrupole moments.

In postbounce evolution, convective instability is a central feature of core-collapse supernova. According to the Schwarzschild-Ledoux criterion, convective overturn develops in the presence of negative radial entropy or lepton composition gradients. These can be driven by:

- *prompt convection* which may occur immediately after bounce.

  As the stalling bounce shock passes through outer core material, it leaves behind a negative entropy gradient. Furthermore, following neutrino shock breakout and the associated burst of electron neutrinos, a negative lepton gradient arises at the outer edge of the proto-neutron star immediately below the neutrinosphere. The two negative gradients lead to a convectively unstable region according to the Schwarzschild-Ledoux criterion.

  Neutrino losses and neutrino energy deposition behind the stalling shock smooth out the large negative entropy gradient in the immediate postshock region, but prompt convection can still develop rapidly and last for $\sim 10 - 20ms$ if significant, but not well known, seed perturbations are present in the immediate postbounce flow.

- *proto-neutron star (PNS) convection.*

  Owing to a negative radial lepton gradient, proto-neutron stars are unstable to convective overturn in a radial interval from $\sim 10km$ to $\sim 30km$. Convection sets in $\sim 20 - 50ms$ after bounce and may last for several seconds as the proto-neutron star slowly contracts and deleptonizes after a successful supernova explosion. If the explosion is not successful (or weak) and a black hole is formed, proto-neutron star convection and the associated gravitational wave emission stop abruptly. Moreover, if present, large-amplitude proto-neutron star core g-modes can distort convection and themselves lead to gravitational wave emission much stronger than that due to the convective motions.

- *neutrino convection* in the postshock heating region.

  Neutrino heating below the stalled shock peaks in the inner part of the gain region and decreases outward. This establishes a negative radial entropy gradient and makes the gain region unstable to convective overturn. Convection develops within $30 - 50ms$ after bounce in the gain region which extends at these times typically from $50 - 80km$ out to almost the radius of the stalled shock at $150 - 250km$. Furthermore the SASI instability is believed to be caused by either an advective-acoustic or a purely acoustic feedback cycle, leading to the growth of perturbations in the stalled shock.

Table 1.3 provides an overview of the gravitational wave emission from prompt, proto-neutron star and neutrino-driven convection. We provide rough values for typical h, emitted energies, typical emission frequencies and emission durations.

Finally for what concerns the second-generation interferometric gravitational wave detectors, the even optimistic estimate for detection rate is not more than $\sim 1 - 2$ events per century in the Milky Way ($D \sim 10 - 15kpc$) and the Magellanic Clouds ($D \sim 50 - 70kpc$).

Process	$h_{typ} \cdot 10^{-21}$	$E_{GW} \cdot 10^{-10}(M_{\odot}c^2)$	$f_{peak}(Hz)$	duration $\Delta t(ms)$
Prompt	$0.01 - 1$	$\leq 0.01 - 10$	$50 - 1000$	$0 - 30$
PNS	$0.02 - 0.05$	$\leq 1.3(\frac{\Delta t}{1s})$	$300 - 1500$	$500 - 1000$
Neutrino	$0.01 - 0.1$	$\geq 0.01(\frac{\Delta t}{100ms})$	$100 - 800$	$100 - 1000$

Table 1.3: estimates for the typical gravitational wave strain at $10kpc$, the typical emission frequency f, the duration of the emission Δt, and the emitted energy E_{GW}.

This number roughly doubles if one includes the entire local group ($D \sim 1Mpc$). In the region from $3 - 5Mpc$ a number of starburst galaxies increase the predicted and observed integrated supernova rate to $0.5\, yr^{-1}$. At a distance $D \sim 10Mpc$ it is $\geq 1\, yr^{-1}$.

1.3.4 Gamma-Ray Bursts

Gamma-ray bursts (GRB) are the most luminous explosions in the universe: they are short and intense bursts of about $100keV - 1MeV$ which last for $10ms - 1000s$. They were accidentally discovered in 1973 and at first they have thought originated by galactic neutron stars. Then, through follow-up observations of the X-ray, optical and radio emission of GRB and thanks to determination of their sky location, redshift and host galaxy, their extra-galactic origin at cosmological distances became evident. Their principal characteristics are [24]:

- the isotropy on the sky;
- the lack of bright persistent counterparts;
- their non-thermal spectrum.

The cosmological origin of GRB immediately implies that they are much more luminous than previously thought. They release $10^{44} - 10^{46} J$ or more in a few seconds. Furthermore they present sub-second luminosity fluctuations, implying a huge photon density in a small volume; the inner engine that produce the jet must be compact.

For these reasons, such events are rare in the Universe. In fact the dedicated detectors, like BATSE or SWIFT, observe on average one burst per day, that corresponds, with the simplest model, assuming a rate which does not change with redshift, to one burst per million years per galaxy. Of course the rate could be higher if there is a significant beaming of the gamma-ray emission.

Even if there are a lot of data and observations about GRB, their origin and counterparts is almost uncertain.

A generic scheme, called "fireball model", has been developed in the last years, then confirmed by observations. This model presumes that a ultra-relativistic flow, a jet pointed in our direction, is converted to radiation in a optically thin region. The radiation from the jet is greatly amplified by the Doppler boost, since the flow Lorentz factor is of several tens to several hundreds.

But not all the energy of the relativistic matter can be converted to radiation by this process; the remaining kinetic energy will most be dissipated via external shocks

that will produce an "afterglow" in different wavelength. The typical luminosity curve is shown in fig. 1.12 [25].

Thus, the prompt emission is produced within the jet, while an afterglow is due to the interaction of the jet with the matter surrounding the source.

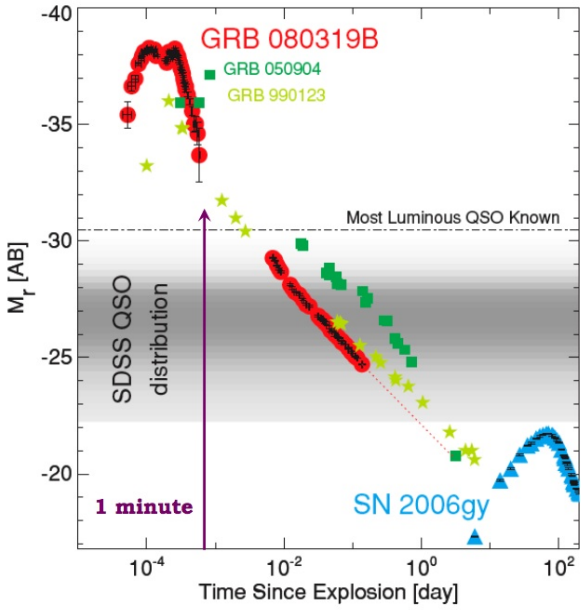

Figure 1.12: Time evolution of the luminosity of $GRB080319B$, $GRB050904$ and $GRB990123$ at visible wavelengths. The transition between the prompt phase and the early afterglow of $GRB080319B$ is clearly seen at time $\sim 1min$. For comparison, the figure shows the luminosities of quasars (QSOs) and of the very bright supernova SN2006gy.

The mechanisms leading to energy dissipation within the jet and the dominant radiation processes are still debated: relativistic shocks or magnetic reconnection are frequently advocated to dissipate the internal energy of the jet, which is then radiated as synchrotron and/or blackbody radiation. The detection of the prompt gamma-rays implies that they are emitted after the jet has become transparent to its own radiation. When the jet becomes transparent, most of its thermal energy should be radiated away as photospheric emission. This thermal emission is not commonly observed, implying that the energy is temporarily stored in non-thermal components (kinetic energy, magnetic fields) and released after the jet has become transparent.

Through observations made by satellite-based gamma-ray observatories, GRB are classified for their duration and spectra [26]:

short-hard GRB they are observed at low redshifts and are associated with a variety of galaxy types without active star forming regions including early-type elliptical and lenticular galaxies. Currently, it is widely thought that merger of binary neutron star or neutron star-black hole systems are the progenitors of most short-hard GRB. Some small fraction of short GRB (less than 15% of known short GRB) may be caused by soft-gamma-repeater flares.

So, for such systems, the gravitational wave signal will be a chirp during the inspiral, followed by a burst-type signal associated with the merger, and subsequently a signal from the ring-down phase of the newly formed black hole [27].

long-soft GRB they are always associated with late-type star-forming host galaxies. It is therefore thought that core-collapse stars (collapsars) are the progenitor of long GRB. This kind of sources differs from supernovae explosions, even if it is not yet clear why some massive stars die as supernovae and others as relativistic GRB.

In this scenario, the high rotation required to form the centrifugally supported disk that powers the GRB, should produce gravitational wave emission via bar or fragmentation instabilities that might develop in the collapsing core and/or in the disk. Moreover, asymmetrically infalling matter is expected to perturb the final black hole geometry, leading to a ring-down phase [28].

The models of gravitational wave emission by GRB are difficult to do, in particular for what concerns the extreme stellar collapse. We can use an ad-hoc model for describing the gravitational wave emission by a rigidly rotating quadrupolar mass moment with a Gaussian time evolution of its magnitude. For such a source with a rotation axis inclined by an angle i with respect to the observer the received gravitational signal is a sine-Gaussian [30]:

$$\begin{pmatrix} h_+(t) \\ h_\times(t) \end{pmatrix} = \frac{1}{r}\sqrt{\frac{5G}{4\pi^{3/2}c^3}\frac{E_{gw}^{iso}}{f_0 Q}} \begin{pmatrix} (1+\cos^2 i)\cos(2\pi f_0 t) \\ 2\cos i \sin(2\pi f_0 t) \end{pmatrix} e^{-\frac{(2\pi f_0 t)^2}{2Q^2}} \tag{1.26}$$

where the signal frequency f_0 is equal to twice the rotation frequency, t is the time relative to the signal peak time, Q characterizes the number of cycles for which the quadrupolar mass moment is large, r is the distance between the observer and the source andE_{gw}^{iso} is the total isotropic radiated energy.

It is evident from eq. 1.26 that the polarization of the gravitational waves provides evidence about the emission geometry of the GRB sources, because the relative strengths of the + and × polarizations is a function of the inclination angle.

GRB-triggered gravitational wave searches have adopted two kinds of time windows [29]:

- on-source time window of few minutes (long GRB) or few seconds (short GRB) around the GRB trigger time. In fact, for long GRB, the time delay between the gravitational wave signal and gamma-ray trigger is thought to be dominated by the time necessary for the fireball to push through the stellar envelop of the progenitor ($10-100s$). On the other hand, for short GRB, the merger is believed to occur quickly, and be over within a few seconds (naturally accounting for the short nature of these bursts).

- off-source window of three hours surrounding the on-source data. In this way, processing them identically to the on-source data, it is possible to evaluate the background noise. The same noise properties of the GRB time are taken into account: in particular the same data-quality cuts, sky position relative to the

Earth are applied. For each sample of off-source segments, the loudest event is determined, to give an empirical measure of the significance of the loudest event in the on-source data.

With this triggered analysis method, it is estimated a factor of ~ 2 improvement in sensitivity with respect to untriggered ones.

For what concerns the detection rate, calculated by eq. 1.15, we distinguish short from long GRB:

$$\dot{N}_{long} \approx 1 \cdot 10^{-6} \frac{R_{long}}{0.5 Gpc^{-3} yr^{-1}} \left(\frac{E_{gw}^{iso}}{0.01 M_{\odot} c^2} \right)^{3/2} \tag{1.27}$$

$$\dot{N}_{short} \approx 2 \cdot 10^{-5} \frac{R_{short}}{10 Gpc^{-3} yr^{-1}} \left(\frac{E_{gw}^{iso}}{0.01 M_{\odot} c^2} \right)^{3/2} \tag{1.28}$$

where R are the observed GRB rates; for these expressions we have used the typical detector horizon limits, which depend on event energy, $D \sim 15 MPc\,(E_{gw}^{iso}/0.01 M_{\odot} c^2)$, evaluated for a signal at frequencies around $150 Hz$.

Actually, recent studies report that there exists a local population of underluminous long GRB with an observed rate density 10^3 times the one of the high luminosity population:

$$\dot{N}_{local} \approx 1 \cdot 10^{-3} \frac{R_{local}}{500 Gpc^{-3} yr^{-1}} \left(\frac{E_{gw}^{iso}}{0.01 M_{\odot} c^2} \right)^{3/2}$$

All these detection rate could be multiplied by a factor 5 for advanced detectors.

1.3.5 Stochastic sources

The superposition of large number of unresolved sources of gravitational waves produces a stochastic background. The reason for which detectors can not distinguish between this kind of sources is simple and depends on the angular resolution and on the field of view.

To better understand, we can draw a comparison with the electromagnetic detectors. If we study an optical source, somewhere in the sky, using a telescope with a certain angular resolution, then details of the source can be resolved if the angular resolution of the telescope is smaller than the angular size of the features or objects being studied. In the case of the interferometer detectors, the angular size of the antenna pattern is of order $\pi/2$. Hence, almost any source is "unresolved" in the sense that it makes a significant contribution to the detector output for almost any orientation of the detector and the source. When many sources are present, even if they are pointlike, the resulting signal has a stochastic nature.

There are two types of contribution:

1. a cosmological background, i.e. a memory of the early stage of the universe;

2. an astrophysical background, due to the galaxies evolution, star formation and all overlapped emitting celestial bodies.

The most important feature in studying this kind of source is the possibility of detecting radiation produced at very early epoch, $t \sim 10^{-22}s$ after the Big Bang. In fact, similar to what happens for electromagnetic field, a gravitational wave of a certain frequency is produced when the characteristic time for the matter and energy in the universe to change is comparable to the period of the wave. So, at time $t \sim 10^{-22}s$ after the Big Bang, the universe is extremely small and dense, with a mean temperature of $10^7 GeV$. For this reason, detecting a background of cosmological origin would give us a glimpse of the universe at much earlier times than we can obtain in other ways.

In general, for stochastic background it is preferable to use the fractional energy density Ω, as in cosmology.

We can define [31]:

$$\Omega_{gw}(f) = \frac{1}{\rho_{cr}} \frac{d\rho_{gw}}{d \ln f} \tag{1.29}$$

where ρ_{gw} is gravitational wave energy density and ρ_{cr} is the critical energy density of the universe:

$$\rho_{cr} = \frac{3c^2 H_0^2}{8\pi G} \approx 9 \cdot 10^{-10}\ J/m^3$$

The variability of this quantity depends on the uncertainty of the Hubble constant H_0; in this work I will take the value $H_0 = 72\ km/sMpc$.

It is not clear the frequency dependence of Ω_{gw}: in some cosmological models, Ω_{gw} is considered frequency-independent, but this is not true for other models. The important thing is that any spectrum of gravitational radiation can be described by an appropriate function $H(f)$. With the correct dependence on frequency, it can describe a flat spectrum or a black-body spectrum or any other specific distribution of energy with frequency.

We calculate the expected value of the strain due to stochastic background. We can start from the expression of a plane wave of a gravitational perturbation:

$$h_{ab}(t, \vec{x}) = \sum_A \int_{-\infty}^{\infty} df \int_{S^2} d\hat{\Omega} h_A(f, \hat{\Omega}) e^{2\pi i f(t - \hat{\Omega}\cdot\vec{x}/c)} e^A_{ab}(\hat{\Omega}) \tag{1.30}$$

where A indicate the two gravitational wave polarizations + and $\times$, h_A is the wave amplitude, e^A_{ab} are the polarization tensors, which depend only upon the direction of the wave vector; the integration is over $\hat{\Omega}$, the unit vector on the two-dimension sphere S^2.

From eq. 1.29 we need to know how to express the energy density ρ_{gw}. We can use the relation between the stress-energy tensor and the gravitational wave amplitude [3]:

$$T_{\mu\nu} = \frac{c^2}{32\pi G^2} < h_{ab,\mu} h^{ab}{}_{,\nu} >$$

The time coordinate T_{00} is equal to the energy density ρ, so we can write:

$$\rho_{gw} = \frac{c^2}{32\pi G^2} < \dot{h}_{ab} \dot{h}^{ab} >$$

So, assuming that the stochastic noise is stationary and Gaussian, we can express the average of the gravitational wave amplitude in general:

$$< h^*_A(f, \hat{\Omega}) h_{A'}(f', \hat{\Omega}') >= \delta(f - f')\ \delta^2(\hat{\Omega}, \hat{\Omega}')\ \delta_{AA'}\ H(f)$$

where $H(f)$ is real non-negative function related to the spectrum of $\Omega_{gw}(f)$.

Substituting the plane wave expression 1.30 into this formula we obtain:

$$\begin{aligned} < \dot{h}_{ab}\dot{h}^{ab} > &= \sum_A \int_{-\infty}^{\infty} df \int_{S^2} d\hat{\Omega}\ 4\pi^2 f^2 H(f)\ e^A_{ab}(\hat{\Omega}) e^{ab}_A(\hat{\Omega}) = \\ &= 64\pi^3 \int_{-\infty}^{\infty} df\, f^2 H(f) = \\ &= 128\pi^3 \int_0^{\infty} df\, f^2 H(f) \end{aligned}$$

where we have considered $\sum_A e^A_{ab} e^{ab}_A = 4$ and $\int d\hat{\Omega} = 4\pi$

Thus, the energy density fraction Ω_{gw} is:

$$\Omega_{gw} = \frac{f}{\rho_{cr}} \frac{d\rho_{cr}}{df} = \frac{32\pi^3}{3H_0^2} f^3 H(f) \tag{1.31}$$

where we have left the spectrum behaviour $H(f)$ explicitly expressed.

In the following we examine in detail three different *cosmological physical processes* which might have taken place in the early universe, which give rise to different spectra of Ω_{gw}.

Inflationary models In this model, as the universe cooled, it passed through a phase in which the energy density of the universe was dominated by vacuum energy Λ and the scale factor increased as rapidly as a power law or an exponential function. In its simplest version, this scenario is tightly constrained by the cosmic microwave background radiation (CMB) observational data. When this constraint is taken into account, the stochastic gravitational wave background predicted by the simplest inflationary cosmological models are far too weak to be observable by either the initial or advanced interferometer detectors. This weakness is due to the long period of inflation that damps out any classical or macroscopic perturbations, leaving behind only the minimum allowed level of fluctuation, required by the uncertainty principle.

In this case, the energy density fraction is [32]:

$$\Omega_{gw} = \frac{16c^7}{9\hbar G^2} \frac{\rho_\Lambda}{1 + z_{eq}} \tag{1.32}$$

where ρ_Λ is the energy density in the vacuum-dominated era and z_{eq} is the redshift of the universe when the matter and the radiation energy density were equal.

The frequency dependence in eq. 1.32 is not obvious and it is given in fig. 1.13.

The inflationary spectrum rises rapidly at low frequencies (waves which reentered the Hubble sphere after the universe became matter-dominated) and falls off above the (appropriately redshifted) frequency scale f_{max} associated with the fastest characteristic time of the phase transition at the end of inflation. The amplitude of the flat region depends only on the energy density during the inflationary stage; we have chosen the largest amplitude consistent with the COBE constraint $\Omega_{gw} < 7 \cdot 10^{-11}$ at $10^{-18} Hz$.

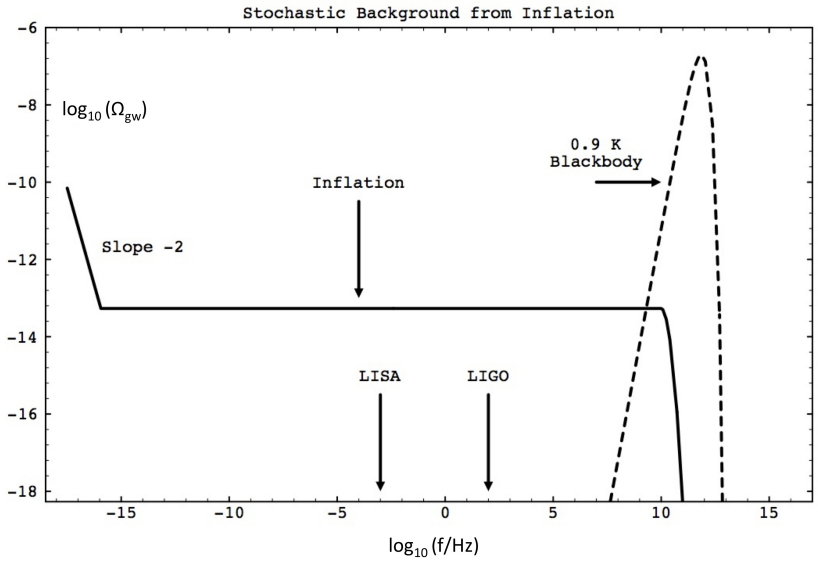

Figure 1.13: the spectrum of stochastic gravitational waves in inflationary models is flat over a wide range of frequencies and is shown as the solid curve. The horizontal axis is $\log_{10}$ of frequency, in Hz. The vertical axis is $\log_{10} \Omega_{gw}$. The spectrum of a $0.9K$ blackbody is shown for comparison; at LIGO and LISA frequencies, $\Omega_{gw} < 8 \cdot 10^{-14}$.

Cosmic strings In this model, as the universe cooled, long string-like defects were formed at a phase transition. These "cosmic strings" form a network which self-intersects and chops off small loops of string. These small loops oscillate relativistically and, as they do so, they emit a characteristic spectrum of gravitational waves. In contrast with the previous example, for reasonable values of the parameters, the cosmic string scenario predicts a stochastic background which is large enough to be observable with the advanced interferometer detector. In common with the previous example, the string network is described by a "scaling" solution, with the consequence that the spectrum of Ω_{gw} is flat over a wide range of frequencies (fig. 1.14).

The expression of Ω_{gw} is quite complicated to obtain [31]:

$$\Omega_{gw} = \frac{16\pi A\gamma}{9\alpha} \left(\frac{G\mu}{c^2}\right)^2 \frac{\beta^{3/2} - 1}{1 + z_{eq}}$$

where:

- α is a dimensionless constant indicating the size L_{loop} of the string loop at the time of formation f_{form}

$$L_{loop} = \alpha c t_{form}$$

- A is the number of long strings which pass through the Hubble volume ($A = 52$, value obtained from simulations);

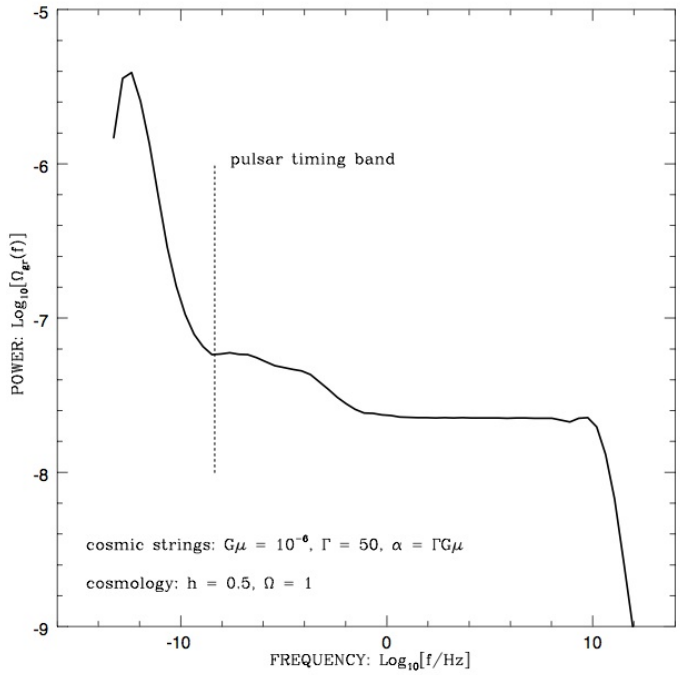

Figure 1.14: the spectrum of gravitational radiation background produced by a cosmic string network; around the Virgo sensitivity frequency band $f \sim 100Hz$, the spectrum is fairly flat.

– γ is a dimensionless constant linked to the energy-loss rate P of the loops, which does not depends on their size but shape and mass density μ

$$P = \gamma G \mu^2 c$$

– β is the ratio between the death-time and the birth-time of a string

$$\beta = 1 + \frac{\alpha c^2}{\gamma G \mu} > 1$$

Phase transition We consider the case in which the phase transition is strongly first-order and creates vacuum bubbles, which are bubbles of the new (low energy density) phase expanding in the old (high energy density) phase. Within a short time, these bubble walls are moving relativistically and much of the latent energy released by the phase transition is transformed into kinetic energy of the bubble walls. The highly-relativistic and non-symmetric collisions of these bubble walls are a copious source of gravitational radiation, strong enough to be observable in some cases with the initial generation of interferometer detectors. Unlike the previous two examples, this phase transition/gravitational radiation production process is a "one-time" event, characterized by a particular cosmological time and a particular frequency today; so, there is no scaling law in this case. Hence, in contrast with the previous two examples, the spectrum $\Omega_{gw}(f)$ is strongly peaked at a frequency characteristic of this time (fig. 1.15).

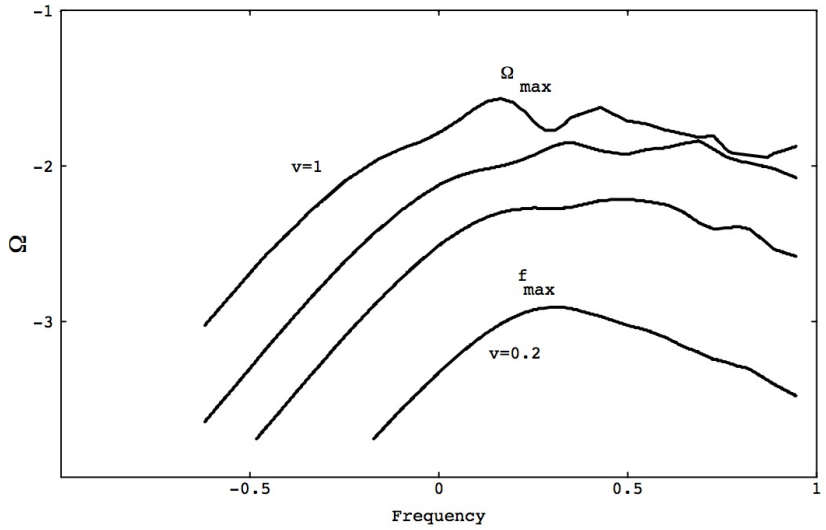

Figure 1.15: typical spectra $\Omega_{gw}(f)$ produced from the collision of bubbles which result from a first-order phase transition. The horizontal axis is $\log_{10}(2\pi f/\beta)$ and the vertical axis is $\log_{10}\Omega_{gw}\beta^2(1+\alpha)^2H^{-2}\alpha^{-2}k^{-2}$. The spectrum peaks at a characteristic frequency f_{max}, depending of the expansion rate and the time at which the bubble collisions occurred. The spectra are shown for bubble wall velocities of $v = 0.2, 0.4, 0.6, 1.0$.

In this case, the amplitude of the energy density fraction is [33]:

$$\Omega_{gw}(f_{max})h_{100}^2 \approx 1.1 \cdot 10^{-6}k^2\left(\frac{\beta}{H_*}\right)^{-2}\left(\frac{\alpha}{1+\alpha}\right)^2\left(\frac{v^3}{0.24+v^3}\right)\left(\frac{g^*}{100}\right)^{-1/3}$$

where:

- f_{max} is the spectrum peak frequency $f_{max} \approx 4.1 \cdot 10^{-3}Hz$;
- k is the fraction of vacuum energy that goes into kinetic energy of the fluid;
- β is the measure of the bubble nucleation rate and H_* the Hubble expansion rate at the phase transition time;
- α is the ratio $\alpha = \frac{\rho_\Lambda}{\rho_{th}}$ between the energy density if the vacuum and the thermal energy density;
- g_* is the number of relativistic degrees of freedom of the universe at a fixed temperature;
- v is the bubbles velocity.

For what concerns gravitational stochastic background given by the *astrophysical sources*, we can say that its detection could put very strong constraints on the physical properties of compact objects, the initial mass function and the star formation history. Let us examine different contributions.

Binary neutron stars Binary neutron star coalescences, which may radiate at frequencies up to $1.4 - 1.6kHz$, may be the most important contribution in the interferometer detector frequency range [34]. In the quadrupolar approximation, the gravitational wave energy spectrum $H(f)$ (see eq. 1.31) emitted by a binary system which inspirals in a quasi-circular orbit is given by:

$$H(f) = \frac{dE_{gw}}{df} = \frac{(G\pi)^{2/3}}{3} \frac{m_1 m_2}{(m_1 + m_2)^{1/3}} f^{-1/3}$$

where m_1 and m_2 are the neutron star masses.

Core collapses Popolation III and Popolation II stellar collapses can produce a background signal. Considering how it is difficult exactly predict the collapse waveform, as seen in sec. 1.3.3, this can be done with 2D numerical simulation, taking into account the effects of general relativity and neutrino transport.

The background is out of reach for Popolation III stellar collapse, but could be detected for Popolation II progenitors. The energy density reaches a maximum of $\Omega_{gw} \sim 10^{-9}$ at $1000Hz$ for the collapse to neutron star and of $\Omega_{gw} \sim (4-7) \cdot 10^{-10}$ at $500Hz$ for the collapse to black hole.

The estimated gravitational wave signal created by all core collapse supernovae, to neutron stars and black holes, using a Gaussian spectrum, is a good approximation to the models [35]:

$$H(f) = Ae^{-\frac{(f-f_0)}{2\sigma^2}}$$

where, considering different models and simulated spectra, we have $\sigma \sim 500$ and $f_0 = 200 - 800Hz$.

Spinning neutron stars: r-modes The stochastic background from r-modes was first investigated without taking into account dissipation mechanisms such as the effect of the solid crust or the magnetic field, which may significantly reduce the gravitational instability. The spectral energy density of a single source is given by [36]:

$$H(f) = \frac{2E_0}{f_{sup}^2} f$$

where f_{sup} is 4/3 of the initial rotational frequency and E_0 is the rotational energy lost within the instability window. Some example for different f_{sup} are reported in fig. 1.16.

Spinning neutron stars: tri-axial emission Rotating neutron stars with a triaxial shape may have a time varying quadrupole moment and hence radiate gravitational waves at twice the rotational frequency. The total spectral gravitational energy emitted by a neutron star born with a rotational period P and which decelerates through magnetic dipole torques and gravitational wave emission is:

$$H(f) = \frac{Kf^3}{1 + \frac{Kf^2}{\pi^2 I_{zz}}}$$

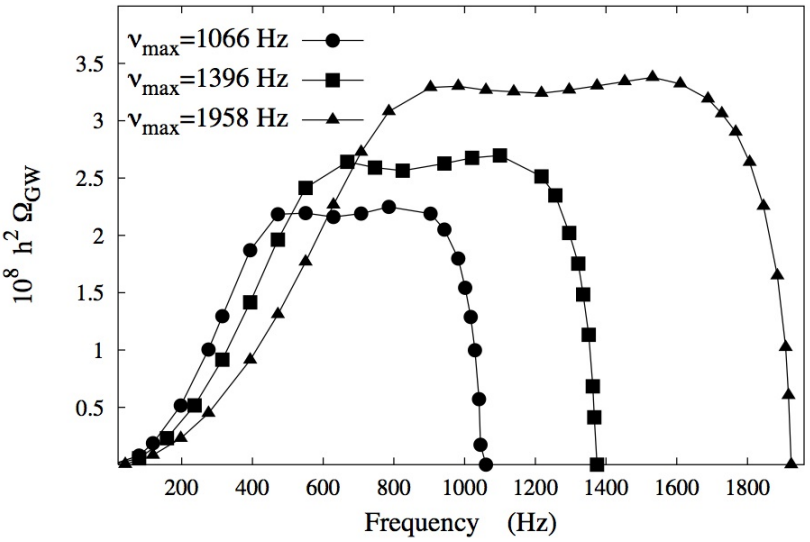

Figure 1.16: the energy density fraction Ω_{gw} as a function of frequencies for r-modes instabilities during initial phase of a spinning neutron star; different maximum frequency values are reported.

where $f \in [0 - 2/P]$, I_{zz} is the principal moment of inertia around axis z and K is:

$$K = \frac{192\pi^4 G I_{zz}^3 \epsilon}{5c^5 R^6 B^2 \sin^2 \alpha}$$

with ϵ the ellipticity factor, R the radius of the star, B its magnetic field and α the angle between the rotation and the dipole axis.

For what concerns the detection of stochastic background, the detectors could not distinguish between different parts and the resulting signal can be perceive as incoherent noise. In principle this noise could be higher than the instrumental noise, preventing the detection of useful but low signals. For example, astrophysical background may mask the cosmological in certain frequency regions.

To distinguish this kind of sources, there are two ways:

- using al least two detectors, searching for a coherent signal with cross-correlation methods; in such methods, the output from a detector works as a template for the signal from the second detector. They can match well if the wavelength of gravitational waves is longer than the separation between detectors, otherwise there are time delay problems.

- having long observation times; if the random field is generated by a sample of sources distributed anisotropically, as galactic sources, then over a year the noise background would be modulated, as the detector change its orientation.

Let us analyze in more detail the first way. We consider two independent detectors in the same location and identically oriented; then we discuss on a more complicate configuration.

In the simplified case, the outputs of the two detectors are:

$$\begin{aligned} s_1(t) &= h_1(t) + n_1(t) \\ s_2(t) &= h_2(t) + n_2(t) \end{aligned}$$

We compute a correlation signal S by multiplying together the outputs of the two detectors and integrating:

$$S =< s_1 s_2 >= \int_{-T/2}^{T/2} s_1(t) s_2(t) dt$$

where T is the integration time.

If the detector noise n_i is greater than the signal s_i, it is possible to write explicitly:

$$\begin{aligned} S &= < h_1, h_2 > + < h_1, n_2 > + < h_2, n_1 > + < n_1, n_2 > \approx \\ &\approx < h_1, h_2 > + < n_1, n_2 > \end{aligned}$$

where, we have dropped terms like $< h_i, n_j >$ because they are smaller than $< n_1, n_2 >$. Note that n_1 and n_2 can be statistically uncorrelated, while the signals h_1 and h_2 are always correlated, since the source is the same for all detectors.

It is possible to compute these two contributions:

$$\begin{aligned} < h_1, h_2 > &\propto |\tilde{h}(f)|^2 \Delta f T \propto \Omega(f) \Delta f T \\ < n_1, n_2 > &\propto |\tilde{n}(f)|^2 \sqrt{\Delta f T} \end{aligned}$$

where f is the central frequency at which the detector is sensitive, Δf is the effective bandwidth and with the symbol $\tilde{x}$ we indicate the Fourier transform of the quantity x. The $< n_1, n_2 >$ term, thanks to its random-walk behaviour, grows on the average like $\sqrt{T}$, while the signal $< h_1, h_2 >$ grows like T.

Computing the S/N ratio from these equations and putting it equal to 1, we can find the minimum detectable signal Ω_{gw}^{min}:

$$\Omega_{gw}^{min} = \frac{|\tilde{n}(f)|^2}{\sqrt{\Delta f T}}$$

With a long observation time one can in principle detect a gravitational wave stochastic background buried in any level of detector noise.

Now we can face to a more rigorous treatment of the signal analysis, taking into account the reduction in sensitivity that results from two effects:

1. the non-parallel alignment of the arms;

2. the time delay between the two detectors.

These two effects reduce the sensitivity of a stochastic background search; they mean that h_1 and h_2 are no longer equal; the overlap between the gravitational wave strains in the two detectors is only partial. To quantify these effects we introduce the overlap reduction function $\gamma(f)$, which depends on the relative positions, the orientations of a pair of detectors and their response to the + and × gravitational wave polarizations.

So, we write the most general possible form of the correlation signal S between two detectors:

$$S = \int_{-T/2}^{T/2} dt \int_{-T/2}^{T/2} dt' s_1(t) s_2(t') Q(t - t') \tag{1.33}$$

where $Q(t-t')$ is a real filter function; it depends upon the locations and orientations of the detectors, as well as on the spectrum of the stochastic background and the noise characteristics of the detectors. So, it depends also to the overlap reduction function $\gamma(f)$.

We can re-write eq. 1.33 in frequency domain:

$$S = \int_{-\infty}^{\infty} df \int_{-\infty}^{\infty} df' \delta(f - f') \tilde{s}_1^*(f) \tilde{s}_2(f') \tilde{Q}(f')$$

If we assume that the stochastic background is isotropic, unpolarized and Gaussian, we can easily calculate the Fourier amplitudes of the strain signal and the strain noise [31]:

$$\begin{aligned} < \tilde{h}_1^*(f), \tilde{h}_2(f') > &= \delta(f - f') \frac{3H_0^2}{20\pi^2} \frac{\Omega_{gw}(f)\gamma(f)}{f^3} \\ < \tilde{n}_i^*(f), \tilde{n}_j(f') > &= \frac{1}{2} \delta(f - f') \delta_{ij} P_i(f) \end{aligned}$$

where the indices i, j label the two different detectors and $P_i(f)$ is the power spectral noise density function, defined for each detector.

In order to find the optimal choice of filter function Q, we need to choose the quantity to maximize. The natural choice here is to maximize the ratio of signal-to-noise S/N. Since the noise in each detector is uncorrelated with the other detector and is uncorrelated with the gravity-wave strain h, after some calculations, we obtain an expression for $\tilde{Q}$:

$$\tilde{Q} = \frac{\gamma(f)\Omega_{gw}(f)}{f^3 P_1(f) P_2(f)}$$

Effectively, the filter includes into the signal only those frequencies at which the detector is most sensitive, weighting each frequency by a positive or negative factor which reflects the relative phasing (at that frequency) of the signals at the two detectors.

One of the interesting peculiarity of this formula for the signal-to-noise ratio is that it depends upon the spectrum of gravitational waves Ω_{gw}, an unknown function. In practice it implies that rather than having a single optimal filter one needs to have a set of such filters.

The idea, then, is to use and to state with some desired reliability that the observed positive mean value of S could not have resulted from detector noise but instead must have resulted from a stochastic background. One way of doing that is to compute the probability that a random variable with a Gaussian normal distribution will lie within a given range.

For example, if S belongs to the range $[< S > -2\sqrt{< N^2 >}, < S > +2\sqrt{< N^2 >}]$, we can detect a stochastic background with $\geq 95\%$ of confidence.

Recently [37], using this analysis method, it is found an upper limit on gravitational wave energy density fraction $\Omega_{gw} \leq 6.9 \cdot 10^{-6}$. This value is smaller than other

values set by the Big Bang nucleosynthesis ($\Omega_{BBN} \leq 1.1 \cdot 10^{-5}$) and from the cosmic microwave background measurements ($\Omega_{CMB} \leq 9.5 \cdot 10^{-6}$).

This is one of the most important result reached by gravitational waves searches.

1.4 Multimessanger astronomy

The search of gravitational waves is a challenge even if, up to now, without results: it is fundamental not only to confirm Einstein's general relativity, but also to keep unique information about a given category of sources or astrophysical event as the inspiraling and merger of neutron stars and black holes or as core collapse in massive stars.

Large gravitational wave detectors using exquisitely laser interferometry, as we describe in the next chapter, have been successfully operating in recent years and are currently being upgraded to greatly improve their sensitivities. Many signals are expected to be detected in the coming decade.

Simultaneous observing through the network of gravitational wave detectors enables us to identify and localize event candidates on the sky with moderate precision, opening up the possibility of capturing optical transients or other electromagnetic counterparts to confirm an event and obtain complementary information about it.

In fact at present we observe the sky in different bands: in addition to the electromagnetic spectrum, many astrophysical sources will have neutrino and gravitational wave counterparts. These observables will add unique information because the data coming from neutrino observatories and from gravitational wave interferometers are unperturbed, since either neutrinos and gravitational waves do not interact with matter.

For these reasons we push toward a "multimessanger astronomy".

Gravitational radiation can give us information about source sky position, its host galaxy type, its distance, its emission characteristics and the occurring astrophysical processes.

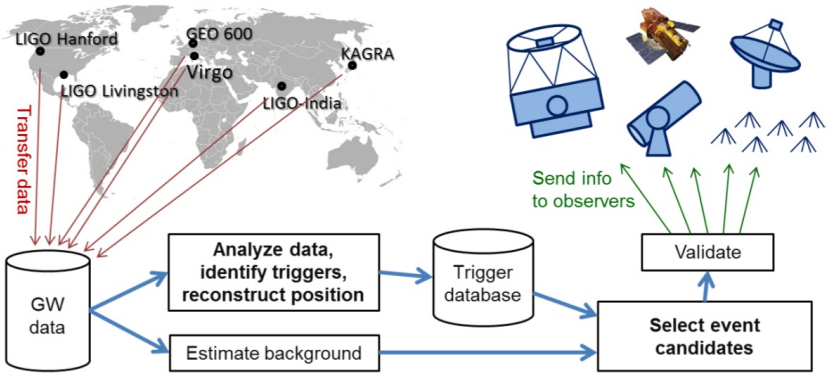

Figure 1.17: main steps in processing data from the gravitational wave detector network; alerts are rapidly generated for follow-up observations.

Furthermore, it is convenient to connect different kinds of observation of the same

astrophysical event or system to trigger the data (see fig. 1.17).

For example, additional "coincidence" tests can enable confident detection of weaker gravitational wave signals: electromagnetic or particle signals may provide complementary information about the gravitational wave source, as for supernova explosions. Even in the worst case in which there are electromagnetically quiet gravitational wave emissions, reconstructed gravitational wave waveforms can be "inverted" to provide precise estimations of source parameters, as for black hole / neutron star coalescences. In the case of transient signals, as those coming from GRB, data from gravitational wave interferometers can be used as reference to point telescopes at the source.

Inside the Virgo-LIGO collaboration a complete low-latency gravitational wave data analysis and alert system have been developed and implemented in 2009 -2010 and used to send alerts to several observing partners [38].

Currently, LIGO and Virgo have formal or informal relationships with:

- the Jodrell Bank Observatory, which is a radio telescope: it provides timing information for known pulsar searches;
- interplanetary Network (IPN) of gamma ray satellites for Soft Gamma Repeaters and GRB searches;

But other collaborations have been planned:

- ANTARES, IceCube, for high energy neutrinos, and Super-K, for low energy neutrinos;
- Swift X-ray telescope, for studying core collapses and for off-line analyses of possible gravitational wave events;
- ROTSE and Tarot, which are wide field optical telescopes, for rapid following up of high threshold gravitational wave events to optical counterparts, to supernovae and GRB afterglows.

Until now no astronomical research groups have approached LIGO or Virgo asking to look at gravitational data, except for those belonging to LIGO/Virgo community: this is because gravitational wave astronomy is not yet an "established" observational field.

To enter properly the multimessanger astronomy, gravitational wave research should wait for the first detection.

Chapter 2

Interferometric detectors for gravitational wave

In this chapter we see how it is possible to measure the effect of gravitational wave with an interferometric detector.

Since the gravitational waves modify the space-time metric, their passage modifies the distance between two fixed objects. To monitor this distance it is possible to use a Michelson-Morley interferometer; in fact this device measures with high precision distance differences along two chosen directions on the base of the time travel of photons produced by a monochromatic laser source.

There are currently four experiments based on that idea: LIGO [39] (USA, with two $4km$-long interferometers), Virgo [40] (Italian and French collaboration, $3km$), GEO600 [41] (English and German collaboration, $600m$), CLIO, upgrated in the future to KAGRA [42] (Japan, $100m$).

In this chapter I talk about the principle of detection. After reporting the most important noise sources, I give an example of an interferometer detector: Virgo in its first configuration and in the advanced project.

2.1 Principle of detection

The classic optical scheme for a gravitational wave detector is a Michelson interferometer. The passage of a gravitational wave induces a change in the relative distance of the mirrors. A consequent variation occurs in the power transmitted at the output port, detected by a photodetector.

A simple Michelson interferometer is shown in fig. 2.1: a laser beam of wavelength λ_L impinges on a half reflecting beam splitter; the two emerging beams are sent toward orthogonal directions, reflected back by two mirrors, at distance l_1 and l_2 from the beam splitter. Finally, they recombine at the beam splitter and go to the photodetector, in a direction symmetrically with respect to the laser source.

If the input power impinging on the beam splitter is P_{in}, the power detected at the output port P_{out} is [43]:

$$P_{out} = P_{in}\, r_{BS}^2\, t_{BS}^2\, (r_1^2 + r_2^2)[1 + Ccos(2k_L \Delta l)] \tag{2.1}$$

where r_x is the reflectivity of the mirror x, t_x is its trasmessivity, k_L is the wave vector

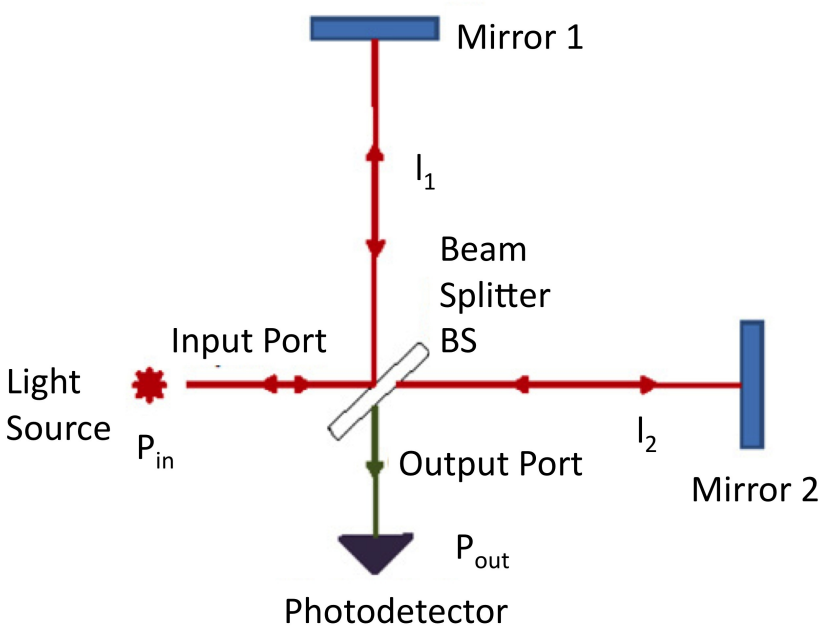

Figure 2.1: scheme of a simple Michelson interferometer.

of the laser beam of wavelength λ_L, $\Delta l = l_2 - l_1$ is the two arms length asymmetry and C is the contrast:

$$C = \frac{2r_1 r_2}{r_1^2 + r_2^2}$$

which depends on the amplitude reflectivity of the two arm mirrors.

For an ideal interferometer, the beam splitter has $r_{BS} = t_{BS} = \sqrt{2}/2$ and the two mirrors have $r_1 \sim r_2 \sim 1$, so that:

$$P_{out} = \frac{P_{in}}{2}[1 + C\cos(\Delta\phi_L)] \tag{2.2}$$

where:

$$\Delta\phi_L = 2k_L \Delta l \tag{2.3}$$

which is the differential phase shift induced in the light returning to the beam splitter.

When a gravitational wave passes through the interferometer, the arm asymmetry Δl changes of a quantity Δl_{gw} depending on the gravitational signal amplitude:

$$h = h_A e^{i\omega t}$$

where h_A is the wave amplitude, ω is the gravitational wave pulsation and t is the time.

Using eq. 1.11, we calculate the gravitational wave contribution to the arm asymmetry:

$$\Delta l_{gw}(t) = \frac{1}{2}\frac{h_A c}{i\omega} e^{i\omega t}(e^{i\omega\frac{2l_1}{c}} + e^{i\omega\frac{2l_2}{c}} - 2) \tag{2.4}$$

Δl_{gw} being a time function, because of the wave passage.

We can approximate this equation in a more simple form, considering the two arm of the same length l_0. Thus, after re-writing the complex exponential with its corrisponding trigonometric function, we obtain:

$$\Delta l_{gw}(t) = h_A l_0 e^{i\omega(t-\frac{l_0}{c})} \frac{\sin(\frac{\omega l_0}{c})}{\frac{\omega l_0}{c}}$$

This equation shows that the effect of a gravitational wave passage on the arm asymmetry is proportional to the initial arm length and to the amplitude of the gravitational wave $\Delta l_{gw} \propto h_A l_0$.

The differential phase shift due to gravitational wave passage becomes:

$$\Delta\phi_L^{gw}(t) = \frac{4\pi}{\lambda_L} h_A l_0 e^{i\omega(t-\frac{l_0}{c})} \frac{\sin(\frac{\omega l_0}{c})}{\frac{\omega l_0}{c}}$$

In that case, the output power detected can be re-written using the eq. 2.2 and substituting the cosine argument with the sum $\Delta\phi_L + \Delta\phi_L^{gw}$; considering the first term approximation of the gravitational perturbation we obtain:

$$P_{out}(t) = \frac{P_{in}}{2}\left[1 + C\cos(\Delta\phi_L) + C\sin(\Delta\phi_L)\Delta\phi_L^{gw}(t)\right] \tag{2.5}$$

Thus, we have linked the detector output power with the gravitational signal.

To have an idea of the order of magnitude of the detectable frequency at which the interferometer could be sensitive, we can use the simple expression which link the frequency with the interferometer arm length l_0:

$$f_{gw} \sim \frac{c}{l_0}$$

So, if we want to detect a $100Hz$ gravitational wave, as the signal produced by a pulsar, we need a $3000km$-long instrument, which is clearly not technically possible to be built on Earth.

For an ideal interferometer, with no sources of noise limiting the detection of power fluctuations, the best choice for the tuning of the output would be the one maximizing the sine in eq. 2.5, that corresponds to having half of the maximum power in the output port. This condition is usually called *gray fringe*, while the tuning that gives minimum and maximum powers are called respectively *dark fringe* and *bright fringe*.

Actually, as we will see in sec. 2.2.1, there is a fundamental limitation to the power sensitivity measurement, due to shot noise. That changes the best tuning condition for a real interferometer.

2.2 Noise sources in an interferometer

There are several noise sources affecting the interferometer, which can be classified as:

- instrumental noise:
  - intrinsic:
    - shot noise;
    - radiation pressure;
    - thermal noise;
  - technic:
    - scattered light;
    - control noises;
- environmental noise:
  - newtonian noise;
  - seismic noise;
  - electromagnetic noise.

2.2.1 Quantum noises

Two fundamental sources of quantum-mechanical noise determine the behavior of the interferometer sensitivity:

1. shot noise: fluctuations in the number of photons impinging on the photodetector;
2. radiation pressure: fluctuations in the number of photons impinging on test masses and transferring them impulse.

Shot noise originates from the discrete nature of the photons impinging on an optical device. It may be dominant when the finite number of particles that carry energy is sufficiently small so that uncertainties due to the photon distribution are significant.

Each source emits a number of photons N following a Poisson distribution, which describes the occurrence of independent random events, with standard deviation:

$$\sigma_N = \sqrt{N} \tag{2.6}$$

So, the output power measured by the photodiode depends on the mean energy $\bar{E}$ arriving in the time unit Δt:

$$P_{out} = \frac{\bar{E}}{\Delta t}\eta = \bar{N}\frac{\hbar\omega_L}{\Delta t}\eta \tag{2.7}$$

where η is the quantum efficiency, $\bar{N}$ is the photon number and ω_L is the laser pulsation. Using eq. 2.6 and eq. 2.7, we can extract the fluctuation ΔN_{shot} of the mean number of photons:

$$\Delta N_{shot} = \sqrt{\frac{P_{out}\Delta t}{\hbar\omega_L\eta}} \tag{2.8}$$

Differentiating eq. 2.7 with respect to N and substituting eq. 2.8, we find the power fluctuation given by shot noise:

$$\Delta P_{shot} = \sqrt{P_{out}\eta\frac{\hbar\omega_L}{\Delta t}} \tag{2.9}$$

Therefore, the best tuning for a Michelson interferometer affected by shot noise and in stationary condition can be found maximizing the signal to noise ratio S/N:

$$\frac{S}{N} = \frac{P_{out}^{GW}}{\Delta P_{shot}} = \sqrt{\frac{P_{in}}{2}\frac{\Delta t}{\eta\hbar\omega_L}}\frac{C\sin(\Delta\phi_L)}{\sqrt{1+C\cos(\Delta\phi_L)}}\Delta\phi_L^{gw}$$

where C is the contrast, P_{in} is the laser input power and $\Delta\phi_L^{gw}$ is the differential phase shift due to gravitational wave passage; the gravitational signal is given by eq. 2.5.

The maximum S/N with respect to the static tuning $\Delta\phi_L$ is:

$$\cos(\Delta\phi_L) = \frac{-1+\sqrt{1-C^2}}{C}$$

Since the contrast C is very close to 1, the best tuning for a real Michelson interferometer is very close to the dark fringe condition.

It is possible to perform more accurate calculations taking into account the real optical configuration of an interferometer, with Fabry-Perot cavities in the arm (see sec. 2.3.1) and the phase modulation of the laser beam (see sec. 2.3.3). In this case the strain sensitivity contribution due to the shot noise $\Delta\tilde{h}_{shot}$ as a function of gravitational wave frequency is [44]:

$$\Delta\tilde{h}_{shot}(f) = \frac{\sqrt{2}\chi}{2}f_{FP}\sqrt{\frac{4\pi^2\hbar}{\omega_L\eta G_{PR}P_{in}}}\sqrt{1+\left(\frac{f}{f_{FP}}\right)^2} \tag{2.10}$$

where ω_L is the laser pulsation, χ is the corrective factor for the modulation (for Virgo $\chi = \sqrt{3/2}$), G_{PR} is the recycling gain factor due to the presence of the power recycling mirror (see sec. 2.3.2 and fig. 2.3) between the laser source and the beam splitter, and f_{FP} is the cavity frequency:

$$f_{FP} = \frac{c}{4l_0\mathcal{F}}$$

with l_0 the interferometer arm length and $\mathcal{F}$ the Fabry-Perot cavity finesse. For Virgo, we have $f_{FP} = 500Hz$.

From eq. 2.10 it is evident that this noise is dominant at high frequencies: high finesse, high power laser on the beam splitter (high $G_{PR}P_{in}$ factor) or large arm length l_0 limit this contribution. Since it is not easy to maintain stable cavity with very high finesse and to increase the power circulating in the interferometer, the power recycling mirror is inserted. In the same way, it is not easy to build interferometer arms longer than some km, so the arms are substituted with Fabry-Perot cavities.

Increasing the power circulating in the interferometer increases the **radiation pressure noise** [45]. It is related to the statistical fluctuation of the photon number impinging on mirrors causing an uncertainty on a macroscopic scale, since the radiation pressure transfers momentum from the electromagnetic field to the mirrors.

This fluctuation sets a limit to the sensitivity [46]:

$$\Delta\tilde{h}_{rad}(f) = \frac{\mathcal{F}}{ml_0\pi^2 f^2}\sqrt{\frac{\hbar G_{PR}P_{in}}{\pi c\lambda_L}}\frac{1}{\sqrt{1+(f/f_{FP})^2}} \tag{2.11}$$

where λ_L is the laser wavelength and m is the mirror mass.

To reduce this noise contribution it is necessary to increase the mirror mass and to decrease the input power $G_{PR}P_{in}$ and the finesse $\mathcal{F}$: this conditions contrast to what find for the shot noise reduction.

So, shot noise and radiation pressure are strongly correlated and it is possible to find a common optimal condition, called Standard Quantum Limit, for which $\Delta\tilde{h}_{shot} = \Delta\tilde{h}_{rad}$:

$$\Delta\tilde{h}_{SQL}(f) = \frac{1}{\pi f l_0}\sqrt{\frac{2\hbar}{m\sqrt{\eta}}}$$

The Standard Quantum Limit represents an intrinsic limit for the sensitivity of the interferometer and can be overpassed in a restricted frequency band, losing information in the other bands, using techniques as the signal recycling mirror [47] or light squeezing [48]. In Advanced Virgo both these solutions are considered.

2.2.2 Environmental noises

The **seismic noise** is the main source of noise at low frequency, below $f < 100Hz$. In this band it is due to human or geological activity. Typically the spectral displacement amplitude generated by the seismic noise is:

$$\tilde{x}_{seism}(f) \sim 10^{-7}\frac{1}{f^2}\ \ [m/\sqrt{Hz}], \qquad f > 0.01Hz$$

In Virgo, this amplitude corresponds to a strain sensitivity:

$$\tilde{h}_{seism}(f) = \frac{2\sqrt{2}}{l_0}\tilde{x}_{seism}(f) \sim \frac{10^{-9}}{f^2}\ \ [1/\sqrt{Hz}]$$

where we have considered the arm length $l_0 \sim 3km$.

The attenuation of the seismic noise in Virgo is obtained by using mainly a passive technique based on a series of mechanical oscillators, called superattenuator (see sec. 2.3.5). For displacements at frequency above the resonance frequency, an oscillator acts as a low-pass filter with cut-frequency equal to its resonance frequency. So, it is crucial to design the mechanical system with very low resonance frequencies.

The **Newtonian noise** is the noise due to the change in the gravitational attraction felt by mirrors of the interferometer. Variations in the position of masses in the proximity of the mirrors or in the ground and atmosphere density around the

mirrors generate a differential gravitational force which acts directly on the mirrors, bypassing the isolation system.

Tipically interferometers are built in areas far from human activity and the contributions from atmosphere movements are estimated well below the sensitivity of this generation of interferometers. The most significant contribution comes from the seismic activity.

There are different models to estimate gravity gradient noise, depending on the used seismic model. According to [49]:

$$\Delta\tilde{h}_{newt} = \beta\frac{2G\rho_E}{\pi l_0}\frac{\tilde{x}_{seism}(f)}{f^2}$$

where β is an order-of-unity parameter that takes into account the seismic noise level in the particular moment under evaluation, ρ_E is the Earth density around the interferometer and l_0 is the arm length.

For Virgo, it has been evaluated a Newtonian contribution of [50]:

$$\Delta\tilde{h}_{newt} \sim \frac{3\cdot 10^{-11}}{f^2}\tilde{x}_{seism}(f)$$

2.2.3 Thermal noise

Thermal noise is produced by microscopic fluctuations of particles forming every physical system in thermodynamical equilibrium. These movements, connected to dissipation processes in the system, give rise at macroscopic scales to an uncertainty of the position and displacement of the system itself. In particular, in an interferometer, that means uncertainty in the position and displacement of mirrors.

The model and the experimental study of thermal noise in Virgo are the main topic of this thesis. I present its theoretical treatment in Chapter 3.

2.2.4 Scattered light

It can happen that photons of the beam are scattered by the mirror imperfections or by the residual gas molecules; those scattered photons could bounce on the pipe walls getting different phases and recombining with the laser beam (see fig. 2.2). This effect introduces a phase noise which limits the sensitivity of the interferometer at low frequencies [51].

The same effect in Virgo is due to the parasite light beam which are back-scattered on the optics and optical benches [52].

The optical coupling of this phase noise to the sensitivity can be estimated from the interferometer optical parameters and from the characteristics of the beam and the optics. If the optics/pipe displacement is $\delta x_{opt}(t)$, the strain sensitivity coupled with gravitational wave signal is:

$$\Delta h_{sc}(t) = K\sqrt{f_{sc}}\ \sin\left(4\pi\frac{\delta x_{opt}(t)}{\lambda_L}\right) \tag{2.12}$$

where λ_L is the laser wavelength, K is a coupling factor which may be derived for each port and f_{sc} is the fraction of the incident beam scattered by the optics and

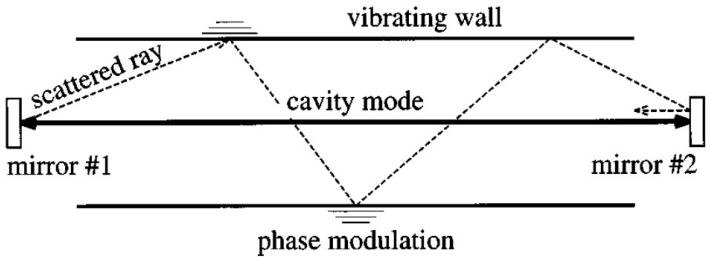

Figure 2.2: recombination of noisy stray light, scattered by a mirror and reflected on a vibrating pipe.

coupled to the main beam:

$$f_{sc} = \frac{P_{scatt}}{P_{in}} = BRDF \frac{\lambda_L^2}{\pi w_0^2}$$

where we have considered the fraction of scattered power over the total input power; this quantity is evaluated using the Bidirectional Reflectance Distribution Function (BRDF), which is the diffusion coefficient per unit of solid angle, multiplied for the beam solid angle (w_0 is the beam waist).

Note that eq. 2.12 is in the time domain: the related formula in the frequency domain is not immediately evident. Considering the simple case $\delta x_{opt}(t) \sim A_0 \sin(\omega_{res} t)$, where ω_{res} is the internal resonance of the vibrating pipe/optics; in the frequency domain we have a bump, where the lower frequency is exactly ω_{res} and the higher frequency depends on the factor $A_0 \omega_{res}/\lambda_L$, i.e. the number of the laser wave fronts overpassed by the oscillator displacement.

In general the quantity $K\sqrt{f_{sc}}$ is directly measured with noise injections (using a shaker at a certain frequency) and episensors [53].

Typically, to avoid the scattered light, a set of mechanical filters made by absorbing steel, called baffles, are usually placed along the pipes and around the optics and the benches.

2.2.5 Control Noises

Control noises are those noises reintroduced in the system or amplified by the control loops used to maintain the correct operating point of the interferometer. They can rise, for example, because of not optimal control filters or noisy error signals or actuators.

We report the principal control noise sources [55]:

- longitudinal control, which manages the distance of the mirrors; it is limiting at low frequencies, below $\sim 50Hz$; the steep roll-off of the control filters above this frequency value ensures that these loops do not affect the sensitivity above $50Hz$;

- angular control, which adjusts the alignment and the angular position of the mirrors; it is prevalent between $30 - 40Hz$;

- noise due to the actuation system (see sec. 2.3.6), formed by permanent magnets and coils; the main source of noise comes from the digital-to-analog converter and from the eddy currents; it is relevant between $50 - 100Hz$;
- frequency noise, due to fluctuation of the laser frequency and to its stabilization loop system; it is dominant in a narrow band around $6kHz$;

2.3 Virgo antenna

The present interferometers for gravitational wave measurement, like Virgo, are more complex than the one presented in sec. 2.1. In particular, the real layout of an interferometer is implemented to reduce the contributions of noise sources. In this work I focus on the Virgo project and its following improvements; I describe its characteristics and the method to minimize noises.

Virgo is a power-recycling Michelson interferometer with Fabry-Perot cavities in the arm and suspended mirrors (fig. 2.3). Above the frequency of the pendulum resonance, suspended mirrors behave as free masses, therefore forming a free falling reference system. Furthermore, thanks to the suspensions, the effect of seismic noise is present only at low frequency (ref. sec. 2.3.5). Instead the reasons for adding the Fabry-Perot cavities and a power recycling mirrors are briefly summarized in the next sections.

The Virgo construction was ended in 2003; from 2003 to 2009, when it has been upgraded in Virgo+ configuration, there has been two long science runs:

- VSR1: from 18th May 2007 at 23:00 LT (21:00 UTC) to 1st October 2007 at 07:00 LT (05:00 UTC);
- VSR2: from 7th July 2009 at 23:00 LT (21:00 UTC) to 8th January 2010 at 23:00 LT (22:00 UTC).

The present work has been carried out with the enhanced configuration of Virgo, called Virgo+: so I will describe in particular this detector layout, which has only small changes respect to the standard configuration of Virgo.

The data samples presented in this work are taken during Virgo+ two long science runs:

- VSR3: from 10th August 2010 at 23:00 LT (21:00 UTC) to 20th October 2010 at 07:00 LT (05:00 UTC)
- VSR4: from 3rd June 2011 at 23:00 LT (21:00 UTC) to 3rd September 2011 at 07:00 LT (05:00 UTC).

2.3.1 Fabry-Perot cavities

Each of the two interferometer arms is constituted by a Fabry-Perot cavity, in order to amplify the optical path of the light inside the interferometer, without modifying the arm length l_0 and in order to reduce the shot noise (see fig. 2.3).

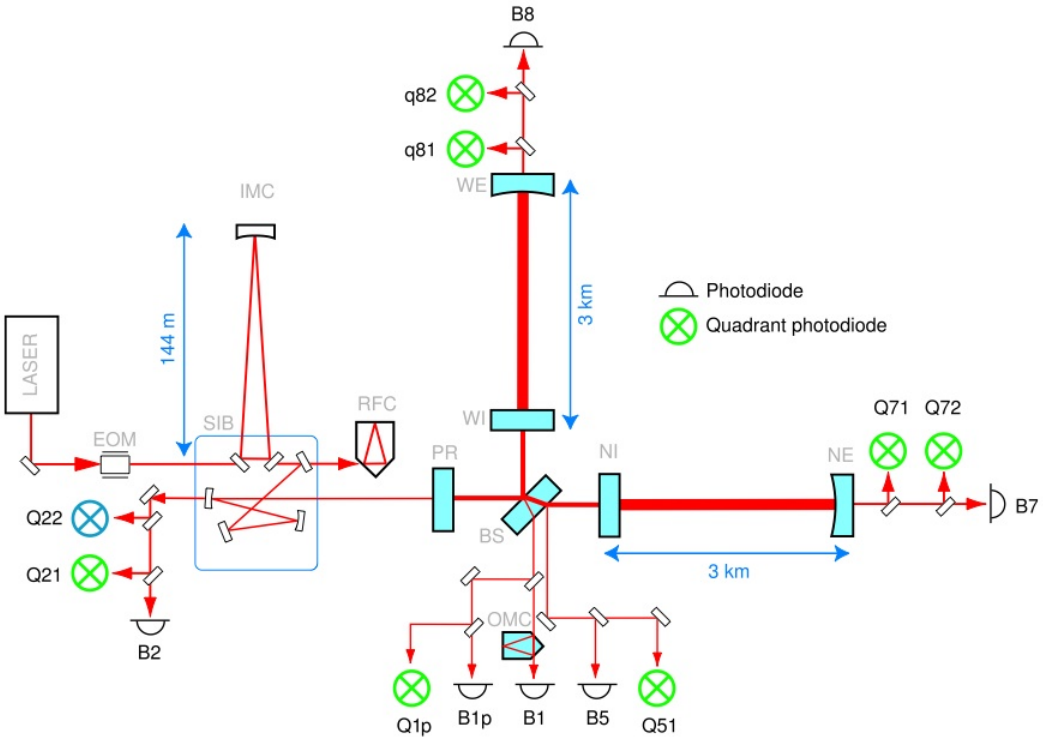

Figure 2.3: schematic optical lay-out of the Virgo detector; the optical surfaces and detected signals are shown. The two arms are directed toward North and West, so the names of the mirrors are abbreviated as NI (North Input), NE (North End), WI (West Input) and WE (West End). NE and WE mirrors high reflection surfaces have a mean radius of curvature of about $3500m$. NI and WI mirrors have all flat surfaces.

When the cavity between input and end mirrors is on resonance, its length is tuned to have constructive interference between the transmitted field by the input mirror and the one which has done a round trip inside the cavity; in this way we obtain the maximum power stored in the cavity and the maximum transmitted power.

It is possible to have different resonances for a same cavity; in fact if we consider a Fabry-Perot cavity where its length is fixed and the laser frequency is variable, for a given length L we have n resonant frequencies:

$$f_{res} = \left(n + \frac{1}{2}\right)\frac{c}{2L}$$

The spacing between two successive resonances is called *Free Spectral Range* (FSR):

$$\Delta f_{FSR} = \frac{c}{2L}$$

and each resonance has full-width-half-maximum value δf_{FWHM} (fig. 2.4).

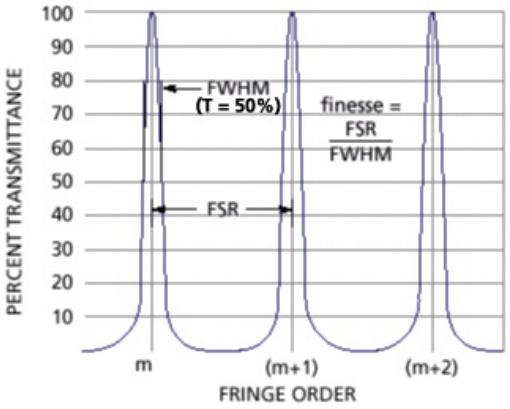

Figure 2.4: power transmitted by a Fabry-Perot cavity for different fringe order: free spectral range and FWHM are reported.

The parameter which describes the cavity is the finesse $\mathcal{F}$, defined in two different way, using the geometrical information of the cavity or the photometric informations of the mirrors [54]:

$$\mathcal{F} = \frac{\Delta f_{FSR}}{\delta f_{FWHM}} \approx \frac{\pi\sqrt{r_{in}r_{out}}}{1 - r_{in}r_{out}}$$

where r_{in} and r_{out} are the reflectivity of input and output cavity mirrors.

Thus, the optical path of the light L_{opt} inside the cavity is increased of a gain factor G which depends on the finesse cavity $\mathcal{F}$ [55]:

$$L_{opt} = LG = L\frac{2\mathcal{F}}{\pi}$$

In the case of Virgo, the two Fabry-Perot cavities have length equal to $L_1 = L_2 = 3km$ and the distance between the input mirrors and the beam splitter is $l = 6m$.

We evaluate the output power P_{out} with a gravitational wave passage, in a similar way of what obtained for eq. 2.5 and we have:

$$P_{out} = \frac{P_{in}}{2}\{1 + C\cos[(\Delta\phi_{FP}) + 2k_L\Delta l]\}$$

where $\Delta\phi_{FP}$ is given by:

$$\Delta\phi_{FP} = 2k_L\frac{2\mathcal{F}}{\pi}\Delta L^{GW} = 2k_L\frac{2\mathcal{F}}{\pi}\frac{1}{2}h(L_2 - L_1)$$

It is evident that, in this configuration, the phase shift induced by the gravitational wave passage is increased[1] with respect to the single mirror case, of the same quantity G.

However, when we take into account the time delay induced by the cavity resonance, we conclude that, in the case of a real interferometer, this amplification depends on gravitational wave frequency. Since the speed of light has a finite value, the detector acts as a low-pass filter with cut-off frequency $f_{cut\ off}$:

$$f_{cut\ off} = \frac{c}{4\mathcal{F}L}$$

where L is the cavity length. Note that the quantity $\mathcal{F}L/c$ is proportional at the storage time of the cavity and effect on interferometer response becomes relevant when the period of the gravitational wave is comparable to the storage time. For Virgo the cut-off frequency is $\sim 500Hz$.

In fig. 2.5 we show the transfer function of the end mirror motion to the transmitted signal, approximated at first order with a simple-pole function.

2.3.2 Power recycling mirror

We have seen that for a real interferometer the optimal tuning is the dark fringe: that means all the incoming power is reflected back to the laser. Therefore introducing the power recycling mirror, between the laser and the beam splitter, the power circulating inside the interferometer is enhanced and the shot noise reduced.

The effect of such a mirror can be computed describing the Michelson Fabry-Perot interferometer as an equivalent mirror of reflectivity r_{MICH} (close to one in absolute value if the interferometer is tuned at dark fringe). Therefore the full power recycled interferometer is equivalent to a Fabry-Perot cavity composed by this equivalent mirror and the power recycling mirror (with reflectivity r_{PR} and trasmessivity t_{PR})[56]. The recycling gain is defined as the ratio between the input power and the power circulating inside the central part of the interferometer:

$$G_{PR} = \left(\frac{t_{PR}}{1 - r_{PR}r_{MICH}}\right)^2$$

which is inverse proportional to the total losses of the interferometer mirrors. So the gain factor G_{PR} can be increased by reducing, as much as possible, the losses,

[1]The amplification given by the cavity is valid only if the period of the gravitational wave is longer than the storage time of the light inside the cavity.

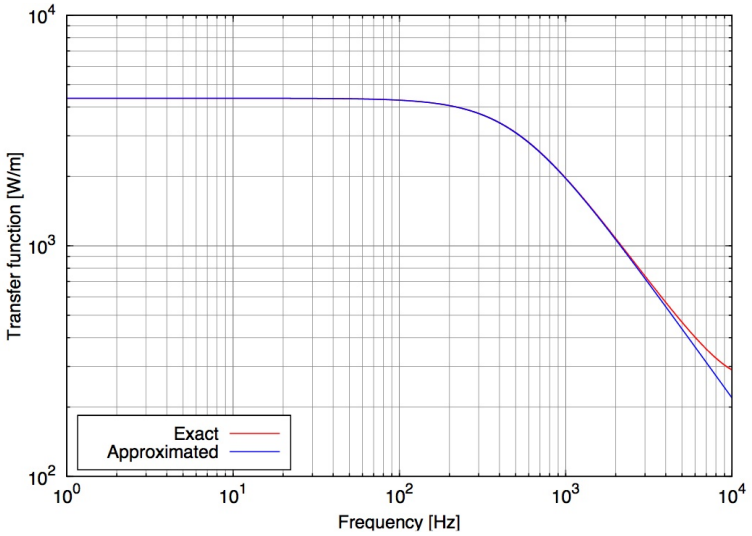

Figure 2.5: transfer function from longitudinal motion of the cavity end mirror to the transmitted demodulated signals, for a Fabry-Perot cavity with parameters $L = 3km$, $\mathcal{F} = 50$; the red curve is the exact expression, while the blue one is the usual one-pole approximation.

due to the light diffusion and absorption. In Virgo the mirror coatings should fulfill the constraint the wavefront surface deformation to be less than $\lambda/100$ and the total losses are of the order of tens of ppm. It follows that the nominal recycling gain is $G_{PR} \approx 50$.

In conclusion the limit detectable gravitational wave amplitude for a Michelson interferometer with the Fabry-Perot cavities and the power recycling mirror, sed by shot noise [57]:

$$\tilde{h}_{shot} = \frac{1}{4(L_1 + L_2)\mathcal{F}} \sqrt{4\pi\hbar \frac{\lambda_L c}{\eta G_{PR} P_{in}} \left[1 + \left(\frac{f}{f_{cut\,off}}\right)^2\right]}$$

which is $10^{-23} 1/\sqrt{Hz}$ for Virgo.

2.3.3 Injection system

The interferometer light source is a couple of lasers, emitting at a wavelength of 1064 nm; they are hosted in the laser bench, joint at ground and in air. The beam injected in Virgo is produced by a high power laser, the $Nd{:}TVO_4$ slave laser, locked to a high stability solid state $Nd{:}YAG$ master laser. In this way the higher power and frequency stability of the master laser is transferred to the slave. The two lasers are connected with a series of diodes in order to obtain a resulting power of $20W$ stable at the emitted frequency.

The light beam generated by the slave laser is modulated in phase by two *Electro-Optical Modulators* (EOM in fig. 2.3), at three different modulation radio-frequencies: $6MHz$, $8MHz$ and $22MHz$.

We define the laser electromagnetic field:

$$E = E_0\, e^{i\omega_L t}$$

and the phase modulation signal:

$$V = V_0\, e^{i\Omega t} \tag{2.13}$$

Thus, the resulting field is:

$$E' = E_0\, e^{i[\omega_L t + m\sin(\Omega t)]}$$

where m is the modulation depth.

The resulting field can be expressed as a series of the Bessel functions $J_n(m)$:

$$E' = E_0 \sum_{n=-\infty}^{\infty} J_n(m) e^{i(\omega_L + n\Omega)t}$$

that for $m \ll 1$, we approximate by considering just the first three terms:

$$E' \approx E_0[J_0(m)e^{i\omega_L t} + J_1(m)e^{(\omega_L+\Omega)t} - J_{-1}(m)e^{(\omega_L-\Omega)t}]$$

The field is described by three frequency component, i.e. two sidebands around the main carrier frequency, spaced by multiples of the modulation frequency Ω (see fig. 2.6).

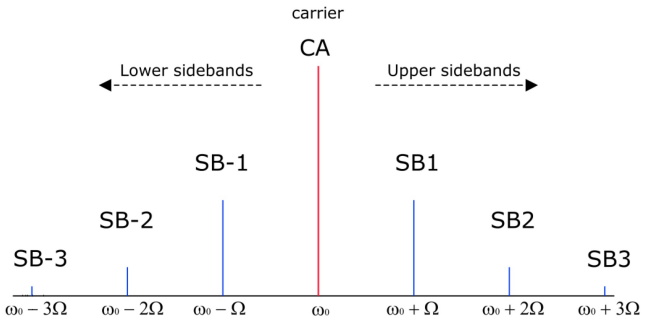

Figure 2.6: laser light modulation; it is possible to distinguish between the *carrier* (CA) and the *sideband* (SB).

The advantages of shifting at a AC detection method, respect to the DC scheme, consist in reducing the contribution of the power and frequency noise of the laser. Moreover, the control of the interferometer gets simpler.

In fact the Michelson interferometer is slightly modified introducing a macroscopic asymmetry in the arm lengths (in realty $L_1 \neq L_2$), called the *Snupp asymmetry*. In this way it is possible to have different resonance conditions for the carrier and the sidebands: in particular the carrier is tuned to have destructive interference while the sidebands are still present in the output port. The photodiode output signal is then extracted by mixing it with a reference sine or cosine oscillating at the same

frequency Ω; after applying a low-pass filter with a corner frequency much lower than Ω, the demodulated signal contains contributions coming from the beating of the carrier with the first two order sidebands.

The effect of the passage of gravitational waves is to introduce an additional dephasing to the two beams recombined at the dark port: in this way, the carrier beam is not more in destructive interference condition and it is detected in the output port. Therefore the response of the demodulated signal is linear.

After the two EOMs, the beam is sent to the *Beam Monitoring System* (BSM) which control the pointing of the beam thanks to two mirrors mounted on piezo-electric actuators. Then, the laser beam is sent to the *Internal Injection Bench* (SIB in fig. 2.3), a suspended bench in vacuum. Here, there are the output mirrors of the Input Mode Cleaner (IMC), a triangular cavity $144 - m$ long and with finesse of $\mathcal{F} = 1000$. As in all cavities, the IMC is a first order low-pass filter for power and frequency fluctations of the laser, with a cut-off frequency equal to its cavity pole ($f_0 = \frac{c}{4L\mathcal{F}} \sim 500Hz$). In particular the role of the IMC is to filter the laser beam suppressing all transverse modes different from the fundamental Gaussian[2] one and to reduce the beam jitter [55].

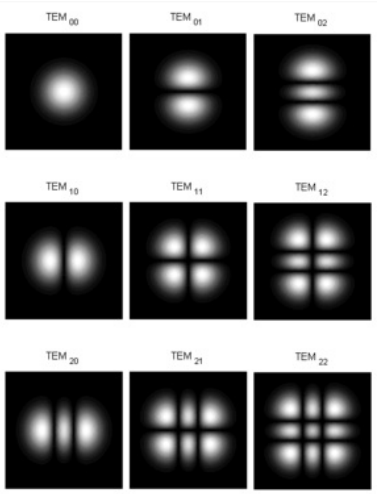

Figure 2.7: the first nine Transversal Electromagnetic Modes.

A small part of the IMC transmitted beam is sent to the *Reference Frequency Cavity* (RFC) a $30cm$-long rigid cavity used as part of the laser frequency pre-stabilization system.

2.3.4 Detection system

There are several relevant beams coming out from the interferometer and taken as reference for control the cavities. The laser power impinges on photodetectors, which

[2]In the para-axial approximation, the light beam is not propagated in a radially symmetric way, but there are contributes from other directions, forming different beam shapes [58]. Those shapes are described by the Hermite-Gauss functions, as known as Transverse Electromagnetic Modes, TEM_{mn} (see fig. 2.7).

can be either quadrant-split photodiodes (useful to angular control, see sec. 2.3.6), as simple photodiodes (useful to longitudinal control); the typical power hitting a photodetector can range from some μW to $100mW$.

In fig. 2.3 they are reported photodiodes (indicated with the letter B) and quadrant photodiodes (Q) of Virgo:

B1 and Q1 are the most important photodiodes, which bring the gravitational signal: they are at the antisymmetric port, the recombination of the differential mode signal coming form the two interferometer arms;

B2 and Q2 are the interferometer reflection signals, coming from the power recycling mirror and bringing information about the common mode of the two arms;

B5 and Q5 are the pick-off beams from the secondary face of the beam splitter; they are used as an indicator of the field inside the recycling cavity and they are sensible to the phase shift between the carrier and the sidebands;

B7/B8 and Q7/Q8 are the transmission beams of the two arm Fabry-Perot cavities, the North and the West arm; they are sensible to variation of the arm lengths and control the input mirror positions.

The detection system is divided in two parts: the suspended detection bench placed in vacuum, called *Output Mode Cleaner* (OMC), and the external detection bench not suspended and in air where there are $B1$, $B5$, $Q1$, $Q5$ photodiodes.

The Output Mode Cleaner is a rigid $2.5 - cm$ long optical cavity with finesse $\mathcal{F} = 50$, kept in resonance by controlling its temperature. This cavity increases the contrast C of the output interference signal: it transmits only the fundamental Gaussian mode, while it reflects all the higher Gaussian modes, produced by mismatching or mis-alignment of the interferometer.

The dark fringe signal, coming from the Output Mode Cleaner is sent to the external detection bench. Here the photodetector outputs are converted in digital signals by ADC boards, after passing into the compression and the anti-aliasing filters.

2.3.5 Suspension system

The Virgo main optics are suspended in vacuum (high tower residual pressure = $10^{-6}mbar$; low tower residual pressure = $10^{-9}mbar$) to multi-stages pendulums, called superattenuators.

The superattenuator (see fig. 2.8) has two roles:

- it reduces the seismic noise (see sec. 2.2.2) of a factor $\sim 10^{12}$ at frequency $10Hz$; it attenuates the effects due to vertical, horizontal and torsional motions; moreover, at frequencies higher than its resonance frequency $\sim 0.5Hz$, it keeps the test masses in the free-falling status:

- it permits to apply the actuation forces through a coils and magnets system (see sec. 2.3.6); in this way it is possible to align correctly the optical surfaces of the interferometer.

The superattenuator is formed by [59]:

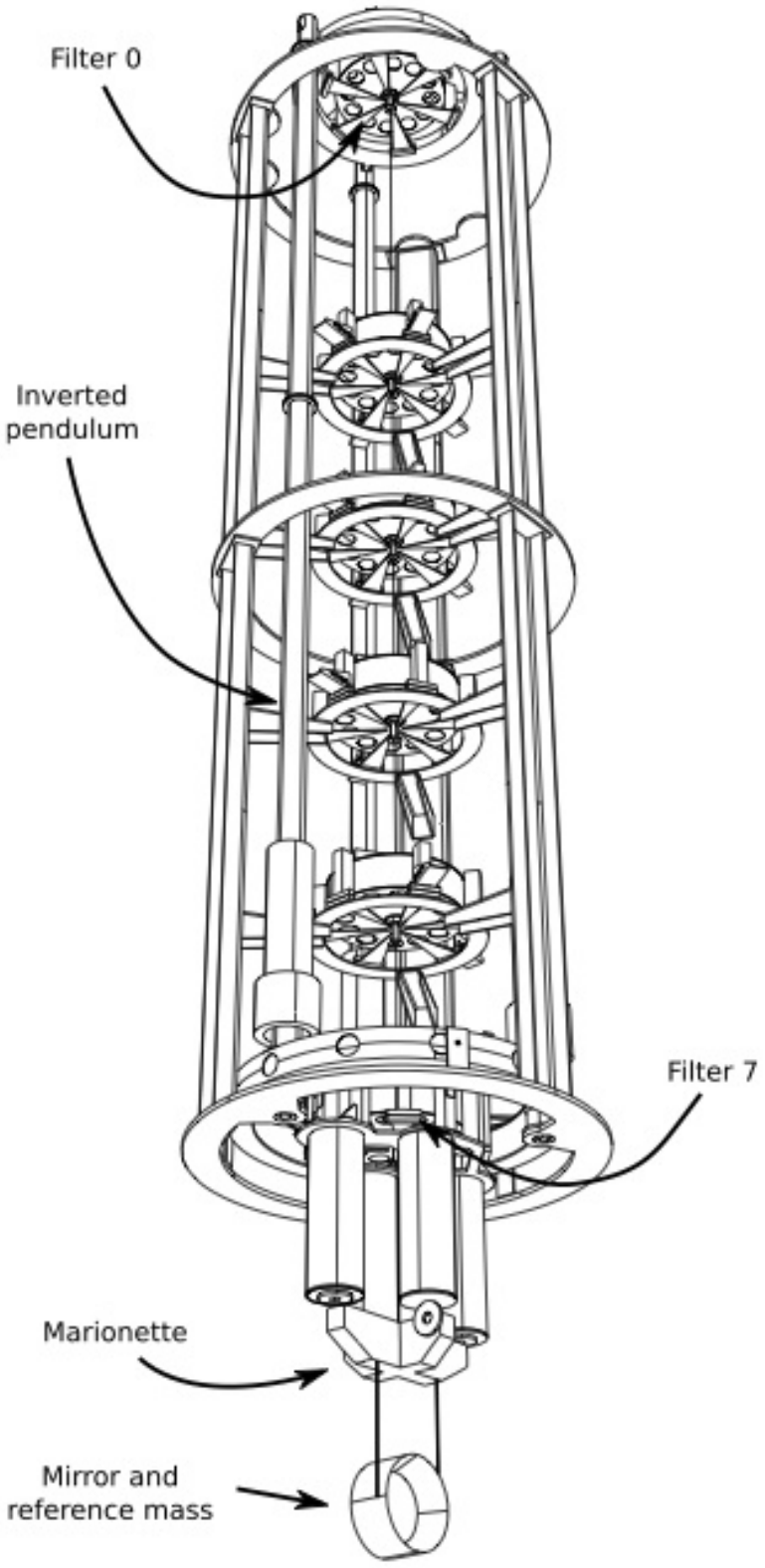

Figure 2.8: mechanical scheme of the superattenuator; they are reported several parts which form it, included the last stage suspension, the payload.

inverted pendulum it is a three-legs structure, $6m$ high, suspended with three elastic joints at ground and supporting a metallic ring on its top, the so-called top-stage; this system acts as a second-order low-pass filter, forming a pre-isolator for the seismic noise. It assures a very low resonance frequency f_0^{IP}, since the effect of the gravitational force is subtracted to the elasticity of the joint:

$$f_0^{IP} = \frac{1}{2\pi}\sqrt{\frac{k}{m}\frac{g}{l}}$$

where k is the joint elastic constant, m is the suspended mass and l is the pendulum length. Inserting the Virgo value, one obtains $f_0^{IP} \sim 30mHz$. To obtain the same low resonance frequency with a standard pendulum, it would be necessary a $\sim 280m$-long structure!

mechanical filters a $9m$-long chain of six filters is connected to the top stage. Each filter is a rigid steel cylinder suspended from its barycenter with steel wires, with a total mass of about $100kg$; the horizontal resonance frequency is of $\sim 0.45Hz$. To obtain an attenuation also in the vertical direction, each filter has got a series of triangular blades (see fig. 2.9(a)) with resonance frequency at $\sim 1.5Hz$. This low frequency value is acquired with two sets of magnets in repelling configurations, the magnetic anti-springs (see fig. 2.9(b)) [60]. For the torsional isolation, each filter has a high momentum of inertia with a resonance frequency of $\sim 1Hz$

The overall seismic attenuation is reported in fig. 2.10: they are shown the measured horizontal and vertical transfer functions from seismic motion of the ground to mirror displacement. The vertical transfer function is rescaled by a factor 10^{-2}, assuming a estimated coupling of vertical to horizontal motion of one hundredth.

payload that is the name of the last stage suspension, formed by the marionette, the reaction mass and the mirror (see fig. 2.12). For a more detailed description see the next paragraphs.

The last stage mirror suspension

The last stage mirror suspension permits:

1. to damp the external residual disturbances coming from the superattenuator, especially for the torsional degree of freedom θ_y (see fig. 2.11 to know the reference frame), where there is a residual motion of some μrad, and for the longitudinal d.o.f. z, where there is a residual motion of some μm; for a correct interferometer working point condition, these residual motions must be lower than $1\mu rad$ and $1\mu m$;

2. to adjust the initial mirror position with a dedicated control system (see also sec. 2.3.6); in this way the interferometer can use this pre-alignment system to reach its working point.

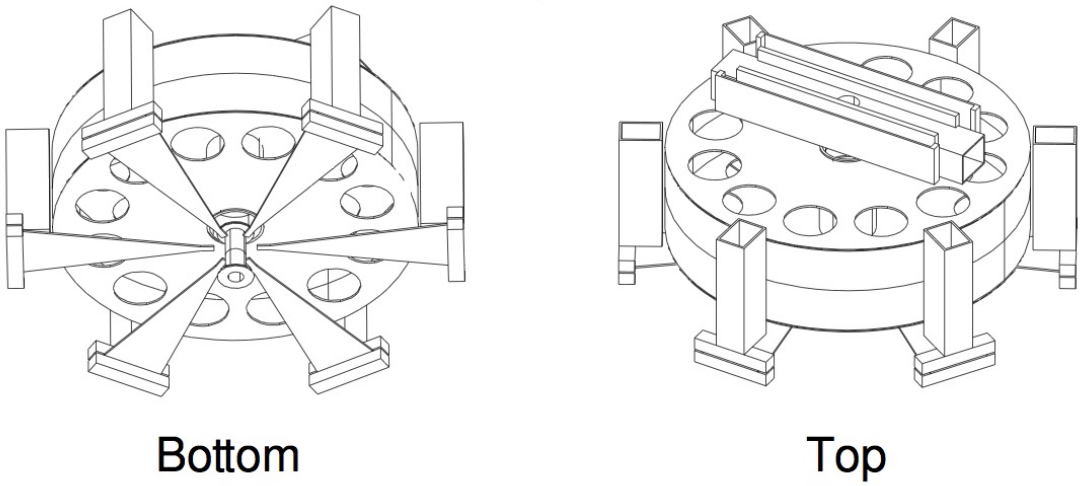

(a) full filter view from the bottom and from the top

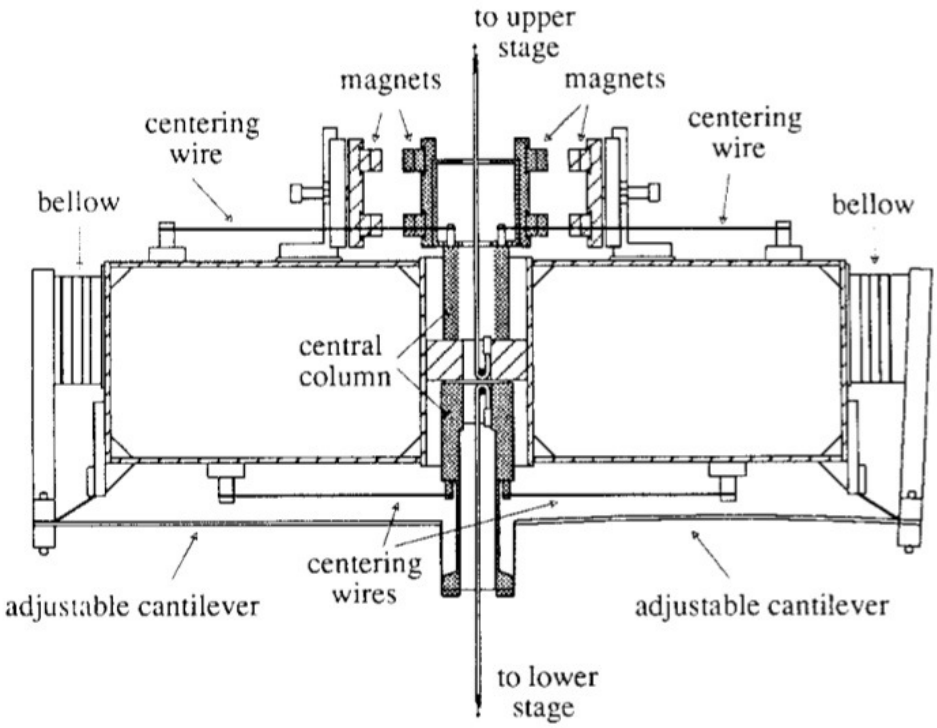

(b) schematic drawing of the isolation filter

Figure 2.9: schemes of vertical isolation filter.

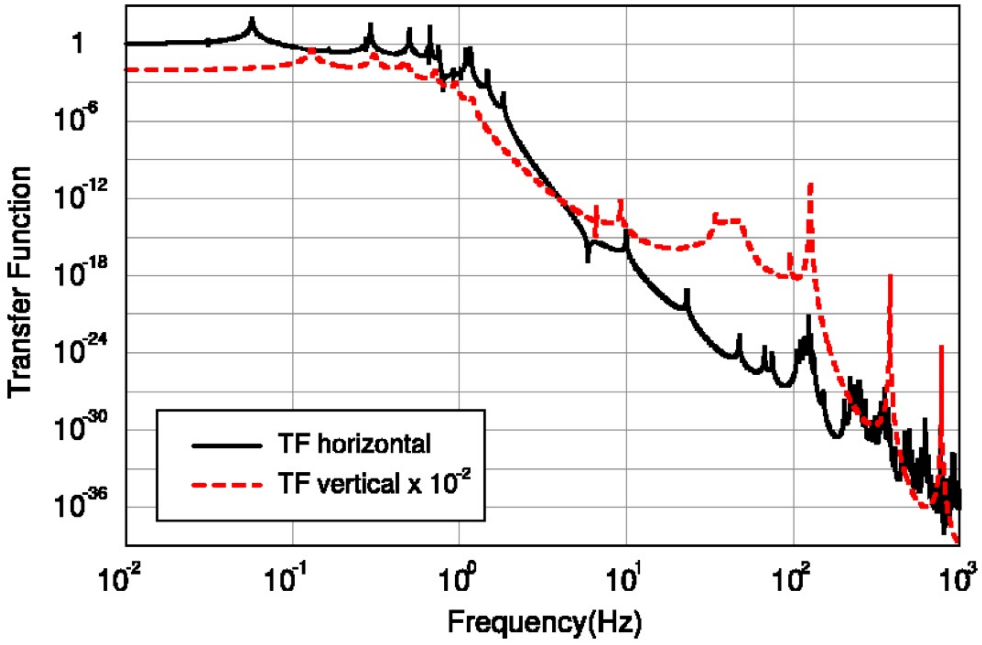

Figure 2.10: the measured horizontal and vertical transfer functions; note that the vertical transfer function is rescaled by a factor 10^{-2}.

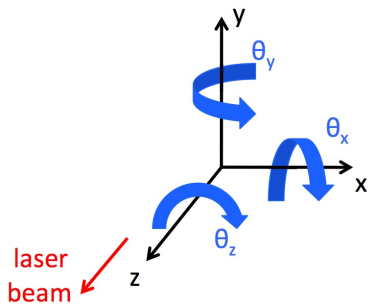

Figure 2.11: payload reference frame: the z axis is parallel to the laser beam; the angular movements are emphasized.

The technical design of the payload has been carefully studied [61] to fit several constraints:

- the mechanical resonance frequencies of the last stage elements must be as high as possible to avoid spurious thermal noise contributions to the interferometer output;
- the payload limits the dust contamination of the optical elements during the assembly phase and in operation (class 1 clean-room compatibility);
- then, it limits the cross-talk effects among the various degrees of freedom to be controlled; this implies an accurate design of the electromagnetic actuators and a careful design of the suspension point of the mechanical elements.

Displacement of the mirrors along the beam directions are controlled through four coils placed on the reaction mass, acting on magnets glued to the back of the mirror. By controlling the current flowing through these coils we apply longitudinal and torsional forces to the mirror, using the reaction mass as reference suspended point. In that way the control is free from any contamination with the ground micro-seismic motion in the detection bandwidth.

Both the mirror and the reaction mass are separately suspended to the marionette by four wires. In addition we steer the marionette along three different degrees of freedom: θ_x, the torsion around x axis, θ_y, the torsion around y axis and z, the longitudinal displacement along z axis.

To this purpose there are further four magnets attached to the marionette itself and four coils attached to four legs coming down from the last vertical isolation filter (filter 7). Any current applied to these coils results in a force on the marionette, which is then transmitted by the last pendulum stage to the mirror and the reference mass.

The marionette (see fig. 2.12) has a steel parallelepiped body with four lateral support for the magnets of the actuation system. An electric motor is set into the marionette central body: it is used to adjust the marionette alignment. The marionette is suspended through a single steel wire of maraging at the last superattenuator filter; then it supports two unconnected concentric series of four wires which surround the reaction mass and the mirror.

The reaction mass supports the four actuation coils and protects the mirror from falling in case of wire breaks or impacts. Furthermore it damps the most large elongation of the mirror through four peek stops. On the edge of the reaction mass four markers are positioned: their function is to allow the coarse alignment of the mirror and the damping of the larger oscillations.

The mirror is a suprasil cylinder (the substrate or bulk) where several reflective coating layers, low refractive index and high refractive index alternating, are deposited [62]. The input mirrors of the Fabry-Perot cavity are flat, while the end mirrors have a concave shape with radius of curvature (RoC) equal to $\sim 3400/3500m$: in this way it is easier to maintain the beam stable in the cavity. On the back face of the mirror there are four small magnets, overlooked at the reaction mass coils, for the actuation and control of the mirror position.

In Virgo and in Virgo+ the mirror mass is of about $20kg$: in Advanced Virgo the mass is doubled to reduce radiation pressure contribute.

In the Virgo initial configuration all the mirrors are suspended with steel wires. Instead in the Virgo+ configuration, to limit the contribution of the suspension thermal noise the steel wires have been substituting with fused silica fibers, made up and assembled in the Virgo laboratories [63]. These fibers are attached to the mirrors through silica ears silicate bonding on lateral flattened sides of the mirrors. For more details see sec 4.1.

2.3.6 Damping and control systems

Suspension and apparatus controls are crucial for the correct functioning of the interferometer. Two control level are present:

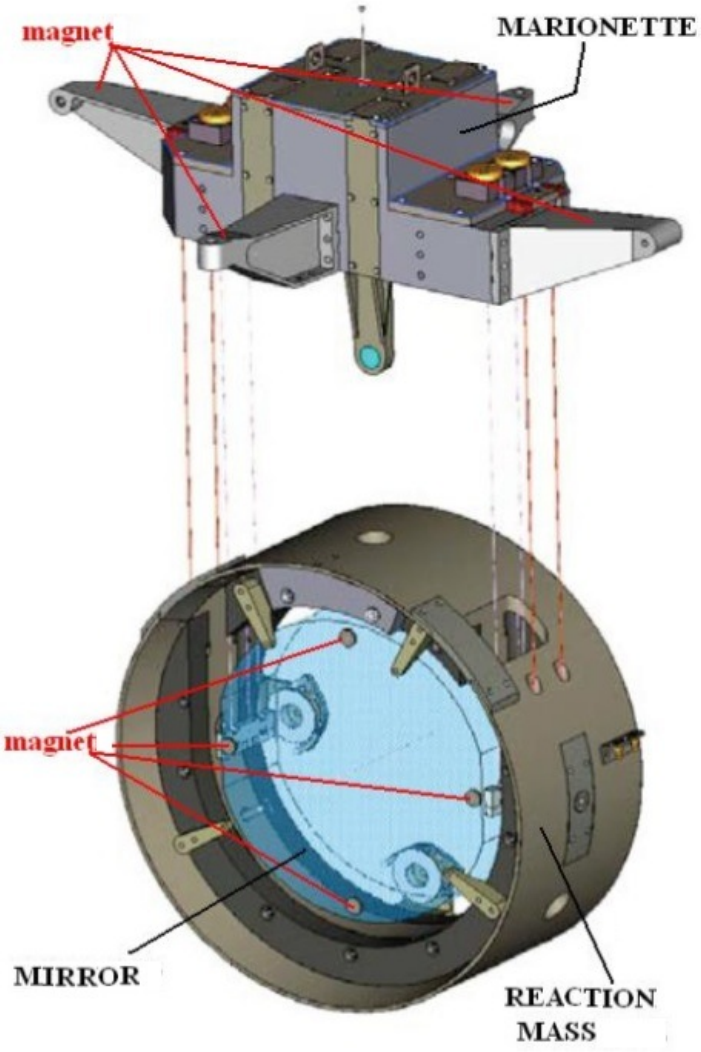

Figure 2.12: Virgo+ payload: they are shown the marionette, the reaction mass, the mirror and the magnet positions.

- local control and inertial damping: they deal with the correct positioning of the optics respect to the ground; they are based on the error signals provided by the various systems of optical levers, accelerators and position sensors, monitoring each suspension.

- global control: it is based on the error signals derived from the interferometer; it deals with the correct linear and angular positioning of the optics, one respect each other;

Local control and Inertial damping

The goal of the inertial damping and local control is to control the position of the mirror respect to the ground and to damp the internal modes of the suspensions.

The inertial damping deals with the superattenuator movements, controlling them from the top stage of the inverted pendulum. Here, there is a set of accelerometers and position sensors, as shown in fig. 2.13. The position sensors are Linear Voltage differential transformers, LVDT, and measure the absolute position of the top stage respect to the ground. The accelerometers and the LVDT signals are combined together, using the LVDT at low frequencies ($f < 50 - 100mHz$) and acceleraometers at higher frequencies, where they are less noisy. In that way it is possible to control the horizontal, vertical and rotational motion and to modify the top stage position, correcting the position of all the superattenuator. Thanks to its very low stiffness, the superattenuator can be moved by applying very small forces through coil-magnet actuators.

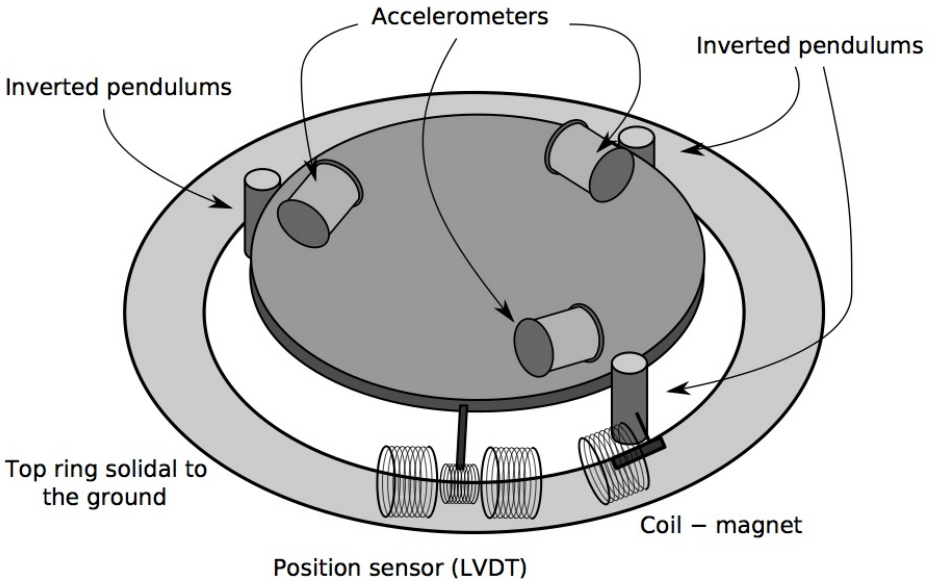

Figure 2.13: scheme of the top stage of the superattenuator, hosting the sensors and actuators used for the inertial damping system. For simplicity only one LVDT is shown.

The local control monitors the payload position. It is designed to damp the internal angular and longitudinal modes involving the mirror, that the inertial damping is not able to control. In that way, it is possible to recover the reference position of each mirror separately and to approach the interferometer working point.

Longitudinal and angular mirror positions are reconstructed by means of two optical levers based on two low-power red laser diodes: one laser beam points directly the mirror, while the second one is reflected by an auxiliary mirror installed below the marionette. The reflected beams are detected by the position sensing devices, PSD (see fig. 2.14).

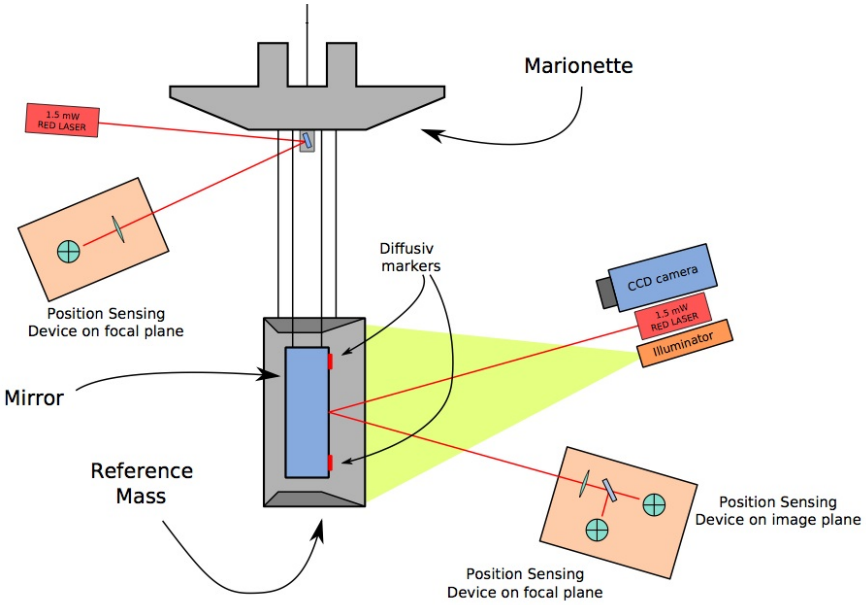

Figure 2.14: scheme of the local control sensing system, including the marionette and mirror optical levers.

When the oscillation amplitude is larger than the dynamical range of the PSD sensors, the coarse position is reconstructed using a camera CCD which monitors the relative position of the diffusive markers attached to the mirror itself.

The local control system also receives the global interferometric signals for the longitudinal and angular sensing and control, transmitted to the central and terminal buildings by digital optical links (DOL).

In order to reduce as much as possible the required dynamics of the actuators, part of the control force is re-allocated from the mirror-reaction mass actuators to higher stages: the very low frequency component is sent to the inertial damping control system (in particular to the filter 0); the intermediate frequency component is actuated on the marionette and only the high frequency part of the signal is sent to the reaction mass coils.

The local control of the mirror position has an accuracy of $\sim 1 \mu rad$ and it is not sufficient to fulfill the interferometer requirements for keeping the detector on the resonance condition. Furthermore, this control system is referred to the ground,

then limited by the seismic motion, and it is also affected by the temperature drift. So it is not stable for long time period. It is for these reasons that global control is necessary.

Global control

The global control uses optical signals of all the interferometer photodetectors to compute the forces to be applied to the mirrors which keep the resonance conditions [66]. The global control is split in two parts:

- the *locking system* (error signals coming from the photodiodes B, shown in fig. 2.3) reconstructs and controls the longitudinal position of the six mirrors to maintain the correct resonance conditions of the light inside the detector;

- the *automatic alignment* (error signals coming from the quadrant photodiodes Q) reconstructs and controls the angular position of the mirrors, one respect each other and respect the incoming beam.

The locking system control the lengths of the cavities. If the length of given cavity is not controlled, the resonance condition changes and the reflected and transmitted powers are not stable.

To keep a cavity on resonance it is necessary to find an optical signal which is sensitive to the length variation with respect to the resonant length. The signal transmitted by the cavity would be maximum at resonance, but it decreases both if the cavity gets longer or shorter. Therefore it does not contain enough information for control purposes.

A possible solution is the detuned locking: the cavity is kept slightly away from resonance and therefore the transmitted power signal has a non-zero slope against length changes. This method is used also in Virgo, thanks to the frontal phase modulation: it is called Pound-Drever-Hall technique [64, 65]

The resonance conditions to satisfy are:

1. the carrier field must be resonant inside the long arm Fabry-Perot cavities, to enhance as much as possible the optical response to a gravitational signal;

2. the carrier field must also be resonant in the central part of the interferometer, namely in the compound cavity composed of the power recycling and the two input mirrors, to take advantage of the increase of internally circulating power;

3. the carrier field must finally undergo destructive interference at the output port, to have the highest signal-to-noise ratio configuration (dark fringe);

4. the two sideband fields must be totally reflected from the long arm cavities and used as reference for the carrier dephasing;

5. the two sideband fields must also be resonant in the central cavity, to take advantage of the circulating power increase. In general they are not interfering destructively at the dark port.

In principle, we will have six degree of freedom to satisfy these resonance conditions, corresponding to the six longitudinal displacement of the mirrors. Actually, only four of these are fundamental [67] (for the lengths, refer to fig. 2.15):

1. the common mode motion of the long cavities (CARM) → seen in the $B2$ and $B5$ photodiodes (the carrier beam is greatly sensitive to CARM changes):

$$L_{CARM} = \frac{L_{NE} + L_{WE}}{2}$$

2. the differential mode motion of the long cavities (DARM) which contains the gravitational signal → seen in the $B7$ and $B8$ photodiodes:

$$L_{DARM} = \frac{L_{NE} - L_{WE}}{2}$$

3. the differential motion of the central Michelson interferometer (MICH) → seen in the $B2$ and $B5$ photodiodes (the sideband beams are greatly sensitive to MICH changes):

$$L_{MICH} = L_{NI} - L_{WI}$$

4. the length change of the power recycling cavity (PRCL) → seen in the $B2$ photodiode:

$$L_{PRCL} = L_{PR} + \frac{L_{NI} + L_{WI}}{2}$$

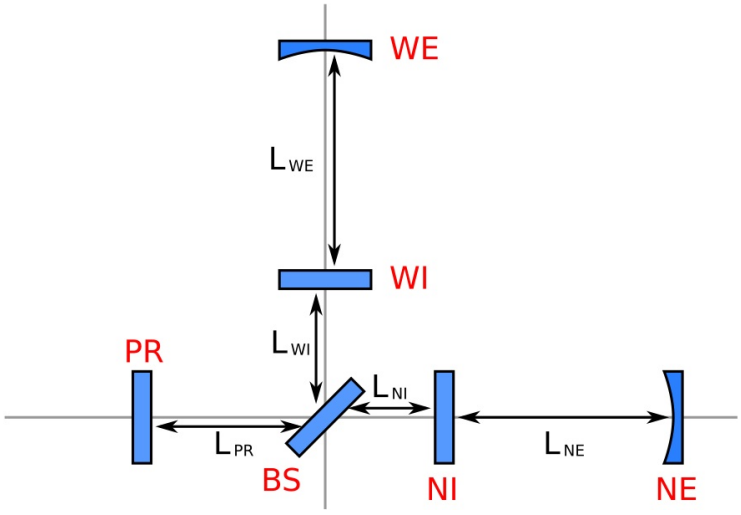

Figure 2.15: definition of lengths in a power-recycled Fabry-Perot interferometer as Virgo.

These four physical degrees of freedom give us the error signals and must be converted to the actual corrections to be sent to every single mirror.

Since the motion of a mirror changes also other cavity length, the correction signals are combined together:

$$\begin{aligned} C_{NE} &= C_{CARM} + C_{DARM} \\ C_{WE} &= C_{CARM} - C_{DARM} \\ C_{BS} &= \frac{1}{\sqrt{2}} C_{MICH} \\ C_{PR} &= C_{PRCL} + \frac{1}{2} C_{MICH} \end{aligned}$$

Actually, the coefficients of the driving matrix are different from what reported here, because they must take into account the coils-magnets actuator gain differences for each mirror.

Angular misalignments of the mirrors spoils the stability of the longitudinal control; for this reason the automatic alignment has been developed to control two degrees of freedom θ_x and θ_y for each of the six main mirrors. Furthermore a control of the input beam pointing must be implemented to avoid slow drifts that might move the beams out of the mirror centers, leading to worse performances of the detector.

To build a system capable of controlling the alignment of a resonant cavity it is necessary to extract error signals that measure the position of the mirrors with respect to the beam axis. The most common technique is called wave-front sensing [68]. It uses quadrant-split photo-detectors (shown in fig. 2.3 with Q symbols) where the sensitive area of these photo-diodes is divided into four sectors. Each quadrant produces several output signals: the power impinging on each one of the four sectors and the demodulated difference between opposite sectors. The normalized difference of the powers detected by opposite sectors can be computed to obtain signals sensitive to the beam position on the quadrant.

These sensors are able to detect the superposition of different TEM modes: in fact, when there is a misalignment respect to optical beam reference system inside the cavity, the higher order modes are produced. In general only the first mode TEM_{00} of the carrier beam is resonant inside the cavity, while all the other components are reflected.

In Virgo it is used the Anderson technique with the light transmitted from the cavity to extract complete information on the misalignment of the cavity [69].

When a cavity is locked, we have:

- for the carrier:
  - TEM_{00} mode is resonant;
  - TEM_{10} and TEM_{01} modes are not resonant;
- for the sidebands:
  - TEM_{00} modes is anti-resonant and almost completely reflected by the cavity;

– TEM_{10} and TEM_{01} modes of one of the two sidebands, the upper for example, is made resonant inside the cavity, choosing an appropriate modulation frequency (in particular an integer multiple of the frequency difference between the first and the second of TEM mode).

Any misalignment generates one of high order mode that, being resonant, is present in the transmission port. Here a wave-front sensor detects the beating of any TEM_{00} and TEM_{10} modes: the only possible combination is the carrier for the first and the upper sideband for the second. This component can be extracted using a demodulation technique on the difference signals of the quadrant sensor and this is used as an error signal for the alignment system.

The bandwidth of the control in this configuration is of the order of few Hz. The angular correction is normally applied at the level of the marionette. In this configuration the local control system is completely switched off [70].

2.3.7 Thermal Compensation System

The Thermal Compensation System (TCS) is designed to sense and correct for a wide range of thermal effects in the core optics [71].

In fact, the optical power impinging on the mirrors of the Fabry-Perot cavity[3] is predominantly absorbed by the mirror high reflective coating ($\sim 50mW$) producing a gradient of temperature inside the substrate.

Two different effects originate from the heating of the test mass:

- nonuniform optical path length distortions (thermo-optic effect, also termed thermal lensing, mirror figure errors, inhomogeneity of the substrate refraction index) mainly due to the temperature dependency of the index of refraction;

- change of the profile of the high reflective surface, due to thermal expansion (thermo-elastic deformation) and, so, the consequent change of the profile of the beam circulating into the interferometer.

TCS must reduce thermal effects to a level that allows the interferometer to acquire the lock and such that the sensitivity of the detector is not spoiled. Furthermore TCS could help when some optics should not meet the specifications (mirror radius errors, higher or non-uniform absorptions).

In the case of Virgo/Virgo+ the main thermal effect is the thermal lensing, affecting the Power Recycling Cavity: in presence of thermal lensing, which changes the cavity mode, the input laser no longer matches the power recycling cavity, the coupling coefficient between the laser mode TEM_{00} and the cavity mode TEM_{00} is less than one.

[3]While the input power is equal to $P_{in} = 20W$, the circulating power in the interferometer is:

$$P_{itf} = \frac{P_{in}}{2}\mathcal{F}_{PR} \cdot \mathcal{F}_{FP} = \frac{20}{2}50 \cdot 50 = 25kW$$

where $\mathcal{F}_{PR}$ is the finesse of the power recycling cavity, $\mathcal{F}_{FP}$ the finesse of the Fabry-Perot cavity. The factor 2 depends on the two interferometer arms.

Thermal expansion changes the profile of the high reßective surface. A bump raises in the center of the test mass faces, making their surface profile non-spherical. Given uniform absorption at the $0.5ppm$ level expected in advanced detectors, this departure from sphericity does not make the arm cavity resonant modes significantly non-Gaussian. The cavity becomes less concentric and the spot sizes at the mirrors will shrink. The resulting increase of thermal noise has been estimated to be of the order of 15%. To maintain the arm cavity mode structure, it is necessary to control the radii of curvature of all test masses.

For Virgo+ the basic idea of TCS is to impinge on the mirrors with an additional and independent CO_2 laser, with a single axicon heat pattern (fig. 2.16): in this way the mirrors are uniformly heated and the deformations are reduced.

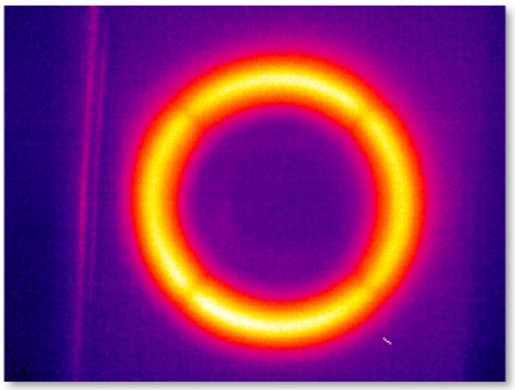

Figure 2.16: laser TCS heating pattern on the test mass in the IR bandwidth.

Presently, in Virgo+, the correction of mirror RoC is assigned to a different device, the Central Heating RoC Correction (CHRoCC) [72]. In fact, after the Virgo+ mirrors installations, it was noted that the end mirrors have different RoC (the difference is around $130m$) and a large astigmatism; these asymmetries cause problems in interferometer lock acquisition and sensitivity.

In fact the dark fringe power is dominated by high order TEM modes (in particular the fifth) and the total output power before the OMC was equal to $\sim 3.4W$.

The idea of the CHRoCC is to increase the radius of curvature of the high reflectivity surface of the end mirrors by sending a shaped beam heating pattern to the mirror (see fig. 2.17). This change in radius of curvature is obtained due to the thermal expansion of the Fused Silica mirror substrate.

In addition we need to correct for higher order aberrations such as astigmatism. In that way it would be possible to “match” the shape of the West end and North end mirror minimizing the residual light power reflected by the interferometer which arrives at the dark port ($\sim 540mW$ before the OMC after CHRoCC installation). The CHRoCC sources are blackbody emitters made of bare heating resistors or Alumina with an embedded heating resistor.

The CHRoCC were installed in the end towers before the fourth Virgo scientific run VSR4.

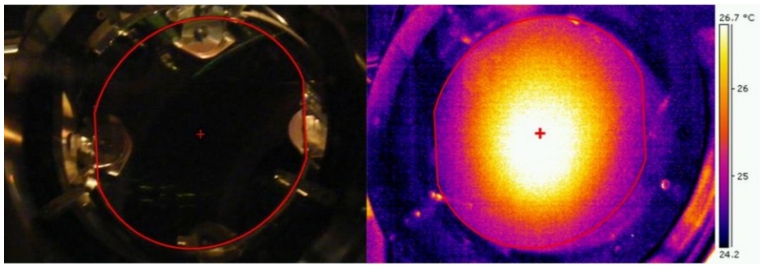

Figure 2.17: CHRoCC heating pattern on the test mass: on the left it is shown the mirror in the optic bandwidth; on the right the IR bandwidth.

2.3.8 Sensitivity curve

The sensitivity curve indicates the minimum detectable intensity of a gravitational wave from the interferometer with respect to frequency.

We estimate the design sensitivity curve from the expected contribution of the different noise spectral densities: we report the Virgo sensitivity in fig. 2.18 [57]. We show the Virgo+ case in fig. 2.19 [73]. The design curves are computed using a Matlab code (GWINC) developed inside the LIGO community and modified for Virgo [74].

The general features of the sensitivity curve are the following:

- for frequencies less than $\sim 10Hz$ the residual seismic noise is dominant;
- for frequencies between $\sim 10Hz$ and $\sim 300Hz$ it is prevalent the suspension and bulk thermal noise;
- for frequencies more than $\sim 300Hz$ the shot noise is dominant.

We compare this curve with the measured one, during the different scientific run of Virgo and Virgo+ in fig. 2.20. It is evident a discrepancy between what expected for Virgo+ and what measured in the $10 - 300Hz$ frequency band. In that region the expected noise contributions are the suspension and bulk thermal noise. Then, it is crucial to verify this prediction with a dedicated thermal noise measurement campaign. This is the key point of this thesis: I will present and discuss the results obtained measuring the quality factor resonances in the next chapter. It should permit to infer the real thermal noise contribution in the Virgo+ configuration.

2.4 Advanced Virgo

Advanced Virgo is the project to upgrade the Virgo detector to a second generation instrument. The aim of Advanced Virgo is to improve the original Virgo by one order of magnitude in sensitivity, which corresponds to an increase of the detection rate by three orders of magnitude and a universe volume explored about 1000 times larger than Virgo.

Advanced Virgo will be a dual recycled interferometer (see its optical layout in fig. 2.22). Beside the standard power recycling, a signal recycling cavity will be

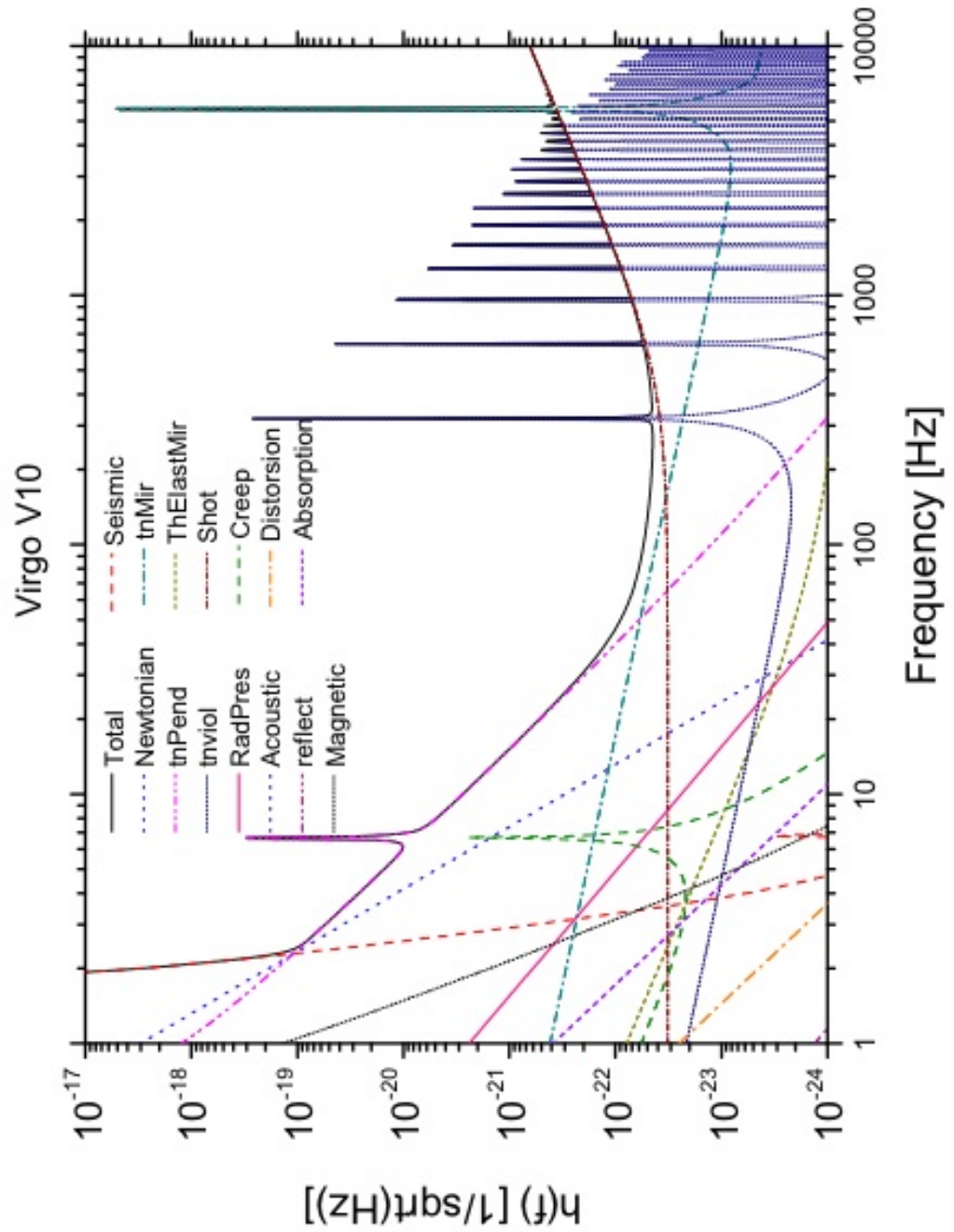

Figure 2.18: design sensitivity curve for Virgo: note the contribution of different noise surces.

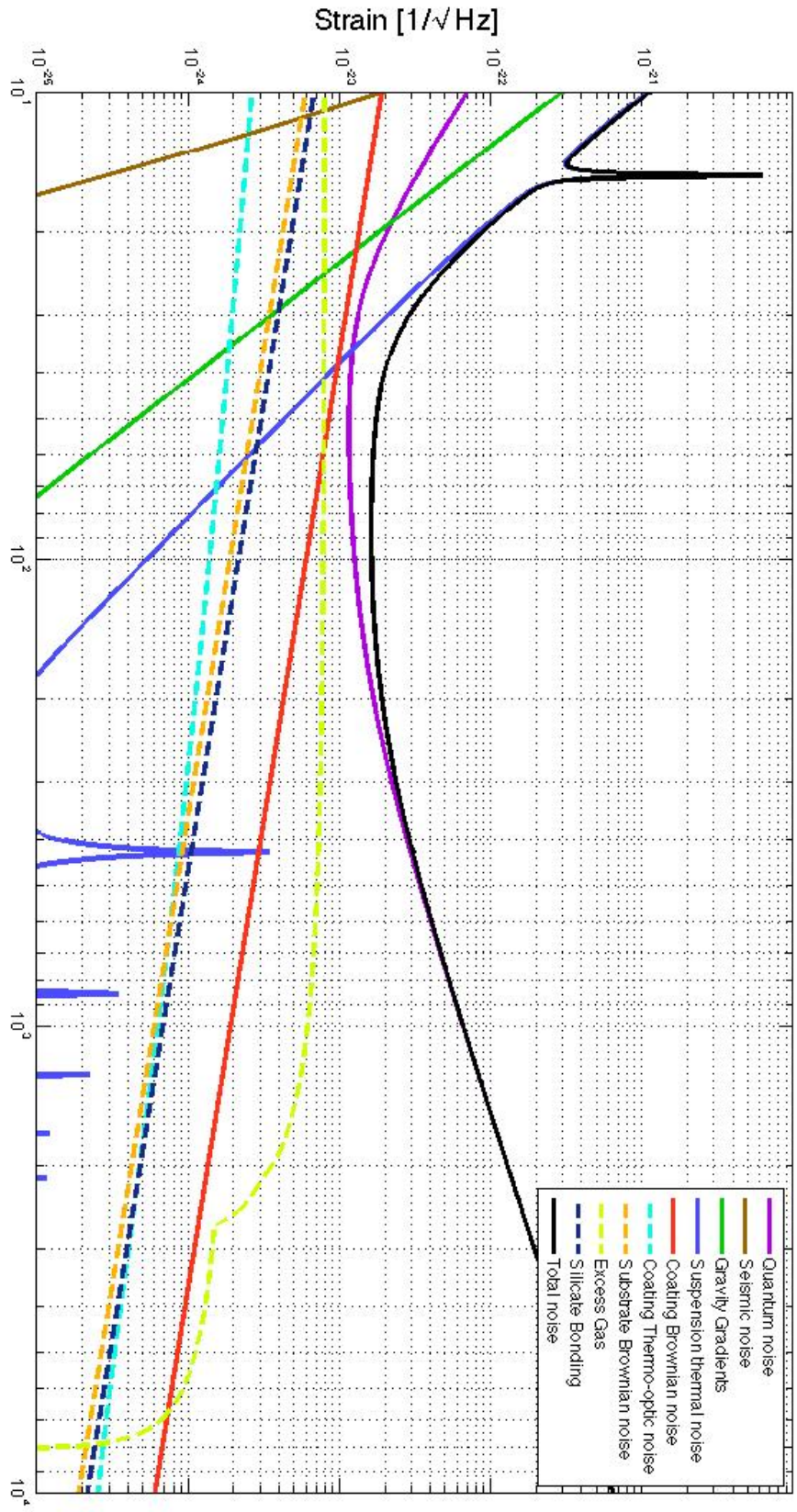

Figure 2.19: design sensitivity curve for Virgo+.

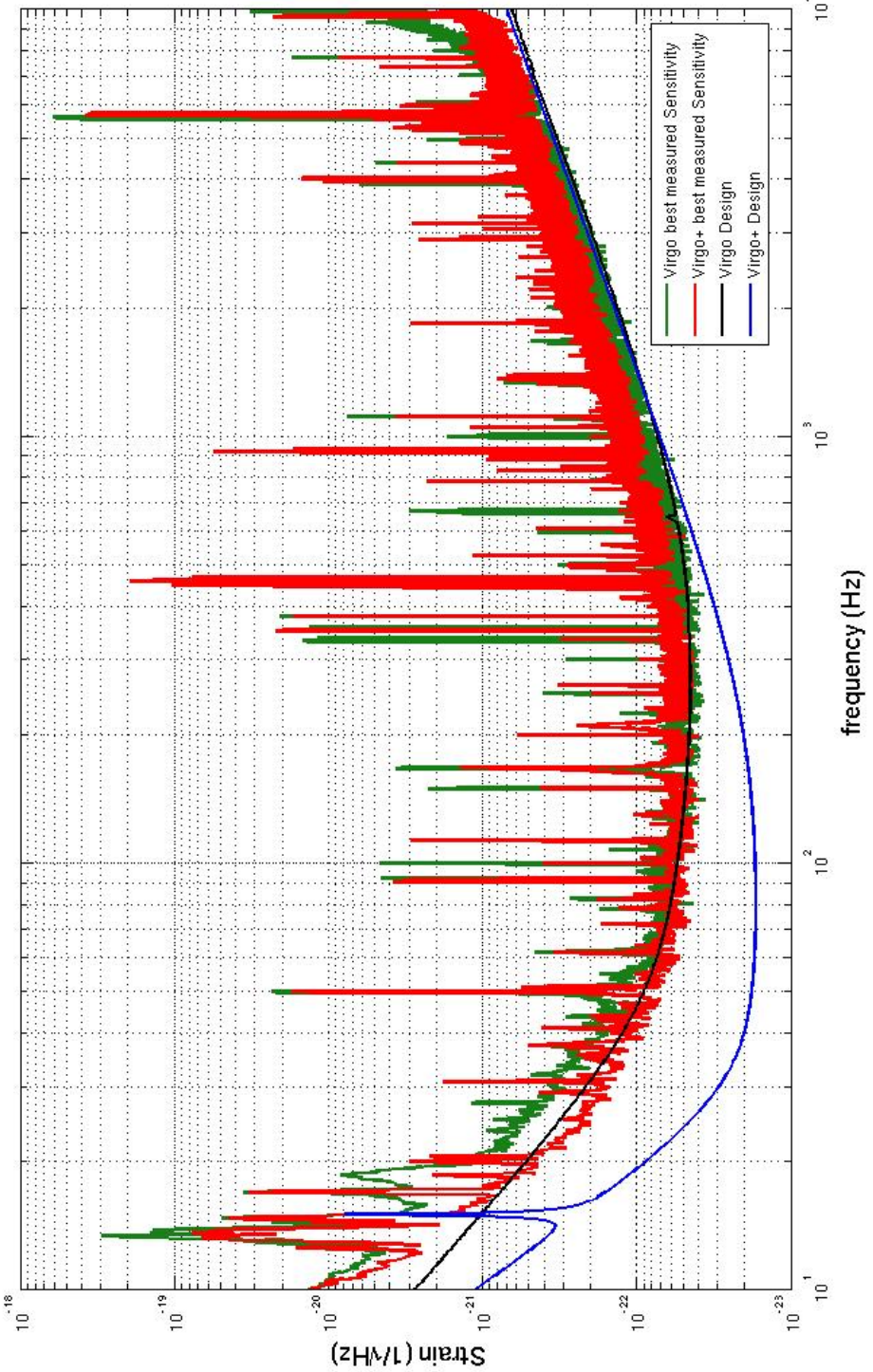

Figure 2.20: comparison between Virgo and Virgo+ sensitivity curves: they are reported the design and the best measured curves.

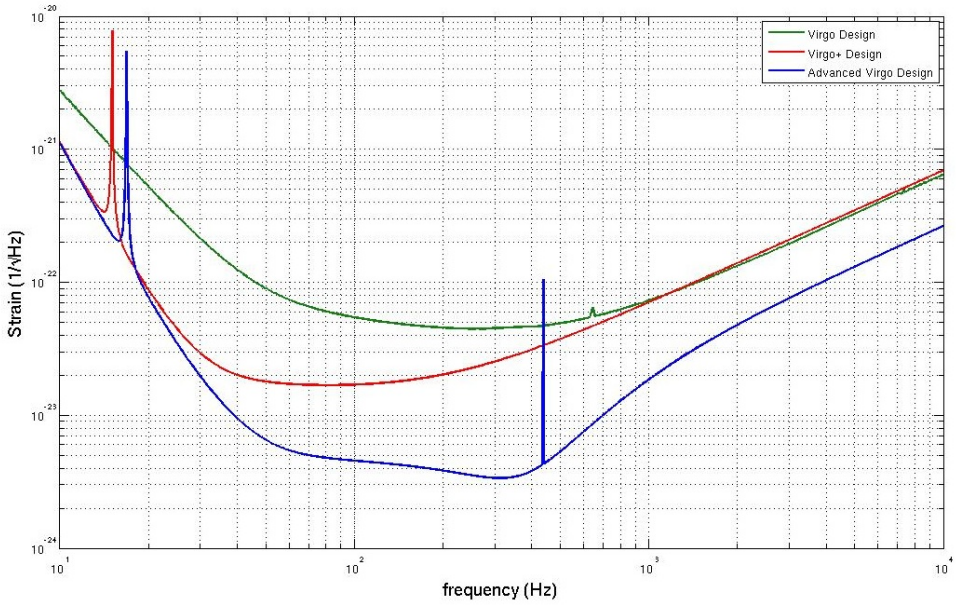

Figure 2.21: comparison of Advanced Virgo sensitivity with the design sensitivity of Virgo and Virgo+; the "BNS optimized" is representative of a range of possible sensitivity tunings.

present. The tuning of the signal recycling parameter allows to change the shape of the sensitivity curve and to optimize the detector for a given astrophysical source by scientific or commissioning motivations.

This sensitivity shaping is possible because of the connection between quantum noises, shot noise and radiation pressure. In fact the effect of the signal recycling mirror is to correlate these two noise sources through the mixing of the quadratures at the output of the interferometer.

The Advanced Virgo reference sensitivity [75] as well as the main noise contributions are shown in fig. 2.21. The curve corresponds to a dectector configuration with $125W$ at the interferometer input and signal recycling parameters chosen in order to maximize the sight distance for binary neutron stars. The corresponding inspiral ranges are $\sim 135Mpc$ for binary neutron stars system and $\sim 1Gpc$ for $30M_{\odot}$ binary black holes system.

Instead in fig. 2.24 are shown different sensitivity curve shapes, depending of the signal recycling tuning.

2.4.1 Advanced Virgo subsystem improvements

To reach the new design sensitivity, most of the detector subsystems have to deliver a largely improved performance [76].

As said in the sec. 2.2.1, the Virgo design sensitivity is limited at high frequencies by the shot noise. To reduce this contribution it is necessary to increase the laser power (see eq. 2.10) from a value of $20W$ to $125W$; but that causes two different effects:

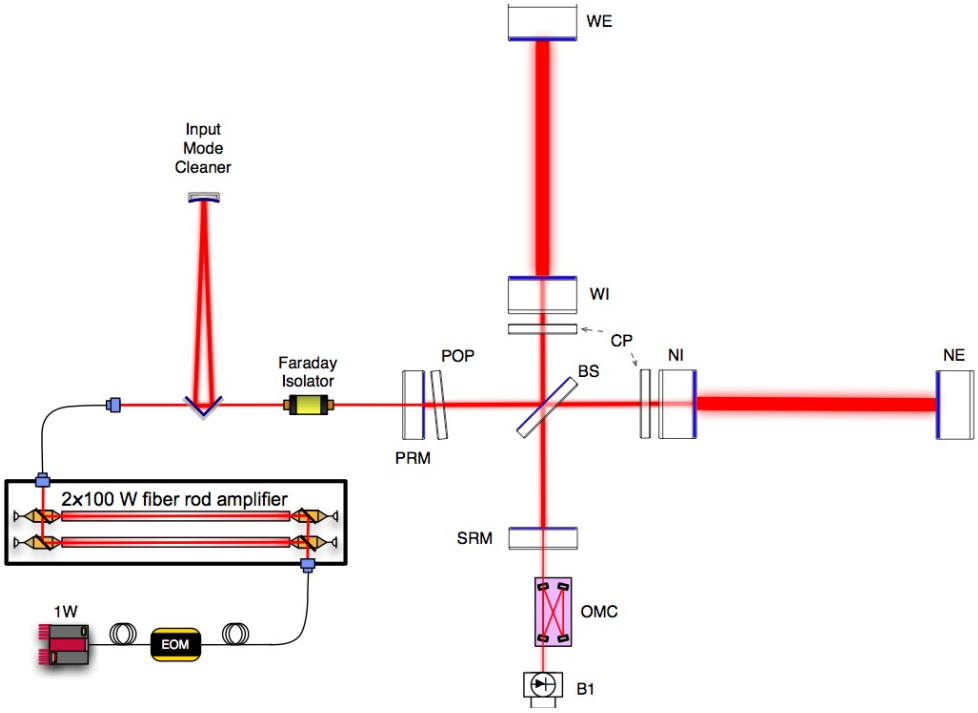

Figure 2.22: Advanced Virgo optical layout: note the two recycling mirrors, the power recycling (PRM) and the signal recycling (SRM), the compensation plate (CP) and the pick-off plate (POP).

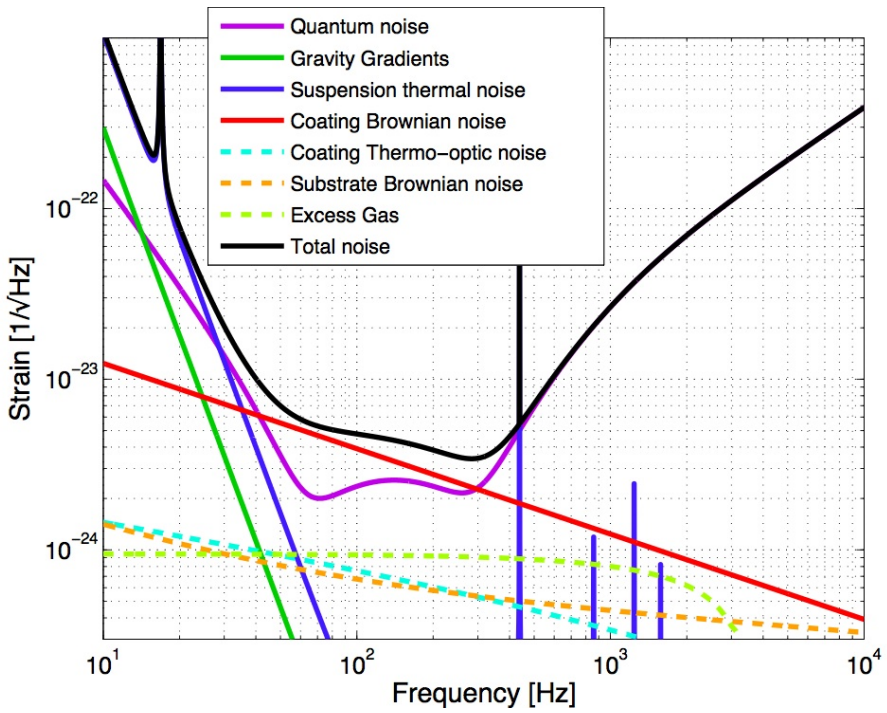

Figure 2.23: reference Advanced Virgo sensitivity and expected noise contributions; the chosen signal recycling tuning optimizes the inspiral range for coalescing binary neutron stars.

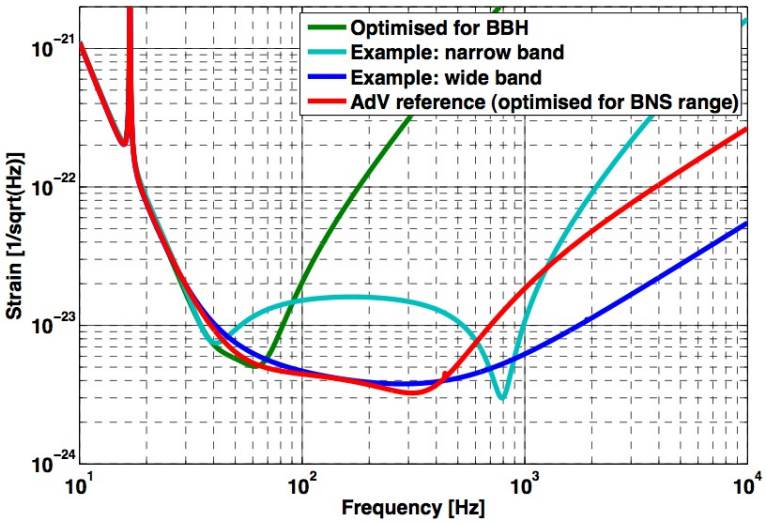

Figure 2.24: tuning the Advanced Virgo sensitivity by changing the signal recycling parameters; the red curve corresponds to the reference sensitivity and maximizes the inspiral range for binary neutron star system. The green curve is optimized for binary black holes system detection and is obtained with a low input power ($9W$). The cyan curve shows a narrow band tuning, useful to target a monochromatic source, while the blue "wide-band" tuning allows to improve the high frequency sensitivity.

1. there will be more radiation pressure (see eq. 2.11) which will give rise to larger mirror fluctuations: to limit this effect the mirror masses must be larger;

2. there will be a larger circulating power in the cavities and so bigger mirror deformations: to limit this effect the TCS will be essential.

Furthermore to reduce the impact of the coating thermal noise in the mid-frequency range the spot size on the test masses has been enlarged. Therefore, unlike Virgo, the beam waist will be placed close to the center of the $3km$ Fabry-Perot cavities, resulting in beam radii of $48.7mm$ and $58mm$ for the input and end mirrors, respectively. The cavity finesse will be higher with respect to Virgo: a reference value of $\mathcal{F} = 443$ has been chosen.

Here I will report the main subsystem changes:

Laser The required input laser power (after the input mode cleaner) is equal to $125W$. Therefore, considering the losses of the injection system, the laser must provide a power of at least $175W$. A $100W$ prototype is undergoing the final tests. The $200W$ ultimate power will be achieved by coherent summation of two $100W$ amplifiers.

Injection system The input optics for Advanced Virgo must be compliant with the 10 times increased optical power. Proper electro-optic modulators and Faraday isolators able to withstand high power have been developed. By using better optics the throughput of the IMC will be significantly improved to guarantee the required power at the interferometer input.

Mirrors Given the much larger optical power in the cavities, radiation pressure noise becomes a limit in the low frequency range and heavier test masses are needed to reduce it. The Advanced Virgo test masses have the same diameter as the Virgo ones ($35cm$) but are twice as thick ($20cm$) and heavy ($42kg$). Deviations from required flatness is the main source of scattering losses. Stricter flatness requirements ($< 0.5nm_{rms}$) call for a better polishing. The flatness of the mirrors will be improved by using the corrective coating technique after a standard polishing phase. The baseline for the Advanced Virgo coating is the use of optimized multilayer and Titanium doped Tantala for the high-refractive index layers.

Thermal Compensation System In the case of Advanced Virgo, the thermal effect will also be relevant due to the much higher circulating power in the Fabry-Perot cavities: the input power is $P_{in} = 125W$, with the chosen finesse, gives a Fabry-Perot cavity power of $\sim 800kW$. The power absorbed by the mirrors will be $\sim 0.5W$. Then, the system will be more complex: because of the more massive mirrors it is more convenient heating an additional plate, instead the mirror itself, with a double-axicon pattern laser. This additional plate, called *compensation plate*, is a transmissive optic placed in front of each mirror. To control the radii of curvature of the test masses, a shielded ring heater, placed around each mirror, will be used.

Detection Advanced Virgo will use a DC detection scheme, which improves the quantum noise and reduces the impact of some technical noises (such as Radio-Frequency phase noise) which would be (close to) limiting the detector sensitivity in case of heterodyne readout. The main photodiodes will be placed on the suspended optical bench (in vacuum) to improve the rejection of seismic and acoustic noise. A new output mode cleaner compliant with the new requirements on sidebands filtering will be installed.

Stray light control Out of the $125W$ power entering into the interferometer, about $100W$ will be lost mainly by scattering around the mirrors and towards the pipes. In order to limit the phase noise due to part of this light being back-scattered into the interferometer, new diaphragm baffles will be installed either suspended around the mirrors, or ground connected inside the vacuum links.

Payloads The payloads will be modified to be compliant with the thicker and heavier mirrors and to suspend the new components. A new payload layout has been developed, getting rid of the recoil mass and offering the possibility to suspend baffles around the mirrors, compensation plates on the input payloads and ring heaters. The test masses will be suspended by fused silica fibres, as in Virgo+.

Superattenuators The Virgo superattenuators provide a seismic isolation compliant with the Advanced Virgo requirements. However, some upgrades are necessary to improve the robustness in bad weather conditions:

- new monolithic inverted pendulum legs will be mounted: it will have resonance frequency higher than the present inverted pendulum. This will allow to increase the bandwidth of the inertial damping servos;

- piezo actuators will be installed in the inverted pendulum feet, allowing to perform a control of the tilt;
- the steering filter (or filter 7) must be modified to match the new design of the payloads.

Chapter 3

Thermal Noise

Consider a system left free to evolve in thermodynamical equilibrium at a temperature T with a heat bath: the variables describing it are subject to spontaneous fluctuations. Those fluctuations limit the interferometer sensitivity in the frequency band between $20Hz$ and $500Hz$.

To give an idea of the order of magnitude of the thermal fluctuation rms amplitude of a simple physical system, we use the principle of equipartition: in fact most of the energy of the thermal fluctuation is concentrated near the mechanical resonances of the system. The result is:

$$\sqrt{\overline{x^2}} = \sqrt{\frac{k_B T}{m\omega_0^2}}$$

where $\sqrt{\overline{x^2}}$ is the rms of the displacement of the oscillator, T is the temperature, and m and ω_0 are the mass and the resonant angular frequency of the mechanical oscillator, respectively. Considering, as an example, an internal mode of the payload of Virgo at $\sim 10Hz$, we obtain a rms amplitude fluctuation of $\sqrt{\overline{x^2}} \sim 2 \cdot 10^{-13} m$: if the mirror moves with this amplitude, it will be impossible to detect a gravitational wave.

In this chapter I introduce the fluctuation-dissipation theorem, which allows the thermal noise estimation. After presenting the simple case of a harmonic oscillator, with structural and viscous losses, I show the main dissipation models, focusing the description on the suspension and the bulk thermal noise.

3.1 Fluctuation-dissipation theorem

Callen, Welton and Greene developed the so called fluctuation-dissipation theorem, a fundamental theorem of non-equilibrium statistical mechanics is commonly used to predict thermal noise in all physical systems.

The fluctuation-dissipation theorem links irreversible processes and fluctuations acting in a physical system: knowing the nature of the irreversibility, it is possible to quantify the power spectrum of the thermal noise [77, 78, 79, 80].

For a linear dissipative system[1], we define the impedence Z, which is simply related to the proportionality constant between the power and the square of the

[1] A physical system may be said dissipative when it absorbs energy if subjected to a time-periodic

perturbation. The information of the dissipation of the system is embedded in the impedence Z.

3.1.1 One-dimensional system

Consider a linear dissipative one-dimensional system in thermodynamical equilibrium. Let $F(t)$ be an external perturbation in the time domain and $X(t)$ the response of the system derived from the equation of motion. Since the system is one-dimensional, X will be the unique generalized coordinate.

The Hamiltonian which describes the system will have a new term $\mathcal{H}_{int}$ depending on the generalized force:

$$\mathcal{H}_{int} = -F(t)X(t)$$

The physical system can be described using the impedence Z in the frequency domain:

$$Z(\omega) = \frac{\tilde{F}(\omega)}{\tilde{\dot{X}}(\omega)} = \frac{\tilde{F}(\omega)}{i\omega\tilde{X}(\omega)}$$

where the symbol $\sim$ stands for the Fourier transform.

It is also useful to define the transfer function of the system $H(\omega)$ connected to the impedence as follows:

$$H(\omega) = \frac{\tilde{X}(\omega)}{\tilde{F}(\omega)} = \frac{1}{i\omega Z(\omega)}$$

The fluctuation-dissipation theorem states that the power spectrum of the thermal noise for the quantity X is:

$$S_X(\omega) = -\frac{4k_BT}{\omega}\mathcal{I}m[H(\omega)] \tag{3.1}$$

where T is the temperature of the system thermal bath.

For what concerns the power spectrum of the generalized force, we have:

$$S_F(\omega) = 4k_BT\mathcal{R}e[Z(\omega)]$$

where the resistance R has the role of the impedence of the system.

Considering eq. 3.1, the fluctuation-dissipation theorem connects the dissipation of a system (embedded in the transfer function) to the fluctuations of the physical variable X. If we want to reduce the thermal fluctuation, for example in a gravitational wave detector, we could proceed in two different ways:

- decreasing the temperature T of the heat bath: that is the method commonly used for the cryogenic gravitational wave resonant bars;
- decreasing the dissipation sources in the physical system: that gives a severe constraints in designing several mechanical components of the detector.

external perturbation F. Furthermore, a system may be said linear if the power dissipation is quadratic in the magnitude of the perturbation.

3.1.2 n-dimensional system

The previous introduction can be extended to a general physical system with n coordinates X_i [81]. In that case we have also n generalized forces F_i and the Hamiltonian of the system is:

$$\mathcal{H}_{int} = -F_i(t)X_i(t) \tag{3.2}$$

The impedence of the system is described by a $n \times n$ matrix $Z_{ij}(\omega)$; hence the transfer function is defined by the matrix $H_{ij}(\omega)$.

Since the energy can be exchanged between different degrees of freedom, the relationship between the generalized coordinates and the forces is expressed as:

$$\tilde{F}_i(\omega) = Z_{ij}\dot{\tilde{X}}_j(\omega)$$

The fluctuation-dissipation theorem is:

$$S_{X_iX_j}(\omega) = -\frac{4k_BT}{\omega}\mathcal{I}m[H_{ij}(\omega)] \tag{3.3}$$

where $S_{X_iX_j}$ is the cross spectrum density, i.e. the Fourier transform of the cross correlation function between X_i and X_j; the cross spectrum for $i = j$ is identical to the power spectrum density of X_i.

3.1.3 Linear combination of coordinates

In many practical cases a read-out system is coupled to the mechanical system and probes its behavior by gathering into the same signal the contribution of a weighted selection of internal modes.

In the interferometer, the read-out interaction is provided by the laser beam profile which maps the mirror shape deformed by internal modes.

The new coordinate X_{new} of the n-dimensional system is defined as a superposition of the old coordinates X_i, weighted with a real function P_i:

$$X_{new} = \sum_{i=1}^{n} P_iX_i \tag{3.4}$$

The fluctuation-dissipation theorem is applicable also in that case. We rewrite the new term in the interaction Hamiltonian, considering the generalized force F_{new} which drives only the momentum conjugate to X_{new}:

$$\mathcal{H}_{int} = -F_{new}(t)X_{new}(t) = \sum_{i=1}^{n} F_{new}(P_iX_i) = \sum_{i=1}^{n}(F_{new}P_i)X_i \tag{3.5}$$

Comparing eq. 3.5 with eq. 3.2, it is evident that the Hamiltonian described by X_{new} can be reinterpreted as a Hamiltonian of a n-dimensional system where P_iF_{new} plays the role of F_i:

$$\tilde{X}_i = \sum_{j=1}^{n} H_{ij}P_j\tilde{F}_{new}$$

So, the new transfer function H_{new} is:

$$H_{new} = \frac{\tilde{X}_{new}}{\tilde{F}_{new}} = \sum_{i=1}^{n} \frac{P_i \tilde{X}_i}{\tilde{F}_{new}} = \sum_{i=1}^{n}\sum_{j=1}^{n} \frac{P_i H_{ij} P_j \tilde{F}_{new}}{\tilde{F}_{new}} = \sum_{i=1}^{n}\sum_{j=1}^{n} P_i P_j H_{ij}$$

From eq. 3.3 and eq. 3.4 we evaluate the power spectrum density $S_{X_{new}}$:

$$\begin{aligned} S_{X_{new}}(\omega) &= P_i P_j S_{X_i X_j}(\omega) = -\frac{4k_B T}{\omega} \mathcal{I}m \left[\sum_{i=1}^{n}\sum_{j=1}^{n} P_i P_j H_{ij}(\omega) \right] = \\ &= -\frac{4k_B T}{\omega} \mathcal{I}m \left[H_{new}(\omega) \right] \end{aligned} \tag{3.6}$$

to be compared to the one-dimensional case expressed in eq. 3.1.

If X is a function of a continuos parameter $\vec{r}$ (instead of eq. 3.4), we have:

$$X_{new} = \int P(\vec{r}) X(\vec{r}) d^3 r$$

and all the previous calculations are still valid, with the Hamiltonian as:

$$\mathcal{H}_{int} = -\int F_{new} P(\vec{r}) X(\vec{r}) d^3 r$$

Since $F_{new} P(\vec{r})$ plays the role of $F(\vec{r})$ we can write:

$$\tilde{X}(\vec{r'}) = \int H(\vec{r}, \vec{r'}) \tilde{F}(\vec{r}) d^3 r = \int H(\vec{r}, \vec{r'}) P(\vec{r}) \tilde{F}_{new}(\vec{r}) d^3 r$$

and re-define the new transfer function:

$$H_{new}(\omega) = \frac{\tilde{X}_{new}}{\tilde{F}_{new}} = \frac{\int P(\vec{r'}) \tilde{X}(\vec{r'}) d^3 r'}{\tilde{F}_{new}} = \int P(\vec{r'}) P(\vec{r''}) H(\vec{r'}, \vec{r''}) d^3 r' d^3 r'' \tag{3.7}$$

Therefore the spectrum of the thermal noise is still eq. 3.6 with the transfer function given by eq. 3.7.

3.2 The simple case of the harmonic oscillator with losses

Consider a very simple one-dimensional physical system as a harmonic oscillator of mass m and resonance frequency ω_0.

If we take an ideal oscillator without losses, the equation of motion is:

$$m\ddot{x} + m\omega_0^2 x = F(t)$$

where $F(t)$ is the generalized force acting on the mass.

Going in the frequency domain:

$$-m\omega^2 \tilde{x} + m\omega_0^2 \tilde{x} = \tilde{F}(\omega)$$

The transfer function is immediately deduced:

$$H(\omega) = \frac{1}{m(\omega_0^2 - \omega^2)}$$

When no dissipation is involved, the response of the system diverges for $\omega \to \omega_0$; furthermore, the transfer function is real, so the fluctuation-dissipation theorem (eq. 3.1) gives a null result. This means that there is no thermal noise acting on the system.

But in the real system, the resonance peak is finite in value; that means there are some dissipation processes acting on the oscillator.

Now, consider two kinds of idealized dissipation: the viscous damping and the structural damping [43, 82].

3.2.1 Viscous losses

The viscous loss is represented as a resistance force proportional to velocity. The equation of motion for a viscous damped harmonic oscillator is:

$$m\ddot{x} + \beta\dot{x} + m\omega_0^2 x = F(t)$$

where β is the viscous friction coefficient. In the frequency domain we have:

$$-m\omega^2\tilde{x} + i\beta\omega\tilde{x} + m\omega_0^2\tilde{x} = \tilde{F}(\omega)$$

that leads to the transfer function:

$$H(\omega) = \frac{1}{m\left[(\omega_0^2 - \omega^2) + i\frac{\beta\omega}{m}\right]}$$

The imaginary part of the transfer function is:

$$\mathcal{I}m[H(\omega)] = \frac{-\beta\omega}{m\left[(\omega_0^2 - \omega^2)^2 + \frac{\beta^2\omega^2}{m}\right]} \tag{3.8}$$

Defining at the resonance the quality factor Q_{visc} due to viscous losses:

$$Q_{visc} = \frac{\omega_0 m}{\beta} \tag{3.9}$$

the application of the fluctuation-dissipation theorem drives to the thermal noise spectrum:

$$S_X(\omega) = \frac{4k_BT}{mQ_{visc}} \frac{\omega_0}{\left[(\omega^2 - \omega_0^2)^2 + \frac{\omega_0^2\omega^2}{Q_{visc}^2}\right]} \tag{3.10}$$

The typical behavior of the spectrum of the thermal noise due to viscous losses is shown in fig. 3.1:

- below the resonant frequency $\omega \ll \omega_0$ the power spectrum is described as:

$$S_X(\omega) = \frac{4k_BT}{m\omega_0^3 Q_{visc}} = \text{const}$$

- above the resonant frequency $\omega \gg \omega_0$ the thermal noise could be approximated as:

$$S_X(\omega) = \frac{4k_BT\omega_0}{mQ_{visc}} \frac{1}{\omega^4}$$

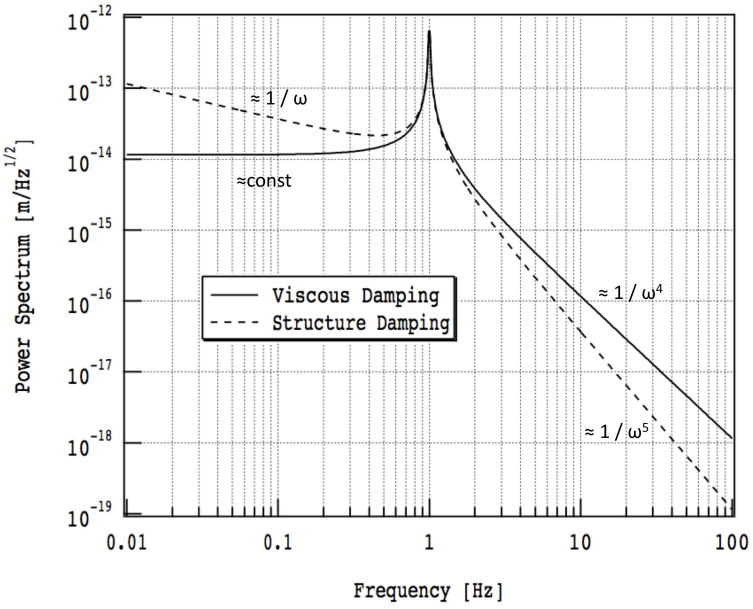

Figure 3.1: examples of the power spectrum density of the thermal noise of a harmonic oscillator, in the case of viscous damping (solid line) and structural damping (dotted line); the oscillator has the mass equal to $1kg$, the resonant frequency, $\omega_0/2\pi = 1Hz$, and quality factor $Q = 5 \cdot 10^5$.

3.2.2 Structural losses

The internal friction explains what happens at the microscopic level in the material forming a real system. In fact, the elastic response to the external force $F(t)$ is not immediate: even in a small sample, where the finiteness of the speed of sound could be neglected, a finite time is required for the microscopic degrees of freedom forming the solid physical system to achieve a new thermal equilibrium when the macroscopic parameters vary.

Thus, the elongation x is shifted in time, causing a deviation from the Hooke's law called anelasticity. The effect of anelasticity is that a dissipation process is present and there is a damping, which make the resonance peak finite. The easiest way to make a connection between anelasticity and damping is to represent it in the frequency domain.

Consider an elastic, homogeneous and isotropic body [83]; if we apply a force F to the system, it can react with a length deformation Δl. We define:

- the *stress* σ which is the force F applied to the system per unit area $\sigma = F/S$;
- the *strain* ϵ which indicates the relative displacement over the initial body length l_0, i.e. $\Delta l/l_0$.

Hooke's law connects these two quantities with the Young's modulus E:

$$\sigma(\omega) = E(\omega)\epsilon(\omega) \tag{3.11}$$

The structural loss is described with an imaginary term of the Young's modulus:

$$E(\omega) = E_r(\omega) + iE_i(\omega) = |E|e^{i\phi(\omega)}$$

where the phase angle ϕ is called *loss angle*.

We write the strain as:

$$\epsilon(\omega) = \epsilon_0 e^{i\omega t}$$

and the stress as:

$$\sigma(\omega) = |E|\epsilon_0 e^{i\omega t + \phi(\omega)} \approx |E|(1 + i\phi(\omega))\epsilon(\omega) \tag{3.12}$$

The loss angle represents the phase lag between the excitation (the stress) and the system response (the strain).

At macroscopic level, we generalize the elastic constant k with an imaginary part:

$$k = m\omega_0^2 \ \rightarrow m\omega_0^2(1 + i\phi(\omega)) \tag{3.13}$$

Suppose the loss angle frequency independent (for a complete treatment see sec. 3.3.1): in that case the equation of motion is:

$$m\ddot{x} + m\omega_0^2(1 + i\phi)x = F(t)$$

Going in the frequency domain:

$$-m\omega^2\tilde{x} + m\omega_0^2(1 + i\phi)\tilde{x} = \tilde{F}(\omega)$$

that leads to the transfer function:

$$H(\omega) = \frac{1}{m[(\omega_0^2 - \omega^2) + i\omega_0^2\phi]} \tag{3.14}$$

The imaginary part of the transfer function is:

$$\mathcal{I}m[H(\omega)] = \frac{-\omega_0^2\phi}{m[(\omega_0^2 - \omega^2)^2 + \omega_0^4\phi^2]}$$

The application of the fluctuation-dissipation theorem drives to the thermal noise spectrum:

$$S_X(\omega) = \frac{4k_BT}{m\omega}\frac{\omega_0^2\phi}{[(\omega^2 - \omega_0^2)^2 + \omega_0^4\phi^2]}$$

The typical behavior of the spectrum of the thermal noise due to viscous losses is shown in fig. 3.1:

- below the resonant frequency $\omega \ll \omega_0$ the power spectrum is described as:

$$S_X(\omega) = \frac{4k_BT\phi}{m\omega_0^2}\frac{1}{\omega} \tag{3.15}$$

- above the resonant frequency $\omega \gg \omega_0$ the thermal noise could be approximated as:

$$S_X(\omega) = \frac{4k_BT\omega_0^2\phi}{m}\frac{1}{\omega^5} \tag{3.16}$$

3.2.3 Quality factor and loss angle

In the previous sections we have introduced two new quantities, the quality factor Q and the loss angle ϕ. In this section we show how they connect each other.

Consider a system excited by a time periodic strain $\epsilon = \epsilon_0 e^{i\omega t}$: the loss angle is strictly related to the amount of the energy lost in a cycle of the periodic motion over the total amount of the stored energy. In fact, the energy density of the oscillator is [83]:

$$\mathcal{E} = \frac{1}{2}\mathcal{R}e[\sigma]\mathcal{R}e[\epsilon]$$

In the limit of low dissipation, with the imaginary term of the energy density lower than the real term ($\mathcal{E}_i \ll \mathcal{E}_r$), and using the eq. 3.11, the maximum energy density stored in the oscillation is[2]:

$$\mathcal{E}_{max} = \frac{1}{2}\mathcal{R}e[\sigma]\mathcal{R}e[\epsilon]_{max} = \frac{1}{2}\epsilon_0^2 E_r(\omega) \tag{3.17}$$

while the mean energy density dissipated in a cycle is the integral of the dissipated power per unit volume dW_{diss}/dV:

$$\mathcal{E}_{diss} = \int_{cycle} \frac{dW_{diss}}{dV} dt = \int_{cycle} \mathcal{R}e[\sigma]\mathcal{R}e[\dot{\epsilon}]dt = \pi\epsilon_0^2 E_i(\omega) \tag{3.18}$$

Taking the ratio between the eq. 3.18 and the eq. 3.17, we obtain:

$$\frac{\mathcal{E}_{diss}}{\mathcal{E}_{max}} = 2\pi\frac{E_i(\omega)}{E_r(\omega)} = 2\pi\phi(\omega) \tag{3.19}$$

Even if the strain pattern in the body has a very general form, this definition of loss angle maintains its validity. Since energy losses add linearly, the superposition of different loss sources, with different loss angles $\phi_i(\omega)$ is correctly described by this sum:

$$\phi_{tot}(\omega) = \sum_i \phi_i(\omega)$$

where the frequency dependence is still present.

The quality factor Q is also associated with the loss mechanisms present in the system: it is a dimensionless measure of how small the dissipation is at the resonant frequency ω_0. In particular it depends on the ϕ value as:

$$Q = \frac{1}{\phi(\omega_0)} \tag{3.20}$$

As fluctuation-dissipation theorem says, in order to estimate the thermal noise spectrum, we need to know the loss angle $\phi(\omega)$ at every frequency. Since the measurement of the loss angle far from the resonance and over arbitrarily wide frequency

[2]To obtain the following relations, we write the real part of a complex quantity z as:

$$\mathcal{R}e[z] = \frac{z + z^*}{2}$$

where z^* is the complex conjugate of z.

range is difficult, the value of loss angle is often derived from eq. 3.20, only at the resonance frequency. That is reductive, because the off-resonance slope can be very different (see fig. 3.1): the overall thermal noise must be predicted and carefully taken into account in the detector design. Some assumptions are required to extrapolate the frequency dependence of the loss angle far from the resonance region: I show some examples in appendix. A and in sec 3.3.

There are two methods to evaluate the quality factor Q (see fig. 3.2):

1. the most common method is the measurement of the decay time of the resonant motion after an excitation.

   Take a harmonic oscillator with resonance frequency equal to ω_0. We can excite this resonance by sending a white noise to the system or using a force at the same resonant frequency.

   The response of the system in the time domain will be:

   $$A(t) = A_0 \sin(\omega_0 t) e^{-\frac{t}{\tau_0}} \tag{3.21}$$

   where A_0 is the initial elongation and τ_0 is the characteristic decay time. The quality factor is the number of radians of oscillation it takes for the amplitude of the free oscillation to fall by $1/e$ [43]:

   $$Q = \pi \tau_0 \left(\frac{\omega_0}{2\pi}\right) \tag{3.22}$$

   This method is used when the decay time is very high $\tau_0 \gg 1$.

2. the second most common method is the measurement of the half width of the resonance peak in the transfer function; in particular the half width $\Delta\omega_0$ is given by:

   $$\left| H\left(\omega_0 \pm \frac{\Delta\omega_0}{2}\right)\right|^2 = \frac{|H(\omega_0)|^2}{2}$$

   The Q-value is:

   $$Q = \frac{\omega_0}{\Delta\omega_0}$$

   This method is used when the associated decay time is very low $\tau_0 \ll 1$.

If we want to minimize thermal noise in a physical system, as a gravitational wave detector, we need to reduce mechanical dissipation losses.

Practically, the idea is to design a detector with very high Q-values mechanical resonances for the test masses and their suspension system. In that way the energy of a dissipation process is concentrated in very narrow frequency bands centered on the payload resonant frequency modes. These narrow frequency bands can be then filtered out of the sensitivity spectrum with negligible reduction of the observation bandwidth.

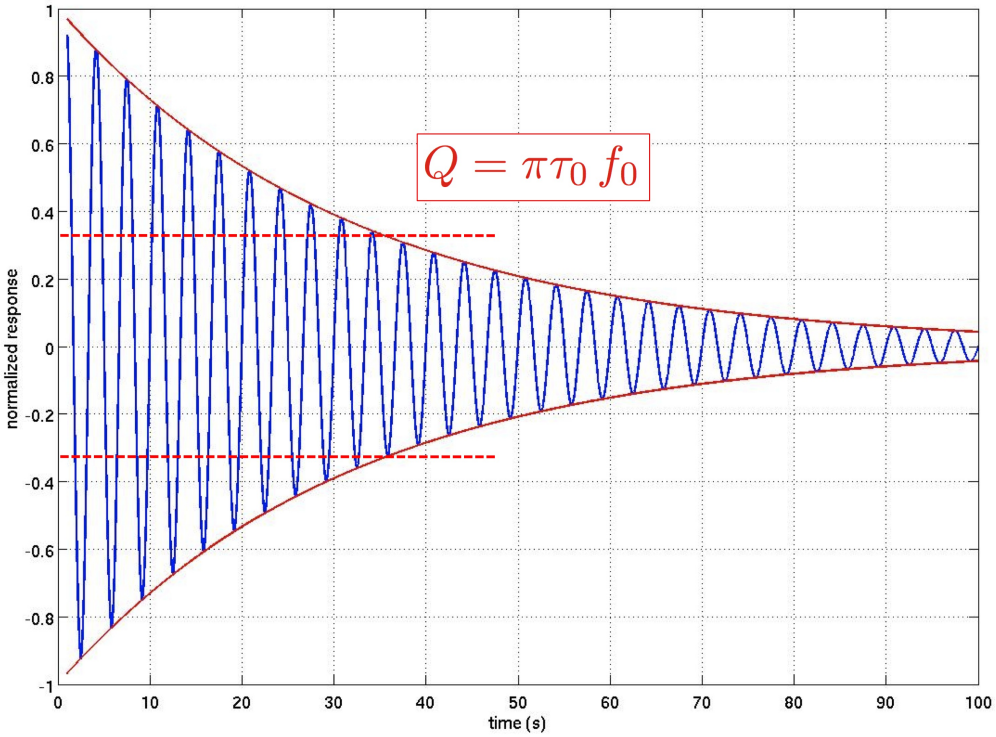

(a) Exponential decay

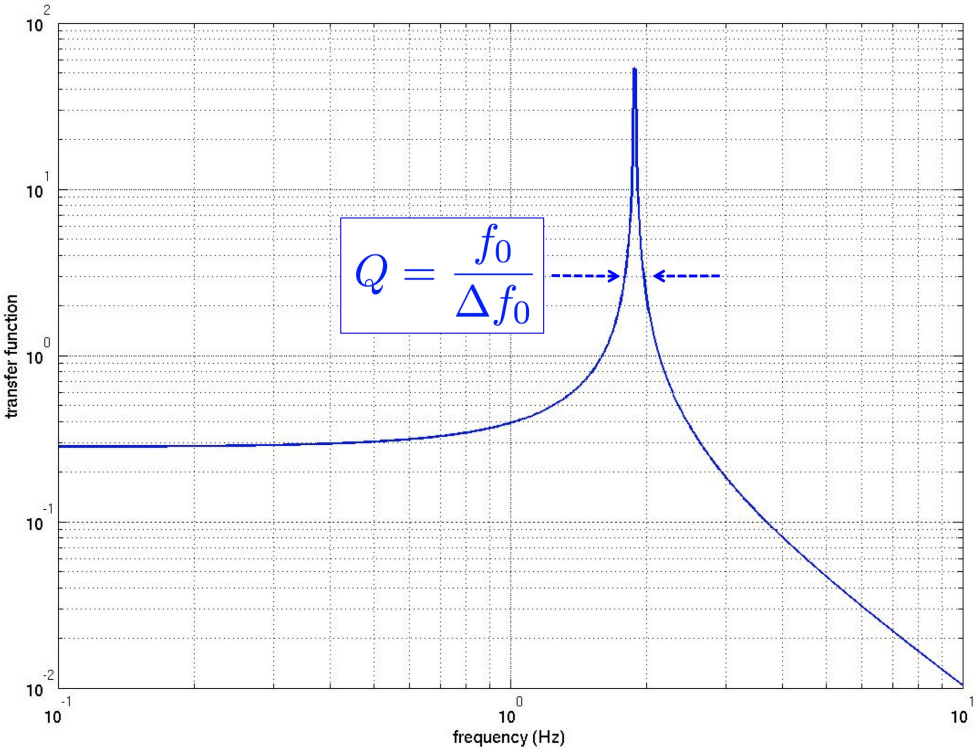

(b) Lorentzian

Figure 3.2: Two different manifestations of the quality factor of an oscillator.

3.3 Dissipation models

There are several kinds of dissipation: the level and the frequency dependence of thermal noise depends strongly on the frequency dependence of the dissipation processes acting on. In general we divide them in two categories:

1. internal processes:
   - structural damping;
   - thermoelastic damping;
   - superficial losses;
2. external processes:
   - air damping;
   - recoil losses.

3.3.1 Structural damping

Structural losses are related to the orientation or the displacement of atoms and molecules, or the presence of defects and non-homogeneities in the lattice forming the body. For example, if an imperfect lattice is vibrationally excited, it can change its geometry toward a more stable configuration: local vibrations of the impurities could be energetically preferred.

All these structural processes are thought to be "thermally activated", when a certain energy ΔU is reached. The population of particles with the needed energy ΔU is set by the Boltzmann's distribution, so that the time constant of these anelastic processes depends on temperature T and on activation energy ΔU, following an Arrehnius' exponential law:

$$\tau_r = \tau_{r_0} e^{\frac{\Delta U}{k_B T}} \tag{3.23}$$

This relaxation time is used in eq. A.2 to derive the frequency dependence of the loss angle $\phi(\omega)$, known as *Debye's peak*:

$$\phi(\omega) = \Delta \frac{\omega \tau_r}{1 + \omega^2 \tau_r^2} \tag{3.24}$$

where Δ is a constant depending on the physical parameter of the material (see eq. A.3).

Experimental data do not agree with the Debye's peak dependence. For unloaded metallic wire sample, the loss angle is almost frequency indipendent in the frequency range between $500 - 10000 Hz$ [86, 87].

Anyway, this flat model shows mathematical difficulties. In fact, it is not possible that the loss angle is constant in the whole frequency range.

The loss angle must go to zero in low and high frequency limits. If the loss angle was constant in these limits, the displacement would be divergent when a step-function force is applied [88]. Therefore, the structural damping model should be considered valid only for those dissipations which have weak dependence on the frequency.

To describe this behavior we image a unique relaxation time τ_r, but activation energies distributed with a density $f(\Delta U)$ almost constant over a great interval $[U_1, U_2]$:

$$f(\Delta U)dU = \frac{dU}{U_2 - U_1}$$

The total loss angle is the sum of the single contributions given by eq. 3.24; substituting eq. 3.23 at different energies:

$$\begin{aligned}
\phi_{tot}(\omega) &= \Delta \int_{U_1}^{U_2} \frac{\omega\tau_r}{1+\omega^2\tau_r^2} \frac{dU}{U_2 - U_1} \\
&\approx \frac{\Delta}{U_2 - U_1} \int_{U_1}^{U_2} \frac{\omega\tau_r}{1+\omega^2\tau_r^2} dU \\
&\approx \frac{\Delta}{U_2 - U_1} \int_{U_1}^{U_2} \frac{\omega\tau_{r_0} e^{\frac{\Delta U}{k_B T}}}{1+\omega^2\tau_{r_0}^2 e^{\frac{2\Delta U}{k_B T}}} dU \\
&\approx \frac{\Delta}{U_2 - U_1} k_B T[\arctan(\omega\tau_1) - \arctan(\omega\tau_2)]
\end{aligned}$$

where:

$$\tau_{1,2} = \tau_{r_0} e^{\frac{U_{1,2}}{k_B T}}$$

The total loss angle $\phi_{tot}(\omega)$ is poorly dependent in frequency and the flatness of the behavior increases with the widening of the interval $[U_1, U_2]$.

There are many study on internal dissipation processes. In amorphous objects, the dissipation is well described by the thermal activation discussed here. On the contrary, in the crystals and in the metals we distinguish between those dissipation processes which act even in a perfect crystal, and those due to the presence of defects in the microscopical structure [89].

By the way, one must keep in mind that the history of each individual sample affects the measured structural loss angle: purity, grain size, thermal treatments (such as annealing) and irradiation damages have a relevance in the internal friction processes.

3.3.2 Thermoelastic damping

The thermoelastic damping is caused by the coupling between the inhomogeneous strain and the temperature field inside a vibrating body; this coupling happens because there is a non-zero thermal linear expansion coefficient:

$$\alpha = \frac{1}{L}\frac{\partial L}{\partial T}$$

i.e. length changes are connected with temperature changes.

When an elastic solid is set in motion, the mechanical vibration creates periodic contractions and stretching in the bending region. The body is driven out of equilibrium, since it has an excess of kinetic and potential energy.

On the other hand in a thermoelastic solid, the contractions and the stretching generate temperature changes: as the body flexes, the compressed parts heat up

and the stretched ones cool down. So a heat flux is originated between the two regions at different temperatures, attempting to restore equilibrium. The elastic energy is dissipated owing this irreversible heat flux in time-varying inhomogeneous deformations. The reaching of the equilibrium requires a characteristic time that has been calculated by Zener in 1937 [90, 91]. He started from the equation of the heat diffusion, which links temperature T to the divergence of the strain ϵ:

$$\frac{\partial T}{\partial t} = \frac{D}{c_V}\nabla^2 T - \frac{E\alpha T_0}{c_V(1-2\sigma)}\frac{\partial(\nabla\cdot\vec{\epsilon})}{\partial t}$$

where E is the (unrelaxed) Young's modulus of the materials, σ is the Poisson ratio, α is the linear coefficient of the thermal expansion, c_V is the specific heat per unit volume and D is the thermal diffusion coefficient.

Solving this equation, Zener showed that this mechanism is well described by the Standard Anelastic Model as a single relaxation process with a single peak. The parameters of the Debye's peak (eq. 3.24) are [92, 93]:

$$\begin{aligned}\Delta &= \frac{E\alpha^2 T}{c_V}\\ \bar{\tau} &= \frac{c_V d^2}{2.16\cdot 2\pi D_{st}}\end{aligned}$$

where d is the typical distance the heat flow must cross. This relaxation mechanism depends only on material properties and not on details of its structure or composition.

The thermoelastic loss angle ϕ_{therm} is:

$$\phi_{therm}(\omega) = \Delta\frac{\omega\bar{\tau}}{1+\omega^2\bar{\tau}^2} \tag{3.25}$$

The characteristic time $\bar{\tau}$ corresponds to a frequency ω_T where the loss angle has a maximum (see. fig. A.2). One can understand qualitatively why there is a peak in that way:

- when $\omega \ll \omega_T$ the system is mechanically vibrating at frequency smaller than the effective relaxation rate ω_T: the system remains substantially in equilibrium and the process is *isothermal*, because the thermalization between the compressed and the expanded regions occurs almost instantaneously;

- when $\omega \gg \omega_T$ the system is mechanically vibrating at frequency greater than the effective relaxation rate ω_T: the system has no time to relax and the process is *adiabatic*, because the temperature has not enough time to reach equilibrium between expansion and contraction.

Thermoelastic damping is dominant in vibrating objects with a small section, like wires, fibers and strings: it is particularly relevant for the wire first resonant transversal mode.

In general, a good model for describing the total internal loss angle of wires in the frequency range $1 - 10^3 Hz$ is given by the sum of the thermoelastic contribution (eq. 3.25) and structural losses ϕ_s [92] (see fig. 3.3):

$$\phi_w(\omega) = \phi_s + \Delta\frac{\omega\bar{\tau}}{1+\omega^2\bar{\tau}^2} \tag{3.26}$$

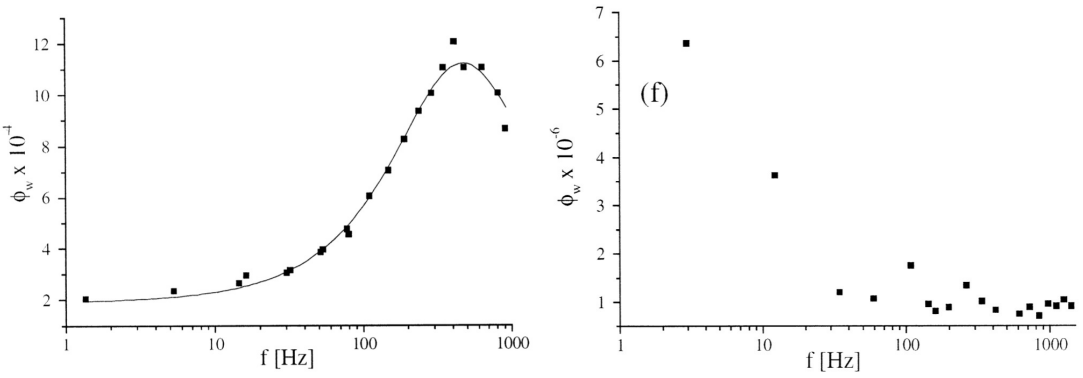

(a) C85 (b) Fused Silica

Figure 3.3: experimental results of internal loss angle ϕ_w (structural and thermoelastic) versus frequency in thin wires: note that for C85 the Debye's peak is clearly visible, contrarily to what happens for Fused Silica.

3.3.3 Superficial losses

In the previous section we have not considered the loss spatial distribution. But the region near the surface of the body is continually exposed to damages (due to chemical or mechanical contacts) causing the most of the dissipation.

In particular geometric configurations, materials with very low value of bulk loss angle appear to have greater losses because of superficial effects.

Surface contribution can be included in the total loss angle, starting from eq. 3.19:

$$\phi_{tot} = \frac{1}{2\pi} \frac{\Delta\mathcal{E}_{bulk} + \Delta\mathcal{E}_{surf}}{\mathcal{E}_{tot}} \tag{3.27}$$

where $\mathcal{E}_{tot}$ is the total energy density stored in an oscillation, $\Delta\mathcal{E}_{bulk}$ and $\Delta\mathcal{E}_{surf}$ the amount of energy density dissipated in the volume and on the surface respectively.

It is rather reasonable to assume that $\Delta\mathcal{E}_{bulk}$ is proportional to the volume V and $\Delta\mathcal{E}_{surf}$ to the surface S [94]:

$$\frac{\Delta\mathcal{E}_{surf}}{\Delta\mathcal{E}_{bulk}} = \mu d_S \frac{S}{V}$$

where the dimensionless constant μ depends on the sample geometry and on the class of resonances excited, taking into account the relative amount of the elastic deformation occurring at the surface:

$$\mu = \frac{V}{S} \frac{\int_S \epsilon^2(\vec{r}) d^2r}{\int_V \epsilon^2(\vec{r}) d^3r} \tag{3.28}$$

While, d_S is called *dissipation depth* and provides a direct measure of the total dissipation induced by a surface layer, normalized to the dissipation in the bulk:

$$d_S = \frac{1}{\phi_{bulk} E_{bulk}} \int_0^h \phi(n) E(n) dn$$

where n is a coordinate measuring the distance inward from the surface and h is the thickness of the superficial region of dissipation. In uncoated samples, the dissipation

depth quantifies physical and chemical damages suffered by the surface of the sample. In the case of Virgo+ fused silica fibers $d_S \sim 200\mu m$.

We re-write eq. 3.27, considering that $\mathcal{E}_{tot} \approx \mathcal{E}_{bulk}$ and defining $\phi_{bulk} = \Delta\mathcal{E}_{bulk}/\mathcal{E}_{bulk}$:

$$\phi_{tot} = \frac{1}{2\pi}\left(\frac{\Delta\mathcal{E}_{bulk}}{\mathcal{E}_{tot}} + \frac{\Delta\mathcal{E}_{surf}}{\mathcal{E}_{tot}}\right) = \phi_{bulk}\left(1 + \mu d_S \frac{S}{V}\right)$$

For cylindrical fibers of diameter d, oscillating transversally to the axis of the fiber, we have from eq. 3.28 $\mu = 2$; since $V/S = d/4$, the superficial loss angle:

$$\phi_{surf} = \phi_{bulk}\left(\frac{8d_S}{d}\right) \tag{3.29}$$

The superficial effects become relevant when $d_S < d$. If the Young's modulus and the loss angle are constant over the entire body, it follows:

$$\phi_{surf} \simeq \frac{d_S}{h}\phi_{bulk}$$

3.3.4 Air damping

Air damping is an external dissipation source present when a body vibrates in a fluid; thus, it is well modeled with a viscous friction proportional to velocity, in particular when the oscillating body is kept under vacuum.

From a comparison between eq. 3.8 and eq. 3.14 we determine the expression of loss angle due to gas friction:

$$\phi_{gas}(\omega) = \frac{\beta\omega}{m\omega_0^2} \tag{3.30}$$

While in dense fluids the friction includes the effect of shear forces, in a rarefied gas the dissipation is mainly caused by the momentum transfer between the body and the gas molecules which are moving with a mean thermal velocity equal to $\bar{v} = \sqrt{k_B T/m}$. In that case the mean free path of molecules of mass m_{gas} is larger than the typical dimensions of the oscillator and the viscosity coefficient can be written as [43]:

$$\beta = \frac{1}{4}\rho_{gas} A \bar{v}$$

where ρ_{gas} is the gas density, determined by the residual pressure P_{res} and temperature T via the usual thermodynamical equation of state $\rho_{gas} = P_{res} m_{gas}/k_B T$; A is the cross sectional area of the body in which collisions with gas molecules occur.

Thus, eq. 3.30 is written:

$$\phi_{gas}(\omega) = \frac{\rho_{gas} A \bar{v}}{4m\omega_0^2}\omega$$

For vibrating cylindrical wires, the gas damping loss angle will be [94, 95]:

$$\phi_{gas}(\omega) = \frac{\rho_{gas}\bar{v}}{2\rho d\omega_0^2}\omega$$

where ρ is the wire density and d its diameter.

Using eq. 3.9 we derive the expression of the lower limit on the Q-value Q_{gas} limited by air damping:

- for a cylindrical wire

$$Q_{gas} = d\frac{\rho\omega_0}{n\sqrt{m_{gas}k_BT}}$$

where d is the diameter of the wires, ρ its density, n is the numeric density of the gas, m_{gas} its mass and ω_0 the angular resonant frequency of the oscillator;

- for a cylindrical test mass, as the one used in Virgo [96]

$$Q_{gas} = \frac{4m\omega_0}{\pi r^2 P_{res}}\sqrt{\frac{\pi k_B T}{8m_{gas}}} \tag{3.31}$$

where m is the mass of the mirror and r its radius.

3.3.5 Recoil losses

If a low-loss vibrating body is suspended to a structure with high-loss resonances, then the loss at the resonance frequency can be substantially degraded.

In the ideal case, the frame is infinitely massive and rigid; but in reality the structure is flexible and its mass is finite: so part of the vibration energy can be transmitted to the supporting frame and dissipated.

The system can be approximated by considering two coupled oscillators, as shown in fig. 3.4; M is the mass of the frame, while m is the mass of the oscillating body. The two bodies are connected with a spring of elastic constant k_m and dissipation loss angle ϕ_m, while we suppose the frame joined rigidly with a spring of elastic constant k_M and loss angle ϕ_M.

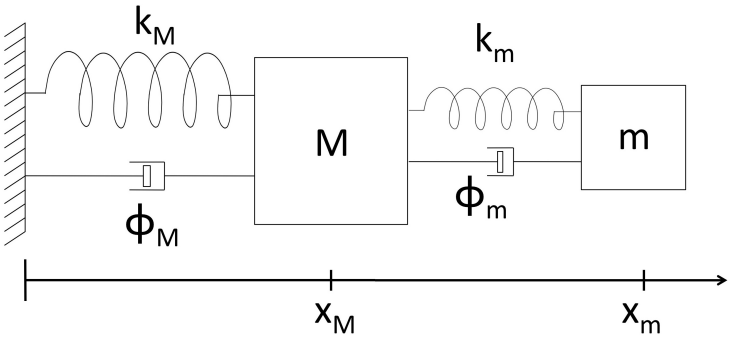

Figure 3.4: model of coupled oscillator system to schematize the recoil losses.

The two elastic constants are complex number, as described in eq. 3.13:

$$k_M = M\omega_M^2(1 + i\phi_M) \qquad k_m = m\omega_m^2(1 + i\phi_m)$$

where ω_M and ω_m are the proper vibration frequencies of the frame and of the body.

The equations of motion are:

$$\begin{cases} M\,\ddot{x}_M &= -k_M x_M + k_m(x_m - x_M) \\ m\,\ddot{x}_m &= -k_m(x_m - x_M) \end{cases}$$

As it is well known, the solution of these equations are two oscillators with two coupled vibration modes, whose frequencies ω_+ and ω_- are related to the frequencies of uncoupled oscillators ω_m and ω_M as [97]:

$$\omega_\pm = \sqrt{\frac{1}{2}\left\{[\omega_m^2(1+\mu)+\omega_M^2] \pm \sqrt{[\omega_m^2(1+\mu)+\omega_M^2]^2 - 4\omega_m^2\omega_M^2}\right\}} \tag{3.32}$$

where $\mu = M/m$.

If the two uncoupled oscillators have the same resonant frequency $\omega_m = \omega_M = \omega_0$, eq. 3.32 can be simplified as:

$$\omega_\pm = \omega_0\sqrt{\frac{2+\mu \pm \sqrt{\mu^2+4\mu}}{2}}$$

We write the displacement x_M and x_m of two masses when an impulsive force F is applied to M at time $t = 0$:

$$x_M = A[\sin(\omega_+ t) + \sin(\omega_- t)] = A\sin(\omega_0 t)\cos(\omega_b t) \tag{3.33}$$

$$x_m = A[\sin(\omega_+ t) - \sin(\omega_- t)] = \frac{A}{\mu}\cos(\omega_0 t)\sin(\omega_b t) \tag{3.34}$$

where the amplitude of the oscillation A can be found from the initial conditions, and the beat frequency of the system ω_b is defined as:

$$\omega_b = \frac{\omega_+ - \omega_-}{2}$$

Eq. 3.33 and eq. 3.34 show that the two masses move in phase opposition and that the energy of the system is transferred continuously and totally from one oscillator to the other at frequency ω_b. Only if $\omega_m \neq \omega_M$ not all the energy of the first mass is transferred to the second one.

It is possible to derive the total dissipation of such a system, described by a coupled loss angle ϕ_{coup}, when the structure frame mass is much greater than the oscillator mass and when $\phi_M \gg \phi_m$:

$$\phi_{coup} = \phi_m + \phi_M\frac{\omega_m^2\omega_M^2}{\mu(\omega_M^2 - \omega_m^2)}$$

It is evident that this kind of loss has a small effect if $\mu \ll 1$; on the contrary, if the two uncoupled oscillators have close resonance frequencies, recoil losses are not negligible.

3.4 Thermal noise calculation methods

As already seen, the thermal noise estimation is obtained from the application of the fluctuation-dissipation theorem: it suffices to know the imaginary part of the transfer function (see eq. 3.1). The problem is that this kind of measurement is very difficult, since the imaginary part of $H(\omega)$ is much smaller than the real one [98, 99, 100].

So, different methods have been developed to calculate $\mathcal{I}m[H(\omega)]$ or to measure directly thermal noise:

- the normal-mode expansion, [82, 101] where each resonance is considered orthogonal to the others and the loss distribution homogeneous;
- the advanced-mode expansion, elaborated by Yamamoto [100], in which losses are considered inhomogeneously distributed;
- the direct approach, proposed by Levin [102], where there is no mode decomposition, but a direct application of the fluctuation-dissipation theorem.

3.4.1 Normal mode expansion

This method allows to evaluate the imaginary part of transfer function $\mathcal{I}m[H(\omega)]$ decomposing the transfer function in a sum of independent harmonic oscillators. Thermal noise power spectrum density will be derived from eq. 3.6. Let's see how to proceed.

Consider an observable physical quantity X of a system:

$$X(t) = \int \vec{u}(\vec{r}, t) \cdot \vec{P}(\vec{r}) dV \tag{3.35}$$

where $\vec{u}(\vec{r}, t)$ is the displacement vector of the system at the position $\vec{r}$ and time t, while $\vec{P}(\vec{r})$ is a weighting function vector.

For example, in Virgo interferometer, the observable quantity is the laser beam arriving at the dark port, $\vec{r}$ is on the mirror underformed surface, $\vec{u}$ is the mirror surface displacement due to its internal modes and the weighting vector $\vec{P}(\vec{r})$ is the gaussian laser beam profile:

$$\vec{P}(\vec{r}) = \frac{1}{\pi r_0^2} \, e^{-r^2/r_0^2} \hat{r} \tag{3.36}$$

where r_0 is the radius of the laser beam.

Now, consider to apply a generalized force $F(t)\vec{P}(\vec{r})$ to the system. Neglecting the dissipation, the equation of motion will be:

$$\rho \frac{\partial^2 \vec{u}}{\partial t^2} + \mathcal{L}(\vec{u}) = F(t)\vec{P}(\vec{r}) \tag{3.37}$$

where ρ is the density and $\mathcal{L}$ is a linear operator representing the elastic response of the system.

In order to find the solution of this equation we decompose the displacement $\vec{u}$ in a superposition of basis functions $\vec{w}_n(\vec{r})$:

$$\vec{u}(\vec{r}, t) = \sum_n \vec{w}_n(\vec{r}) q_n(t) \tag{3.38}$$

where the functions q_n represent the time evolution.

The basis functions are the solution of the eigenvalues problem:

$$\mathcal{L}(\vec{w}_n(\vec{r})) = \rho \, \vec{w}_n(\vec{r}) \, \omega_n^2 \tag{3.39}$$

where ω_n is the angular resonant frequency of the n-mode.

Furthermore the basis functions are orthogonal:

$$\int \rho(\vec{r})\ \vec{w}_i(\vec{r}) \cdot \vec{w}_j(\vec{r}) dV = m_i \delta_{ij} \tag{3.40}$$

and they are normalized:

$$\int \vec{w}_n(\vec{r}) \cdot \vec{P}(\vec{r}) dV = 1 \tag{3.41}$$

The parameter m_i is called *effective mass* of the i-th mode. Now, we substitute eq. 3.38 in eq. 3.37:

$$\rho \frac{\partial^2}{\partial t^2} \left[\sum_n \vec{w}_n q_n \right] + \mathcal{L} \left(\sum_n \vec{w}_n q_n \right) = F(t) \vec{P}(\vec{r})$$

multiplying by $\vec{w}_m$:

$$\rho \frac{\partial^2}{\partial t^2} \left[\sum_n \vec{w}_n \cdot \vec{w}_m q_n \right] + \mathcal{L} \left(\sum_n \vec{w}_n \cdot \vec{w}_m q_n \right) = F(t) \vec{P}(\vec{r}) \cdot \vec{w}_m$$

integrating on volume:

$$\frac{\partial^2}{\partial t^2} \left[\sum_n \left(\int dV \rho\, \vec{w}_n \cdot \vec{w}_m \right) q_n \right] + \sum_n \left(\int dV \rho \vec{w}_n \cdot \vec{w}_m \right) \omega_n^2 q_n = F(t) \left(\int dV \vec{P}(\vec{r}) \cdot \vec{w}_m \right)$$

where we use eq. 3.39 to determine the expression of the linear operator $\mathcal{L}$.

Using the condition given by eq. 3.40 and eq. 3.41:

$$\frac{\partial^2}{\partial t^2} \left(\sum_n \delta_{mn} m_n q_n \right) + \sum_n \left(\omega_n^2 q_n \delta_{mn} m_n \right) = F(t)$$

i.e.

$$m_n \ddot{q}_n(t) + m_n \omega_n^2 q_n(t) = F(t) \tag{3.42}$$

In that way we obtain the time evolution of the n-th mode: it is like a harmonic oscillator of mass m_n and resonant frequency ω_n with an external force $F(t)$ acting on it.

Putting eq. 3.38 in eq. 3.35 we have:

$$X(t) = \sum_n q_n(t)$$

i.e. the observable quantity can be simply described as a superposition of the motion of the harmonic oscillators q_n. Thanks to this equation, it is possible to find the transfer function for the coordinate X, by writing eq. 3.42 in frequency domain:

$$-m_n \omega^2 \tilde{q}_n + m_n \omega_n^2 [1 + i\phi_n(\omega)] \tilde{q}_n = \tilde{F}(\omega) \tag{3.43}$$

So, the transfer function is:

$$H_X(\omega) = \frac{\tilde{X}}{\tilde{F}} = \frac{\sum_n \tilde{q}_n}{\tilde{F}} = \sum_n \frac{1}{-m_n \omega^2 + m_n \omega_n^2 [1 + i\phi_n(\omega)]}$$

The thermal noise fluctuation power spectrum is:

$$S_X(\omega) = \sum_n \frac{4k_BT}{\omega} \frac{\omega_n^2 \phi_n(\omega)}{m_n[(\omega^2 - \omega_n^2)^2 + \omega_n^4 \phi_n^2(\omega)]} \tag{3.44}$$

Thus, we verify that the thermal motion of the system is the sum of the harmonic oscillators of the normal-mode expansion. The eq. 3.44 allows to estimate the thermal noise knowing for each mode:

- the loss angle
$$\phi_n(\omega_n) = \frac{1}{Q_n(\omega_n)}$$
directly measured at resonant frequency from experiment;

- the effective mass
$$m_n = \frac{\int \rho(\vec{r}) \, |\vec{w}_n(\vec{r})|^2 dV}{\left| \int \vec{w}_n(\vec{r}) \cdot \vec{P}(\vec{r}) dV \right|^2}$$
estimated, as instance, from finite element analysis.

3.4.2 Advanced mode expansion

The normal-mode expansion has been commonly used to estimate thermal noise in the interferometer. But it becomes inadequate when, for example, a system has inhomogeneously distributed losses [100, 102, 103, 104].

In that case, the mode expansion result is not correct since the inhomogeneity of the losses causes correlations and couplings between different degrees of freedom, which are not included in the standard expansion.

The physical reason of this coupling becomes clear considering the decay of a single resonant mode. When the loss is homogeneous, the phase of its decay does not depend on the position and so the displacement shape does not change with respect to the time. On the contrary, if the loss is concentrated in a region, a phase lag appears in this place: as a consequence, the shape of the displacement changes when the other modes are excited.

Majorana and Ogawa gave a simple example [104]: they estimated the thermal noise of a double-coupled oscillators with inhomogeneous losses (see fig. 3.4) using the normal-mode expansion and then applying directly the fluctuation-dissipation theorem. While the normal-mode expansion is a pure sum over all the resonance contributions, neglecting the possible off-resonance couplings:

$$S_{ii}^{exp}(\omega) = -\frac{4k_BT}{\omega} \sum_{i=1}^{n} \mathcal{I}m[H_i^{uncoupl}(\omega)]_i$$

the fluctuation-dissipation theorem for n degrees of freedom is given by eq. 3.3:

$$S_{ii}^{FDT}(\omega) = -\frac{4k_BT}{\omega} \mathcal{I}m[H_{ii}(\omega)]$$

where $\mathcal{I}m[H_{ii}(\omega)]$ can be simply computed knowing the physical parameters of the system.

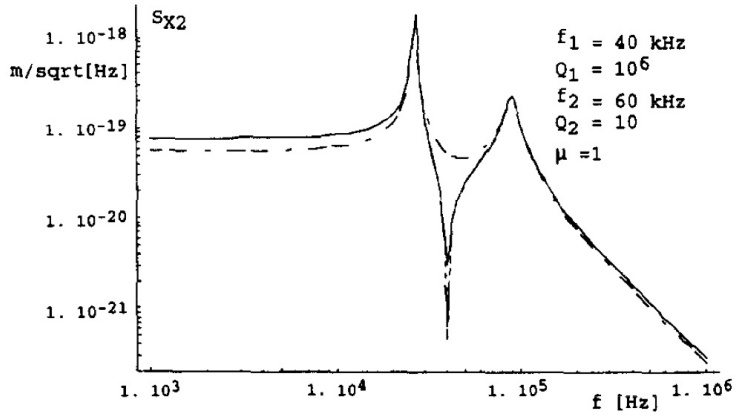

Figure 3.5: thermal noise predictions for a simplified-to-double-mode structure: normal-mode expansion (dotted line) and fluctuation-dissipation theorem calculation (solid line). In the plot mechanical parameters are reported.

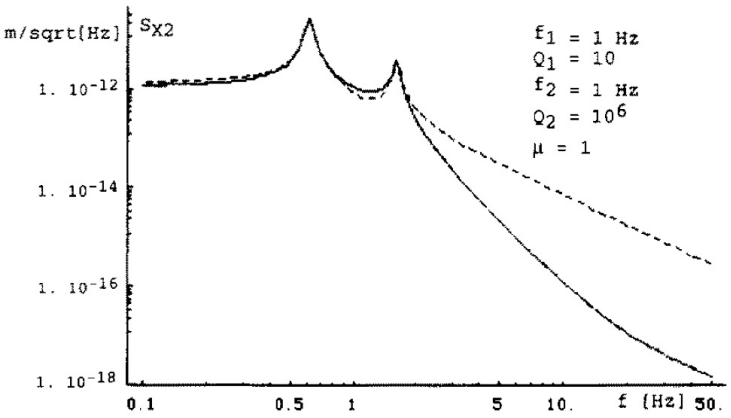

Figure 3.6: high frequency tail for the thermal noise when the modes of the double coupled oscillators are not orthogonal with a quality factor lesser than other: normal-mode expansion (dotted line) and fluctuation-dissipation theorem calculation (solid line). In the plot mechanical parameters are reported.

They found some differences between the two estimation methods, in particular in the off-resonance regions and in the high-frequency tail (see figs. 3.5 and 3.6).

Yamamoto developed a more accurate mode expansion, called *advanced mode expansion*, to compute the thermal noise contribution [100].

The difference between this expansion and the traditional one relies on the introduction of the dissipation term in the equation of motion from the very beginning and not after the mode decomposition (see eq. 3.43).

For the viscous damping, the eq. 3.37 becomes:

$$\rho\frac{\partial^2\vec{u}}{\partial t^2} + \rho\Gamma(\vec{r})\frac{\partial\vec{r}}{\partial t} + \mathcal{L}(\vec{u}) = F(t)\vec{P}(\vec{r}) \tag{3.45}$$

where $\Gamma(\vec{r})$ is the coefficient function of the friction forces.

Now, we follow the same procedure as in the previous section, decomposing the displacement vector $\vec{u}$ with the basis functions (see eq. 3.38). Since the losses are small, we consider the dissipation term as a perturbation. Then, we can repeat the same passages to find the equation of motion for the time functions q_n.

In the frequency domain, we have:

$$-m_n\omega^2\tilde{q}_n + m_n\omega_n^2[1 + i\phi_n(\omega)]\tilde{q}_n + \sum_{k\neq n} i\alpha_{nk}\tilde{q}_k = \tilde{F}(\omega) \tag{3.46}$$

where α_{kn} is the cross correlation term:

$$\alpha_{nk} = \omega\int \rho(\vec{r})\Gamma(\vec{r})\vec{w}_n(\vec{r})\cdot\vec{w}_k(\vec{r})dV \tag{3.47}$$

and the loss angle ϕ_n is defined as:

$$\phi_n(\omega) = \frac{\alpha_{nn}(\omega)}{m_n\omega_n^2}$$

As it is easy to see, eq. 3.46 differs from eq. 3.43 for the cross correlation term given by α_{nk}: this term contains the contributions to one mode due to couplings of all the others. The two different expansion methods match when all the couplings terms α_{nk} vanish, i.e. when the friction coefficient Γ is independent from position $\Gamma(\vec{r}) \equiv \Gamma$ and the losses are distributed homogeneously.

For the structural losses, the equation of motion for an elastic isotropic body is:

$$\rho\frac{\partial^2 u_i}{\partial t^2} + \frac{\partial\sigma_{ij}}{\partial x_j} = F(t)P_i(\vec{r})$$

where u_i and P_i are the i-th component of the displacement $\vec{u}$ vector and of the weighting function $\vec{P}$; while σ_{ij} is the stress tensor:

$$\sigma_{ij} = \frac{E_0[1 + i\phi(\omega,\vec{r})]}{1+\sigma}\left(\epsilon_{ij} + \frac{\sigma}{1-2\sigma}\epsilon_{kk}\delta_{ij}\right)$$

where E_0 is the Young's modulus, σ the Poisson ratio, ϵ_{ij} the strain tensor and $\phi(\omega, \vec{r})$ is the structural loss angle.

Following the same procedure as in the case of the viscous damping, we arrive at an expression similar to eq. 3.46, where α_{nk} is defined:

$$\alpha_{nk} = \int \frac{E_0 \phi(\omega, \vec{r})}{1+\sigma} \left(\epsilon_{n,ij}\epsilon_{k,ij} + \frac{\sigma}{1-2\sigma}\epsilon_{n,ll}\epsilon_{k,ll} \right) dV \tag{3.48}$$

Note that $\epsilon_{n,ii}$ corresponds to the trace of the strain tensor.

The advanced mode expansion works when the dissipation can be treated as a perturbation, i.e. the following condition on the distance between the resonant peaks is verified:

$$|\alpha_{nk}|^2 \ll \frac{m_n m_k}{4} \left|\omega_n^2 - \omega_k^2\right|^2$$

From eq. 3.47 and eq. 3.48, considering the Cauchy-Schwarz's inequality, it is possible to derive the maximum value of the coupling coefficient modulus α_{nk} [100]:

$$|\alpha_{nk}|_{max} = \sqrt{m_n \omega_n^2 \phi_n(\omega) m_k \omega_k^2 \phi_k(\omega)}$$

where m_n is the effective mass, ω_n is the resonant frequency and ϕ_n is the loss angle. The maximum of the absolute value of the coupling coefficient is reached when the typical size of the region where the losses are localized is smaller than the wavelength of the n-th and k-th modes.

The sign of the coupling coefficient depends on the observation area and on losses distribution. Measurements of the transfer function in a wide frequency band at various points of the system should give information about the sign of the couplings; in particular off-resonance measurements are fundamental, since measurements near the resonant peak are difficult and not so much accurate.

3.4.3 Direct approach

Nowadays the most used technique to calculate thermal noise is the direct approach in which there is no modal decomposition.

As for the normal mode expansion, consider an observable physical quantity X of a system (eq. 3.35):

$$X(t) = \int \vec{u}(\vec{r}, t) \cdot \vec{P}(\vec{r}) d^2 r$$

where $\vec{u}(\vec{r}, t)$ is the displacement vector of the system at the position $\vec{r}$ and time t; while $\vec{P}(\vec{r})$ is a weighting function vector, for example a Gaussian function (see eq. 3.36).

Thermal noise for a system described with a linear combination of coordinates is given by eq. 3.6, where the transfer function associated with the new coordinate is defined as in eq. 3.7.

In Levin's method [102], to work out thermal noise at a particular frequency ω, one should apply an oscillating pressure at that frequency on the observed surface of the test mass and then compute the system response $\mathcal{I}m[H(\omega)]$.

The oscillatory continuous force $F(\vec{r},t)$ is defined:

$$F(\vec{r},t) = F_0 \cos(\omega t) P(\vec{r})$$

which corresponds to a generalized force $F_{new}(t) = F_0 \cos(\omega t)$.

It is possible to evaluate the mean dissipated power $\langle W_{diss} \rangle$:

$$\begin{aligned}
\langle W_{diss} \rangle &= \langle \mathcal{R}e[\tilde{F}_{new} \tilde{\dot{X}}_{new}] \rangle = \\
&= \langle \mathcal{R}e[\tilde{F}_{new} i\omega \tilde{X}_{new}] \rangle = \\
&= -\langle \omega \, \mathcal{I}m[\tilde{F}_{new} \tilde{X}_{new}] \rangle = \\
&= -\langle \omega \, \mathcal{I}m[\tilde{F}^2_{new} H_{new}] \rangle = \\
&= -\langle \omega \, F_0^2 \mathcal{I}m[\cos^2(\omega t) H_{new}] \rangle = \\
&= -\frac{1}{2} \omega F_0^2 \mathcal{I}m[H_{new}]
\end{aligned}$$

So, we rewrite the eq. 3.6 in the form:

$$S_X(\omega) = \frac{8 k_B T}{\omega^2} \frac{\langle W_{diss} \rangle}{F_0^2} \tag{3.49}$$

For a cylindrical fused silica test mass with homogeneously distributed losses monitored by a circular Gaussian laser beam whose radius is much smaller than the test mass radius, the dissipated power can be evaluated analytically, starting from eq. 3.19:

$$W_{diss} = \int_V \omega \, \phi(\omega) \, \mathcal{E}_{max} \, dV = \omega \phi(\omega) U_{max}$$

where $\mathcal{E}_{max}$ is the maximum stored energy density and U_{max} is the energy of the maximum elastic deformation due to the oscillatory pressure.

This analytical approach is not always possible, in particular when there are inhomogeneously distributed losses. To avoid all the problems connected to it, Numata [105] performed a finite element analysis of the system. In that way the equations of motion are solved numerically and then the dissipated power is achieved to be used in eq. 3.49.

This method is particularly useful to model the interferometer mirrors: in fact it is possible to include separately the thermal noise contribution of bulk, coating, ears and magnets attached on the back of Virgo mirrors. Eq. 3.49 becomes a sum over all the single contributions:

$$S_X(\omega) = \frac{8 k_B T}{\omega F_0^2} U_{tot} \left(\sum_i \phi_i(\omega) \frac{U_i}{U_{tot}} \right) \tag{3.50}$$

where U_i is the maximum energy stored in the i-th part of the mirror, ϕ_i is the corresponding loss angle and U_{tot} is the maximum energy stored in all the system. The fraction U_i/U_{tot} is given by the finite element analysis, while the loss angles ϕ_i can be estimated from direct measurements.

3.5 Thermal noise in Virgo

Thermal noise of interferometric gravitational wave detectors is composed by two contributions:

1. suspension thermal noise, generated by the fluctuations of the mirror centers of mass due to thermal vibrations of the suspension system;

2. mirror thermal noise, corresponding to surface deformations of the mirrors caused by thermally-excited elastic-vibrations of the mirrors themselves.

Each contribution is a sum over the four test masses, the two input mirrors and the two end ones: we consider only the Fabry-Perot mirrors because of the high number of light reflections, which make their thermal noise contribution larger than the one of the other interferometer optics.

3.5.1 Suspension contribution

The suspension system allows to damp the seismic excited motions, as already seen in sec. 2.3.5, through a chain of filters, pendula and blades. In Virgo the last suspension stage of the test masses is constituted by a marionette that suspends the mirror through four fused silica fibers (see fig. 2.12). All these filters introduce noise in each degree of freedom, according to the fluctuation dissipation theorem [106, 107].

This problem can be divided into four separate contributions:

- pendulum mode thermal noise of the mirror suspension fibers: at that frequency, the mirror and the reaction mass moves concordantly, while the marionette is at rest; the mirror is uncoupled with the payload;

- vertical modes thermal noise of the mode of the mirror and the reaction mass concordantly with the marionette at the rest and of the mode of the mirror and the reaction mass oppositely to the marionette;

- violin modes thermal noise of the mirror suspension fibers;

- tilt/rotational modes thermal noise, that are in general negligible because coupling on horizontal degree of freedom is quite small due to the mechanical configuration of the payload.

Pendulum mode

The choice of a pendulum as the final suspension stage in gravitational wave interferometer is based on the determination to minimize thermal noise. In fact, in a pendulum, the primary "spring" for horizontal motion comes from the gravitational field, which is lossless; while the vertical displacement comes from the flexural elasticity of the wire, which is dissipative.

The two forces acting on a pendulum of mass m and length l have different constants:

- gravitational constant $k_g = mg/l$;

- elastic constant $k_{el}(1 + i\phi_{struct})$, where k_{el} is defined from eq. B.4 and ϕ_{struct} is the loss angle of the wire material.

Considering the equation of motion:

$$m\ddot{x} = k_g x - k_{el}(1 + i\phi_{struct})x$$

which is equivalent to:

$$m\ddot{x} = -(k_g + k_{el})\left(1 + i\frac{k_{el}}{k_g + k_{el}}\phi_{struct}\right)x$$

therefore it is possible to define an effective loss angle ϕ_{eff} equal to:

$$\phi_{eff} = \frac{k_{el}}{k_g + k_{el}}\phi_{struct} \approx \frac{k_{el}}{k_g}\phi_{struct}$$

since usually $k_{el} \ll k_g$. The factor k_{el}/k_g is called *pendulum dilution factor* D_p [108] and it is equal to:

$$D_p = \frac{k_{el}}{k_g} = \frac{1}{2}\sqrt{\frac{EI}{\mathcal{T}L^2}}$$

where E is the Young's modulus, I is the moment of the cross section, $\mathcal{T}$ is the tension applied to the wire and L is its length.

Thanks to this factor, the effective measured loss angle for the pendulum mode is much lower than the internal ϕ_{struct}, depending from the wire material.

If the pendulum is suspended by n wires, the dilution factor is multiplied by $\sqrt{n}$.

The thermal noise estimation for the pendulum mode is:

$$S_X^{pend}(\omega) = \frac{4k_B T}{m\omega}\frac{\phi_{eff}\omega_p^2}{(\omega^2 - \omega_p^2)^2 + \phi_{eff}^2\omega_0^4} \tag{3.51}$$

where $\omega_p = \sqrt{g/l}$ is the simple pendulum resonant frequency.

In the case of Virgo, the computation of the effective loss angle takes into account the thermoelastic contribution ϕ_{therm} (eq. 3.25) and the superficial one ϕ_{surf} (eq. 3.29). Furthermore, there are also recoil losses, quantifiable with the loss angle ϕ_{recoil}. So, the effective pendulum loss angle is [92]:

$$\phi_{eff} = D_p(\phi_{struct} + \phi_{therm} + \phi_{surf}) + \phi_{recoil}$$

Thus, pendulum quality factor measurements are limited by recoil damping of the support structure (see sec. 3.3.5). The limiting quality factor due to the recoil losses [96]:

$$Q_{lim} = \frac{k_S l}{mg\Phi}$$

where k_S is the spring constant of the supporting structure at the pendulum frequency, Φ is the phase angle between the force applied to the structure and its displacement (i.e. the loss angle), m is the mass of the pendulum and l its length.

To avoid these problems, it is useful to measure the violin mode quality factors, instead of the pendulum one. In fact, the violin modes can be protected from recoil

losses using a double pendulum configuration, as in Virgo. Moreover, the violin modes are determined by the same theory as the one of the pendulum mode and should be affected by most of the same excess loss mechanisms. The fact that many quality factors can be measured over a wide range of frequencies gives an important diagnostic tool.

Anyway, it is possible to estimate pendulum thermal noise taking into account all the payload and so the possible recoil losses. The effect of the other masses like the marionette and the reaction mass is negligible in the bandwidth of interest only if the marionette mass is higher than those ones of the mirror and the reaction mass, because its recoil is negligible under these hypotheses. This assumption is no more valid for Advanced Virgo, because marionette and mirror masses will be likely comparable [109].

In LIGO the difference between the single pendulum and the triple pendulum suspension test mass is calculated in [110, 111]. The resulting thermal noise estimations are shown in fig. 3.7. The triple pendulum is constituted by three identical stages, with the same masses and elastic constants, but different loss angles. All the loss angles are taken independent of frequency, as in the case of structural damping: in particular the first stage loss angle is greater than the others. The single stage is identical to the last stage of the triple pendulum.

The triple pendulum thermal noise is much greater than the one of the single pendulum thermal noise in the low frequency region. If we compute the thermal noise of a triple pendulum with just the contribution of its last stage, we largely underestimate it.

Vertical mode

Since the Earth gravitational field is not uniform, local vertical directions at both ends of the arms are not parallel to each other (see fig. 3.8). That implies that a fraction of the vertical motion can be seen in the horizontal one: then, it causes a change in the cavity length that can be confused with a gravitational wave signal.

The coupling between the vertical motion and the horizontal one is exactly equal to the angle θ_0 under which an arc of length $L_{arm}/2$ is seen from the center of the Earth. The expected value for the coupling is $\theta_0 \sim 0.24 \mu rad$.

For that reason a part of the thermal noise associated with vertical oscillations is seen on the horizontal direction; its contribution is:

$$S_X^{vert}(\omega) = \theta_0 \frac{4k_B T}{m\omega} \frac{\phi_{eff}\omega_v^2}{(\omega^2 - \omega_v^2)^2 + \phi_{eff}^2 \omega_v^4} \tag{3.52}$$

where ϕ_{eff} is the effective loss angle, sum of different contributions as the structural, thermoelastic and superficial loss angles, and ω_v is the vertical resonance frequency of the system:

$$\omega_v^2 = \frac{k_{vert}}{m} = \frac{ES}{l}\frac{1}{m}$$

being m the mass of the mirror, k_{vert} the vertical elastic constant, E the Young's modulus, S the wire section and l its length.

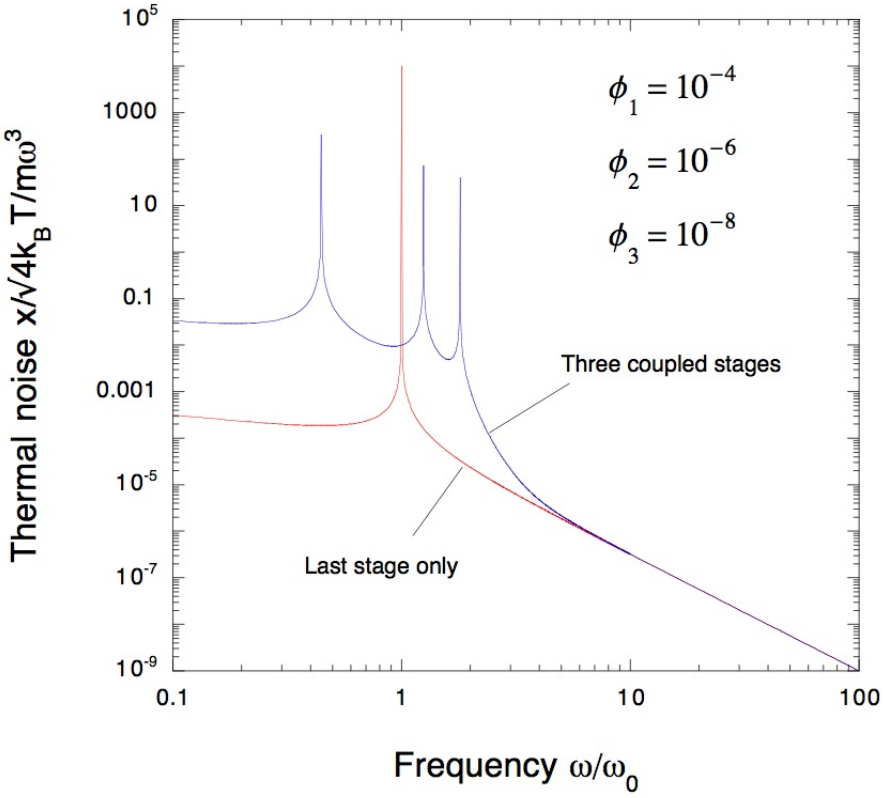

Figure 3.7: comparison between thermal noise in a three-stage system with identical masses and spring constants but different loss angles, showed in the plot, and thermal noise spectrum of a single stage isolation; the single stage is identical to the last stage of the triple pendulum.

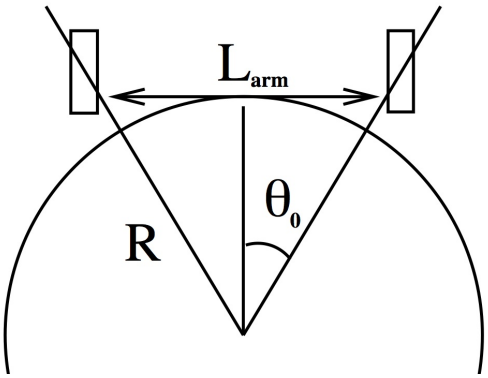

Figure 3.8: the vertical directions at the ends of the arm are not parallel and give origin to a coupling between the vertical and the horizontal displacements of the mirrors.

Violin modes

Consider a wire as a distributed system and not as a massless spring: it exhibits transversal oscillations called violin modes (see fig. 3.9), when its extremities are fixed.

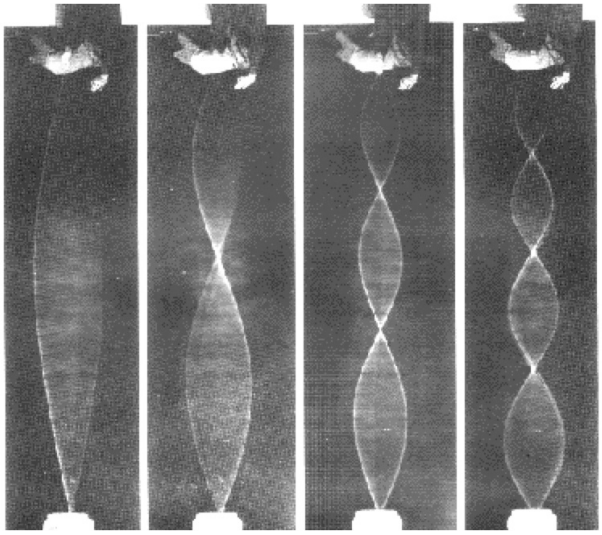

Figure 3.9: standing waves in a string: the fundamental and the first three overtones which form a harmonic series.

In the case of Virgo the N wires suspending the mirror have the upper extremities clamped to the marionette, while the downer ends are attached to the mirror, under a tension $\mathcal{T} = mg/N$ due to the mirror mass m.

Violin modes are weakly coupled to the interferometer output, since there is a large mechanical impedence mismatch between the wires and the test mass. Anyway, their resonant frequencies lie in an important region of the interferometer bandwidth, around several hundred Hz.

The resonance angular frequency of the n-mode is [82]:

$$\omega_n = \frac{n\pi}{L}\sqrt{\frac{\mathcal{T}}{\rho_{lin}}} \tag{3.53}$$

where n is the violin order, ρ_{lin} is the linear density of the wire, L its length.

This expression does not consider the anharmonicity effect of the violin modes: wires bend more with increasing the mode number [112] (see fig. 3.10):

$$\omega_n = \frac{n\pi}{L}\sqrt{\frac{\mathcal{T}}{\rho_{lin}}}\left[1 + \frac{2}{k_e L} + \frac{1}{2}\left(\frac{n\pi}{k_e L}\right)^2\right] \tag{3.54}$$

where k_e is the elastic flexural stiffness of fibers, depending on the frequency ω, on the wire Young's modulus E and on its moment of cross section I:

$$k_e(\omega) = \sqrt{\frac{\mathcal{T} + \sqrt{\mathcal{T}^2 + 4EI\rho_{lin}\omega^2}}{2EI}} \tag{3.55}$$

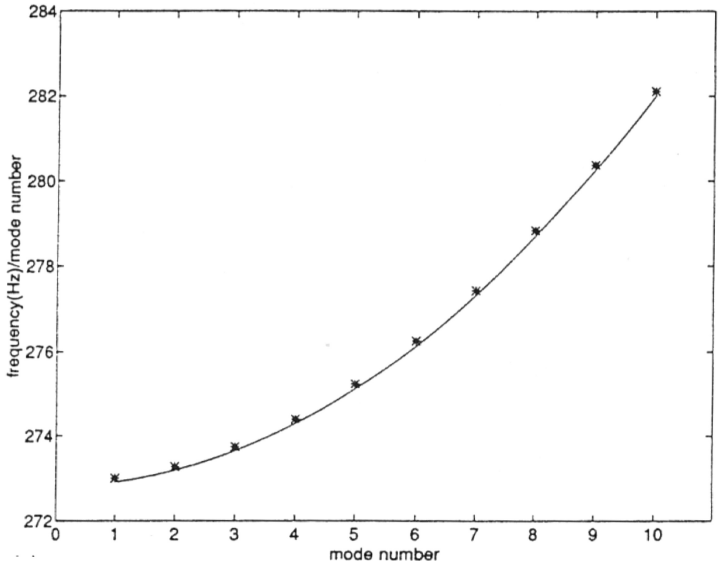

Figure 3.10: the anharmonicity of the violin mode frequencies: the plot shows the normalized frequency of the n-mode with respect to the mode number.

This elastic stiffness can be approximated at low frequency (see also eq. B.3 and sec. 4.3.1 for more details):

$$k_e \approx \sqrt{\frac{\mathcal{T}}{EI}}$$

For what concerns the loss angle, we expect that the n-th mode loss angle ϕ_n depends on the ratio between the elastic energy E_{el} and the gravitational one E_{grav}, in a similar way of what happens for the pendulum mode with the dilution factor D_p:

$$\phi_n = \frac{\phi}{D_v^n} = \phi \frac{2}{k_e L}\left(1 + \frac{n^2\pi^2}{2k_e L}\right) \tag{3.56}$$

where ϕ is the sum of the structural and the thermoelastic loss angles $\phi(\omega) = \phi_{struct} + \phi_{therm}(\omega)$ and $D_v^n = E_{el}/E_{grav}$ is the *violin dilution factor*.

For a two-wire suspension configuration, the elastic energy of the lowest violin modes is about twice the one of the pendulum mode, since in the violin mode the wire bends as much at the bottom as at the top, while the pendulum mode loss is produced only at the top [113]. For higher violin modes, the contribution due to the wire bending along its length should be considered.

In the four-wires suspension configuration, the elastic energy of the lowest violin modes and of the pendulum mode is approximately the same [85].

On the other hand, the gravitational energy of the pendulum mode is by a factor 2 larger than the one of violin mode. For violin modes of each wire, the gravitational energy is:

$$E_{grav}^v = \frac{1}{4} N \mathcal{T} L \theta_m^2 = \frac{1}{4} mgL\theta_m^2$$

where θ_m is the maximum angle of swinging during the motion.

This expression is exactly one half of the gravitational energy of the pendulum mode:

$$E^p_{grav} = \frac{1}{2} m \omega_p^2 L^2 \theta_m^2 = \frac{1}{2} m g L \theta_m^2$$

That explains the difference between the loss angle of the pendulum mode and the violin mode for the two-wires configuration ($D_v \sim 4D_p$) or for the four-wires configuration ($D_v \sim 2D_p$).

The violin modes thermal noise contribution can be evaluated using the normal mode expansion [82], since their off-resonance contribution is small:

$$S_X^{viol}(\omega) = N \frac{4 k_B T}{\omega} \sum_n \frac{\phi_n \omega_n^2}{m_n \left[(\omega^2 - \omega_n^2)^2 + \phi_n^2 \omega_n^4 \right]} \tag{3.57}$$

where N is the number of suspending wires, m_n is the effective mass of the n-th order violin, ϕ_n is the loss angle given by eq. 3.56, and ω_n is the violin resonance frequency, given by eq. 3.54.

The effective mass of the n-th violin is [114]:

$$m_n = \frac{1}{2} N m \left(\frac{\omega_n}{\omega_p} \right)^2 \approx \frac{\pi^2 m^2 n^2}{2 \rho_{lin} L} \tag{3.58}$$

where m is the mass of the suspended body, ω_p is the pendulum resonant frequency, n is the violin order, ρ_{lin} is the wire linear density and L its length.

Another important feature of the violin modes is that they have two polarizations per wire, causing two slightly different frequencies. In the Virgo reference frame (see fig. 2.11) these two polarizations are along the z-axis and the x-axis, due to the fact that the wire clamping system fastens differently in these two directions.

3.5.2 Mirror contribution

Mirror thermal noise contribution depends on thermally excited internal mode vibrations of the test-mass bulk and coating.

Either for the bulk, either for the mirror coating, it is worthwhile to consider the structural and the thermoelastic loss angle (for a complete treatment see [115] ♡).

In fig. 3.11 some internal modes of the mirror bulk are reported as an example: they are computed with a finite element analysis. The displacement amplitude is indicated with different colors.

Note the difference between "butterfly" modes, which are characterized by two or more nodal lines, and "drum" modes, which are characterized by one or more nodal circumferences. In general an internal mode is identified with a couple of numbers (l, m) where l is the number of nodal circumferences and m is the number of nodal lines.

For the bulk, thermal noise can be estimated using the normal mode expansion, the advanced mode expansion or the direct approach.

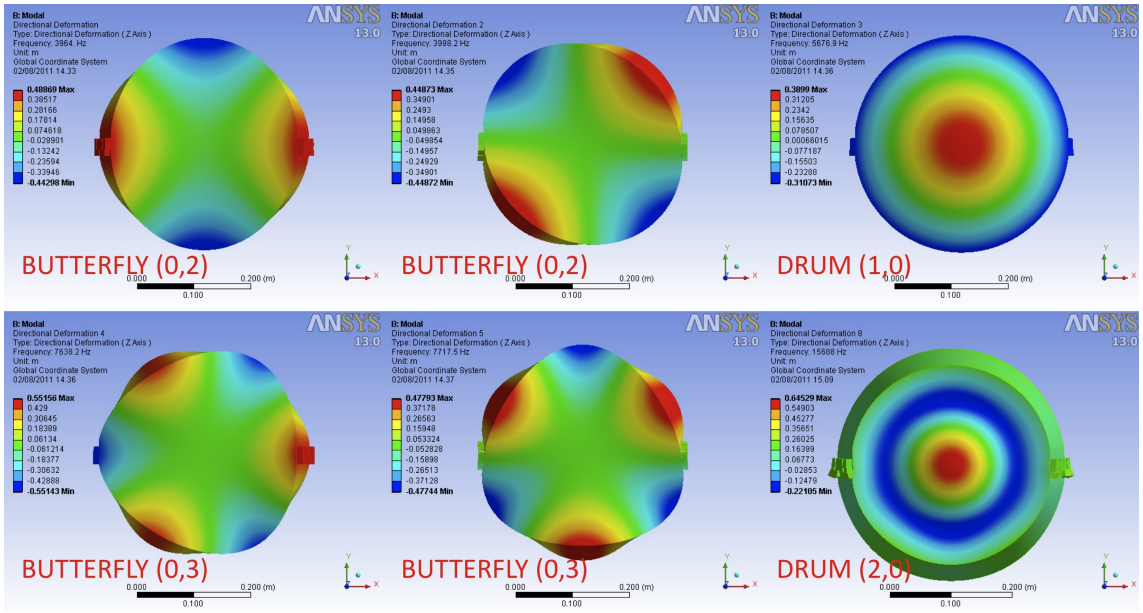

Figure 3.11: examples of internal mirror bulk modes: the "butterfly" modes and the "drum" modes are reported. Different colors stand for the displacement amplitude.

Normal mode expansion

Applying the first method for the mirror thermal noise, the eq. 3.44 can be approximated since the frequency band of interest is well below the resonant frequency of the lowest vibrational mode of the mirror (see eq. 3.15):

$$S_X^{mi}(\omega) = \sum_i \frac{4k_B T}{m_i \omega_i^2} \frac{\phi_i(\omega)}{\omega} \tag{3.59}$$

where m_i is the effective mass of the i-th internal mode of the mirror at frequency ω_i and $\phi_i(\omega)$ is its relative loss angle.

Supposing the same loss angle for all internal modes[3] $\phi_1(\omega) = \phi(\omega)$, the main problem is the estimation of the effective mass for each mode.

To solve this problem, we approximate the mirror to a traction-free-surfaces isotropic cylinder. For such a body it is possible to use the theory of elasticity in continuous media which is mainly analytic and partially numerical. Thanks to this method, the vibrational eigenmodes and eigenfrequencies are computed [116]. Then, from these results, the displacement amplitude of the mirror surface at each point (weighted with the gaussian profile intensity beam), the time dependence mode shapes and the effective masses can be calculated [101, 117].

The amplitude of the displacement of the mirror surface at each point in cylindrical coordinates for the n-th mode is $\vec{u}_n(r, \theta)$, normalized to a fixed energy U.

The optical modes of the interferometer is described by the Hermite-Gauss functions TEM_{mn}; as seen in sec. 2.3.3, the interferometer typically operates with the

[3]This assumption is valid if the losses are internal and there is no contribution due to the friction between the mirror and the wires supporting it.

fundamental mode $TEM_{00} \equiv \psi_{00}$ on resonance. This optical mode is subjected to a phase shift upon reflection from a mirror excited in a particular vibrational mode:

$$\psi_{00}(r,\theta,z) \rightarrow \phi_{00}(r,\theta,z)e^{i2\vec{k}\cdot\vec{u}_n} \approx \psi_{00}[1 + i2\vec{k}\cdot\vec{u}_n - 2(\vec{k}\cdot\vec{u}_n)^2] \tag{3.60}$$

where $\vec{k}$ is the wave vector and $|\vec{k}\cdot\vec{u}_n| \ll 1$ for all the points on the mirror surface.

This perturbed mode can be expressed in terms of unperturbed modes:

$$\psi = \sum_i \sum_j c_{ij}\psi_{ij}$$

where the coefficient c_{ij} are integrated in the mirror surface S:

$$c_{ij} = \int_S \psi^*_{ij}\psi_{00}\, e^{i2\vec{k}\cdot\vec{u}_n} dS$$

So, the perturbed mode ψ can be written as:

$$\psi \simeq \psi_{00}\left[1 + i2\int_S \psi^*_{00}\psi_{00}\,\vec{k}\cdot\vec{u}_n dS - 2\int_S \psi^*_{00}\psi_{00}\,(\vec{k}\cdot\vec{u}_n)^2 dS\right] \tag{3.61}$$

The imaginary term of eq. 3.61 contains the phase shift form which the apparent length change Δl_n can be determined:

$$\Delta l_n = \frac{1}{|\vec{k}|}\int_S \psi^*_{00}\psi_{00}\,\vec{k}\cdot\vec{u}_n dS$$

while the second integral in the eq. 3.61 describes the light which is scattered out of the TEM_{00} mode.

From these definitions, it is possible to derive the effective mass m_n of the n-th mode [101]:

$$m_n = \frac{U}{\frac{1}{2}\omega_n^2\Delta l_n^2}$$

The effective mass can be directly measured with a Michelson interferometer, like Virgo, exciting the internal mode of the mirror with a coil-magnet system (see sec. 2.3.5). The apparent motion of the mirror surface at the resonance is the rms displacement $\bar{x}$:

$$\bar{x} = \frac{Q_n}{m_n\omega_n^2}\bar{F}$$

where $\bar{F}$ is the rms force applied to the mirror through the coils, Q_n is the mechanical quality factor of the resonance and ω_n is the resonance frequency.

The main question that raises in using the formula 3.59 is how many modes must be counted in the sum to achieve an accurate estimation of the thermal noise of a gravitational wave interferometer. In the past, thermal noise estimation included only the lowest few mirror vibrational modes, generally considering the coupling between the longitudinal motion of the mirror vibration and the optical path length.

Gillespie and Raab [101] found that more modes must be considered to estimate accurately thermal noise, since there are many modes strongly coupled to the interferometer laser probe.

The point is that the thermal noise contribution of each individual mode decreases with the resonant frequency due to the ω_n^2 term in the denominator of eq. 3.59, but the mode density increases linearly with frequency; at the same time, there is a general decrease of the value of the effective mass m_n. The result is a cumulative contribution which increases almost linearly with the maximum resonance frequency included.

But, the sum of all these contributions do not diverge: it converges depending upon the beam spot size. In fact, the contributions increase linearly until the laser beam spot diameter d_{spot} becomes comparable to half an acoustic wavelength of the vibrational internal mode of the mirror λ_{mode} (see fig. 3.12):

$$d_{spot} \sim \frac{\lambda_{mode}}{2} \tag{3.62}$$

We rewrite the wavelength with respect to the frequency of the mode f_{mode} and the propagation velocity in the mirror v_{mi}. Then, we compute the velocity knowing the Young's modulus E_{mi} and the density ρ_{mi} of the mirror:

$$\lambda_{mode} = \frac{v_{mi}}{f_{mode}} = \sqrt{\frac{E_{mi}}{\rho_{mi}}} \frac{1}{f_{mode}}$$

For Virgo, the beam spot sizes are of order of cm for input mirrors and of order of $10cm$ for end mirrors. So, the maximum resonance frequencies included in the sum will be of order of $300kHz$ for the input and $30kHz$ for the end test masses.

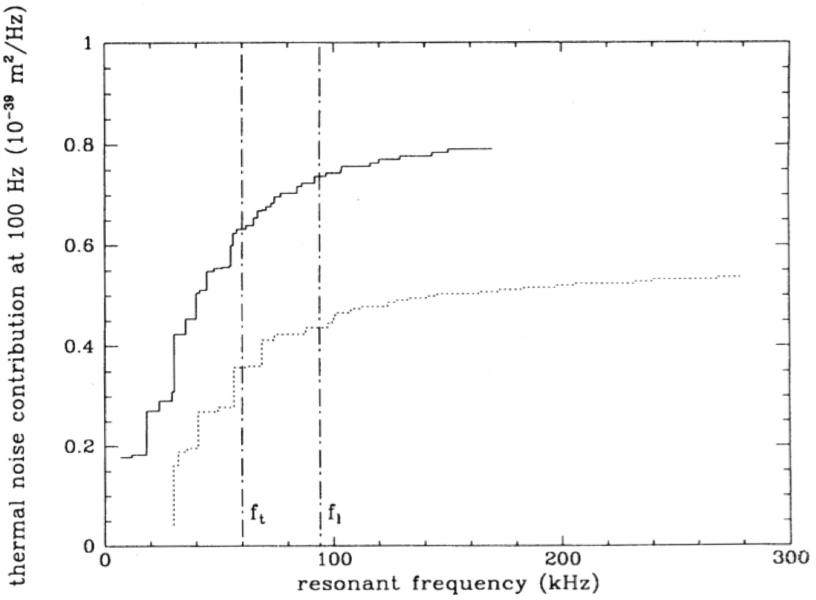

Figure 3.12: cumulative contribution to thermal noise of a $10cm$ mirror (dotted line) and $25cm$ LIGO mirror (solid line), with a $2.2cm$ beam spot; the vertical dot-dashed lines indicate the frequencies at which an acoustic wavelength is of order the beam spot size for both transverse (left line) and longitudinal (right line) waves.

Advanced mode expansion

From the discussion in sec. 3.4.2, we have shown that the normal mode expansion, used frequently to estimate thermal noise, is not correct when the dissipation is inhomogeneous [118, 119]. For example, in the case of mirror bulk thermal noise, we have to consider that our test probe is a laser beam spot, impinging on the mirror surface. If there is a concentrated loss far from the beam spot, the loss has a smaller effect on the thermal noise in the observation band than on measured quality factors. On the contrary, if the concentrated loss is near the beam spot, it generates a thermal noise larger than what estimated with the traditional mode expansion.

We can divide loss processes acting on a mirror bulk in three categories:

- homogeneous losses, corresponding to the intrinsic dissipation of the material of the mirror: its contribution is consistent with the one obtained from the normal mode expansion;
- surface loss models, corresponding to the surface damage caused by the inadequate polish or the loss of the dielectric reflective coating or simply surface accumulation of substrate stress;
- point-like loss models, corresponding to dissipation localizing at points, as small components glued to the mirror (magnets for actuation system or stand-off's for suspension system).

Unfortunately there are no calculations done on mirrors using this method and Yamamoto himself, in his work on it [100], says that the analysis is not performed with this method because it would be necessary to take into account too many modes for having a good convergence of the series.

Direct approach

As seen in sec. 3.4.3, it is possible to evaluate the mechanical transfer function of a physical system using a static deformation on the mirror under a Gaussian pressure.

For the mirror bulk thermal noise, we can firstly treat the simplified case when the mirror has an infinite radius, i.e. the optical spot size is small compared to its size. In that assumption, no radial boundary conditions are applied to the equilibrium equations [120] and the energy of the elastic deformation U_{max} of the mirror at the moment of maximal strain configuration is:

$$U_{max} = \frac{1-\sigma^2}{2\sqrt{\pi}Er_0}$$

where σ is the Poisson ratio, E the Young's modulus and r_0 is the beam spot size.

Thus, the mirror bulk thermal noise is:

$$S_X(\omega) = \frac{8k_BT}{\omega}\phi(\omega)\frac{1-\sigma^2}{2\sqrt{\pi}Er_0}$$

where $\phi(\omega)$ is the loss angle of the mirror.

The calculation of bulk thermal noise considering the finite size of the mirrorwas also made by Bondu, Hello and Vinet [120] and reviewed by Liu and Thorne [121] in the case of a finite size mirror. Their result is:

$$S_X(\omega) = \frac{8k_BT}{\omega}\phi(\omega)(U_0 + \Delta U)$$

where U_0 and ΔU are infinite series of Bessel function with coefficients depending on the material properties and on mirror and beam-spot size dimensions. If compared with the result in the approximation of infinite mirror mass, this calculation gives a correction that, e.g. in the case of the Advanced detector mirrors, starts to be greater than 10% for beam spot sizes greater than $2.5cm$. Considering that there is the project to use flat beams, this correction becomes crucial in estimating the Brownian thermal noise correctly.

Chapter 4

Quality factor measurements in Virgo+ monolithic suspensions

In this chapter I present my work on quality factor measurements on Virgo+ monolithic suspensions. A measurement campaign on quality factors of mechanical resonances is performed to understand the noise level in the sensitivity band between $10Hz$ and $300Hz$.

At first I describe in detail the monolithic suspension layout and the experimental apparatus used for the measurements. Then I show how I analyzed data describing the line identification method through the temperature dependence of the resonance frequency. At the end I present quality factor behavior with respect to frequency for different kind of modes.

4.1 Virgo+ monolithic suspensions

In Virgo the mirror is suspended by two loops of C85 steel wires with an intrinsic loss angle $\phi_{C85} \approx 2 \cdot 10^{-4}$ at $100Hz$ and a tensile strength of about $2.9GPa$; unfortunately they cause an additional friction with the mirror.

To prevent this friction and to reduce thermal noise contribution in the middle frequency band between few Hz up to few kHz, the last stage of the Virgo+ mirror suspension is monolithic, i.e. the mirror, its clamps and suspension wires are made as a monobloc of fused silica.

Moreover it is shown [92, 94, 122] that fused silica has an internal loss angle smaller than steel ($\phi_{FS} \approx 10^{-9}$) and it has a low thermal expansion coefficient $\alpha_{FS} \approx 0.5 \cdot 10^{-6} 1/K$, which reduces the thermoelastic dissipation. On the contrary, its tensile strength is high $4GPa$, leading to a larger dilution factor.

Despite these positive characteristics, fused silica presents some disadvantages: tensile strength is strongly dependent on cracks and defects present on the fiber surface and there is evidence of ageing due to environment pollution [123]. Therefore, it is crucial to avoid contaminants and impurities during their production; also after production, fused silica fibers must be kept in a clean room under vacuum, avoiding any contact, not to spoil tensile strength performances.

Properties	value
Specific heat c	$670 J/(kg\,K)$
Thermal conductivity k	$1.4 W/(m\,K)$
Linear thermal expansion coefficient α	$5.5 \cdot 10^{-7} 1/K$
density ρ	$2.2 \cdot 10^{3} kg/m^{3}$
Young's modulus E	$72.9 GPa$
Young's modulus' temperature dependence β	$1.86 \cdot 10^{-4} 1/K$
Poisson ratio σ	0.17
Tensile strength $\mathcal{T}_{max}$	$4 GPa$
Structural loss angle ϕ_{str}	$3.3 \cdot 10^{-8}$

Table 4.1: mechanical and thermodynamical properties of fused silica.

4.1.1 Fused silica fibers

Fused silica is a silicon compound ($Si\,O_2$) with a glass structure having a glass transition temperature which depends on specific material history and vitrification velocity: it usually lies around $2000K$. The main mechanical and thermodynamical properties of fused silica are shown in tab. 4.1.

For Virgo+, fibers are produced starting from high purity fused silica cylindrical bars commercially available (suitable materials are Herasil or Suprasil), $10cm$-long and $1.5mm$-thick. The central region of the bar is melted and subsequently the two ends are pulled apart. In fact, once melted, the fused silica material becomes highly viscous and it can be plastically deformed. For melting the rod, a $100W$ CO_2 commercial laser with $10.6\mu m$ wavelength is used.

This method has been implemented at the University of Glasgow for GEO and a duplicate of the CO_2 pulling machine has been assembled in a dedicated laser room at Virgo site. A schematic view of the functional parts of the machine is shown in fig. 4.1, while some pictures are shown in fig. 4.2.

The fiber production procedure is the following:

1. the fused silica rod is cleaned with isopropylic alcohol. It is welded to two silica parts, one used for suspending it to the marionette (cone) and the other for attaching it to the mirror (anchor), as shown in fig. 4.5 (see sec. 4.1.2 for more details). After the welding procedure the lower end is blocked to a fixed clamp and the upper one is connected at the top of the moving arm of the CO_2 laser pulling machine.

2. the silica bar is heated by moving the laser spot along the bar axis without pulling, to melt all the imperfections and micro-cracks, whose presence would lower the breaking load of the fiber: this process is called *annealing*. Structural defects produce internal reflections, clearly visible as a diffuse luminosity. Annealing is repeated until no more diffuse light or spots are present inside the fiber, which therefore appears perfectly transparent.

3. the laser beam is directed on a rotating mirror which allows, together with two other conic mirrors, to heat the silica bar all around its axis (see fig. 4.2(b)).

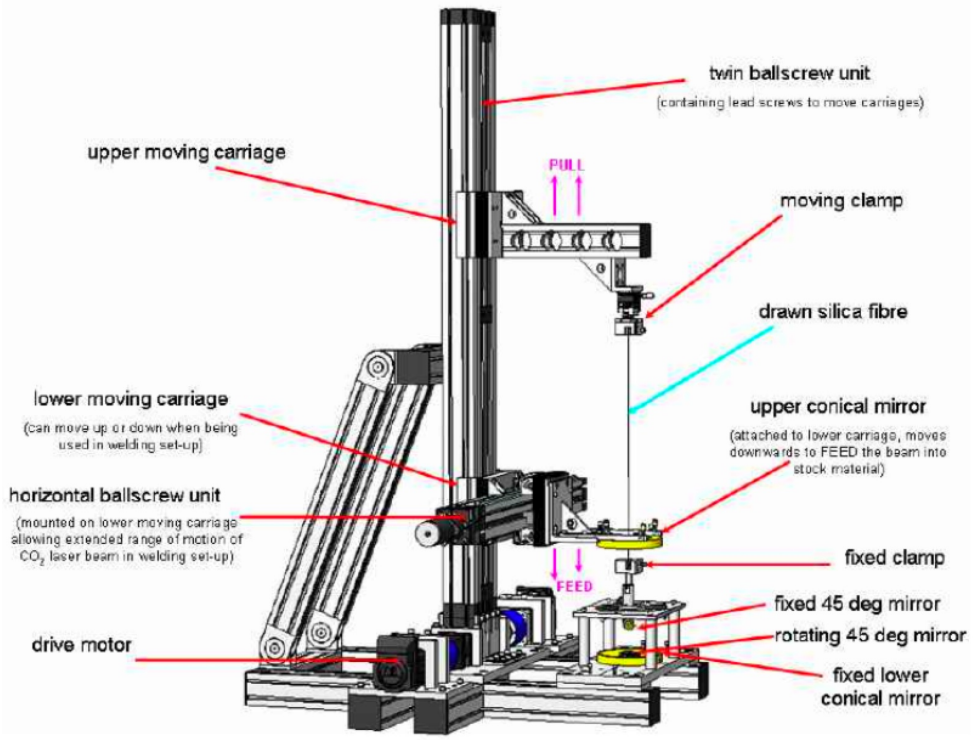

Figure 4.1: schematic drawing of the CO_2 laser pulling machine: the laser beam is delivered onto the fused silica rod by a series of gold coated mirrors.

The upper conic mirror can be moved along the vertical axis, using a PC controlled precision motor. In that way it is possible to move the laser spot along the silica bar. Another identical motor is used to control the moving clamp position [63].

4. once the rod is melted by the laser, the moving arm pulls it upward following a given velocity to produce a thin fiber with the designed profile. In fact, the geometry of the fiber depends critically on the chosen velocity. Since the melting involves a small volume of the rod from which the material is driven away during the pulling, new material must be melt in order to feed the fiber. Therefore, the melting point is shifted downward during the pulling, moving down the conical focusing mirror.

Note that the welded rod ends are not melted during the process, so the fiber maintains thick heads near the cone and the anchor. These small bobs are necessary for allowing a good clamping in all the subsequent operations during the mounting and dismounting. Furthermore it is proved [124, 125] that for minimizing the thermal noise contribution, the best profile choice is a "dumbbell-shaped" fiber, as shown in fig. 4.3.

With this method, thin fibers with a diameter of $(285 \pm 10)\mu m$ and $0.70m$-long are produced, capable of supporting loads as high as 10 kg or more. The laser pulling machine allows a very good reproducibility of the fiber shape, since the numerical control of the motor speed assures to obtain a constant selected diameter fiber (within

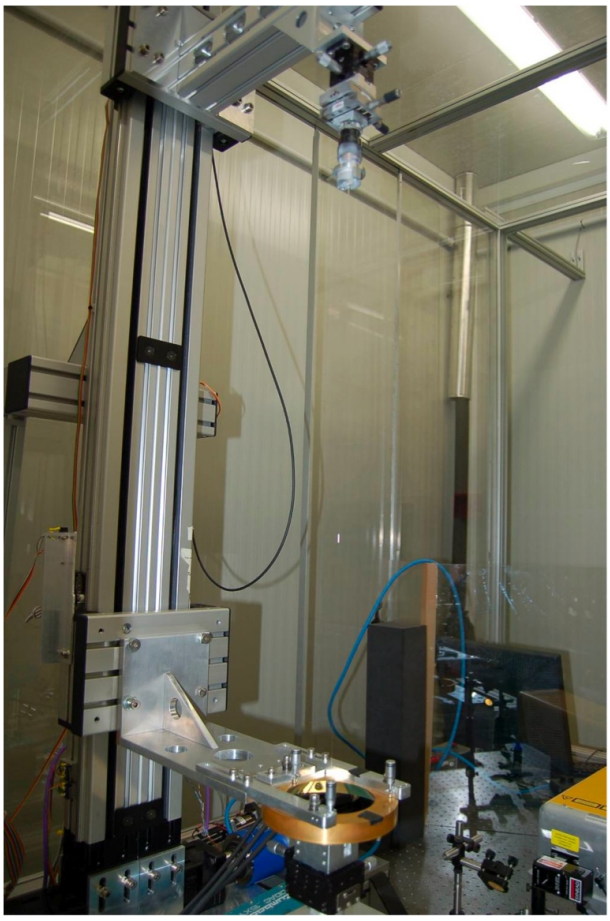

(a) ensemble

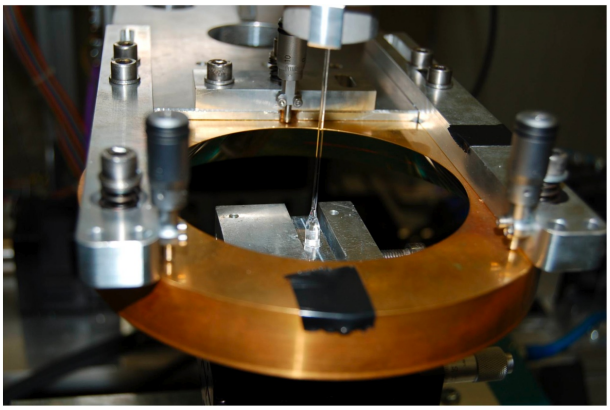

(b) gold mirror detail

Figure 4.2: CO_2 laser pulling machine.

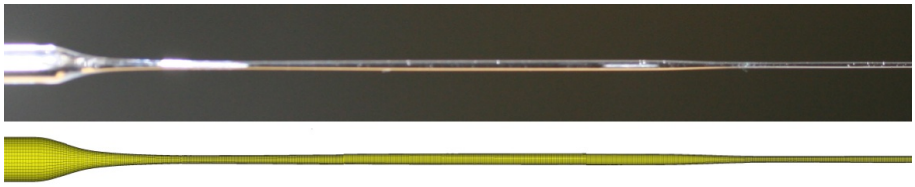

Figure 4.3: dumbbell profile of fused silica fiber: it is reported the picture and the finite-element model.

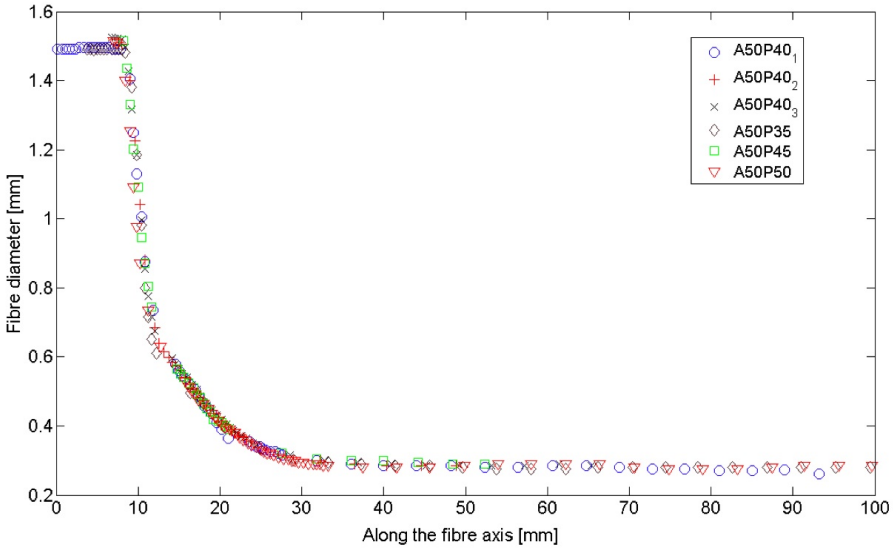

Figure 4.4: profiles of six different fibers measured by a profiling tool with $10\mu m$ precision.

$10\mu m$) and to shape the region where the diameter varies from the bar to the fiber value (neck). This result is shown in fig. 4.4, where the profiles of six fused silica fibers are measured with a profiling tool and then compared.

4.1.2 The clamping system

Virgo+ clamping system has been designed to minimize and distribute in the best way the stresses due to the suspensions (see fig. 4.5).

The upper part of the fused silica rod is welded to a fused silica cone (see fig. 4.6), while the lower part is welded to a $1.5mm$ fused silica bar, called "anchor" (see fig. 4.7).

The upper clamp is formed by two steel parts, fastened one inside the other: the inner one hosts the fused silica cone and can slide in the second external one allowing us to adjust the vertical position of the fiber on the marionette. This adjustment is useful to set up the silica wire tensions and to position the fiber bending point on the horizontal plane passing through the centre of mass of the marionette. With this tool is possible to choose the vertical position of the upper clamp within a range of $5mm$

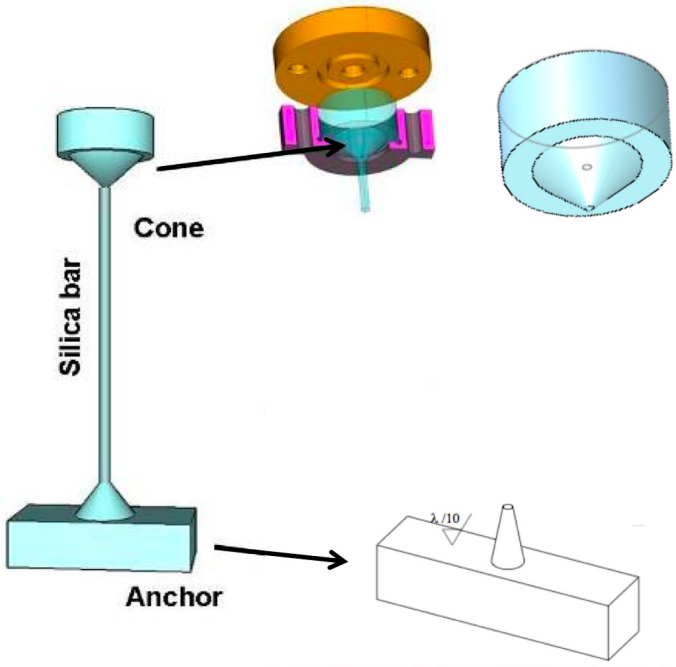

Figure 4.5: schematic design of the fused silica fiber with the upper (cone) and lower (anchor) clamp: their technical designs are reported.

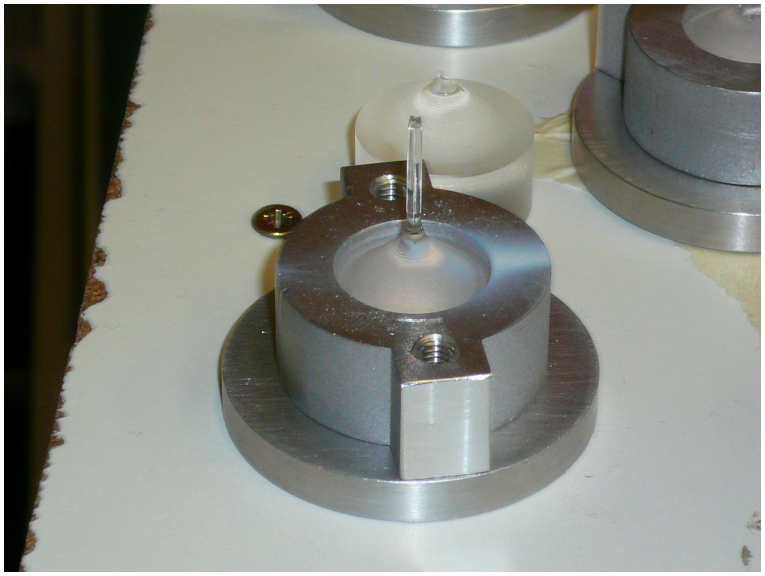

Figure 4.6: a fused silica cone and its steel box used for the fiber clamping on the marionette.

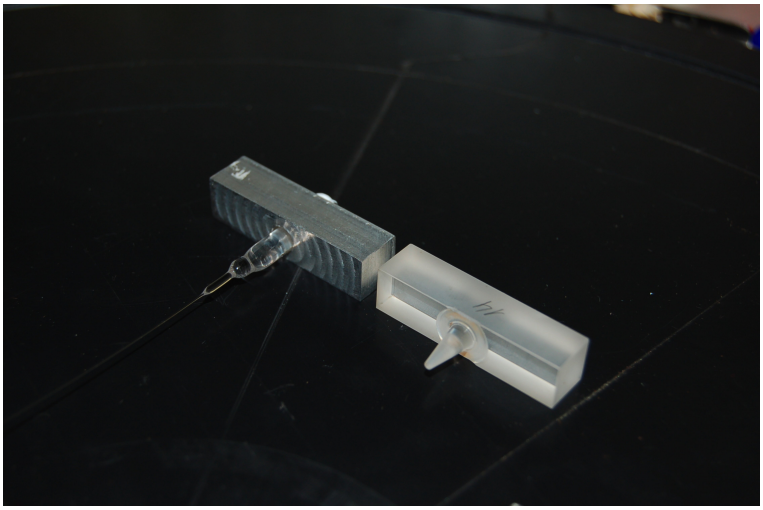

Figure 4.7: a fused silica anchor compared with a dummy steel one, used in the test facility.

and to control also the mirror tilt position. Once the position is set up, the clamp is blocked tightly on the marionette. The two steel boxes are shown in fig. 4.8, where the setting screws are clearly visible.

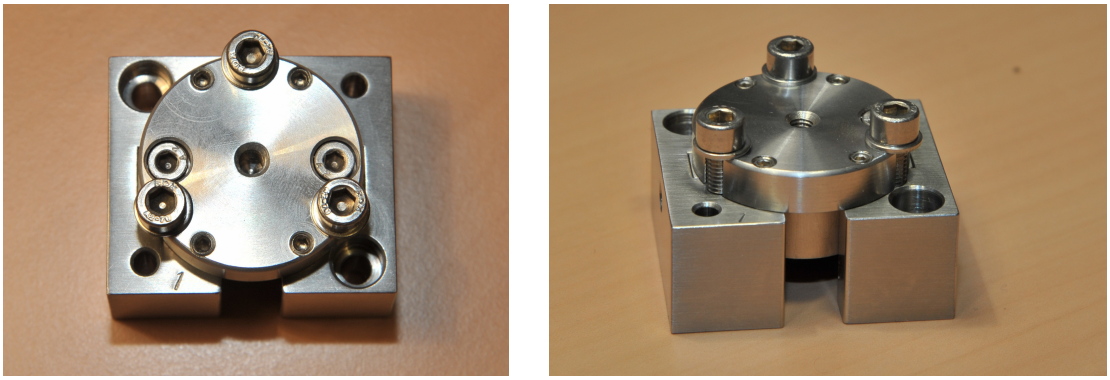

Figure 4.8: the two parts of the upper clamp fastened one inside the other: the regulation screws are well visible.

The anchors are necessary to attach the fiber to the mirror through elements called ears (see fig. 4.9): those are glued to a $\lambda/10$-polished lateral flat surfaces of the mirror through the *silicate bonding* technique [127, 128].

The *silicate bonding* is a chemical gluing referred to as hydroxide-catalyzed hydration-dehydration process; it is typically used for joining oxide materials. The bonding is realized with a strong, rigid, very thin layer of oxide settled among two surfaces with high flatness (that is, flat within $\lambda/10$ where $\lambda = 633nm$). A drop of aqueous hydroxide solution such as KOH or $NaOH$ is deposited among the surfaces; a silicate gel is formed, that solidifies over time.

Mechanical characteristics of silicate bonding have been measured in many experiments. The silica bonding layer obtained with the described method is usually

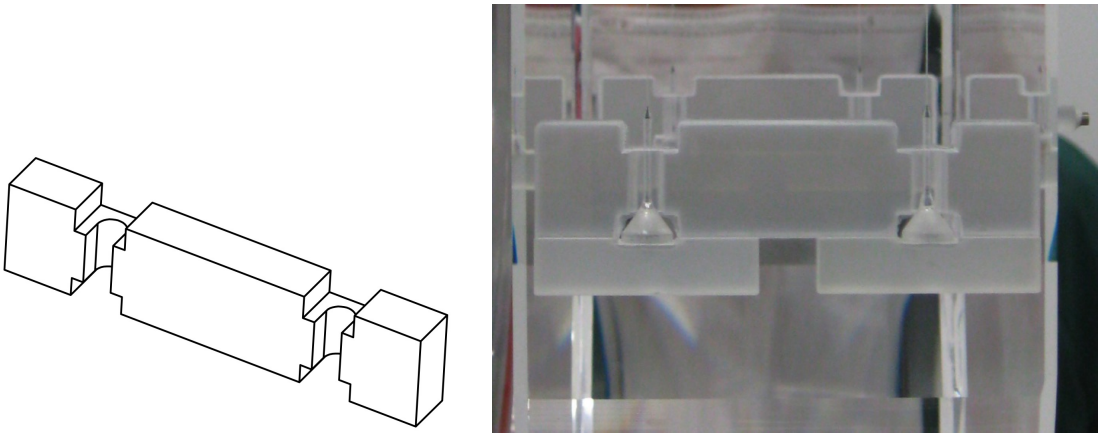

(a) ear technical project (b) ear attached to the mirror

Figure 4.9: fused silica ear design and realization: in the right it is clearly visible the ear attached at the lateral flat of the mirror.

about $100nm$ thick [129, 130].

Quality factors of mirrors and fused silica masses with silicate bonded silica ears have been evaluated, showing that the bonding should not spoil the overall performances [131, 132]. Nonetheless, estimations of intrinsic loss angle of the bonding materials give values around 10^{-1} [129]; this high level of dissipation suggests that the bonding material is substantially different with respect to well-formed glass or silica. The silicate bonding layer can be thought as forming a very imperfect glass with many vacancies, dislocations and incomplete bonds.

The anchors are fixed to the ears with a particular silicate bonding technique called *water glass*. In this method the used chemical mixture is enriched with silicate compounds ($Na_2Si_3O_7$) to speed up the drying time. With this technique the average bond thickness and the average breaking stress are similar to those yielded by silicate bonding, but there are peculiar features:

- the possibility to joint surfaces with $\lambda/4$ polishing;
- the possibility to joint surfaces of different materials (for example silica and alumina);
- a lower tensile strength to the junction, so that a recover procedure, in case of fiber failure, is possible.

The lower clamping system of the mirror is reported in fig. 4.10.

4.1.3 The monolithic payload

The monolithic payload is composed by the marionette, the reaction mass and the mirror (see also sec. 2.3.5).

The monolithic suspension marionette is designed (see figs. 4.11 and 4.12):

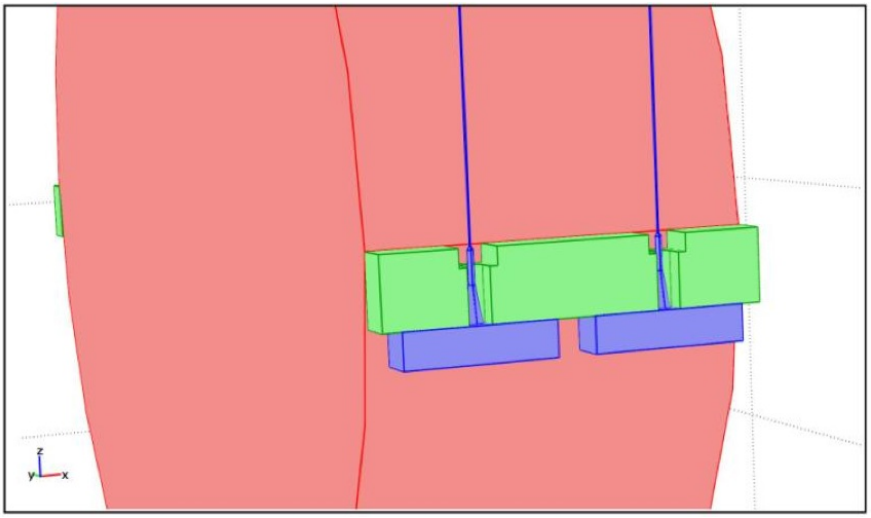

Figure 4.10: design of the lower clamping system on the lateral flat of the mirror: the mirror is in red, fibers with anchors in blue and the ear is in green.

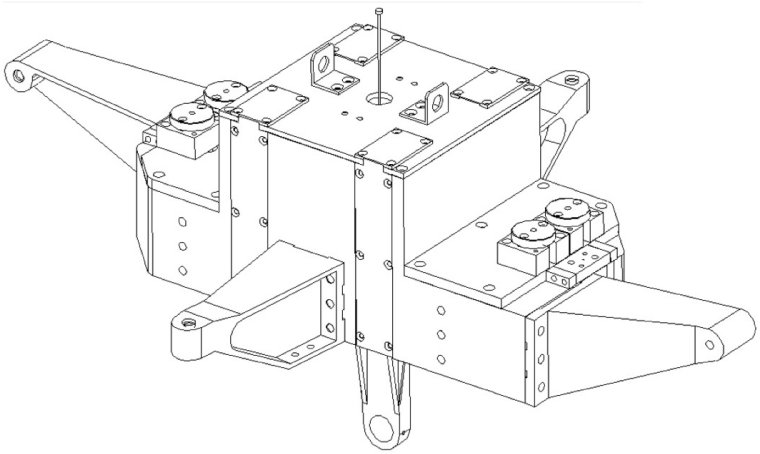

Figure 4.11: technical design of the marionette for the monolithic suspensions.

- to minimize the contact risk for the fused silica fibers with other mechanical parts, making four lateral cuts used to insert the silica fibers to position them at the required distance in suspending the mirror;

- to place correctly the fused silica fibers, so that the bending point of the fibers correspond to the centre of mass plane of the marionette; that is assured using the upper clamps.

Furthermore, the marionette houses a stepper motor: it is necessary for the correct balancing of the payload during the mounting procedure. In fact, the stepper motor is constituted by a large mass which can be moved longitudinally to correct possible payload misalignment.

As described in sec. 2.3.5, the reaction mass is necessary to protect the mirror from falling of fibers break and it is fundamental in the mounting procedure: it works

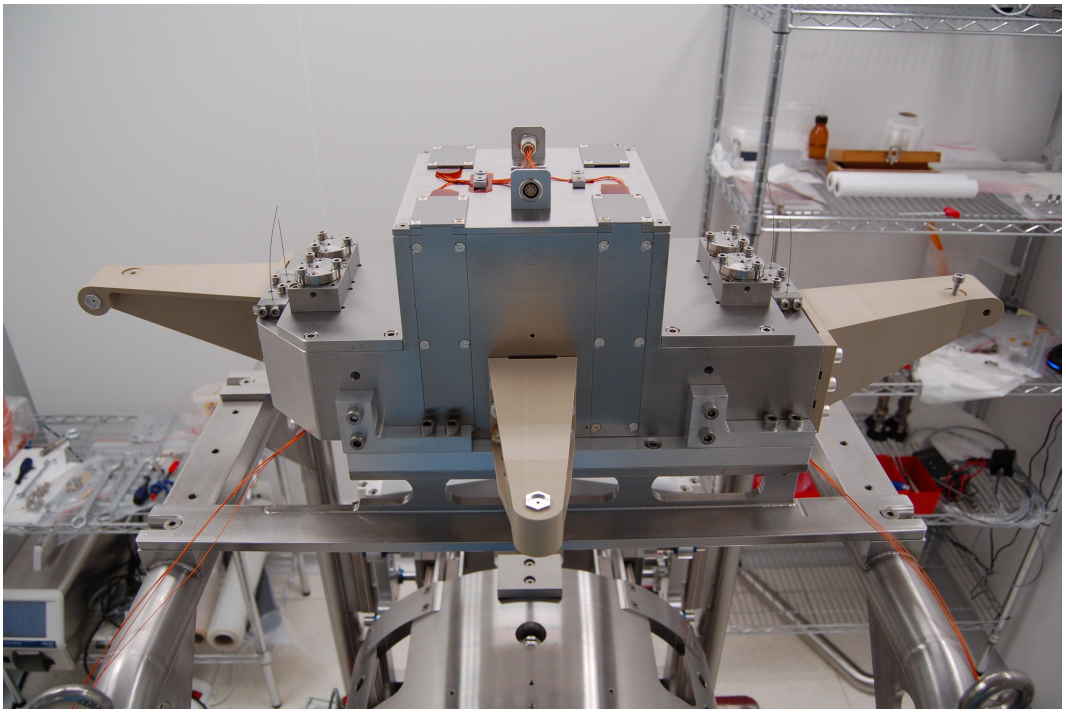

Figure 4.12: monolithic suspension marionette: note the upper clamping system.

as an inner safety structure for the mirror. Since Virgo sensitivity was affected by the eddy currents noise, for the reaction mass a new dielectric material (Tecapeek) is used. Because of that, any conductive material in proximity of the mirror magnets is avoided.

To ensure a feasible resistance of the whole structure the inner part of the reaction mass is made up of steel. In addition the reaction mass houses the actuation coils (see fig. 4.13).

In fig. 4.14 it is shown the monolithic payload mounted in the North-Input tower.

4.2 Quality factor measurement procedure

To excite and study the mechanical resonances of the payloads, I used the global control and the local control systems, depending on the frequency band I was interested in. I performed three measurement campaigns in different frequency intervals (see also tab. 4.2):

0 – 20Hz: lower frequency suspension resonances

In this band there are the pendulum mode ($0.6Hz$), the vertical modes of the mirror and the reaction mass ($\sim 6Hz$ and $\sim 15Hz$) and the roll modes ($\sim 8Hz$ and $\sim 20Hz$). To excite these modes I used two methods:

- for the pendulum mode it was sufficient to send white noise to the reaction mass coils of each payload for few minutes. The interferometer was not locked and the excitation was well visible in the local control optical levers,

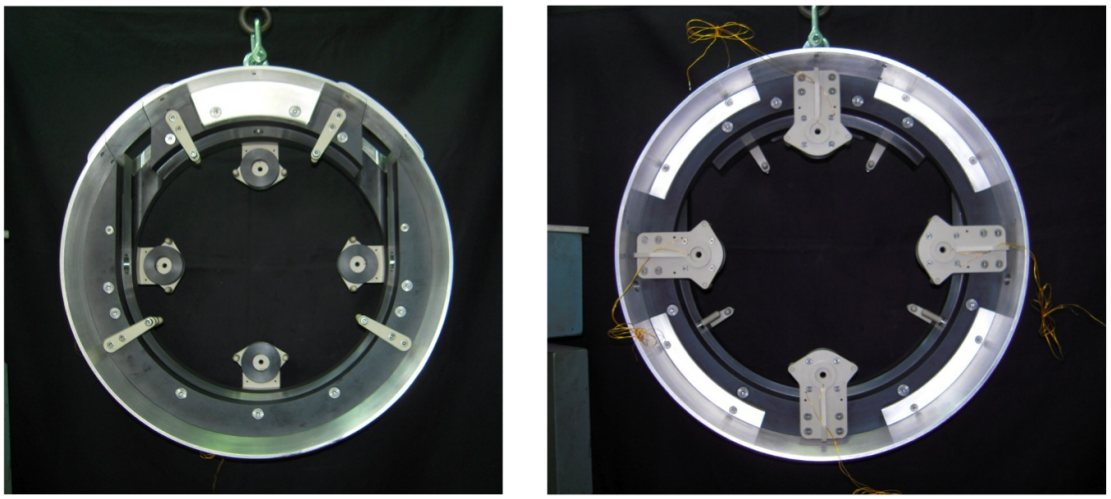

(a) reaction mass front (b) reaction mass back

Figure 4.13: reaction mass for monolithic paylod: note the four coils of the actuation system.

where the longitudinal z-degree of freedom signal is monitored with a dedicated photodiode;

- for the vertical and roll modes I used the balancing stepper motor present inside the marionette; moving the inner mass of the motor by one step, the marionette balance does not change, but it produces a small kick, sufficient to excite those resonance modes. The excitation was well visible in the dark fringe signal Pr_B1_ACp[1], since the interferometer did not lose the locked status.

20Hz – 10kHz: fiber and lower frequency mirror bulk resonances

In this band there are the violin modes of the fused silica fibers (multiples of $\sim 450Hz$) and the first internal modes of the mirror bulk (from $\sim 4kHz$).

Each fiber has two splitted polarized vibrational violin frequencies, along z and x directions, caused by a small ellipticity of the fiber, due to an asymmetry of the wire clamping system. So, in a monolithic payload there are four fused silica fibers, that means eight violin resonances for each violin order multiple.

In total, I expect 32 violin resonances in a given order, even if the two splitted frequencies are not always distinguishable, in particular for the high order modes.

To excite the violin modes and the bulk modes, I applied the same technique used for the vertical modes, moving the balancing motor by one step. The interferometer remained locked and the result was visible in the dark fringe signal.

[1]This channel is the interferometer in-phase output. Since the power coming from the interferometer is too high for a unique photodiode, the output signal is splitted in two parts, to be read by two different photodiodes, whose channels are called Pr_B1_d2_ACp and Pr_B1_d3_ACp. These channels are sampled at $20kHz$ and $80kHz$, while their addition Pr_B1_ACp is sampled at $20kHz$.

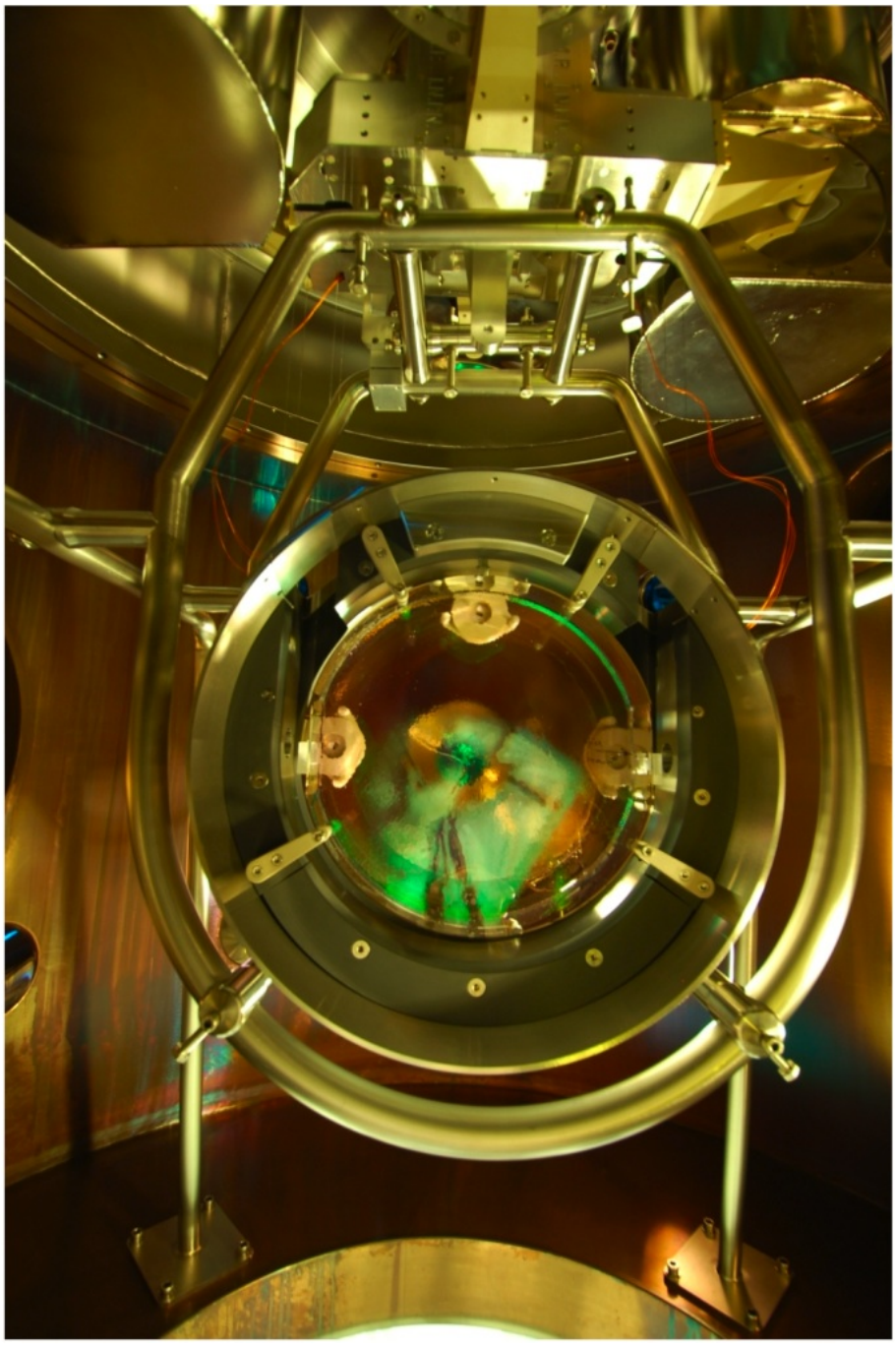

Figure 4.14: North-Input monolithic payload, the first mounted for Virgo+: the mirror, the reaction mass, the marionette, the actuation system colis and the safety structure are visible.

modes	excitation method	channel	sample rate
pendulum	white noise to the reaction mass coils	Gx_NI_z Gx_NI_x	$50Hz$ $50Hz$
vertical	kick with the balancing stepper motor of the marionette	Pr_B1_ACp	$20kHz$
violin	kick with the balancing stepper motor of the marionette	Pr_B1_ACp	$20kHz$
low frequency bulk	kick with the balancing stepper motor of the marionette	Pr_B1_ACp	$20kHz$
high frequency bulk	white noise to the reaction mass coils	Pr_B1_d2_ACp	$80kHz$

Table 4.2: summary of the measurement methods for the different campaigns: note that for the pendulum mode I write only the North-Input channel, for simplicity, but for each tower I took the corresponding channels.

10 – 25kHz: higher frequency mirror bulk modes

In this band the violin modes are no more recognizable (they have too small amplitudes to be measured), while the higher frequency mirror bulk modes are still present.

To excite these modes, I injected a band-limited white noise between $5kHz$ and $25kHz$ to the reaction mass coils of each payload. In order to do a preliminary resonance identification, I gave two excitations using different coil configurations (at first I used the Up-Down coils and then the Left-Right ones). The excitations were visible in the dark fringe, measured with a special photodiode channel (Pr_B1_d2_ACp) sampled at $80kHz$.

In tab. 4.3 I report the GPS start time and the good-data duration for each tower. In fact, after noise injections, the interferometer often unlocked or the noise level became too high, so I had to select only the good data.

The mechanical resonances were identified by looking at the risen lines of the signal spectrum before and after the excitation, as shown in figs. 4.15 and 4.16.

4.3 The line identification problem

In order to quantify correctly the thermal noise contributions (see sec. 3.5), it is mandatory to associate the collected resonance frequencies of each payload with their correlated mechanical modes.

In particular, we have to distinguish between the violin modes and the bulk modes, which often fall into the same frequency regions, causing a certain confusion.

In fig. 4.17 the West-Input spectra in the frequency region where the drum mode is foreseen to be: the quiet spectrum (in red) is compared to the spectrum after excitation (in black). In that region there are at least seven excited peaks given by the XIII order of the violin modes which falls in the same frequency region.

modes	tower	GPS start	duration (s)
pendulum	NI	973036815	$36 \cdot 3600$
pendulum	WI	973036815	$33 \cdot 3600$
pendulum	NE	973036815	$36 \cdot 3600$
pendulum	WE	973036815	$36 \cdot 3600$
vertical/violin/low bulk	NI	972756817	1200
	NI	972840335	1200
	NI	974229150	10800
vertical/violin/low bulk	WI	972758150	600
	WI	972841665	750
	WI	975190045	7200
vertical/violin/low bulk	NE	972758775	620
	NE	972844295	1380
	NE	975434895	4500
vertical/violin/low bulk	WE	972760265	400
	WE	972846515	1500
	WE	974147065	4500
high bulk	NI	992868647	3900
high bulk	WI	992945535	3400
high bulk	NE	994674222	7800
high bulk	WE	994080371	3900

Table 4.3: GPS start time and good-data duration after the excitation of the payload resonances: note that for the vertical/violin/low bulk modes I had three different measurements.

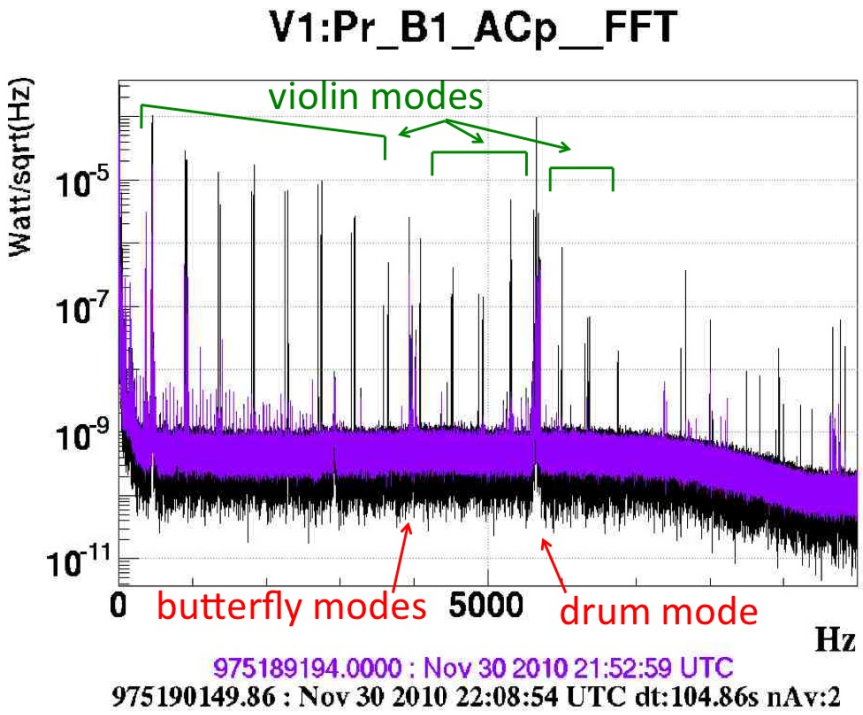

Figure 4.15: comparison between the quiet spectrum (in purple) and the spectrum after the excitation (in black) of the West-Input payload; I report the violin modes frequency regions (in green) and the bulk modes frequency regions (in red).

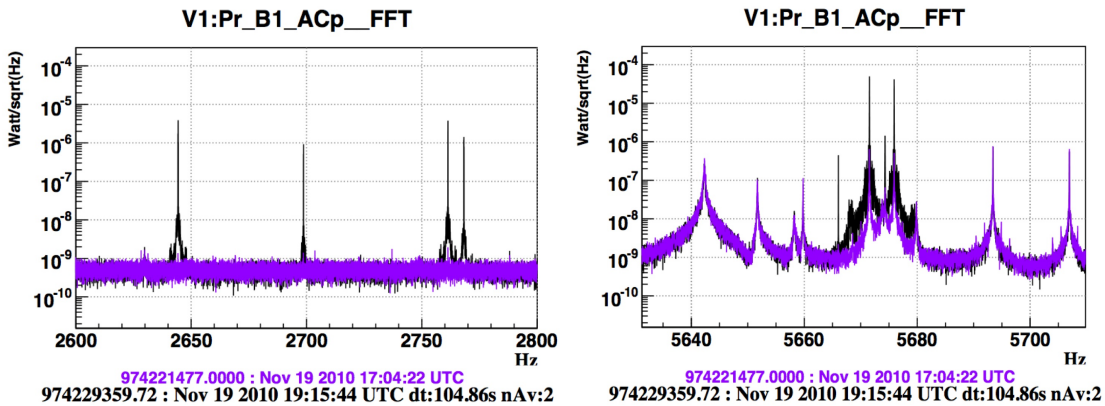

(a) NI VI order violin region

(b) NI drum bulk region

Figure 4.16: measurements of the violin modes and drum bulk mode of the North-Input payload: spectrum before excitation (in purple) and after excitation (in black).

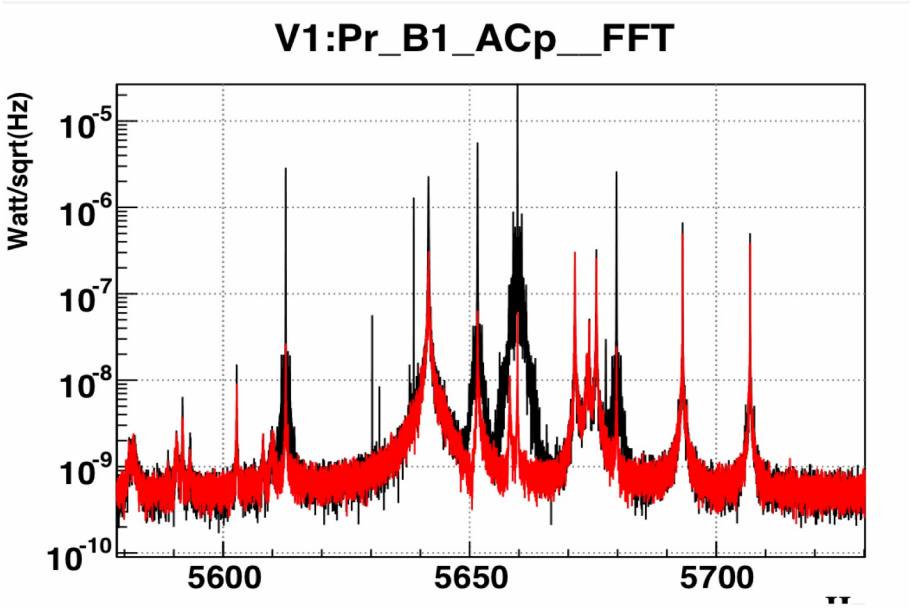

Figure 4.17: spectra of the West-Input payload in the drum frequency region: the quiet spectrum is in red, while the spectrum after excitation is in black.

The main difficulty in distinguishing the violin lines from the bulk modes is that violin frequencies lose their regularity at higher order, due to anharmonicity effects.

Violin mode frequency is expressed by eq. 3.54:

$$f_n = \frac{n}{2L}\sqrt{\frac{\mathcal{T}}{\rho_{lin}}}\left[1 + \frac{2}{k_e L} + \frac{1}{2}\left(\frac{n\pi}{k_e L}\right)^2\right] \tag{4.1}$$

where n is the violin order, ρ_{lin} is the linear mass density of the wire, L its length, k_e is the elastic stiffness and $\mathcal{T}$ the applied tension.

Each suspended fiber has its own length and applied tension: so, there are slightly different fundamental frequency, even in the same payload. These differences are enhanced in higher order modes, thanks to anharmonicity effects. Moreover, after the first bulk mode (the butterfly "×" at $\sim 3950Hz$) the mirror starts to quiver at its own internal resonances, causing a change in the coupling between the fused silica fibers and the mirror: the boundary conditions used for violin mode calculation are no more valid and some peaks in the high frequency harmonics could disappear.

In fig. 4.18(a) and fig. 4.18(b) I show the West-End violins for the II and the IV order, respectively: the harmonic shape is clearly recognizable. On the contrary, in fig. 4.18(c), there are only three visible peaks.

For these reasons, the method I used to distinguish the violin peaks from the bulk modes was their temperature dependence of the frequency.

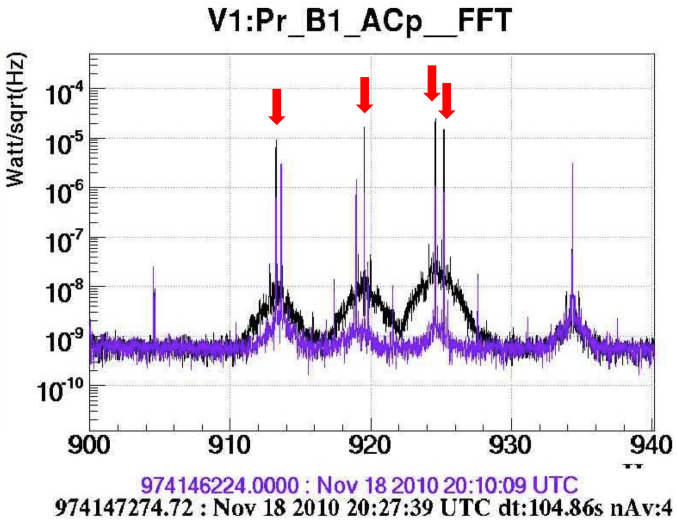

(a) WE II order violin region

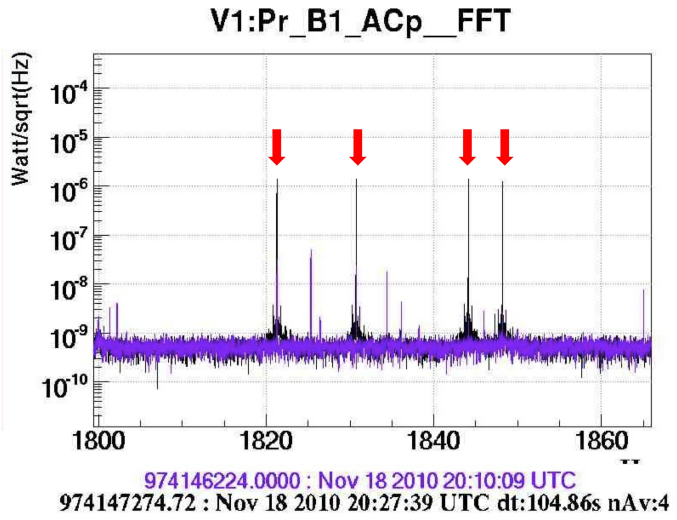

(b) WE IV order violin region

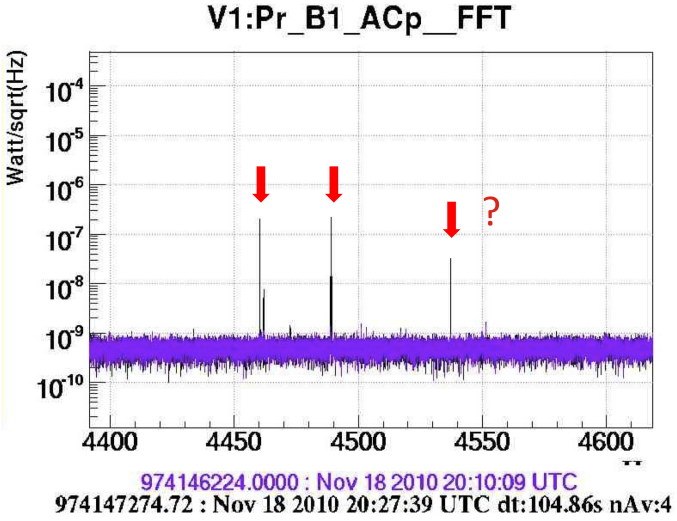

(c) WE X order violin region

Figure 4.18: West-End spectra of three violin-frequency regions: in purple the spectrum before excitation, in black the spectrum after and indicated with red arrows the violin resonances.

coefficient	mode (0,2)	mode (1,0)	mode (0,3)
$\alpha \cdot 10^{-9}(Hz/\sqrt{N})$	1.37	1.88	3.05
A	0.886	0.241	0.841
B	0.0415	0.806	0.0345

Table 4.4: coefficients A_{lm}, B_{lm} and α_{lm} for the Virgo mirrors first three internal modes (the two-nodal-line butterflies, the first drum and the three-nodal-line butterflies).

4.3.1 Temperature-dependence method definition

For what concerns the **bulk modes**, their frequency can be found from the elasticity theory in the cases of the circular shell and the cylindric bars [134, 135] and then estimated with a finite element analysis:

$$f_{bulk} = \frac{\alpha_{lm}\sqrt{E}}{\sqrt{A_{lm}\sigma + 1}\sqrt{B_{lm}\sigma + 1}} \tag{4.2}$$

where the suffix lm indicates the different bulk modes (l specifies the number of nodal diameter, m the number of the nodal circumferences), E is the Young's modulus, σ is the Poisson ratio, A_{lm} and B_{lm} are form factors depending on the mode type and α_{lm} depends on the mode type and on the mirror thickness.

To have an idea of the order of magnitude of the form factors A_{lm} and B_{lm}, and of the coefficient α_{lm}, see the tab. 4.4 [138].

Eq. 4.2 depends on temperature through the Young's modulus E and the Poisson ratio σ. Their dependence with respect to temperature can be approximated as:

$$E = E_0\, e^{\beta T} \tag{4.3}$$
$$\sigma = \sigma_0\, e^{\gamma T} \tag{4.4}$$

where β and γ are the temperature coefficients and T is the temperature .

After substituting eq. 4.3 and eq. 4.4 in eq. 4.2, I approximate it at the first order in temperature changes; it is convenient to write it in terms of the ratio $R = [f(T) - f(T_0)]/f(T_0)$:

$$R = \frac{f(T) - f(T_0)}{f(T_0)} = \frac{f'(T_0)}{f(T_0)}\Delta T \tag{4.5}$$

where $\Delta T = T - T_0$.

After a bit of algebra, computing $f'(T_0)$, the ratio R for the bulk modes becomes:

$$R_{bulk} = \left[\frac{\beta}{2} - \frac{A_{lm} + B_{lm} + 2A_{lm}B_{lm}\sigma_0}{2(A_{lm}\sigma_0 + 1)(B_{lm}\sigma_0 + 1)}\gamma\sigma_0\right](T - T_0) \equiv \lambda_{bulk}(T - T_0) \tag{4.6}$$

where σ_0 is the Poisson ratio at the reference temperature T_0 and λ_{bulk} is here defined.

The first term is correlated with the Young's modulus temperature dependence: if we consider only its temperature dependence, we will find only that term. Instead, the second term depends on the mode form and on the temperature dependence γ of the Poisson ratio, which is comparable to β and of the same sign [139].

mode	$\lambda_{bulk} \cdot 10^{-4}(1/K)$
butterfly (0,2)	0.866
drum (1,0)	0.844
butterfly (0,3)	0.873

Table 4.5: values of the λ_{bulk} coefficients defined in eq. 4.6.

The λ_{bulk} values of the first three internal modes of the mirror are presented in the tab. 4.5.

For what concerns the **violin modes**, considering also the anharmonicity terms, their frequency expression is [136, 137]:

$$f_{violin} = \frac{n}{2L}\sqrt{\frac{\mathcal{T}}{\rho_l in}}\left[1 + \frac{2}{k_e L} + \frac{(n\pi)^2}{2}\frac{1}{(k_e L)^2}\right] \tag{4.7}$$

where k_e is the flexural stiffness, equal to (see eq. 3.55):

$$k_e = \sqrt{\frac{\mathcal{T} + \sqrt{\mathcal{T}^2 + 4EI\rho_{lin}\omega^2}}{2EI}} \tag{4.8}$$

with I the wire cross section moment.

Note that eq. B.3 is an approximation of eq. 4.8: this approximation holds if $4EI\rho_{lin}\omega^2 \ll \mathcal{T}^2$. This is the case of the monolithic suspension: values of this term are reported in fig. 4.19 for the first ten harmonic violin orders. Since the applied tension for each wire is of order of $\mathcal{T} \sim 50N$, the square tension is $\mathcal{T}^2 \sim 2500N^2$: so we can drop the second term of the inner square root of eq. 4.8 ad use eq. B.3. In the next computations, I always use the expression B.3.

Eq. 4.7 depends on temperature through the Young's modulus E and the Poisson ratio σ, as the bulk modes; but, in addition, there is a dependence also through the wire length L and wire radius r:

$$\begin{aligned} L(T) &= L_0\left(1 + \alpha T + \frac{\mathcal{T}}{AE(T)}\right) \\ r(T) &= r_0\left(1 + \alpha T + \sigma(T)\frac{\mathcal{T}}{AE(T)}\right) \end{aligned}$$

where α is the linear expansion thermal coefficient, T is temperature, $\mathcal{T}$ is the applied tension and A is the wire cross section.

I repeat the same passages as done for the bulk modes to find the ratio R for the violin modes:

$$R_{violin} = \left[-\frac{1}{2}\left(\alpha - \frac{\mathcal{T}\beta}{AE_0}\right) + \frac{1}{D_v^n}\left(\alpha + \frac{\mathcal{T}\beta}{AE_0} + \frac{\beta}{2}\right)\right](T - T_0) \equiv \lambda_{violin}(T - T_0) \tag{4.9}$$

where λ_{violin} is here defined and D_v^n, called violin dilution factor, is:

$$\frac{1}{D_v^n} = \frac{2}{k_e L}\left[1 + \frac{(n\pi)^2}{2}\frac{1}{k_e L}\right] \tag{4.10}$$

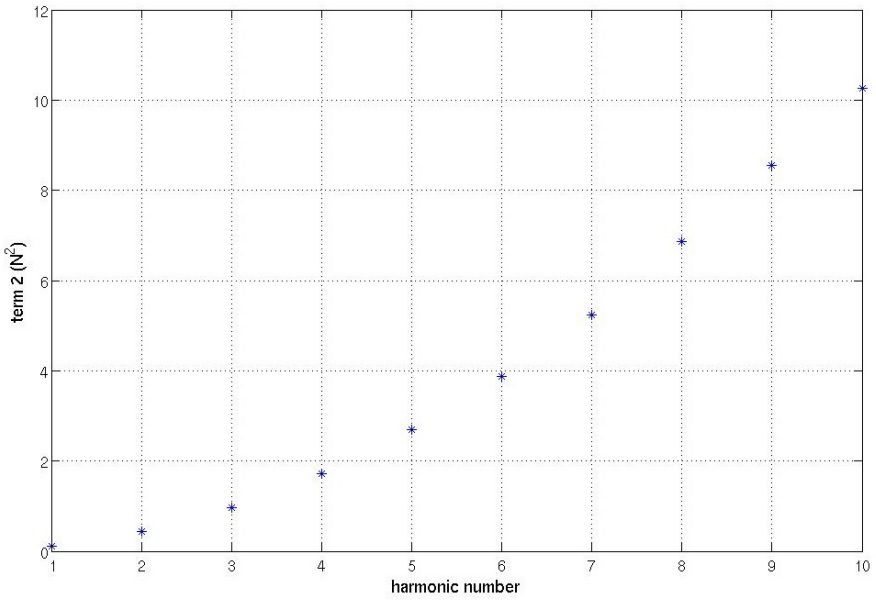

Figure 4.19: values of the second term of the inner square root of eq. 4.8 (term 2 $= 4EI\rho_{lin}\omega^2$) with respect to the harmonic number. For the monolithic suspension the applied tension for each wire is of order of $T \sim 50N$, so $T^2 \sim 2500N^2$.

The dilution factor is closely related to the anharmonicity of the mode frequencies: in fact the dissipation in the fiber is almost entirely due to the bending and not due to the work done against tension (see also sec. 3.5.1).

The values of the first ten violin mode coefficients λ_{violin} of the fused silica fibers are presented in tab. 4.6. The temperature dependence is proportional to the square of the harmonic order number: the frequency change with temperature is more evident for the higher order violins.

A different estimation of the violin modes temperature dependence can be done considering the exact profile of the fused silica fibers. In that case, a finite element analysis is mandatory. That estimation is presented in fig. 4.20 [140], where the temperature derivative of the violin frequency $f'(T)$ is shown, instead of $\lambda = f'(T)/f(T)$, calculated in tab. 4.6.

To compare these two results, I take each value of the red curve on the plot in fig. 4.20 and divide it for its corresponding violin frequency: I obtain a coefficient $\lambda_{viol} = f'_n(T)/f_n(T)$ which is more than a factor 2 bigger than the coefficients in tab. 4.6. That implies the cylindrical-fiber approximation is too rough for a correct estimation of the violin behavior: it is better to consider the exact fiber neck profile.

Anyway, the coefficients λ_{violin}, independently from the method calculation, are two order of magnitude lower than the coefficients λ_{bulk} showed in tab. 4.5. That is enough for a correct distinction between violin and bulk modes.

The different behavior of the bulk modes from the violin modes, in terms of temperature is clearer computing the ratio:

$$\frac{R_{mode}(T)}{R_{butterfly}(T)} = \frac{\lambda_{mode}}{\lambda_{butterfly}} \tag{4.11}$$

mode	$\lambda_{violin} \cdot 10^{-5}(1/K)$
I violin	0.1040
II violin	0.1043
III violin	0.1047
IV violin	0.1054
V violin	0.1062
VI violin	0.1073
VII violin	0.1085
VIII violin	0.1099
IX violin	0.1115
X violin	0.1133

Table 4.6: values of the λ_{violin} coefficients defined in eq. 4.9.

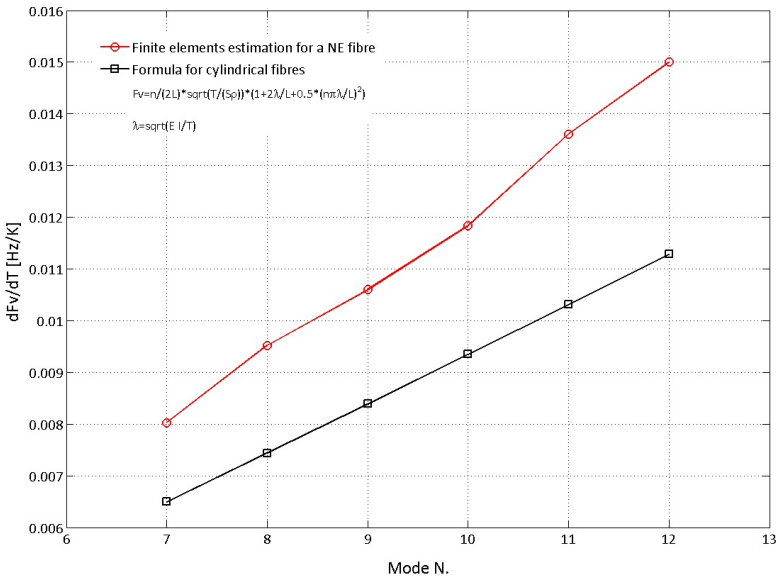

Figure 4.20: temperature dependence of the violin frequencies with respect to the violin harmonic mode n: in red the finite element estimation values, in black the values obtained with eq. 4.1.

where the subscript "*mode*" indicates a generic unidentified mode, while "*butterfly*" indicates the first butterfly mode of a fixed payload. I use the first butterfly mode for each payload as reference, since it is always well recognizable.

If the generic mode is:

- a violin mode:
$$\frac{R_{mode}(T)}{R_{butterfly}(T)} < 1$$
- a bulk mode:
$$\frac{R_{mode}(T)}{R_{butterfly}(T)} \sim 1$$

Since the coefficients λ_{bulk} and λ_{violin} do not depend on temperature T, those relation are valid for each temperature value.

4.3.2 Temperature-dependence method application

The practical application of the theory exposed in the previous section is to follow how a peak frequency changes on a long time scale to compute the temperature correlation, as expressed in eq. 4.6 and eq. 4.9.

To follow the line frequency changes with respect to time (and then temperature), I used a tool developed for the noise analysis and the continuous gravitational waves analysis, called NoEMI [141, 142].

This Python script analyzes the Virgo data to find all persistent lines:

- the Virgo data are divided in chunks, on which the Fourier transforms are computed;
- for each frequency bin, NoEMI computes the critical ratio *CR*, a parameter used to identify a peak; this parameter is defined as the ratio between the FFT value in that bin and the FFT value in the near bins (so, it is possible to evaluate the background);
- if a FFT bin has a *CR* value larger than a certain fixed CR_{min}, it is recognized as a peak;
- if the recognized peak is persistent, i.e. it is present in more than a fixed percentage of the total number of computed FFT in a time period, then the peak is identified as a line and it is written in a database.

I consulted the NoEMI database to find the lines I was interested in. The method procedure, performed on the VSR3 data, is the following:

- for each payload I selected all its resonance peaks present in NoEMI database, considering if there was any frequency variation with respect to time.
- I distinguished between:
    1. lines which did not change, as for example the first order violins (see fig. 4.21);

2. lines which presented a slow variation, as the high order violins (see fig. 4.22);
3. lines which presented a big variation, as the bulk modes (see fig. 4.23);

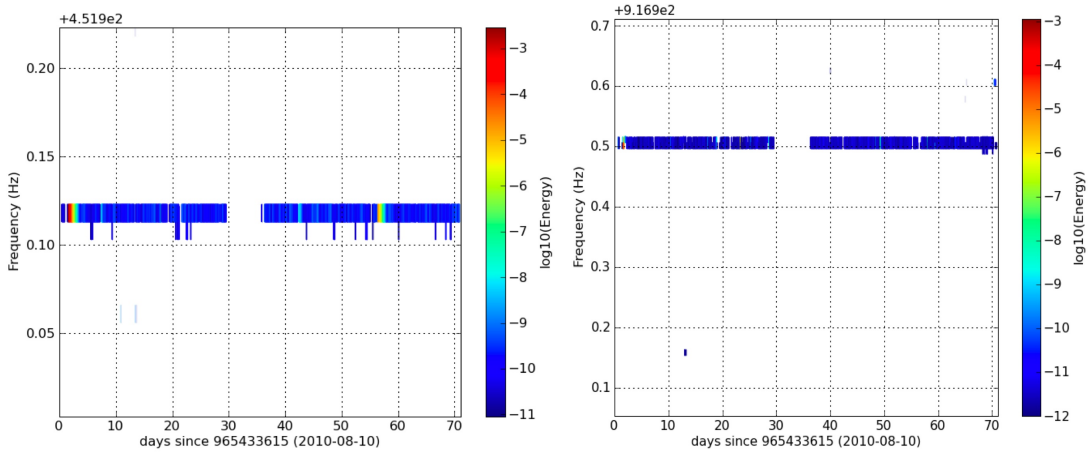

(a) WI I order violin mode

(b) WI II order violin mode

Figure 4.21: NoEMI plots of two West-Input low order violin lines: the line frequency with respect to time (days of the VSR3). Different colors points to different line energy, i.e. the integral of the line. Note the lack of data from day 30, due to a long period of not-science configuration of the interferometer.

- I took into consideration only those lines which showed a frequency variation and computed the ratio R_{mode} for each of them:

$$R_{mode} = \frac{f_{mode}(t) - f_{mode}(t_0)}{f_{mode}(t_0)} \tag{4.12}$$

  where $f(t)$ is the value of the resonance frequency at time t and I took the first day of Virgo Scientific Run 3 as t_0 value. Since temperature is a univocal function of time, eq. 4.12 and eq. 4.5 are equivalent.

- for each payload data set and for each peak resonance, I plotted the ratio R_{mode} (see eq. 4.12) with respect to the ratio $R_{butterfly}$, taken as reference.

  The expected slopes m_R of those lines are reported in tab. 4.7: those values have been found from considerations presented in sec. 4.3.1. In the same table I report also the order of magnitude of the measured slopes, found from linear fits of the data.

  In fig. 4.24 I show the results for the North-End payload: in green a violin mode is reported, in purple a butterfly mode and in red a drum mode. The different modes are well recognizable, since the angular coefficient gets different values, as reported in tab. 4.7.

  In fig. 4.25 I show the plots of the ratio R_{violin} with respect to the $R_{butterfly}$, for three violin harmonics (the XII, the XIII and the XIV orders). The angular coefficient m_R does not significantly change for different violin orders.

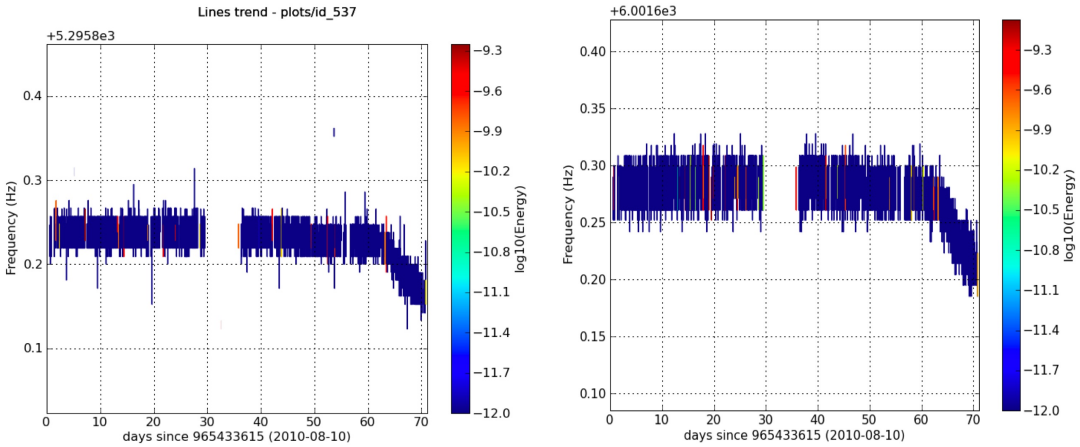

(a) WI XII order violin mode (b) WI XIV order violin mode

Figure 4.22: NoEMI plots of two West-Input high order violin lines: the line frequency with respect to time (days of the VSR3). Different colors points to different line energy, i.e. the integral of the line.

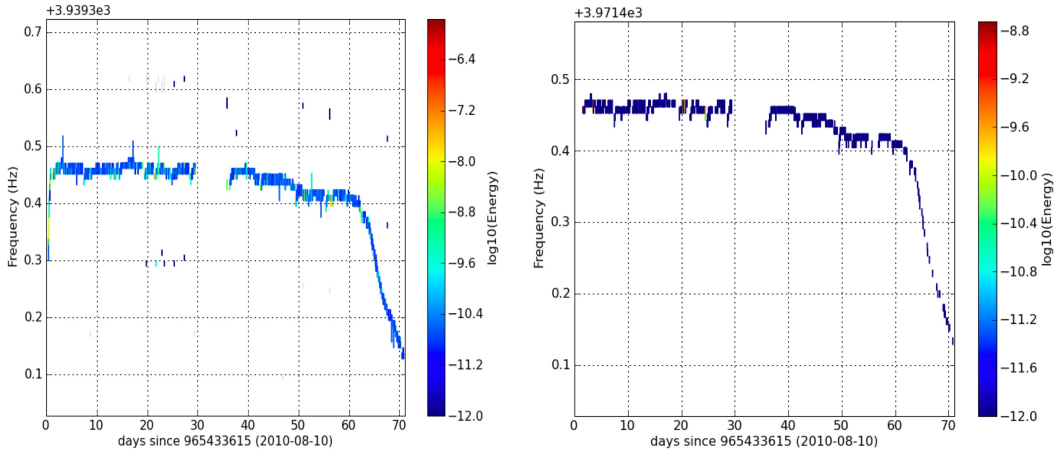

(a) WI butterfly "×" bulk mode (b) WI butterfly "+" bulk mode

Figure 4.23: NoEMI plots of two West-Input bulk lines: the line frequency with respect to time (days of the VSR3). Different colors points to different line energy, i.e. the integral of the line.

mode	$m_R^{expected}$	$m_R^{measured}$
violin	< 1	~ 0.20
butterfly	~ 1	~ 1
drum	> 1	~ 1.50

Table 4.7: slope m_R of the linear relation between the ratio R_{mode} for three different modes (violins, butterflies and drums) and the ratio $R_{butterfly}$ of the reference butterfly mode; in the table I report the expected values $m_R^{expected}$ and the order of magnitude of the measured slope $m_R^{measured}$. Those values are the same for all the four payloads and they have been used to distinguish the different temperature dependence.

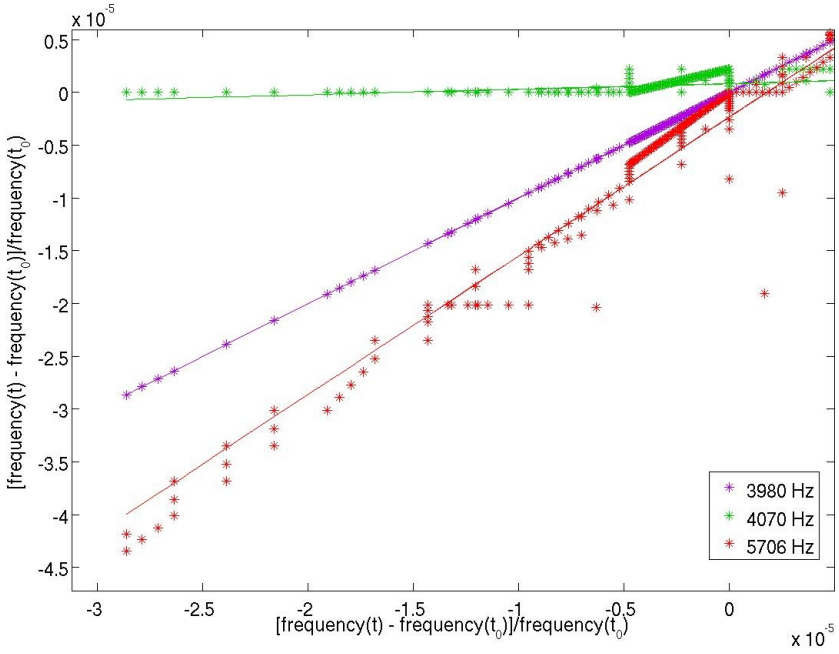

Figure 4.24: plot of the ratio R_{mode} with respect to $R_{butterfly}$ for the North-End internal modes: the violin mode ($4070Hz$) is in green, the first butterfly mode ($3980Hz$) in purple and the first drum mode ($5706Hz$) in red.

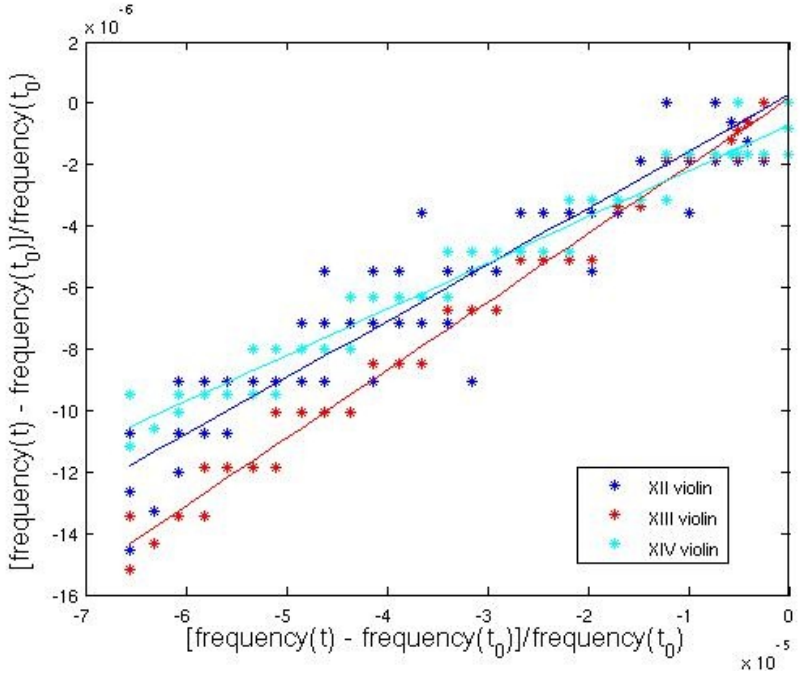

Figure 4.25: plot of the ratio R_{mode} with respect to $R_{butterfly}$ for the West-Input violin modes.

4.4 Temperature dependence of frequency

Finally, after the mode identification, I compared the frequency changes with the temperature data; each tower has temperature sensor in various positions:

- inside the lower part of the vacuum chamber, near the payload;
- inside the upper part of the vacuum chamber, along the superattenuator chain;
- just outside the vacuum chamber, in the tower bottom, where the local control systems are positioned.

In fig. 4.26 I show four different temperature channels of the West-Input tower during the VSR3.

Observing these temperature channels one can understand which is the most efficient heat transfer to the mirror:

- if the conductive process is dominant, the temperature channel to monitor should be the one connected to the superattenuator;
- if the irradiation/convection processes are dominant, the temperature channel to monitor should be the one connected to the bottom part of the tower.

Comparing fig. 4.26 with fig. 4.23, it is easy to understand that the most significant contribution on mirror temperature changes comes from irradiation processes.

It is important to evaluate if there is a time lag between temperature variation and frequency variations, to know how long it is the thermalization time of the payload. For that reason I compute the cross correlation $R_{cc}(t)$:

$$R_{cc}(t') = \int_{-\infty}^{\infty} f(t)T(t+t')dt$$

where $f(t)$ is the frequency value at time t, $T(t+t')$ is the temperature value at time $t+t'$ and t' is the time lag[2].

In fig. 4.27 I report the comparison between the North-End drum mode (1,0) frequency trend and the temperature data with respect to time during VSR3. The data are sampled with a period of $T_{step} = 7200s$, which corresponds to NoEMI sampling period. I subtracted mean values from the two data samples so that they are of the same order of magnitude: moreover this subtraction allows to see clearly the good data coincidence.

In fig. 4.28 I report the cross correlation between the drum mode frequency and the North-End temperature with respect to time lag. The maximum of the cross correlation is at $timelag = 0$. That implies there is a lag between the external temperature change and the mirror temperature change lower than the sampling period: the towers thermalize in less than about two hours.

So I can use the approximated expression of eq. 4.2, without any time translation:

$$f(T) = m_T T + q_T$$

[2]Since I use all physical quantities, which are real variables, I do not specify the complex conjugate transform $f^*(t)$ of the function $f(t)$.

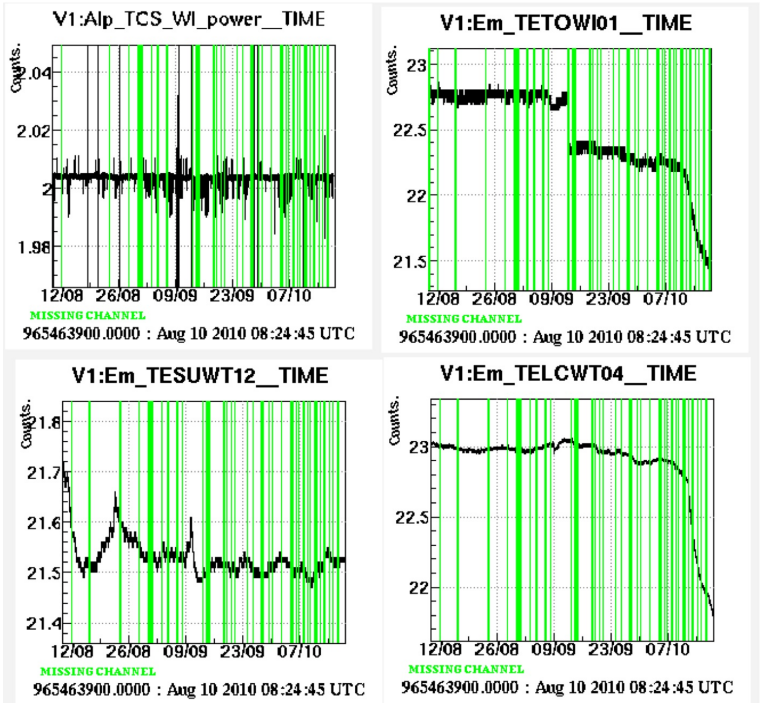

Figure 4.26: four West-Input temperature channels with respect to time during the VSR3: in the top-left corner there are the TCS laser power (this channel is necessary to check there wasn't a big change of laser irradiation on the mirror); in the top-right corner there are temperature data from the sensor inside the vacuum chamber, which is the nearest sensor to the mirror; in the bottom-left corner there are the data from the sensor on the superattenuator system; in the bottom-right corner there are the data from the outside sensor in the bottom part of the tower, where there is the local control system. The green lines on the plots represent the unlock periods of the interferometer.

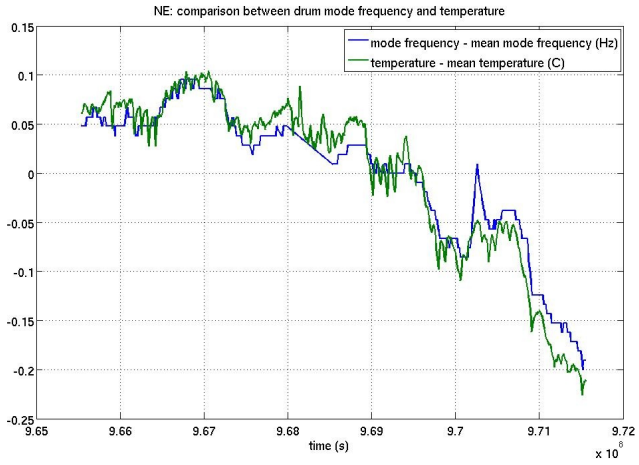

Figure 4.27: comparison between the North-End mirror drum mode frequency and temperature with respect to time during the VSR3: I subtract mean values from each of the two data samples.

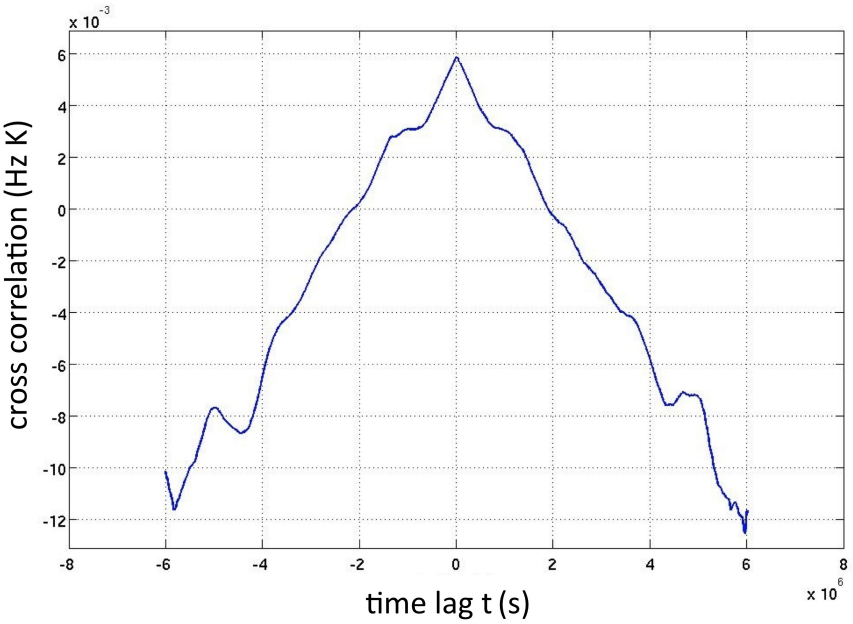

Figure 4.28: cross correlation between the North-End mirror drum mode frequency and temperature with respect to time lag: the maximum of the function is at $timelag = 0$.

where f is the mode frequency, T is temperature, m_T is the frequency slope and q_T is the intercept.

The expected values of the temperature slope m_T are reported in tab. 4.8; they are computed through a finite element simulation of the mirrors [143].

mode	temperature slope $m_T(1/K)$
butterfly (0,2) ×	0.37
butterfly (0,2) +	0.37
drum (1,0)	0.52
butterfly (0,3) |	0.70
butterfly (0,3) –	0.71

Table 4.8: expected temperature dependence of the main bulk modes: these values are found through a finite element simulation.

I plotted the violin and bulk frequency, taken from NoEMI database, with respect to temperature data. As example, I report the plots of the fit frequency versus temperature for the West-Input payload in fig. 4.29 (the butterfly × mode), in fig. 4.30 (the drum mode) and in fig. 4.31 (a XIII order violin mode).

Then, I computed the frequency slope m_T for the first two butterflies (0,2), the first drum (1,0) and the second two butterflies (0,3). The results are reported in tab. 4.9; in those tables I report also the mode frequencies during VSR3 and the measured ratio slope m_R, used for the identification (see tab. 4.7)

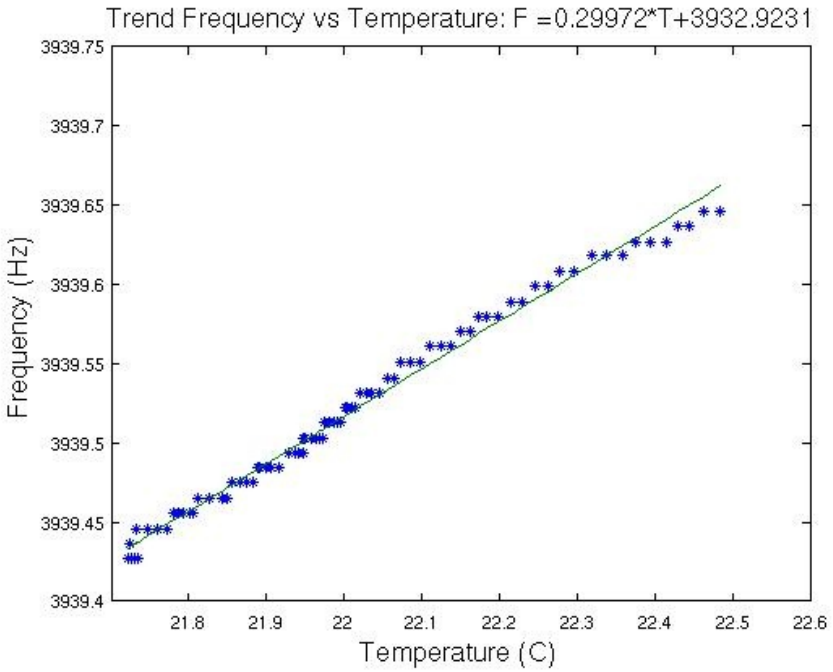

Figure 4.29: temperature dependence for the WI mirror butterfly $\times$ mode: the blue points are the experimental data, the green curve is the best fit: the values of the fit parameters are reported at the top of the figure.

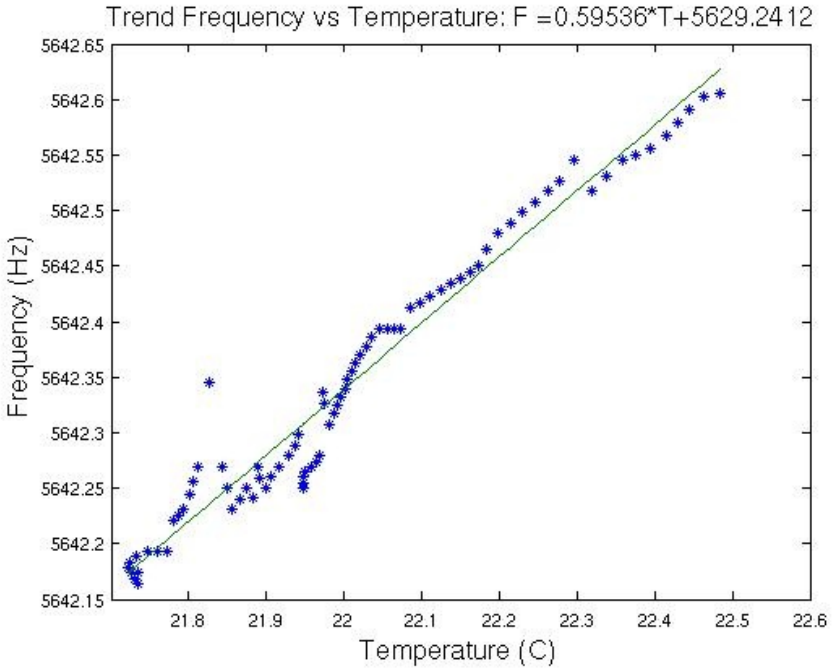

Figure 4.30: temperature dependence for the WI mirror drum mode: the blue points are the experimental data, the green curve is the best fit: the values of the fit parameters are reported at the top of the figure.

(a) North-Input mirror

mode	frequency f (Hz)	ratio slope m_R	temperature slope $m_T(Hz/K)$
butterfly × (0,2)	3964	1	0.2969
butterfly + (0,2)	3996	0.995	0.2991
coupled drum (1,0)	5671	0.566	0.2416
coupled drum (1,0)	5675	0.793	0.3354
butterfly | (0,3)	7710	1.005	0.6021
butterfly – (0,3)	7992	0.967	0.6078

(b) West-Input mirror

mode	frequency f (Hz)	ratio slope m_R	temperature slope $m_T(Hz/K)$
butterfly × (0,2)	3939	1	0.2997
butterfly + (0,2)	3971	1.005	0.3027
drum (1,0)	5642	1.502	0.5954
butterfly | (0,3)	7606	0.952	0.5535
butterfly – (0,3)	7674	1.014	0.5951

(c) North-End mirror

mode	frequency f (Hz)	ratio slope m_R	temperature slope $m_T(Hz/K)$
butterfly + (0,2)	3980	1	0.4015
butterfly × (0,2)	4025	0.952	0.3834
drum (1,0)	5706	1.427	0.8327
butterfly – (0,3)	7667	1.002	0.7736
butterfly | (0,3)	7761	1.015	0.7932

(d) West-End mirror

mode	frequency f (Hz)	ratio slope m_R	temperature slope $m_T(Hz/K)$
butterfly + (0,2)	3969	1	0.3795
butterfly × (0,2)	4014	0.998	0.3999
drum (1,0)	5693	1.386	0.7673
butterfly – (0,3)	7653	0.952	0.8166
butterfly | (0,3)	7745	0.973	0.8315

Table 4.9: measured temperature dependence of the main bulk modes. Note that for NI payload the drum mode is coupled with a violin mode, implying a mixing of temperature correlation coefficients (see sec. 4.6.3).

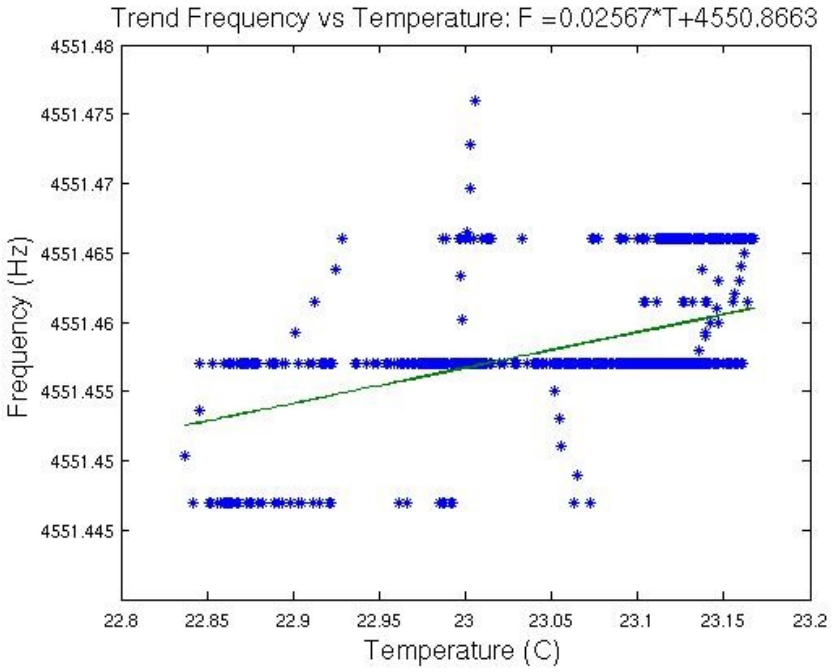

Figure 4.31: temperature dependence for one of the NE X harmonic violin mode: the blue points are the experimental data, the green curve is the best fit: the values of the fit parameters are reported at the top of the figure.

4.5 Quality factor analysis procedure

After the identification of the internal modes with the temperature dependence study, I proceeded to measure the quality factors in the following way:

1. for each payload and for each given resonance frequency f_0 I computed the spectrum immediately after the excitation ($time = 0$, the blue curve in fig. 4.32) to determine its peak amplitude. There are two parameters of the spectrum that must be chosen: the integration time t_{int}, which determines the data time interval to perform the Fast Fourier Transform (FFT) on and the average number n_{ave}, i.e the number of data samples[3] to take for each FFT (for more detail see sec. 4.7). The frequency resolution of the spectrum depends on these two parameters: so they are crucial to resolve correctly the resonance peak, not to confuse it with another near peak.

2. I measured the peak amplitude at the frequency f_0 with a rate depending on a time interval Δt_{meas}, determined by the final decay time, in a recursive way (see the red, the green and the light blue curves in fig. 4.32).

3. I evaluated the peak amplitudes until the peak was recognizable, that means until the signal/noise ratio is equal to 1; in that way I set a time interval T_{tot} in which the measurement made sense (see fig. 4.33).

[3]In general it is preferable to choose data samples with a superposition of 50% of the time window t_{int}: in that way we do not lose any datum at the window edges. In that case I chose the Hanning window.

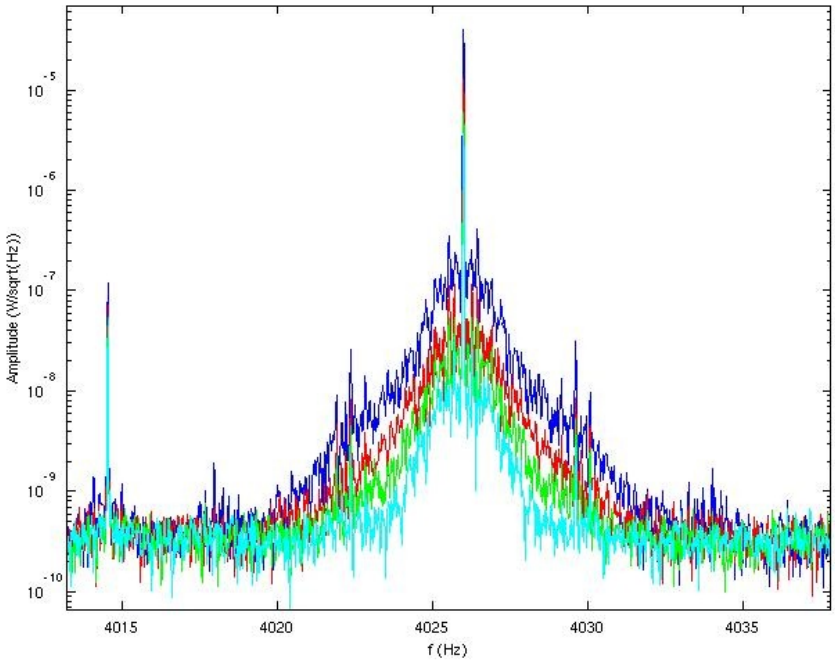

Figure 4.32: spectra of the North-End mirror butterfly + bulk mode resonance at different time, indicated in distinct colours.

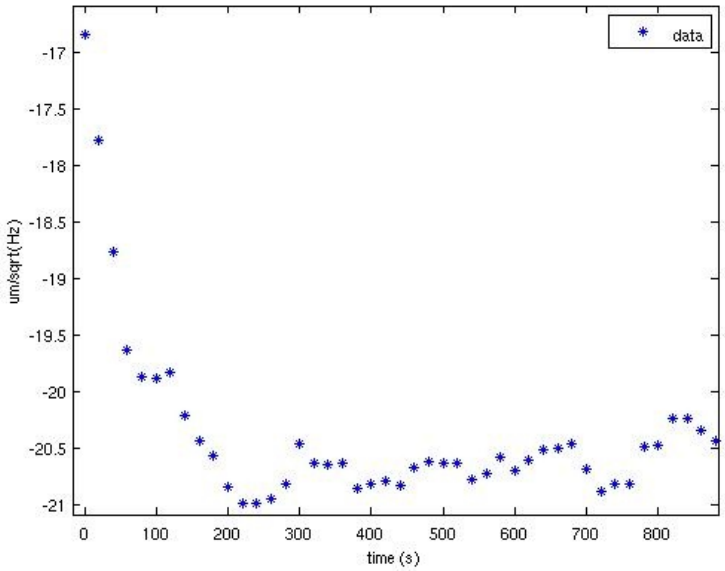

Figure 4.33: North-End mirror butterfly + bulk mode peak amplitudes at different times: it is evident the decaying trend until about $100s$ after the excitation; beyond that value, the peak is not more recognizable and it is confused with the noise level of the spectra.

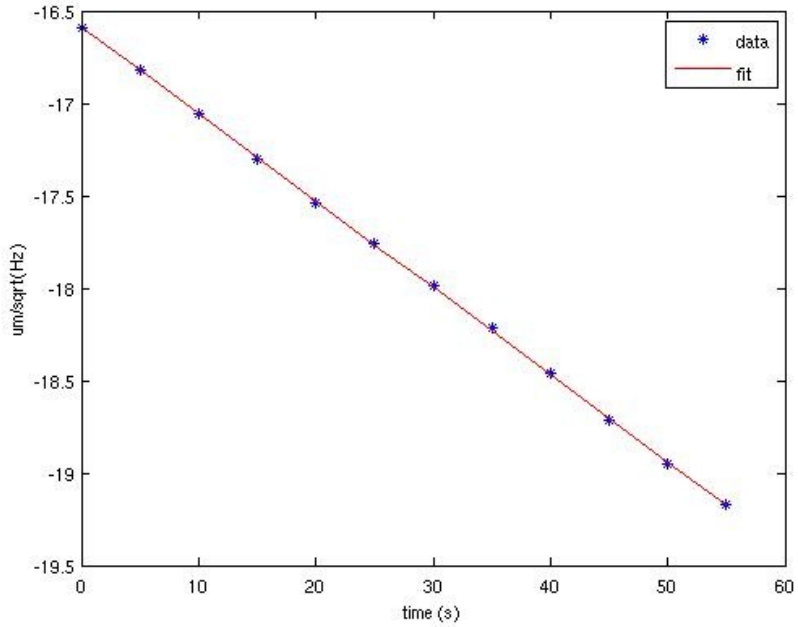

Figure 4.34: North-End mirror butterfly + bulk mode resonance decay: linear fit of the first 60s-data shown in fig. 4.33.

4. I performed an exponential[4] fit of the data from $time = 0$ to $time = T_{tot}$, with as much points as $T_{tot}/\Delta t_{meas}$ (see fig. 4.34). The fitting function is:

$$\begin{aligned} A(t) &= A_0 e^{-\frac{t}{\tau}} \\ &\Downarrow \\ \log A(t) &= -\frac{1}{\tau}t + \log A_0 \end{aligned} \tag{4.13}$$

where t is the independent variable time, $A(t)$ is the peak amplitude at time t, A_0 is the peak amplitude at $t = 0$ and τ is the decay time, connected to the quality factor through (see eq. 3.22):

$$Q = \pi f_0 \tau$$

where f_0 is the resonance frequency.

4.6 Experimental results

In next sections results for pendulum modes, violin modes and bulk modes measurements are reported. For violin modes and bulk modes, since their high number of points, I show plots of quality factors with respect to frequency.

The values of the quality factors for the monolithic suspensions are completely reported in appendix C: in those tables the name of the resonance, its frequency, its

[4]For sake of simplicity I fitted the logarithm of the data with a linear function.

		$\tau_P(s)$	$\omega_P(Hz)$	ϕ_P
NI	z	2.55 E+05	2.43 E-04	+0.42
	x	2.35 E+05	2.43 E-04	$\pi + 0.42$
WI	z	5.74 E+05	2.50 E-04	+0.40
	x	6.81 E+05	2.50 E-04	$\pi + 0.40$
NE	z	1.05 E+05	3.80 E-04	+0.42
	x	1.69 E+05	3.80 E-04	$\pi + 0.42$
WE	z	7.17 E+05	2.60 E-04	+0.60
	x	3.77 E+05	2.60 E-04	$\pi + 0.60$

Table 4.10: pendulum quality factors, beat frequency and phase lag of the beating between z and x degrees of freedom.

decay time τ, the decay time error σ_τ, the quality factor Q, the quality factor error σ_Q and the relative error ϵ_{rel} are reported. Few modes are labeled with a "?", since they have not been identified, even if they are well visible in dark fringe spectrum and in NoEMI database: probably some of them are internal resonances of the marionette or of the reaction mass.

The error on quality factors have been estimated as described in sec. 4.7.

4.6.1 Pendulum mode results

From the local control optical levers, a coupling between z and x degrees of freedom is visible. In fact the pendulum resonance at $0.59Hz$ belongs to both these degrees of freedom and it is well recognizable on two photodiode signals.

That implies the exponential decay of the pendulum peak amplitude is superimposed to a oscillating behavior: the two degrees of freedom continuously pass the energy each other.

I performed an exponential fit on the amplitude data $A(t)$ and then I superimposed also a sinusoidal function, to quantify the beat frequency ω_P and the phase lag ϕ_P between x and z degree of freedom:

$$A(t) = A_0 \cos(\omega_P t + \phi_P) e^{-\frac{t}{\tau_P}} \tag{4.14}$$

where A_0 is the peak amplitude at time t_0 and τ_P is the decay time, linked to the pendulum mode quality factor. The fit results for the pendulum mode are reported in tab. 4.10.

In fig. 4.35 I show the fit for the z pendulum mode of the North-Input payload, while in fig. 4.36 the West-End x pendulum mode is reported.

For all measured x pendulum modes, I noticed an asymmetry behavior of the peak amplitude, due to the saturation of local control photodiodes. So, experimental data and fitting curves do not have a complete correspondence, in particular for what concerns the amplitude A_0 of eq. 4.14. Anyway, that effect influences neither the Q measures, neither beat frequencies or phase lags.

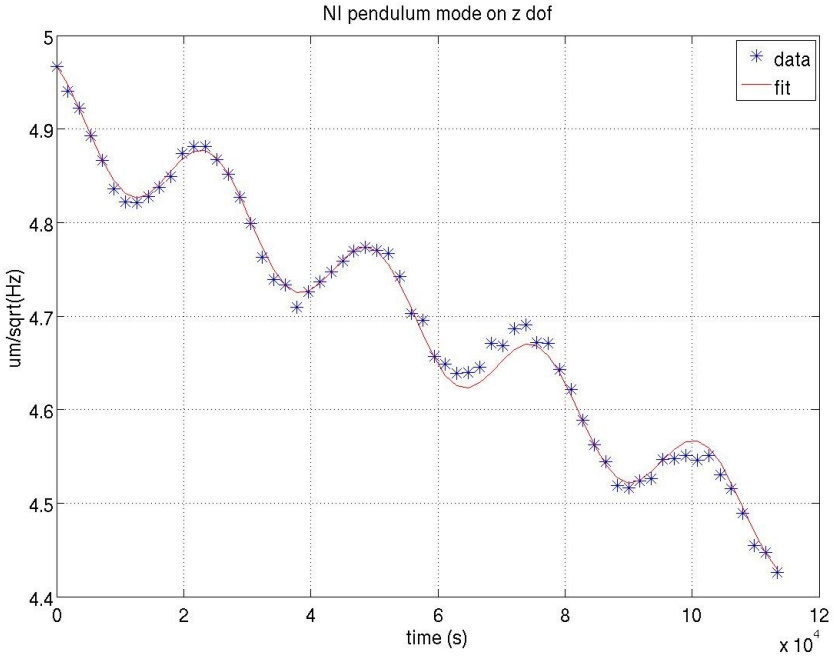

Figure 4.35: exponential-sinusoidal fit for the quality factor estimation of the North-Input z pendulum mode.

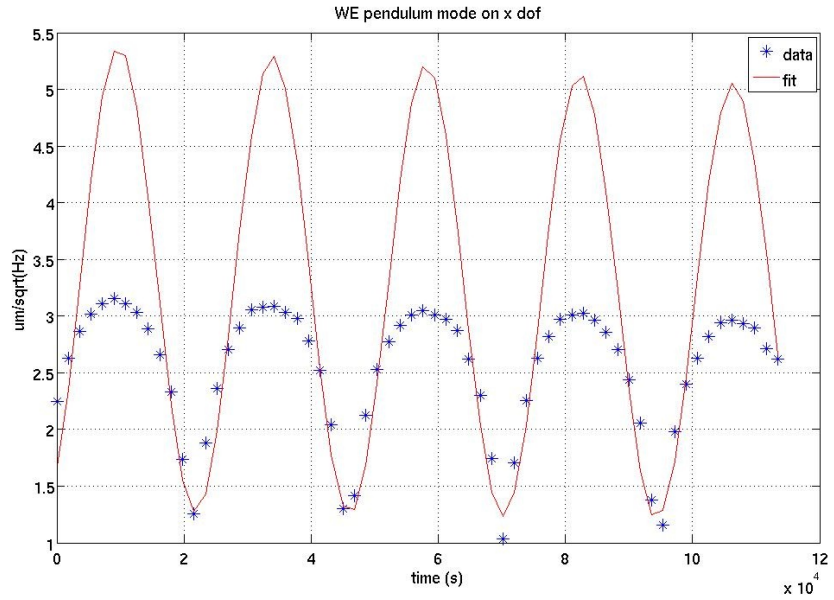

Figure 4.36: exponential-sinusoidal fit for the quality factor estimation of the West-End x pendulum mode.

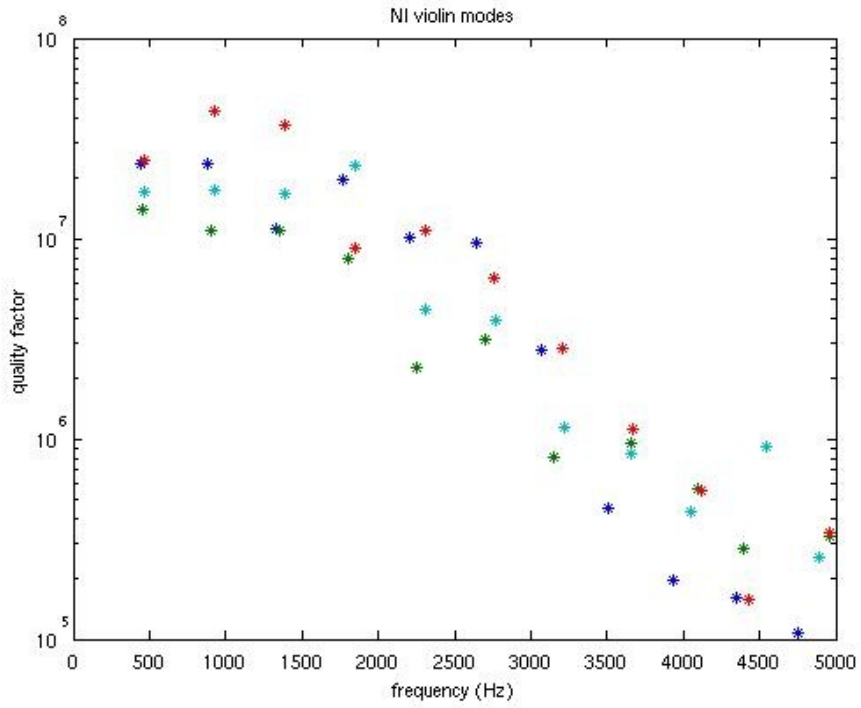

Figure 4.37: quality factors of the North-Input violin modes.

4.6.2 Violin mode results

The results for the violin modes are shown for the four payloads in figs. 4.37, 4.38, 4.39 and 4.40. I plot the quality factor of each fiber with respect to the harmonic frequency, until the violin resonances are recognizable: different colors refer to different fibers.

Looking at the figures, a decreasing trend of quality factors with respect to frequency is evident. Apart that trend, each tower shows a different spread: for example, the data of the North-Input have a low dispersion, while the West-End data are greatly scattered.

Motivations of the different behaviors can be found in the mechanical assembly of the payload: I carried out dedicated measurements on fused silica fibers and their clamping systems, whose results are shown in chapter 5.

4.6.3 Bulk mode results

As for violin modes, the bulk mode quality factors show a decreasing trend. The results for bulk modes of the four payloads (from $3.9kHz$ to $25kHz$) are shown in figs. 4.41, 4.42, 4.43 and 4.44. In the plots I report also the correlation coefficients, which have similar values for different payloads. Moreover, a scattered behavior is evident.

The quality factors of the first order butterflies (0,2), the first order drum mode (1,0), the second order butterflies (0,3) and the drum mode (2,0), with their frequency, are reported in tab. 4.11. The North-Input case, which presents two values of coupled drum modes, is treated in detail in the next section.

Note the swap between the butterflies of the same order for the Input mirrors and

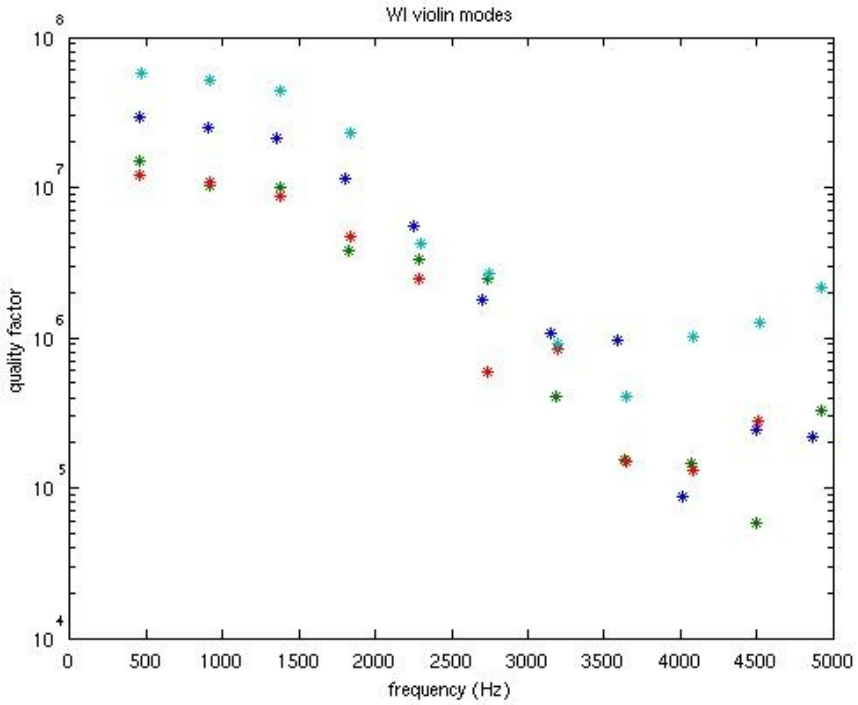

Figure 4.38: quality factors of the West-Input violin modes.

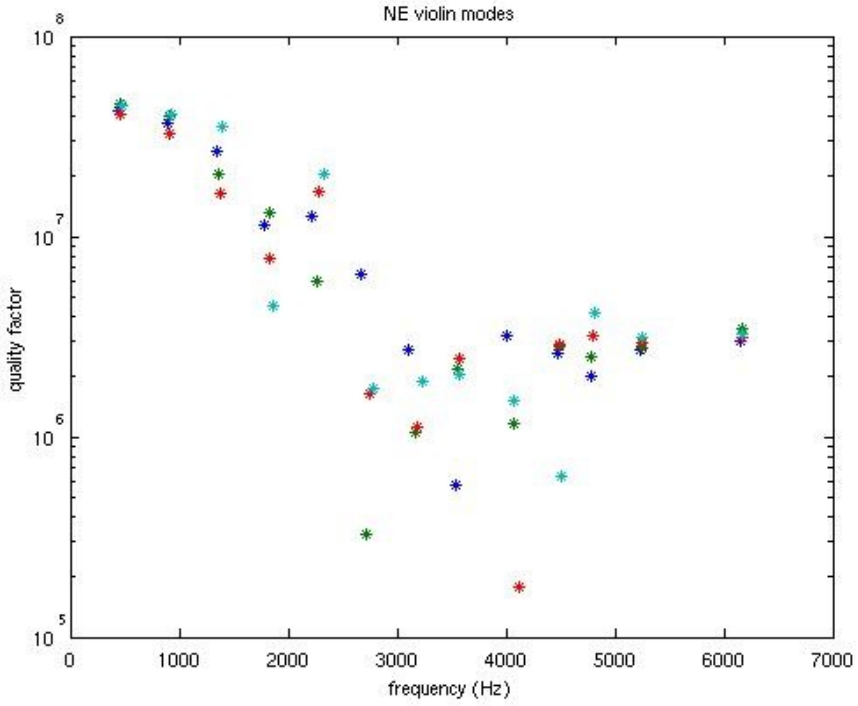

Figure 4.39: quality factors of the North-End violin modes.

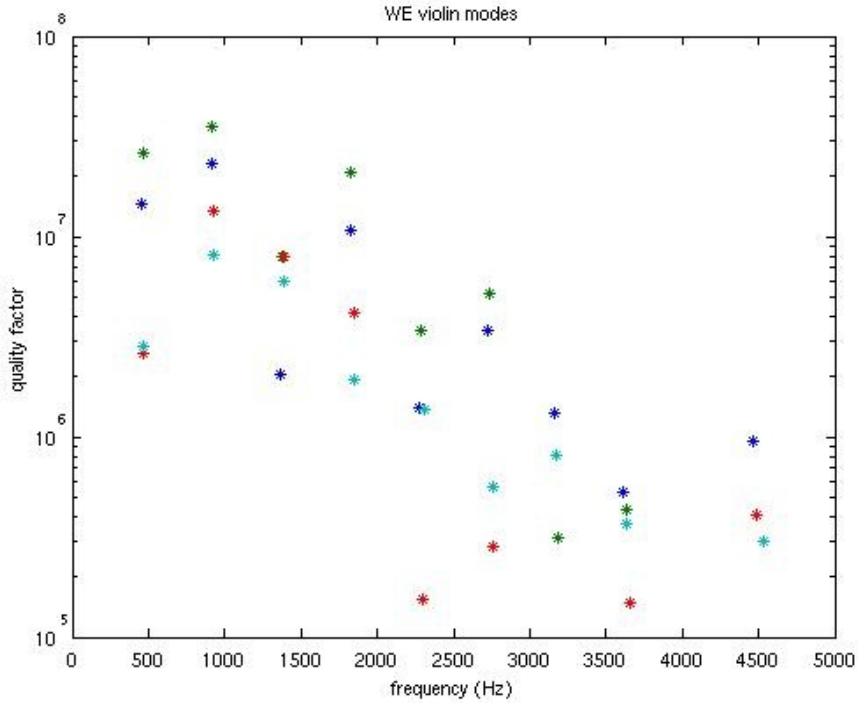

Figure 4.40: quality factors of the West-End violin modes.

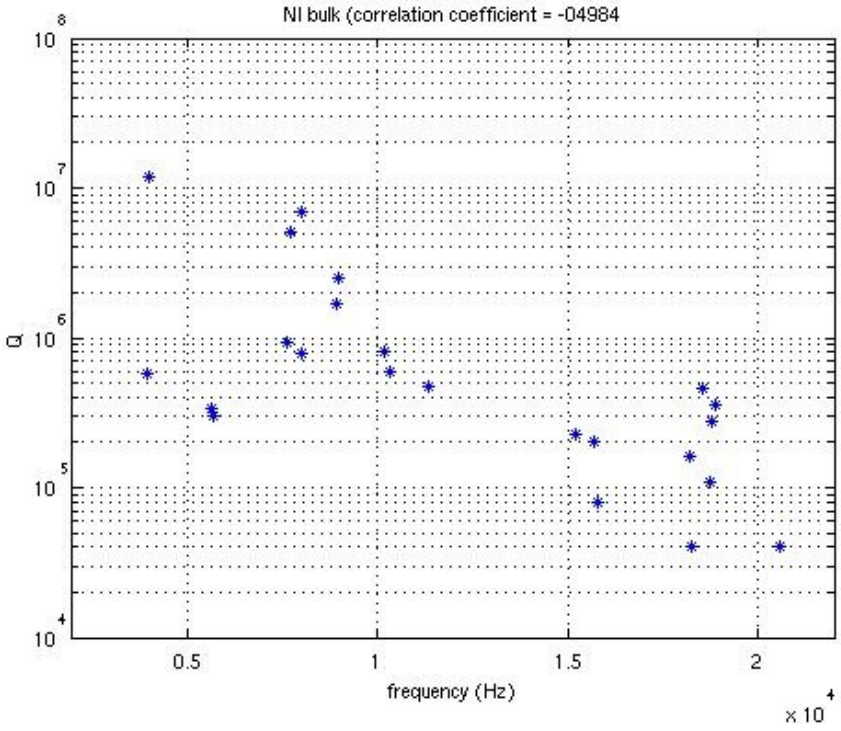

Figure 4.41: quality factors of the North-Input bulk modes.

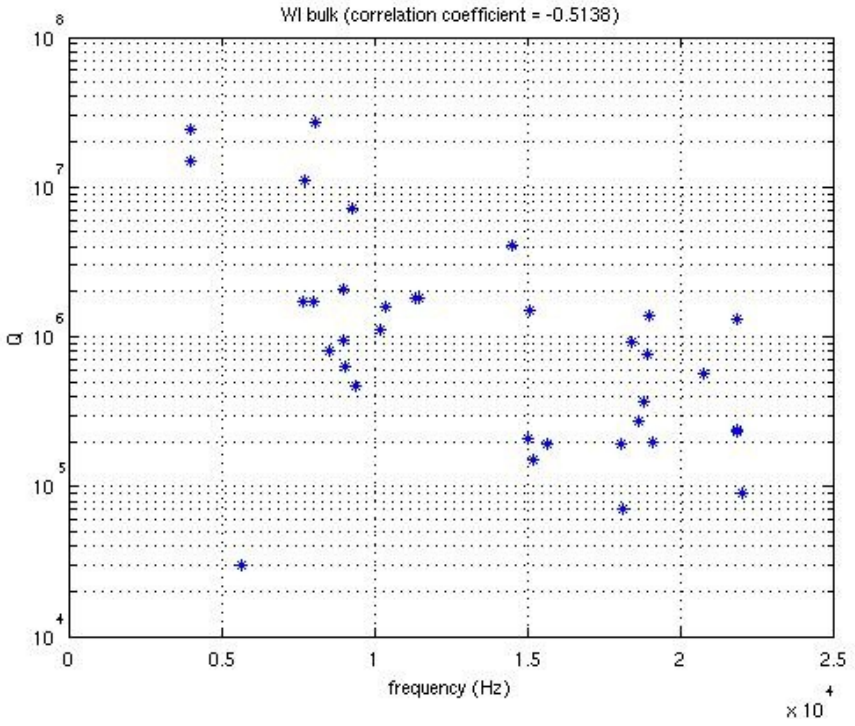

Figure 4.42: quality factors of the West-Input bulk modes.

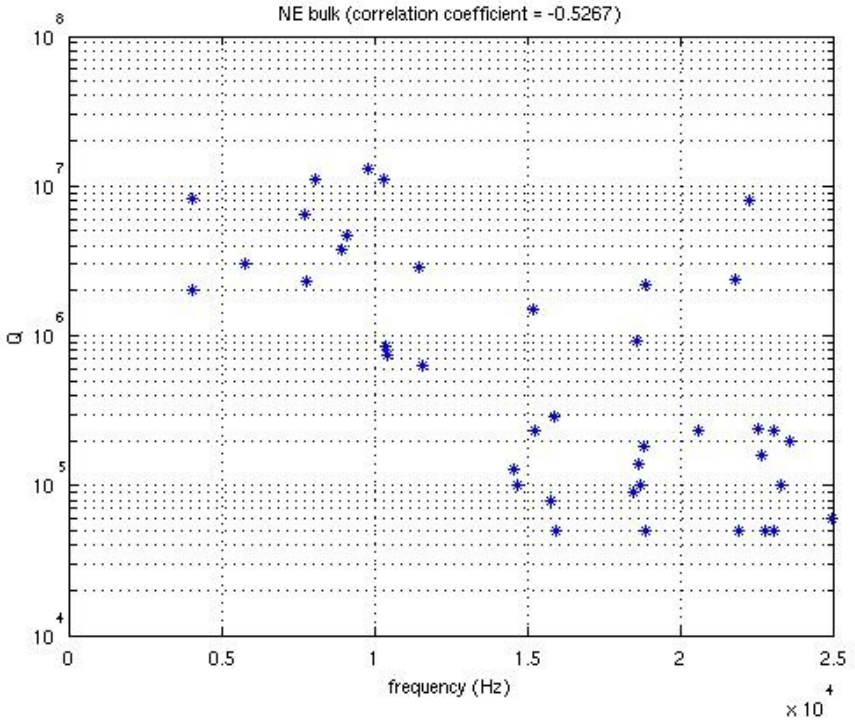

Figure 4.43: quality factors of the North-End bulk modes.

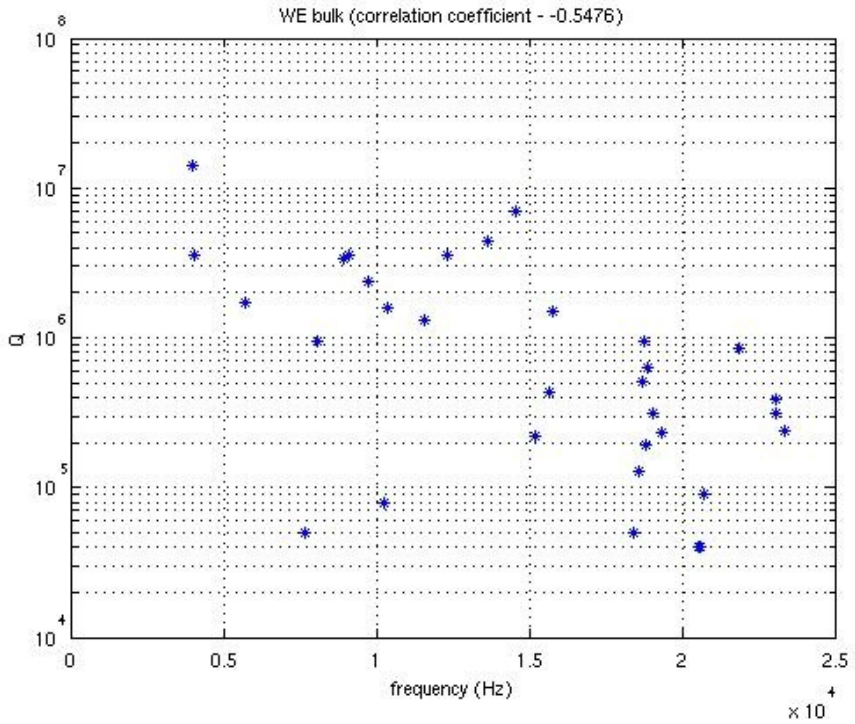

Figure 4.44: quality factors of the West-End bulk modes.

the End mirrors. This exchange depends on different geometric characteristics of the mirrors and, in particular, on the flat dimensions. In fact, each mirror has lateral flats to allow the silicate bonding of the ears (see sec. 4.1.2). While in the Input mirrors the flats are $50mm$ high, in the End mirrors, the flats are $100mm$ high.

I supposed the swap between the butterfly modes from the Q-values: since the butterfly $\times$ and butterfly | cause a bigger strain of the ears and the silicate-bonded area than the butterfly + and butterfly – do, their quality factors are lower than the others. These swaps is also confirmed by finite element simulations.

North-Input case

For the North-Input payload, I found a coupling between the (1,0) drum mode and a XIII order violin mode. In fig. 4.45 I show the North-Input spectra, before excitation (in purple) and after excitation (in black). It is possible to clearly distinguish four excited peaks: from the temperature analysis (see sec. 4.3.2) I found that two of them are XIII harmonic violin modes. On the contrary, other two peaks, which have similar amplitude in the spectrum, showed intermediate characteristics between a violin mode and a drum bulk mode: those results are reported in tab. 4.9 as "coupled drum".

So, it is reasonable to deduce a coupling between the drum mode and a violin mode. The expressions which manage this effect are the same reported in sec. 3.3.5 for two coupled oscillators, with very close resonance frequencies.

If two uncoupled harmonic oscillators have masses M and m, resonance frequencies

tower	mode	$f(Hz)$	Q
NI	butterfly × (0,1)	3964	5.71 E+05
	butterfly + (0,1)	3996	12.0 E+06
	coupled drum (1,0)	5671	3.42 E+05
	coupled drum (1,0)	5675	3.04 E+05
	butterfly | (0,2)	7641	9.44 E+05
	butterfly – (0,2)	7710	5.12 E+06
	drum (2,0)	15673	2.04 E+05
WI	butterfly × (0,1)	3939	15.2 E+06
	butterfly + (0,1)	3971	24.3 E+06
	drum (1,0)	5642	3.07 E+04
	butterfly | (0,2)	7605	1.71 E+06
	butterfly – (0,2)	7673	10.8 E+06
	drum (2,0)	15659	1.92 E+05
NE	butterfly + (0,1)	3980	8.33 E+06
	butterfly × (0,1)	4025	2.07 E+06
	drum (1,0)	5706	3.02 E+06
	butterfly – (0,2)	7667	6.45 E+06
	butterfly | (0,2)	7761	2.34 E+06
	drum (2,0)	15773	8.48 E+04
WE	butterfly + (0,1)	3969	13.6 E+06
	butterfly × (0,1)	4014	3.60 E+06
	drum (1,0)	5693	1.76 E+06
	butterfly – (0,2)	7653	4.67 E+04
	butterfly | (0,2)	7745	–
	drum (2,0)	15763	1.49 E+06

Table 4.11: measured quality factors of the most interesting internal bulk modes for all the towers.

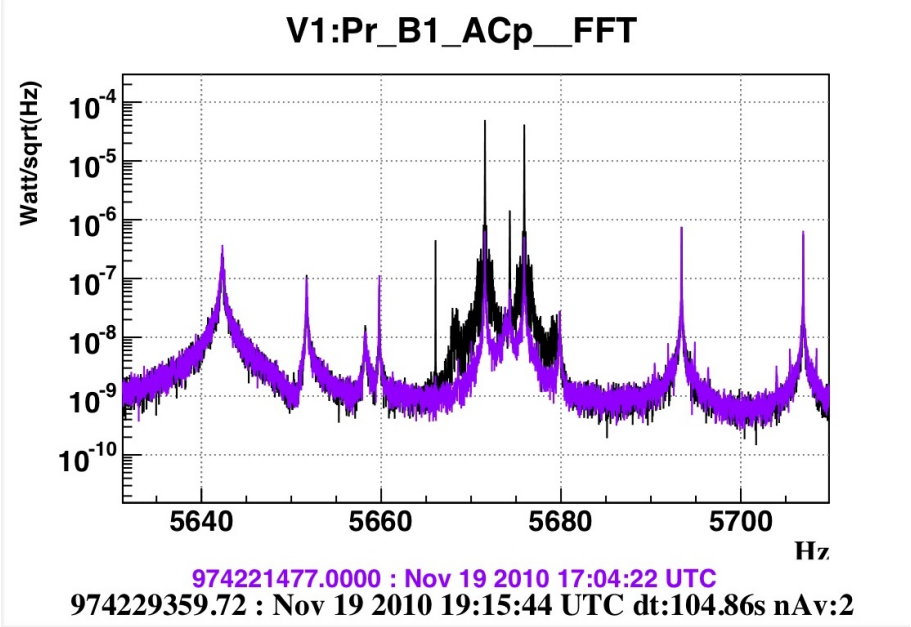

Figure 4.45: North-Input mirror spectra in the drum frequency region: in black the spectrum after excitation, in purple the quiet spectrum. Note the two "horns" in place of the drum mode single-peak.

f_M and f_m and quality factors Q_M and Q_m, the coupled frequencies are [97]:

$$f_\pm = \sqrt{\frac{1}{2}\left\{[f_m^2(1+\mu)+f_M^2] \pm \sqrt{[f_m^2(1+\mu)+f_M^2]^2 - 4f_m^2 f_M^2}\right\}} \tag{4.15}$$

where $\mu = m/M$ is the mass ratio.

For two tuned oscillators ($f_M = f_m = f_0$) the frequency difference between the two peaks depends on the mass ratio as:

$$\Delta f_\pm = f_+ - f_- = f_0\sqrt{\frac{\mu}{1+\mu}}$$

Considering uncoupled decay times $\tau_M = \frac{Q_M}{\pi f_M}$ and $\tau_m = \frac{Q_m}{\pi f_m}$, coupled decay times is:

$$\frac{1}{\tau_\pm} = \frac{1}{2}\left[\frac{1}{\tau_M}\left(1 \pm \frac{\sqrt{\mu}}{\sqrt{4+\mu}}\right) + \frac{1}{\tau_m}\left(1+\mu \pm \frac{\sqrt{\mu}}{\sqrt{4+\mu}}\right)\right]$$

For the North-Input payload, the two harmonic coupled oscillators are the mirror drum mode and a fused silica fiber XIII-order violin mode. The mirror drum mode effective mass m_{mi} is larger than the fiber violin effective mass m_f. So, it is possible to use approximations $\mu \ll 1$ and $\tau_M \ll \tau_m$; in that case coupled decay times are:

$$\frac{1}{\tau_\pm} \approx \frac{1}{2}\left(\frac{1}{\tau_M} + \frac{1}{\tau_m}\right) \approx \frac{1}{2}\frac{1}{\tau_M} \tag{4.16}$$

the coupled decay time is dominated by the most dissipative damping process.

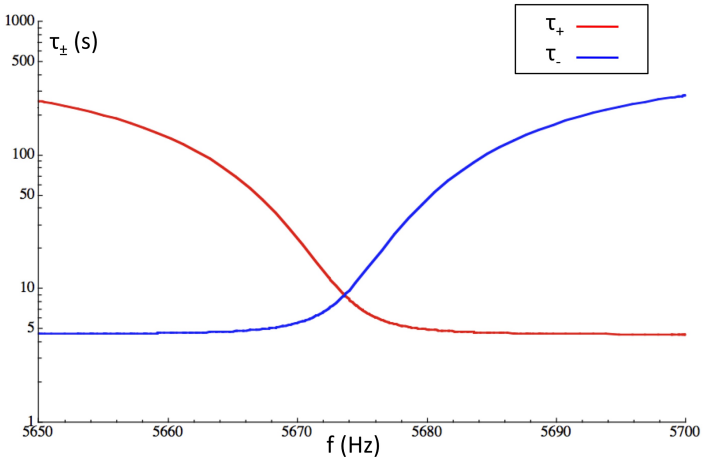

Figure 4.46: theoretical coupled decay times with respect to mirror drum mode frequency: the drum mode quality factor is $Q_M = 1.6 \cdot 10^5$, the violin mode quality factor is $Q_m = 1.6 \cdot 10^7$ and the violin frequency is $f_m = 5673Hz$.

	mirror mode	violin mode
frequency $f(Hz)$	5673.65	5673.65
effective mass $m(kg)$	7.7	$1.3 \cdot 10^7$
loss angle ϕ	$6 \cdot 10^{-8}$	$6.25 \cdot 10^{-6}$
temperature dependence $\alpha(Hz/K)$	0.6	0.1

Table 4.12: simulated parameters of uncoupled oscillators for the mirror drum mode and the fiber XIII violin mode of the North-Input payload.

The theoretical behavior of $\tau_\pm$ expressed in eq. 4.16 is plotted with respect to the mirror drum mode frequency f_M in fig. 4.46: in that case the drum mode quality factor is supposed to be $Q_M = 1.6 \cdot 10^5$, violin mode quality factor is $Q_m = 1.6 \cdot 10^7$ and violin frequency is $f_m = 5673Hz$. When the two oscillators are perfectly tuned in frequency, the decay times $\tau_\pm$ have the same value, very close to the lowest uncoupled decay time (the crossing point of the blue and red curves in fig. 4.46).

Despite the quality factor at resonance can be reduced, the off-resonance region is not affected, neither the thermal noise.

It is possible to estimate the physical parameters of uncoupled oscillators: effective masses, temperature dependences and the drum mode loss angle are evaluated with a finite element analysis; while the violin loss angle can be determined using the loss angle of the nearby XIII violin modes. The results are shown in tab. 4.12. From these values we can estimate the parameters of the coupled oscillators and compare them with experimental measurements.

Supposing thermal noise is the dominant noise source at the mechanical resonance

peaks in the sensitivity spectrum[5], it is possible to perform a Lorentzian fit of the spectrum peaks to find parameters of coupled oscillators. It is necessary to use the gravitational wave h_{rec} signal, instead of dark fringe channel, since the latter one is not calibrated.

So, near the resonance, thermal noise spectrum, considering viscous losses, is (see eq. 3.10):

$$S_h(f) = \frac{1}{l_0^2} \frac{k_B T}{2\pi^3 m_n^{eff} Q_n} \frac{f_n}{\left[(f^2 - f_n^2)^2 + \frac{f_n^2 f^2}{Q_n^2}\right]}$$

where l_0 is the interferometer arm length, T is temperature, m_n^{eff} is the effective mass of the internal mode n at frequency f_n and Q_n is its quality factor.

At resonance:

$$S_X(f) = \frac{k_B T Q_n}{2\pi^3 m_n^{eff} f_n^3} \tag{4.17}$$

It is possible to fit peak data with a Lorentzian function:

$$S_{lor}(f) = \frac{A}{(f^2 - f_n^2)^2 + B^2 f^2}$$

where A is the amplitude, B is a parameter connected to peak width and f_n is the peak frequency. From the fit the coefficients A and B are determined and so the effective mass m_n^{eff} and the quality factor Q_n are derived.

The Lorentzian fit is shown in fig. 4.47: experimental points are in black, their error in red and the Lorentzian fit is in dashed blue line. For each "horn" the fit parameters are reported.

In fig. 4.47 errors are determined considering that the spectrum is the results of $n_{ave} = 9$ averaged periodograms. Each point in the spectrum follows a χ^2 distribution, with $2n_{ave}$ degrees of freedom: the expected value is $\mu_{\chi^2} = n_{ave}$ and the variance is $\sigma^2_{\chi^2} = 2n_{ave}$. Because the spectrum is not normalized, we introduce a constant C: so the expected value is $\mu_{\chi^2} = Cn_{ave}$ and the variance $\sigma^2_{\chi^2} = 2C^2 n_{ave}$. From these two condition it is possible to determine the spectrum variance:

$$\sigma_{\chi^2}(f) = \sqrt{\frac{2}{N_{ave}}} S_h(f)$$

In tab. 4.13 I report the expected values (found from a finite element analysis) and the measured values, from the Lorentzian fit results [144].

4.7 Error estimation

For what concern the error estimation of quality factor measurements, I can not use the same consideration as for the North-Input coupled modes, since the ring-down measurements are not stationary phenomena.

[5]This estimation has been done during a quiet period, without any excitation; in fact the drum mode peak is stationary and always present in the interferometer output, the dark fringe, since it is the best coupled mode with the laser interferometer probe.

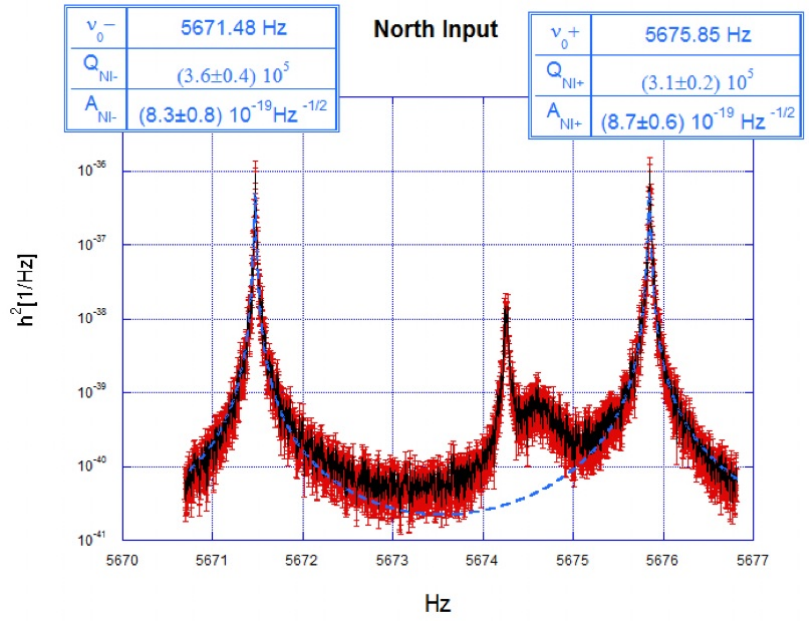

Figure 4.47: North-Input mirror drum mode "horns" with the Lorentzian fit: experimental points are in black, their error in red and the Lorentzian fit is in dashed blue line.

		expected	measured
frequency	$f_-(Hz)$	5671.47	5671.48
	$f_+(Hz)$	5675.83	5675.85
amplitude	$A_-(1/\sqrt{Hz})$	$9.1 \cdot 10^{-19}$	$(8.31 \pm 0.77) \cdot 10^{-19}$
	$A_+(1/\sqrt{Hz})$	$9.1 \cdot 10^{-19}$	$(8.65 \pm 0.64) \cdot 10^{-19}$
quality factor	Q_-	$3.2 \cdot 10^5$	$(3.61 \pm 0.35) \cdot 10^5$
	Q_+	$3.2 \cdot 10^5$	$(3.05 \pm 0.24) \cdot 10^5$
effective mass	$m_-(kg)$	15	21.3 ± 6.0
	$m_+(kg)$	15	16.5 ± 3.8
temperature dependence	$\alpha_-(Hz/K)$	0.35	0.24
	$\alpha_+(Hz/K)$	0.35	0.33

Table 4.13: expected and measured parameters of coupled oscillators for the mirror drum mode and the fiber XIII violin mode of the North-Input payload.

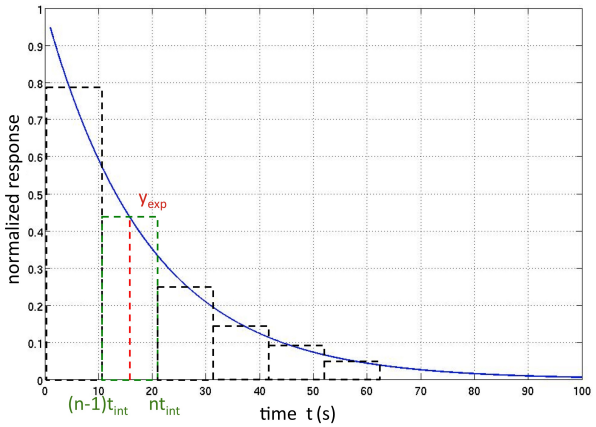

Figure 4.48: exponential function (in blue) splitting in n bins of width t_{int} (in black); taking the n-th sample (in green), the peak amplitude in that time interval will be approximated as y_{exp} (in red).

Quality factor measurement results are related to the specific apparatus mounting. Since there can be recoil losses and couplings between mechanical parts of the payload, it could happen to find different quality factor values for different mountings of the same experimental physical system.

Since we did not dismount and re-mount Virgo payloads, I performed all measurements with the same setting. As shown in tab. 4.3, I have three measurements for the vertical, violin and low frequency bulk modes: for these modes, I evaluated quality factors taking the maximum measured value. Errors are taken from standard deviations.

For those modes of which I did not have several measurements, I attributed them a 10% relative error.

4.7.1 Consideration on FFT parameters

Thanks to the nature of the exponential function, which does not change shape after integration, the decay time of ring-down experiment is not affected by the choice of the FFT parameters, as the integration time or the average number.

In fact, in the FFT integration, we are dividing an exponential function in n bins of width t_{int} (see fig. 4.48); for each n-th bin, we approximate the exponential values with the amplitude y^n_{exp}:

$$\begin{aligned} y^n_{exp} &= \frac{1}{t_{int}} \int_{(n-1)t_{int}}^{n\,t_{int}} A_0 e^{-\frac{t}{\tau}} dt \\ &= \frac{A_0 \tau}{t_{int}} e^{-\frac{n\,t_{int}}{\tau}} \left(e^{\frac{t_{int}}{\tau}} - 1 \right) \end{aligned}$$

Since $t = nt_{int}$, it is immediate to see the exponential function does not change its decay time τ. But, if we choose a large average number n_{ave} or too long integration time t_{int}, respect to decay time τ, we divide the exponential function in few points.

In that case, the last points are affected by noise, since the resonance peak could not be recognizable: the decay time evaluation is altered.

To understand which are the best integration time and average number values, I study how a peak amplitude changes. The results for the North-Input bulk mode at frequency $f = 7992.64Hz$ are reported in figs. 4.49 and 4.50. For that mode the decay time is $\tau = 40.1s$.

To find as the amplitude peak changes with respect to average number n_{ave}, consider that the data for FFT are taken for a total time $T_{tot} = (n_{ave}+1)t_{int}/2$, since the FFT are 50% overlapped:

$$\begin{aligned} A(T_{tot}) &= \frac{A_0}{T_{tot}} \int_0^{T_{tot}} e^{-\frac{t}{\tau}} dt \\ &= \frac{A_0}{T_{tot}} \left(1 - e^{-\frac{T_{tot}}{\tau}}\right) \end{aligned}$$

substituting T_{tot}:

$$A(n_{ave}) = \frac{2A_0\tau e^{-\frac{t_{int}}{2\tau}}}{(n_{ave}+1)t_{int}} e^{-\frac{n_{ave}t_{int}}{2\tau}} + \frac{2A_0\tau}{(n_{ave}+1)t_{int}}$$

re-defing quantities:

$$A(n_{ave}) = A_{n1} e^{-\frac{n_{ave}}{\eta}} + A_{n2} \tag{4.18}$$

where A_{n1} is the exponential amplitude, η is the average number decay constant and A_{n2} is a DC value. In fact, increasing the average number, I integrate the resonance peak in a longer time: since the peak energy is decreasing exponentially with its decay time, the data fit an exponential function. This is true until the noise level is reached: after that value, the peak is no more recognizable and the amplitude is constant.

In fig. 4.49 I show the peak amplitude with respect to average number: I fix the integration time to $t_{int} = 20s$. The decay constant η of the fit is $\eta = 9.5$: since the FFT are 50% overlapped, this decay constant is linked to the decay time τ as:

$$\tau = \frac{\eta t_{int}}{2} \approx 95s$$

longer of a factor 2 than the expected one.

On the contrary, I expect the amplitude peak with respect to integration time t_{int} is a product between a line and a exponential function:

$$A(t_{int}) = A_0 e^{-\frac{t_{int}}{\tau}} (m t_{int} + q) + A_N \tag{4.19}$$

where A_0 is the exponential amplitude, τ is the decay time, m is the line slope, q is the y-axis intercept and A_N is a DC value, due to the noise level.

That trend is due to the fact that:

- for $t_{int} \ll \tau$ the peak in the FFT spectrum is not well resolved: for very low t_{int} value, the resolution is so large that the peak energy is spread in a large bin; going to longer integration time, the resolution decreases and the peak energy linearly increases;

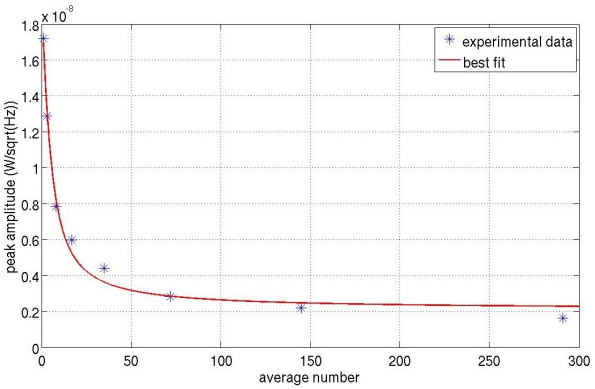

Figure 4.49: peak amplitude of the North-Input mirror resonance mode at frequency $f = 7992.64Hz$ with respect to different average number n_{ave}: in blue the experimental data and in red line the best exponential fit (see eq. 4.18); the integration time is fixed to $t_{int} = 20s$.

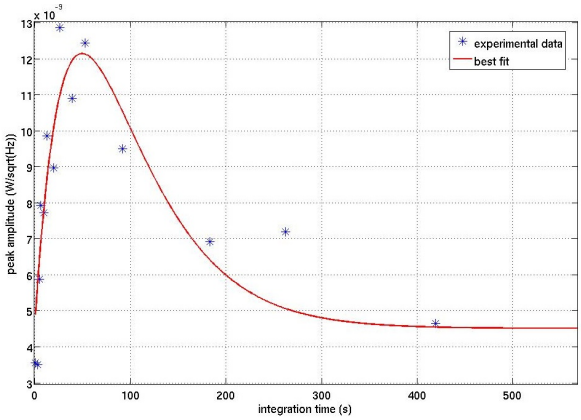

Figure 4.50: peak amplitude of the North-Input resonance mode at frequency $f = 7992.64Hz$ with respect to different integration time t_{int}: in blue the experimental data and in red line the best fit (see eq. 4.19); the average number is fixed to $n_{ave} = 3$.

- for $t_{int} \gg \tau$ the peak amplitude in the FFT spectrum is exponentially decaying with the same decay time τ, since the peak energy is exponentially decaying.

Varying the integration time, the maximum of the peak amplitude is reached around $t_{int} \sim \tau$. In fig. 4.50 I show the peak amplitude with respect to integration time: I fix average number to $n_{ave} = 3$. The decay time coming from the fit is $\tau = 49.5s$.

So, I chose to have the average number equal to $n_{ave} = 3$, which is a reasonable compromise between a good resolution and no large decay time modification. Similarly, I chose the integration time t_{int} for each resonance peak so that it is lower than the exponential decay time τ, $t_{int} \ll \tau$.

Chapter 5

Study on fused silica fibers and their clamping system

In this chapter I present my studies on fused silica fibers and their clamping system in Virgo+ monolithic suspensions.

From the quality factor measurements reported in the previous chapter, it is possible to get informations about the suspension method: in particular violin modes are good probes, even better than the pendulum mode, since they cover a large frequency region allowing us a frequency dependence study. Moreover, violin modes are determined by the same theory as the one of the pendulum mode and should be affected by most of the same excess loss mechanisms.

At first I show anharmonicity studies on fused silica violin frequencies; then I discuss the quality factor dependence with respect to violin frequency.

Finally I report my measurements on fused silica fibers, made with a specific setup at the University of Perugia. These measurements are fundamental for a correct comprehension of Virgo+ results.

5.1 Anharmonicity effect on violin modes

A harmonic oscillator obeys Hooke's law: this idealized expression assumes that a system displaced from equilibrium responds with a restoring force whose magnitude is proportional to the displacement. In nature, idealized situations break down and linear equations of motion fail to describe physical systems.

Anharmonic oscillatiors are characterized by a restoring force no longer proportional to the displacement: they can be approximated with a harmonic oscillator plus an anharmonicity term calculated by the perturbation theory.

For violin modes, the frequency expression is (see sec. 3.5.1 and sec. 4.3.1):

$$f_{violin} = \frac{n}{2L}\sqrt{\frac{\mathcal{T}}{\rho_l in}}\left[1 + \frac{2}{k_e L} + \frac{(n\pi)^2}{2}\frac{1}{(k_e L)^2}\right] \tag{5.1}$$

where n is the harmonic order number, L is the fiber length, $\mathcal{T}$ the applied tension,

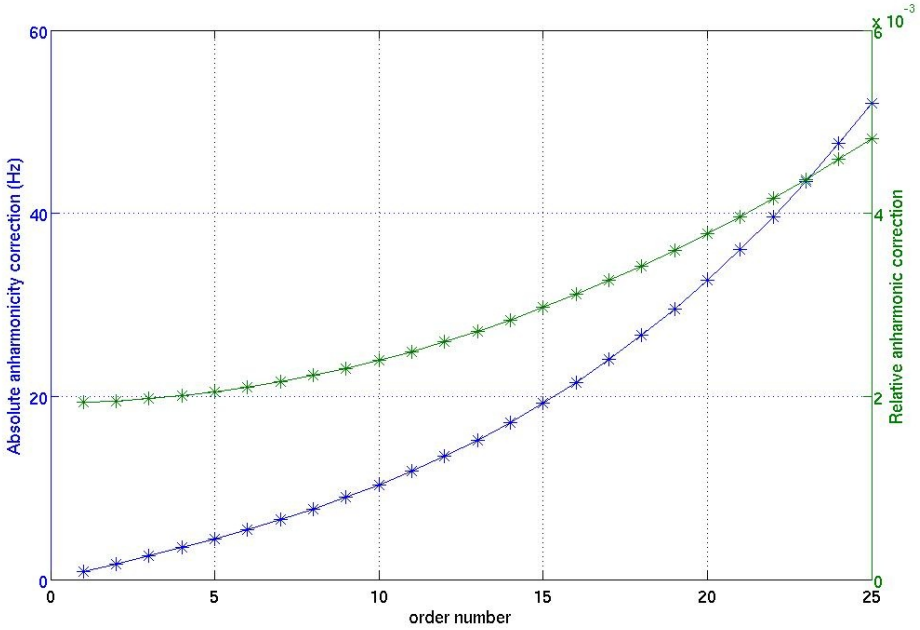

Figure 5.1: anharmonic correction with respect to order number: the absolute correction (in blue) is computed with the expression reported in brackets of eq. 5.1; the relative anharmonic correction (in green) is computed with respect to violin frequencies.

$\rho_l in$ its linear density and k_e is the flexural stiffness, equal to (see eq. 3.55):

$$k_e = \sqrt{\frac{\mathcal{T} + \sqrt{\mathcal{T}^2 + 4EI\rho_{lin}\omega^2}}{2EI}} \tag{5.2}$$

with I the fiber cross section moment and E the material Young's modulus.

The first term of eq. 5.1 is just the violin mode frequency of a perfect string with all the restoring force due to tension. The additional factors in brackets involve the elastic constant k_e and quantify the additional restoring force due to the stiffness EI of the fiber: the first and second order correction in $\frac{1}{k_e L}$ are reported. There is also a third order correction that is due to the recoil of the (nearly) free masses at the ends of the fibers. However, for our suspension this correction can easily be estimated to be only $\sim 0.001\%$ for the first mode and to fall as n^2 with mode number, so it can be safely ignored.

The order of magnitude of anharmonic corrections is reported in fig. 5.1 for the first 25 violin modes: corrections increase for higher order modes. The absolute correction computed with the expression reported in brackets of eq. 5.1 is in blue, while in green the relative correction (of order of 10^{-3}) with respect to violin frequencies.

For Virgo, the steel-wire anharmonicity has been computed [145]: in fig. 5.2 peaks of the first five harmonics of a given wire have been overlapped, dividing by n the frequency range of the nth-harmonic.

Some anharmonicity is present in the flexural stiffness of the suspension wires and this is well evident in figure, where the increase of frequency of the higher modes is

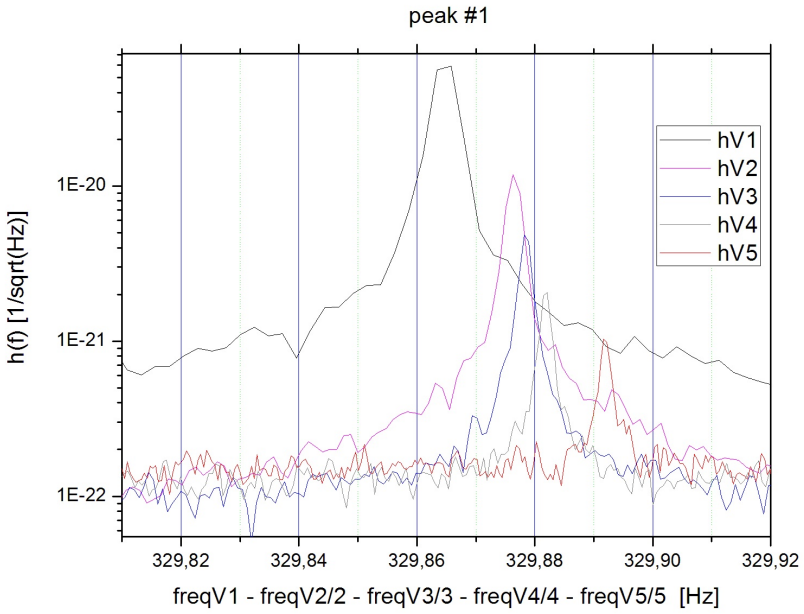

Figure 5.2: Virgo steel wire violin mode: spectrum amplitudes of the first five harmonics peak for a given wire, divided for the mode number. Different harmonics are reported in different colors, following the legend.

clear. Anyway, only few identified peaks could respect a similar law; many others show a more complex behavior, probably due to Virgo suspension asymmetries in clamps and spacers or mode couplings.

I repeated these computation for Virgo+ monolithic suspensions, finding a different anharmonicity behavior (see fig. 5.3). In fact, I observed a decreasing trend with respect to frequency. This effect is due to the dumbbell fiber profile, which implies thicker neck regions.

For the presence of a variable cross section the dynamical behavior of these fibers is different from the one of the perfectly cylindrical ones, even if cylindrical symmetry is preserved. In that case, eq. B.1 is not more applicable. The flexural equation is:

$$E\frac{d^2}{dx^2}\left(\frac{d^2I(x)y}{dx^2}\right) - \mathcal{T}\frac{d^2y}{dx^2} = -\omega^2\rho S(x)y(x) \tag{5.3}$$

where S is the wire section, y is the coordinate along the fiber axis, x is the coordinate orthogonal to the fiber axis and ω is the frequency.

For such an equation, no analytical solution can be found, but it is possible to approximate fused silica fibers with a three-segment constant-section model. A fiber schematization, with bending point positions, is given in fig. 5.4.

We consider the fiber as the sum of three parts: for each part, whose length is reported in fig. 5.4, we can apply eq. 5.2 to compute the flexural stiffness. Its inverse gives the bending point position.

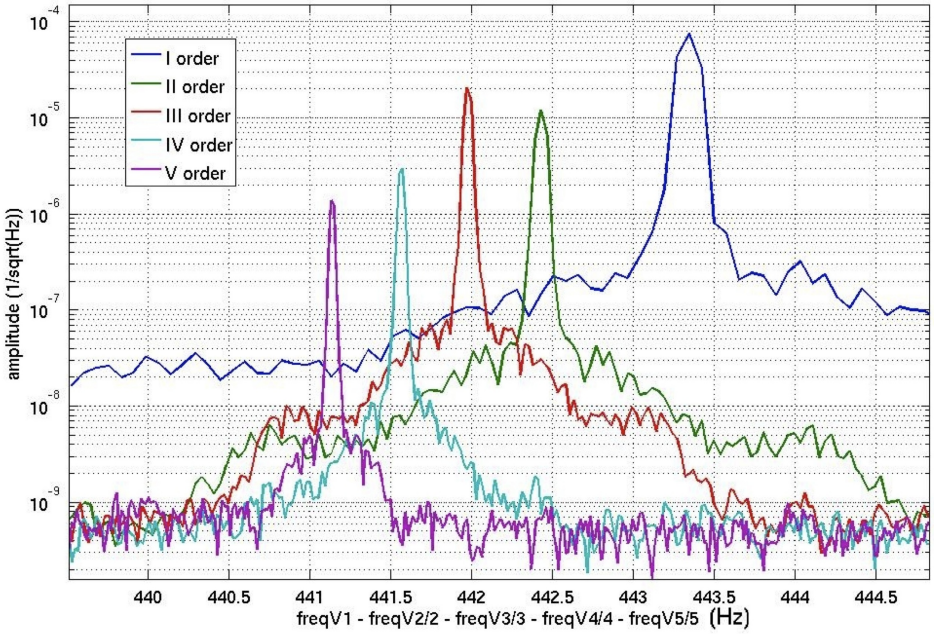

Figure 5.3: Virgo+ fused silica fiber violin mode: spectrum amplitudes of a fixed fused silica fiber for the first five harmonics divided for the mode number. Different harmonics are reported in different colors, following the legend.

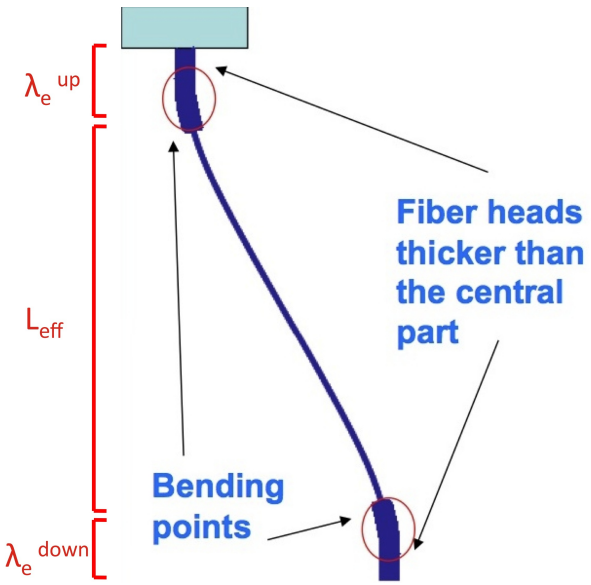

Figure 5.4: schematization of fused silica fiber with thicker neck regions: bending points position, λ_e^{up} and λ_e^{down}, and effective fiber length L_{eff} are indicated.

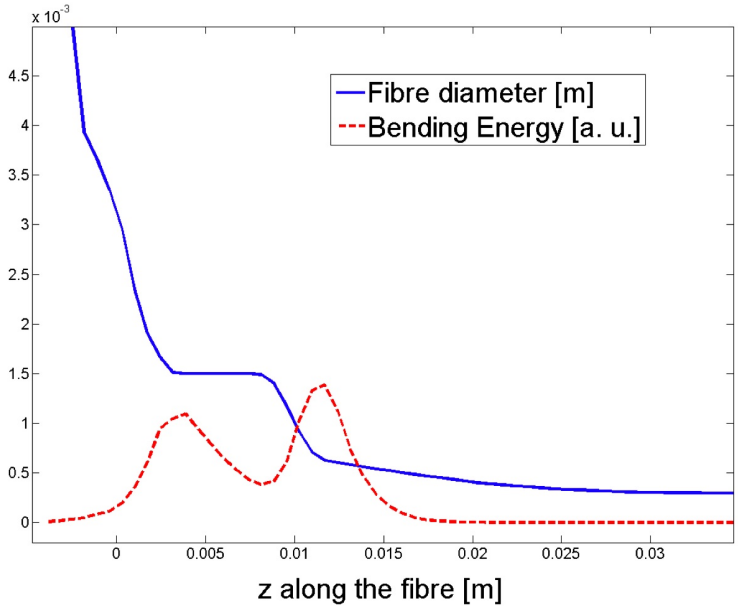

Figure 5.5: comparison between the fiber profile and the bending energy with respect to fiber length: it is evident an energy accumulation around the neck region.

So, going to higher frequencies ($\omega \uparrow$), the flexural stiffness increases ($k_e \uparrow$) and the bending point position decreases ($\lambda_e \downarrow$). The effective length of the fiber L_{eff} increases ($L_{eff} \uparrow$), causing a decreasing of the quantity f_{violin}/n (see eq. 5.1).

Furthermore, since the bending points lie in the neck region, we have a further increase of the flexural stiffness k_e due to the fact that the cross section moment $I \propto r^4$ is larger than in the fiber. So, for a dumbbell-profiled fiber we expect a decreasing of the quantity f_{violin}/n going to higher order harmonics.

To test the validity of the 3-segment model, a finite element simulation of the fiber is realized and the results are compared [146, 147].

The finite element simulation allows us to understand how the energy distribution is. The bending energy for a real suspension fiber is concentrated in the thicker region around the bending points, close to the fiber necks, as shown in fig. 5.5. For that reason, surface and thermoelastic thermal noise contribution to the dissipation can be dropped.

Moreover, the finite element analysis allows to compute the expected values of violin frequencies. We compare frequencies coming from simulations with frequencies coming from the analytical formula for cylindrical fibers (see eq. 5.1). Simulations give a more correct result, comparable with the frequencies measured in Virgo+ payloads [140]: in fig. 5.6 I report the percentage difference between measured frequencies and frequencies simulated with a finite element analysis, compared with the percentage difference between measured frequencies and frequencies computed with eq. 5.1. It is evident that simulated frequencies are closer to measured ones than the frequencies computed through the analytical formula.

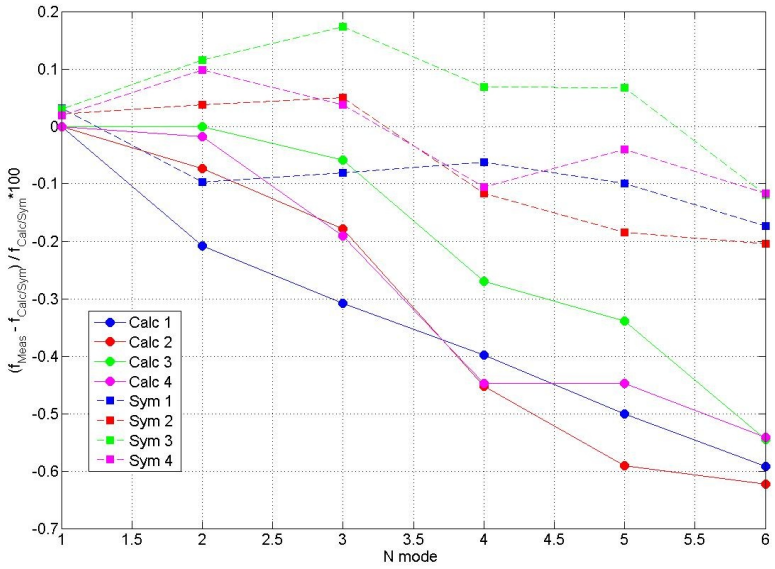

Figure 5.6: comparison between violin frequencies measured for North-Input payload and simulated/computed violin frequencies: we compare finite element analysis results with values obtained from analytical formula for cylindrical fibers (see eq. 5.1).

5.2 Violin quality factor dependence on frequency

I studied the quality factor behavior with respect to violin frequencies.

I expect loss angles for violin modes to depend on the ratio between the elastic energy E_{el} and the gravitational one E_{grav}, in a similar way to what happens for the pendulum mode. The violin dilution factor is defined as $D_n^v = E_{el}/E_{grav}$ and it enters the loss angle as:

$$\phi_n = \phi_{int} D_n^v = \phi_{int} \frac{2}{k_e L} \left(1 + \frac{n^2 \pi^2}{2 k_e L}\right) \tag{5.4}$$

where k_e is the flexural stiffness (given by eq. 5.2 or the approximated expression eq. B.3), n is the violin harmonic order and L is the fiber length.

The anharmonicity of the mode frequencies is closely related to the dilution factor. That is not surprising when one considers that the dissipation in the fiber is almost entirely due to the bending and not due to the work done against tension. Careful measurements of mode frequencies would provide some confidence that the suspension dynamics, and thereby the dilution factor, have been understood.

The internal overall loss angle ϕ_{int} is frequency dependent and is equal to:

$$\phi_{int}(f) = \phi_{struct} + \phi_{therm}(f) + \phi_{surf}$$

i.e. the sum of structural ϕ_{struct}, thermoelastic ϕ_{therm} and surface ϕ_{surf} loss angles. Structural loss angle ϕ_{struct} is a constant: for fused silica we have $\phi_{struct} = 3.3 \cdot 10^{-8}$.

On the contrary, thermoelastic loss angle is computed as (see eq. 3.25):

$$\phi_{therm}(f) = \Delta \frac{f/\bar{f}}{1 + f^2/\bar{f}^2} \tag{5.5}$$

where, taking into account non-linear effects on thermoelastic damping given by temperature dependence of the Young's modulus, Δ and $\bar{f}$ are equal to [136]:

$$\begin{aligned} \Delta &= \frac{ET}{c_V}\left(\alpha - \frac{\beta\mathcal{T}}{ES}\right)^2 \\ \bar{\tau} &= \frac{2.16 D_{st}}{c_V d^2} \end{aligned}$$

where c_V is the specific heat, D_{st} is the thermal conductivity of the wire material, α is the material linear expansion coefficient, β is the temperature dependence of the Young's modulus, $\mathcal{T}$ is the tension applied to the fiber, T is temperature, d is the typical distance the heat flow must cross and S is the fiber section. For the fused silica fibers used in Virgo+ the Debye's peak frequency is $\bar{f} \sim 39Hz$.

The surface loss angle ϕ_{surf} is frequency independent (see sec. 3.3.3):

$$\phi_{surf} = 8\phi_{struct}\frac{d_s}{d_w}$$

where d_w is the fiber diameter and d_s is the dissipation depth, which parametrizes the fiber size at which surface loss becomes important. It is possible to measure directly the dissipation depth from quality factors [148]: a reliable dissipation depth value is $d_s = 200\mu m$. So, for Virgo+ monolithic suspension, the surface loss is $\phi_{surf} = 1.9 \cdot 10^{-7}$.

Theoretical behavior of violin loss angles with respect to frequency are reported in fig. 5.7 taking into account the dilution factor D_n^v. In that figure I computed violin loss angles, considering only structural losses (the blue line), considering only thermoelastic losses (the green line), considering only surface losses (the red line) and considering the overall sum $\phi_n(f) = \phi_{struct} + \phi_{thermo}(f) + \phi_{surf}$ (the pale blue line).

Expected violin loss angles are one order of magnitude lower than the measured ones: the best measured loss angle has been found in the West-Input payload and it is equal to $\phi_{WI} = 1.63 \cdot 10^{-8}$.

Measured violin loss angles with respect to frequency are reported in fig. 5.8: for each payload, the four loss angle values belonging to different fibers have been averaged.

Comparing expected behavior in fig. 5.7 with the measured one in fig. 5.8 it is evident the discrepancy in order of magnitude and slope: there is an unknown damping mechanism probably connected to recoil losses. Furthermore loss angle values are greatly scattered, even for the same payload (see figs. 4.37, 4.38, 4.39 and 4.40). So, it is probably some loss mechanism linked to the monolithic clamping system. To verify this hypothesis, I performed a measurement campaign exclusively on fused silica fibers.

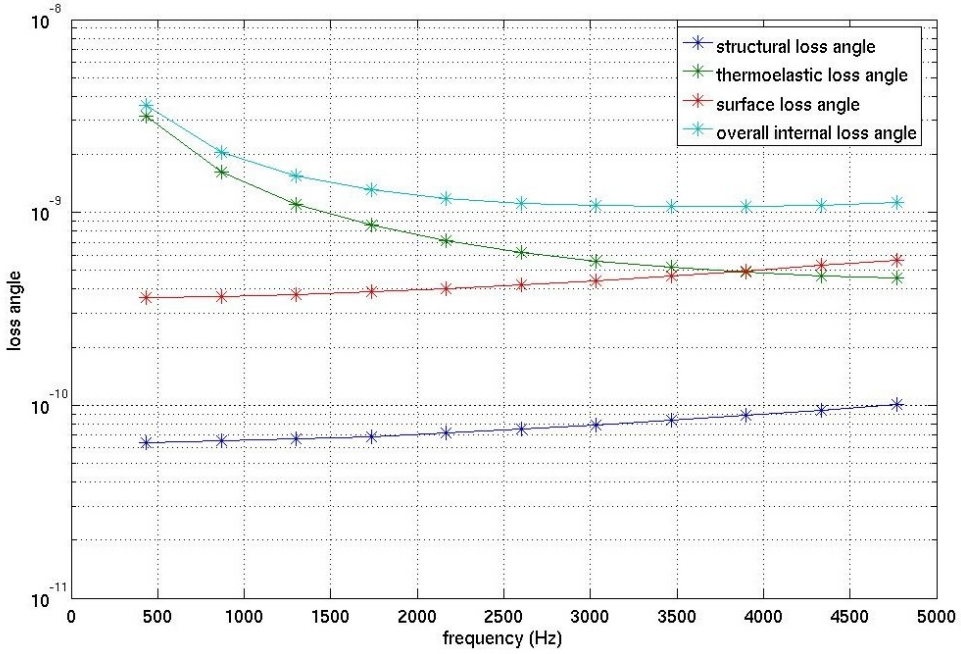

Figure 5.7: theoretical behavior of violin loss angle with respect to violin frequency considering the dilution factor D_n^v: in blue, the loss angle is computed considering only structural losses; in green considering only thermoelastic losses; in red considering only surface losses. The pale blue line is the overall sum.

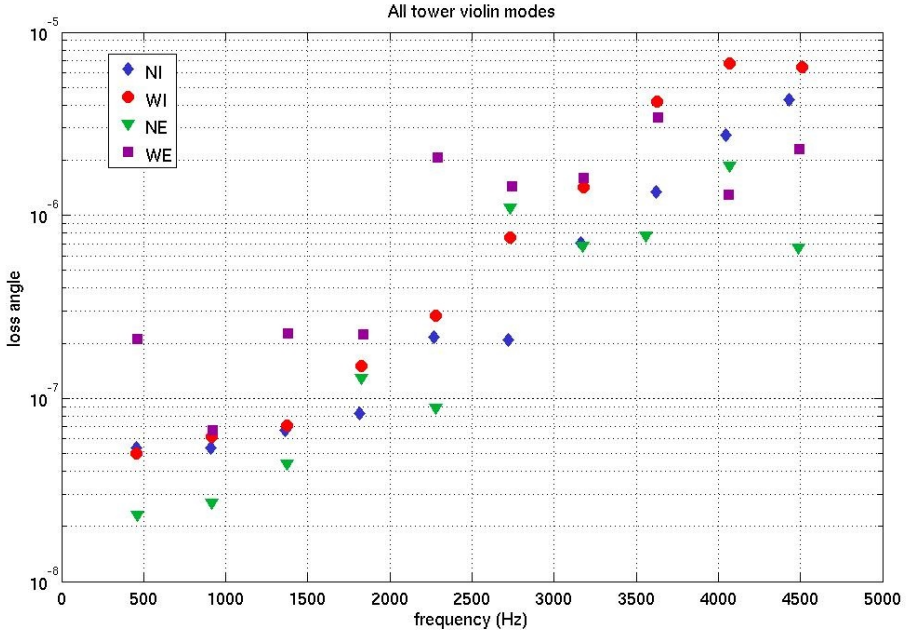

Figure 5.8: measured behavior of violin loss angle with respect to violin frequency: different payload are indicated in different colors and symbols; for each harmonic, the four loss angles values corresponding to different fibers have been averaged.

5.3 Fused silica fibers measurements

To understand what is the loss mechanism going on in Virgo+ fused silica fibers, I measured violin mode quality factors in different configurations. The experimental apparatus is set up at the University of Perugia and has already been employed for former measurement campaign [87, 92, 96].

This apparatus consists of a fixed steel frame that allows to suspend a fused silica fiber. The structure is placed in a vacuum chamber, which reaches a residual gas pressure of $P_{res} \sim 6 \cdot 10^{-5} mbar$. So, the residual gas Q limit for a fused silica fiber is $Q_{gas} \sim 3.5 \cdot 10^9$ (see eq. 3.31).

5.3.1 Experimental setup

The steel frame is shown in fig. 5.9. The fiber is suspended with a Virgo+ clamp in the upper part of the steel structure (see fig. 5.10); a $5kg$-mass steel cylinder is attached to the fiber with another clamp of the same kind (see fig. 5.11) to apply a tension equal to the one used for Virgo+ fibers. The clamps have two lateral screws and four upper screws for fiber position regulations.

The wire violin modes are excited by an electrostatic actuator made of a pair of copper tips placed a few millimeters from the wire.

To find the resonant frequencies the wire was first excited with white noise, coming from a function generator and amplified by a high voltage amplifier. Voltage of one kilovolt is typically used. When a resonance was identified, I excited it with a sine function at its fixed frequency.

Fiber motion is detected with two orthogonal shadow-sensors. In fig. 5.12 the two shadow-sensors, LEDs and photodiodes, are well visible. Two sensors are necessary to monitor at the same time the two degrees of freedom orthogonal to the fiber axis (x and z degrees of freedom, for more detail see sec. 3.5.1).

The acquisition scheme is reported in fig. 5.13: the actuation system is in orange, while the read-out system is in purple. In blue it is reported the fused silica fiber and in green the reference frame. Once the resonance frequency is excited, the driving signal is switched off and the oscillation amplitude of the free decay is recorded on a personal computer, using a LabView script. In this script it is possible to set up the sampling frequency and the resolution; moreover it is possible to follow the time dependence of the signal and to fit the data with an exponential function.

The screenshot of the LabView command window during the fiber first violin mode measurement is reported in fig. 5.14. In the upper left panel there is the plot of the shadow-sensor signal amplitude with respect to time; in the upper right corner, there is the plot of the signal power spectrum, where the resonance peak is well visible at $458Hz$; in the lower panel there is the amplitude of the analytical signal (in white), with the exponential fit (in red).

The analytical signal $z(t)$, associated to a physical signal $y(t)$, is defined as:

$$z(t) = y(t) + \breve{y}(t)$$

where $\breve{y}(t)$ is the Hilbert transform:

$$\breve{y}(t) = \frac{1}{\pi} \int_{-\infty}^{\infty} \frac{y(t')}{t - t'} dt'$$

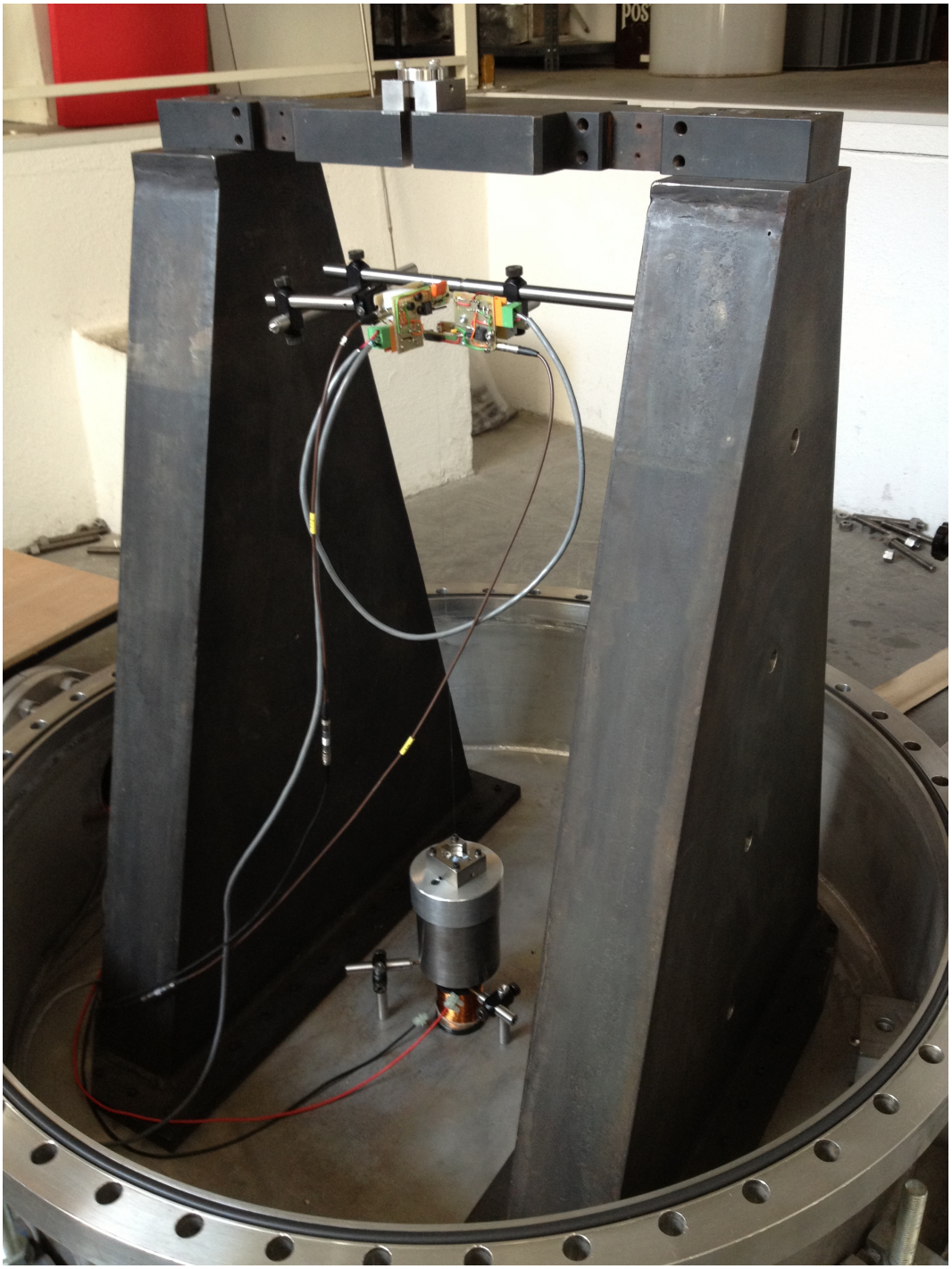

Figure 5.9: fixed steel frame for fused silica fiber measurements.

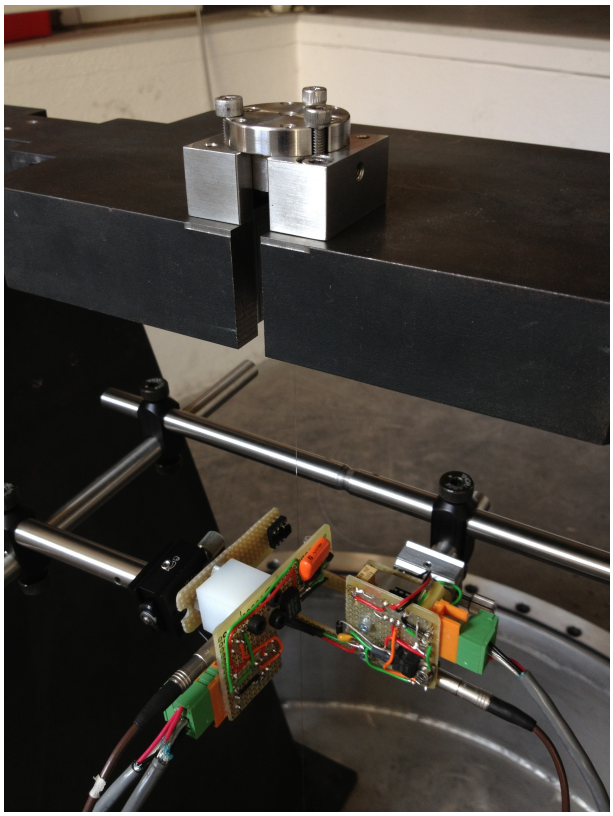

Figure 5.10: upper clamp to suspend the fused silica fiber: the regulation screws and the monitoring system, which is composed by two shadow-meters, are also visible.

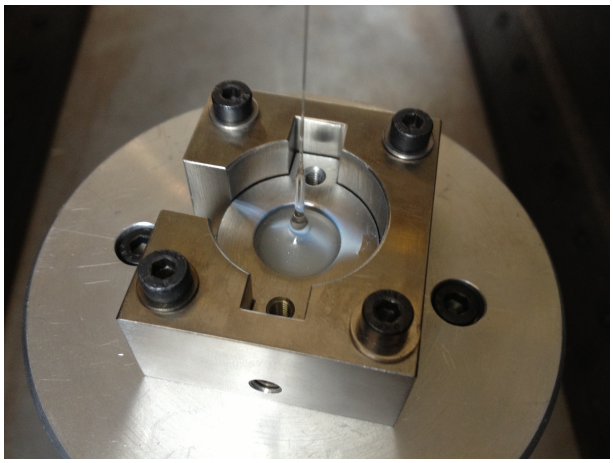

Figure 5.11: lower clamp attached to a $5kg$-mass steel cylinder.

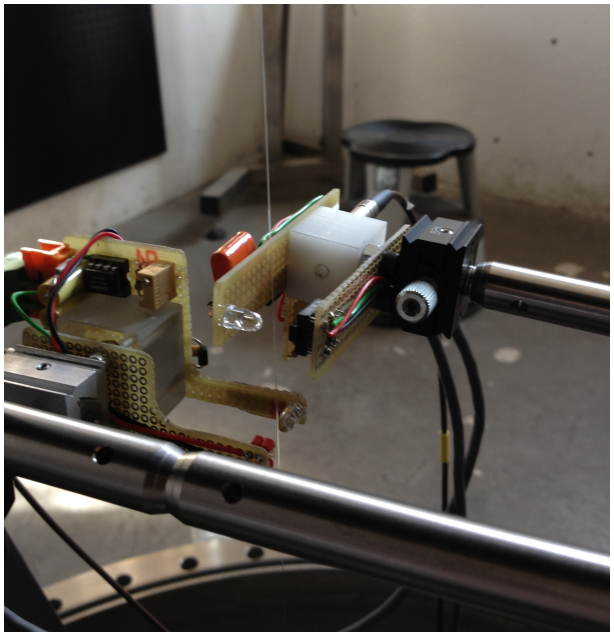

Figure 5.12: shadow-sensors to monitor the fiber position: LEDs and photodiodes are well visible.

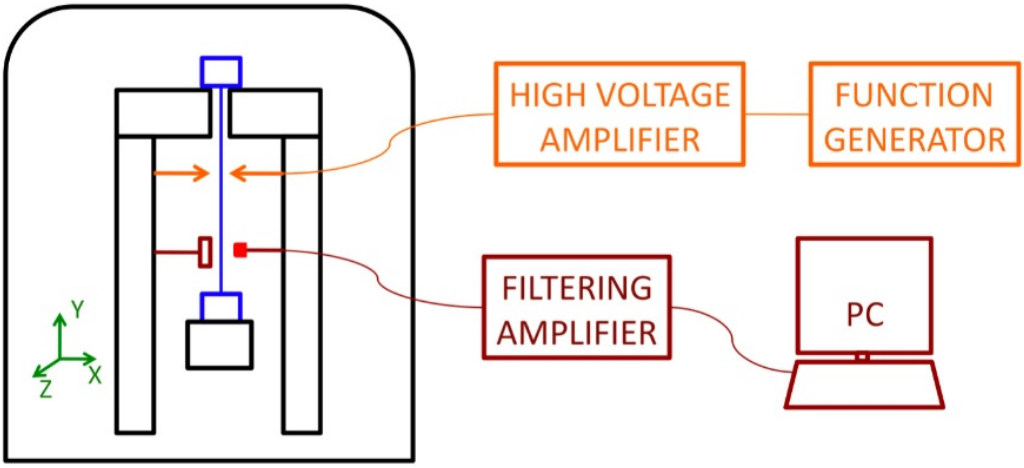

Figure 5.13: schematization of the acquisition procedure and experimental setup for fused silica fiber quality factor measurements: in black the steel structure, in blue fused silica fiber and clamps, in orange the actuation system (with the copper tip pairs) and in purple the read-out system (with LED and photodiode). In green it is reported the reference frame.

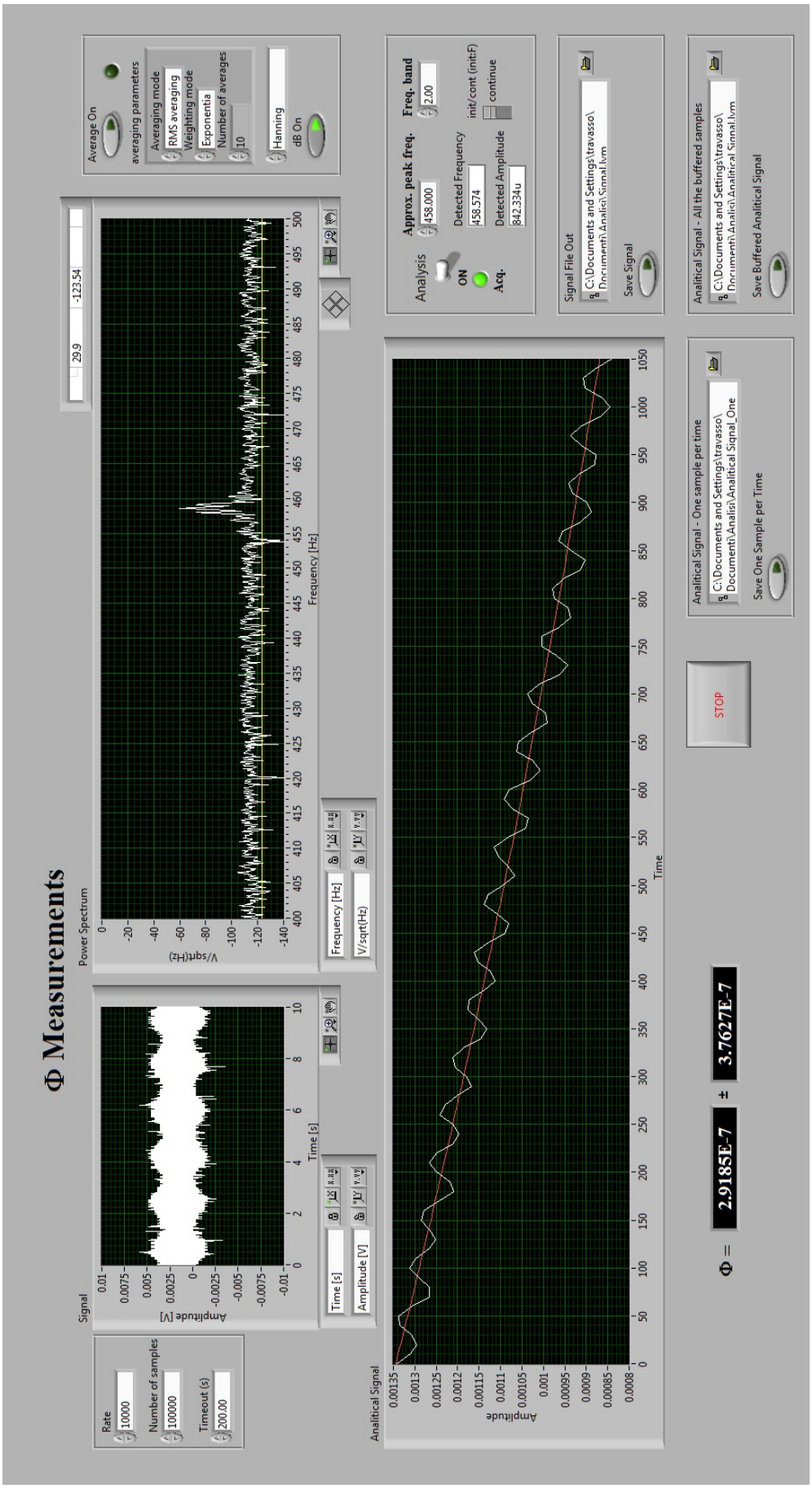

Figure 5.14: screenshot of the LabView command window.

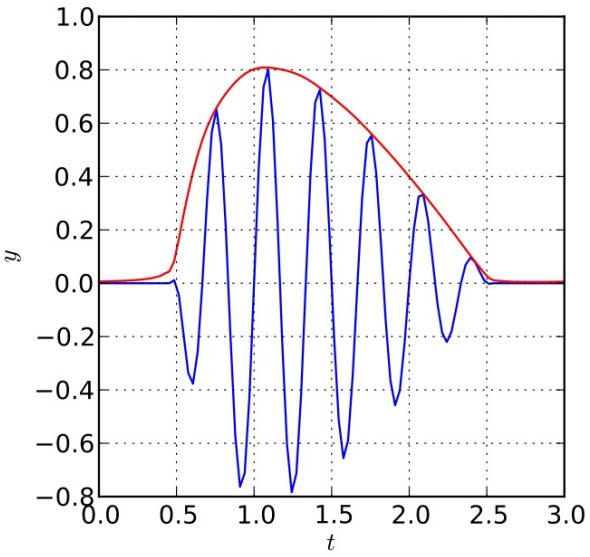

Figure 5.15: example of a real signal amplitude (in blue) and its analytical signal (in red) with respect to time.

The analytical signal amplitude $|z(t)|$ is:

$$|z(t)| = \sqrt{y(t) + \breve{y}(t)}$$

and it is the envelope of the real signal $y(t)$ (see fig. 5.15).

In a ring-down measurement, the analytical signal of the read-out physical quantity should be just an exponential function. In fig. 5.14, the analytical signal presents an oscillating behavior itself, because there is a coupling between the two violin x and z degrees of freedom; in fact, when I excited one of them, the other got often excited, depending on the harmonic.

5.3.2 Experimental results

The fused silica fiber is suspended from its ends with two clamps, identical to the Virgo+ upper clamp. In that way I did not test anchors, but only cones and their steel boxes (see sec. 4.1.2).

Since the steel boxes have several screws, it is possible to fasten or loose them, causing a change in the clamping configuration. Moreover, it is possible to vary the applied tension, changing the cylinder mass attached to the fiber.

I used two different fibers: the first was pulled in May 2012, the second produced in 2008, to check aging effects.

So, I measured violin mode quality factors in different configurations ("standard configuration" means that screws are fastened, but not too tightly, as done in Virgo+; "loose" and "tight" are to be considered with respect to standard configuration):

1. new fiber:

   - suspended mass $m = 5kg$:

  - standard configuration
  - tight upper screws.

2. aged fiber:

   - suspended mass $m = 2kg$:
     - standard configuration;
   - suspended mass $m = 5kg$:
     - standard configuration
     - tight lateral screws;
     - tight upper screws;
     - loose upper screws;

New fiber results

I performed loss angle measurements of a recently pulled fiber, suspended with a mass of $m = 5kg$, to avoid aging effects.

Loss angle results, with a standard screw regulation, are shown in fig. 5.16; while results with a tight upper-screw regulation are shown in fig. 5.17. For both cases, the x-direction data are in blue and the z-direction data in red. Note that the x and z-direction measured loss angles have the same order of magnitude, implying a similar loss mechanism for the two degrees of freedom. Consider that the z-direction is the same of the fiber pendulum mode: so, in general, the loss angle measured in that direction is higher than the one measured along x-axis.

In fig. 5.18 I compare the two different screw regulation results on loss angles. I choose to show, for each regulation, the best measured loss angle between x and z-directions, since in Virgo+ measurements, I was not able to distinguish between the two degrees of freedom. In that figure, it is evident the tight-screw-regulation measured loss angles have greater and more regular, with respect to frequency, values than the standard-screw-regulation ones, at least from the second violin order. Probably with a tight screw regulation the clamping system stiffens, but loss angle performances worse.

Measurements performed on the new fiber have loss angles values comparable with Virgo+ ones: that is true for all four monolithic payloads. In fig. 5.19 I show Virgo+ North-Input quality factor results (in blue) with new-single-fiber results: in magenta there are standard-screw-regulation data and in green the tight-screw-regulation ones. In that plot, for single-fiber data, I used the best measured quality factors between the two degrees of freedom. In fig. 5.20 I superposed the West-End data with the new-single-fiber measurements.

Aged fiber results

To see aging effects on fused silica fibers I performed loss angle measurements on an aged single fiber.

I compared the x-direction violin mode quality factor results obtained attaching to the fiber a mass $m = 2kg$ and a mass $m = 5kg$. Since the violin dilution factor D_n^v

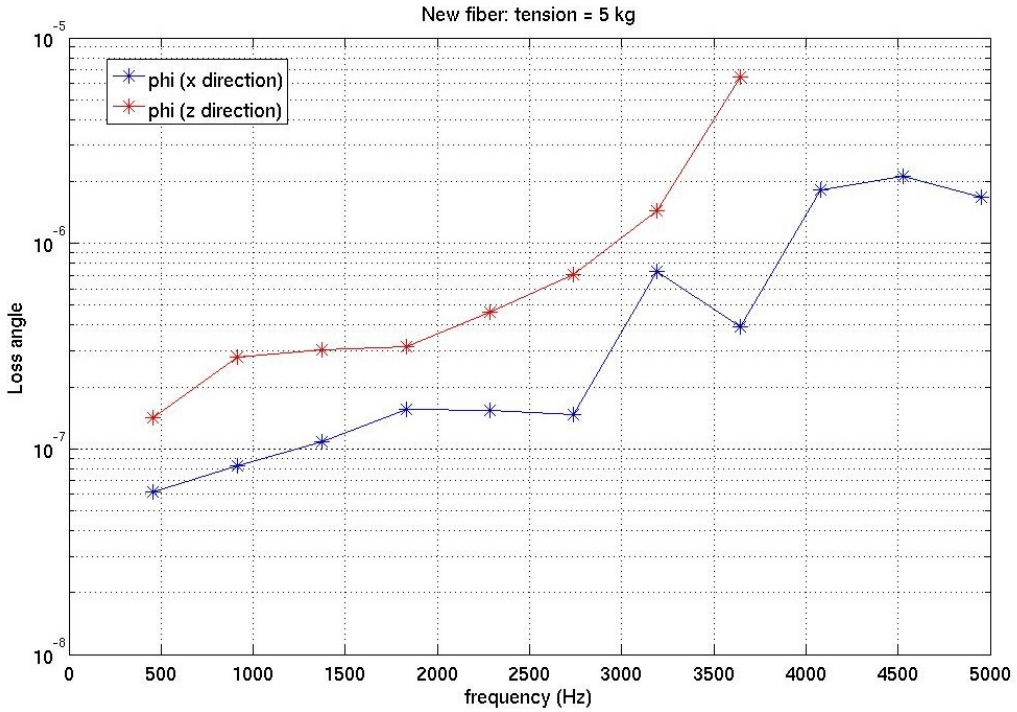

Figure 5.16: new fiber loss angle measurements, with a standard screw regulation: in blue the x-direction data, in red the z-direction ones.

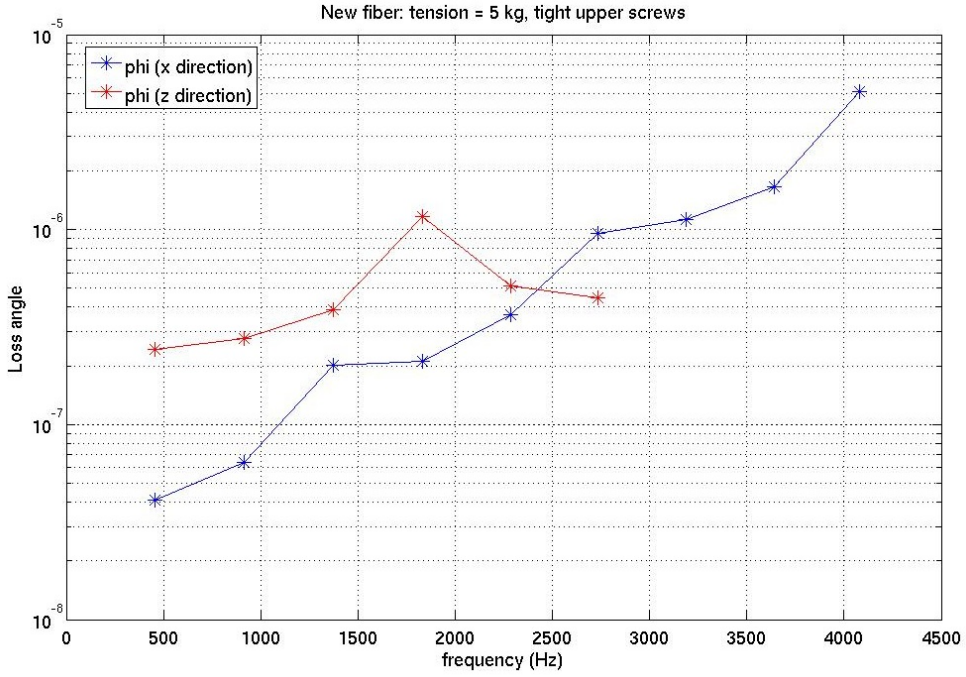

Figure 5.17: new fiber loss angle measurements, with a tight upper screw regulation: in blue the x-direction data, in red the z-direction ones.

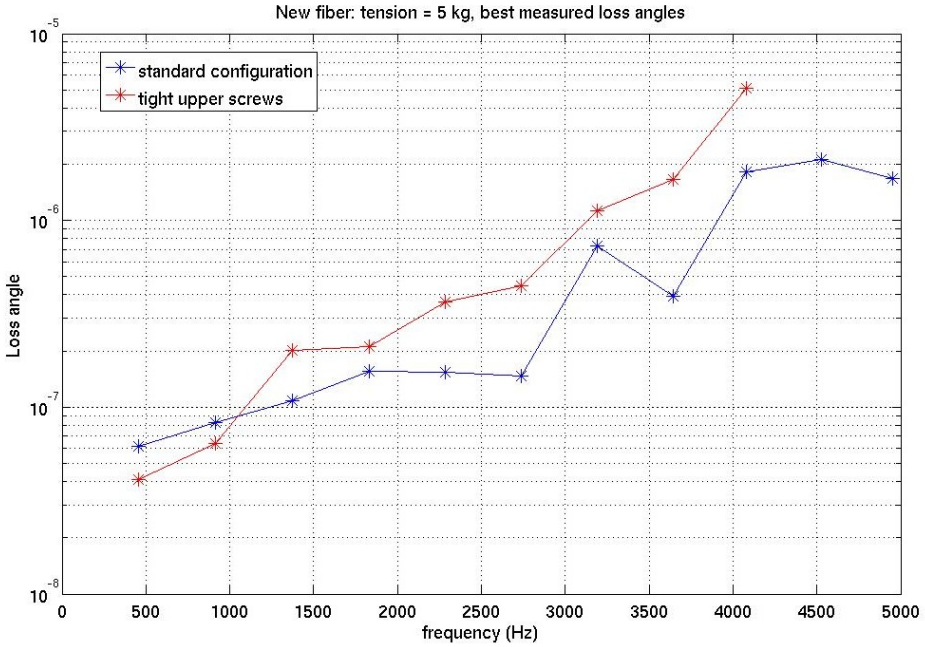

Figure 5.18: comparison between the two different upper screw regulations: in blue the Virgo+ standard regulation, in red the tight one. Note that in this comparison I report the best measured loss angles, not doing any distinction among x and z degrees of freedom.

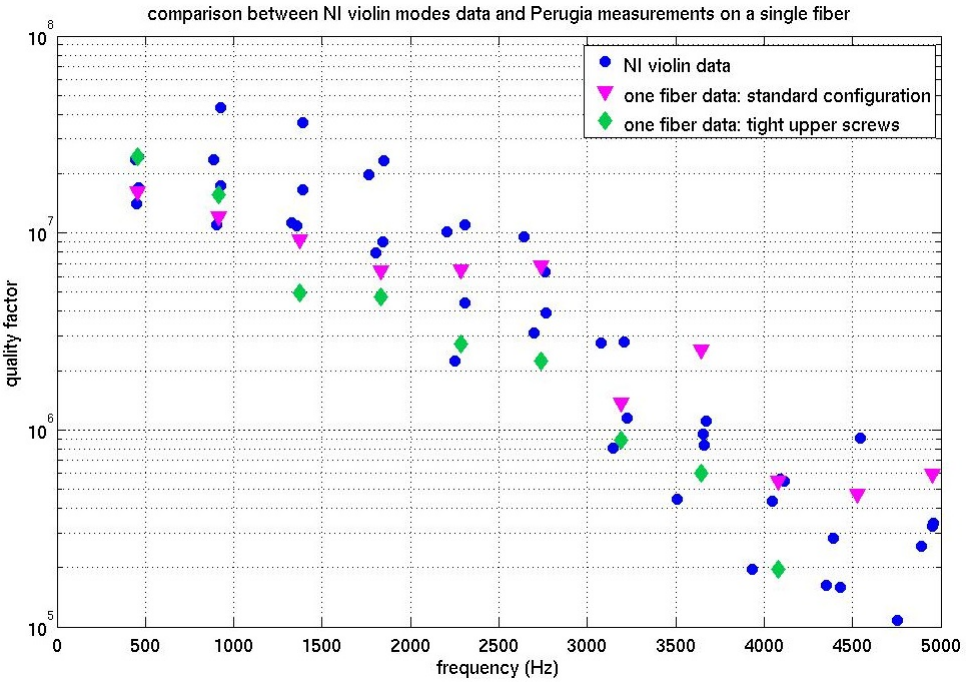

Figure 5.19: comparison between Virgo+ North-Input quality factor results (in blue) with new-single-fiber results: in magenta there are standard-screw-regulation data and in green the tight-screw-regulation ones.

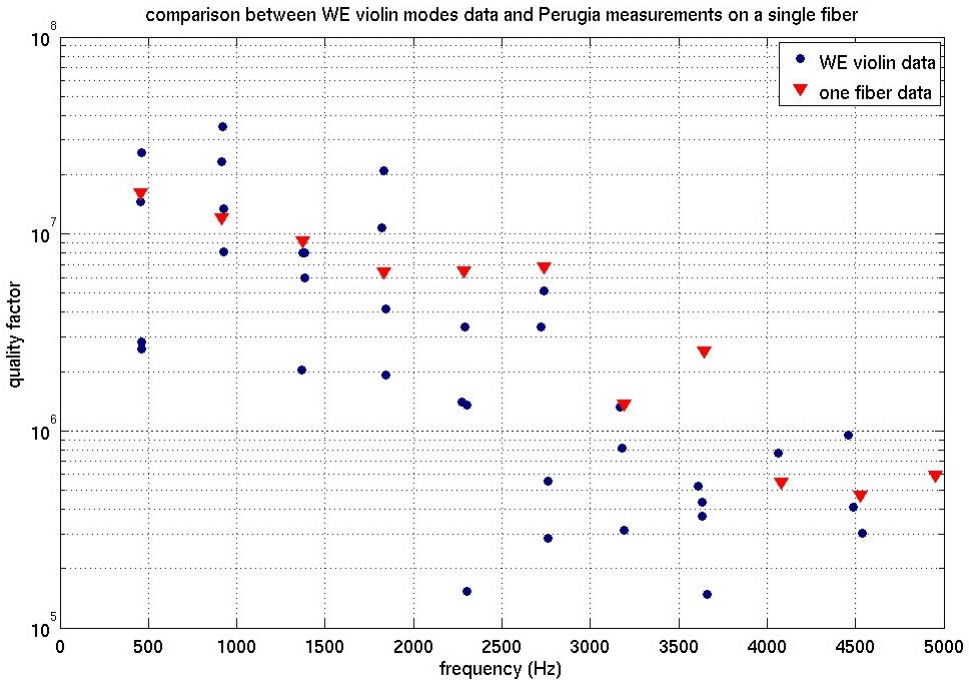

Figure 5.20: comparison between Virgo+ West-End quality factor results (in blue) with new-single-fiber results (in red): single-fiber measurements are performed with a standard screw regulation.

depends on the applied tension (see eq. 5.4), I expect that loss angles ϕ_2 measured with the mass of $m_2 = 2kg$ is greater than loss angles ϕ_5 measured with a fiber tension of $m_5 = 5kg$:

$$\frac{\phi_2}{\phi_5} = \sqrt{\frac{m_5 g}{m_2 g}} = \sqrt{\frac{5}{2}} \sim 1.6$$

Actually this is a very low difference to be measured: in fact, from my experimental results, this is not visible (see fig. 5.21); on the contrary, it appears that loss angles ϕ_2 are lower than ϕ_5. Probably, during the tension change, I changed also the screw configuration of the lower fiber clamp steel box modifying loss angle performances.

So, I tried to change the screw regulation of the upper clamp to see how loss angles are influenced by. Results are reported in figs. 5.22 and 5.23.

It is evident that, changing a bit the screw regulation, loss angles change a lot, not only in absolute value, but also in frequency behavior. Moreover, it is not clea what is the screw configuration which minimize the loss angle values in both directions.

That is a crucial point: the scattered violin quality factors measured in Virgo+ monolithic suspensions depend on the upper-clamp-screw regulation.

I superposed the Virgo+ quality factor results and the single fiber results obtained with the standard screw regulation: in fig. 5.24 I show the North-End data. Even if the two data samples have the same trend, values of the single fiber quality factors are lower than North-End quality factors; the same happens for all the four monolithic payloads.

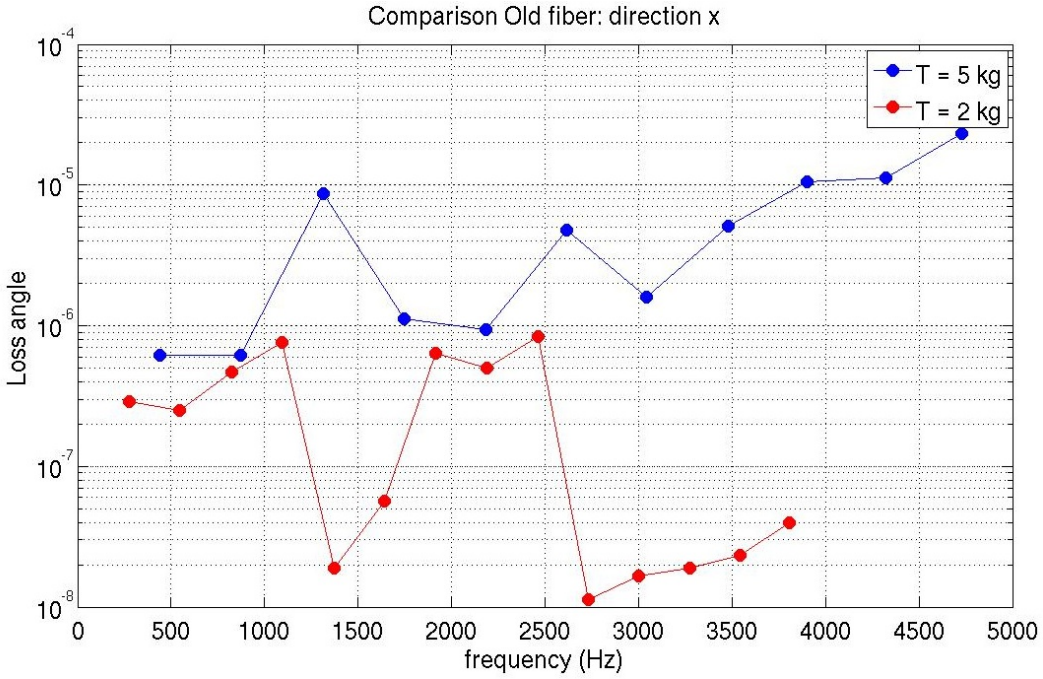

Figure 5.21: comparison between loss angles measured with a suspended mass of $m_5 = 5kg$ (in blue) and loss angles measured with a suspended mass of $m_2 = 2kg$ (in red).

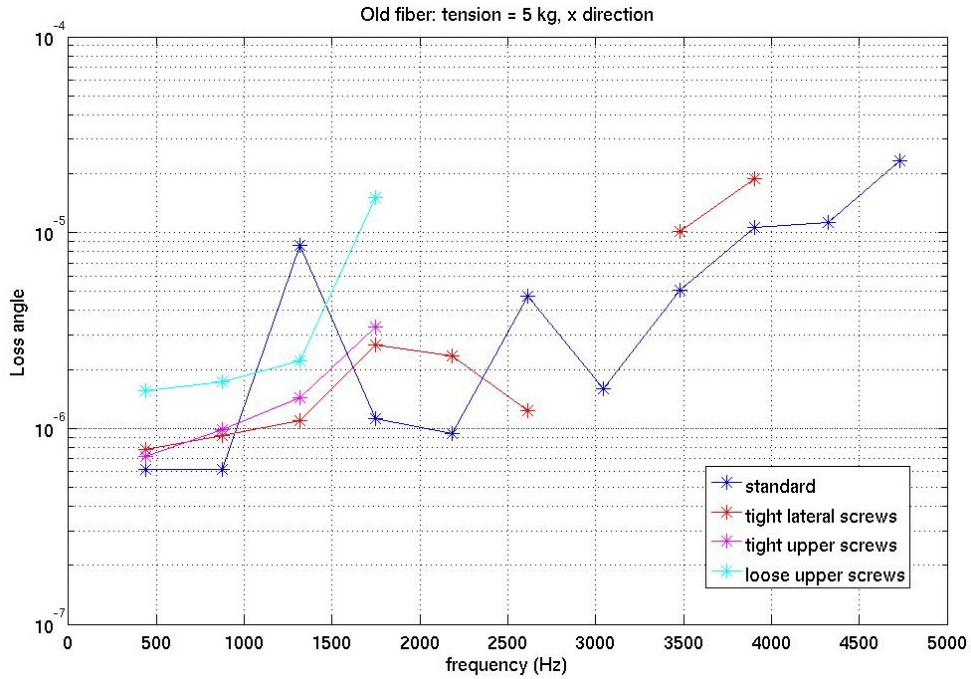

Figure 5.22: comparison between different upper-clamp-screw regulations: measurements of x-direction violin mode: "standard" means a screw regulation similar to Virgo+ one, "tight" means a screw regulation tighter than Virgo+ one and "loose" means a screw regulation looser than Virgo+ one.

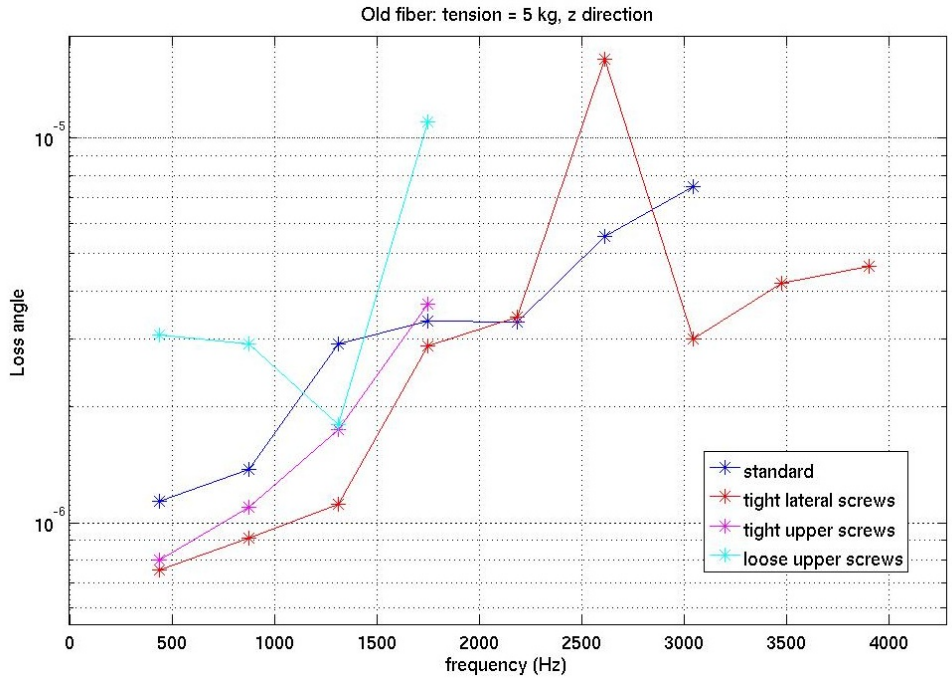

Figure 5.23: comparison between different upper-clamp-screw regulations: measurements of z-direction violin mode.

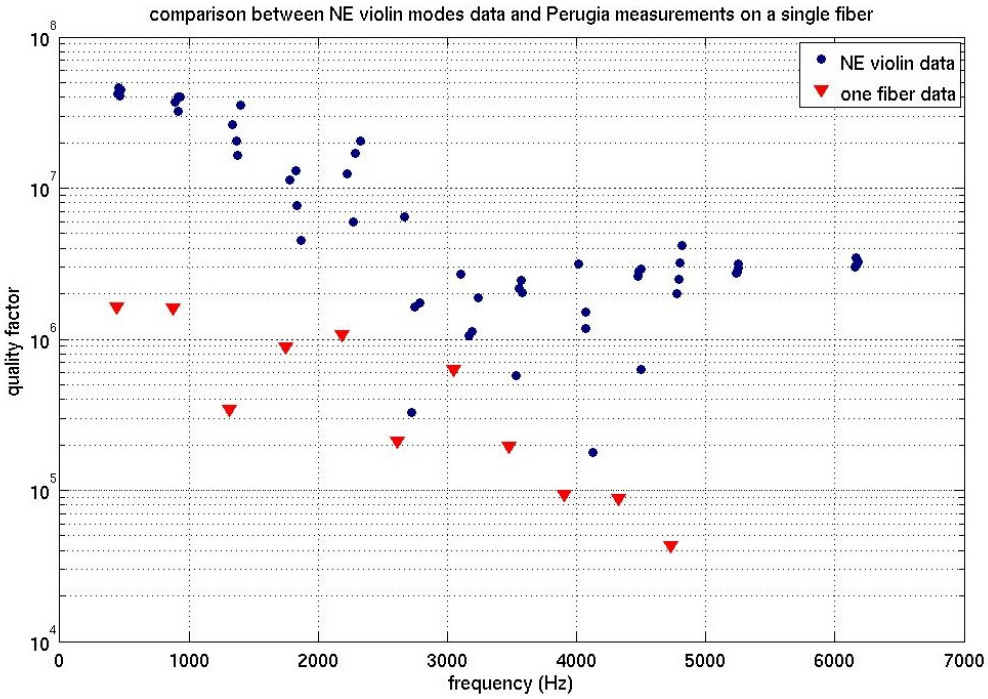

Figure 5.24: comparison between North-End monolithic suspension quality factors (blue circles) and aged single fiber suspension (red triangles).

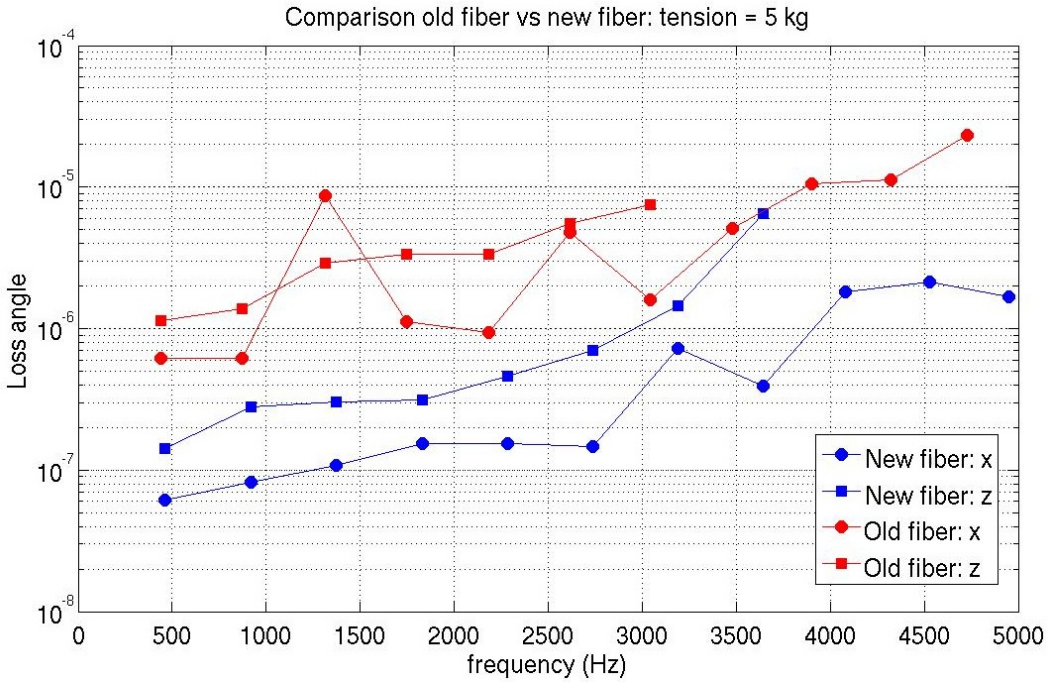

Figure 5.25: comparison between new fiber loss angles (in blue) and aged fiber ones (in red): x degree of freedom data are reported with circles, while the z ones are reported with squares.

That can be explained as an aging of the fiber used for the tests in Perugia: that fiber was pulled in 2008 and then kept in a clean room, under vacuum. Although the fiber was not in a polluted environment, the aging has a relevant effect on loss angle performances.

5.3.3 Single fiber conclusions

Measurements performed on the new fiber have better loss angle values with respect to the aged fiber ones: at least one order of magnitude is gained. This is evident in fig. 5.25, where I show the comparison between new fiber loss angles (in blue) and aged fiber ones (in red), both with a standard screw regulation.

Furthermore, note that the two fibers has slightly different violin resonance frequencies, even if I have used the same suspended mass of $m = 5kg$, since their length is a bit different. The aged fiber first violin is at a frequency $f_{aged} = 438.36Hz$, which corresponds to a fiber length of $L_{aged} = 0.68m$; while the new fiber first violin is at a frequency $f_{new} = 458.50Hz$, which corresponds to a fiber length of $L_{new} = 0.65m$. Consider that, for Virgo+, North-Input first violin mode is at a frequency $f_{NI} = 443.34Hz$, which is consistent with a fiber length of $L_{NI} = 0.67m$: in fact, nominally each Virgo+ fiber has a total length of $L = 0.70m$, including also the two bending lengths.

With this measurement campaign I proved that Virgo+ violin mode quality factors are due to an additional loss mechanism in the upper clamp system. Simply fastening

or loosening a screw of the steel box which contains the fused silica cone welded to the fiber, it is possible to change loss angle values and their frequency dependence.

That implies a changing of fused silica clamping system for Advanced Virgo project; the idea is to use an upper clamp similar to lower clamps, the anchors, to avoid any screw regulation. The design of the new clamping system is currently under evaluation, using both numerical simulation and measurements.

A table with all the single fiber quality factor results is reported in appendix D. In that table errors are estimated with the standard deviation, since I have at least three different measurements for each mode.

Chapter 6

Thermal noise curve estimation

To evaluate thermal noise in Virgo+ we have to take into account the suspension contribution, which includes pendulum, vertical and violins modes, and the mirror bulk one.

A theoretical model is necessary to understand which kinds of loss mechanisms are going on in the physical system. For suspension thermal noise an analytical model has been developed, while for bulk thermal noise a finite element model is required.

In this chapter I present the way to compute Virgo+ thermal noise for each component. At first, I report the analytical model used to describe the mirror pendulum mode [109]. Then, for the bulk analysis, the finite element model of Virgo+ mirror is reported [149]. Finally I show the thermal noise upper limit estimation for Virgo+ interferometer.

6.1 Analysis procedure

The knowledge of mechanical resonance quality factors is not sufficient to evaluate thermal noise affecting a physical system. In fact, a measured quality factor Q_{meas} is the sum of several contributes as:

$$\frac{1}{Q_{meas}} = \sum_i \frac{1}{Q_i}$$

where each Q_i is the quality factor coming from the i-th mechanism loss. As, said in chapter 3, there are many mechanism losses which have different frequency dependence (consider just the difference between structural and viscous losses, see sec. 3.2). Taking into account each mechanism damping is fundamental to a correct evaluation of thermal noise.

A theoretical model could help the loss mechanism understanding: through a comparison between experimental results and predicted values it is possible to have hints on what is going on in the physical system.

The following steps are necessary to correctly estimate thermal noise of a generic physical system:

1. measuring mechanical quality factors: it is much better to have an independent estimation of quality factors for each part composing the physical system; in that way couplings between parts are reduced;

2. defining a theoretical model of the physical system, whether analytical or numerical: it is important to fix as much physical and geometrical uncoupled parameters as possible, to reduce variables in further analysis;

3. optimizing uncoupled parameters to fit measured frequencies and quality factors (see fig. 6.1): this step is the most difficult, since it implies an "inverse problem" solution to evaluate the coupled quality factors;

4. putting uncoupled quality factors in the equations of motion to solve them and to find the impedence Z or the transfer function of the system to apply the fluctuation-dissipation theorem (see sec. 3.1).

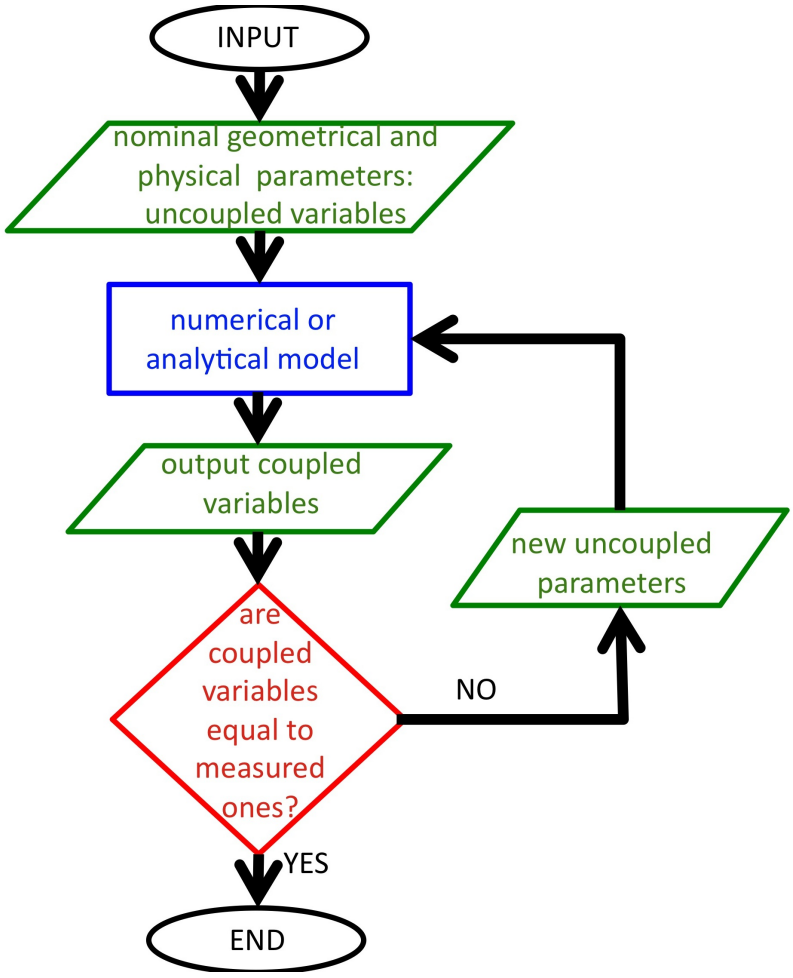

Figure 6.1: analysis procedure flowchart to optimize model parameters and fit experimental results: starting from nominal parameter values, a numerical or analytical model gives some output variables to be compared to measured ones; if the output quantities differ from experimental results, new input parameters are taken.

6.2 Suspension contribution

Pendulum and vertical thermal noise contributions are evaluated using a simple analytical model, as explained in sec. 3.5.1 [109].

The last stage suspension system can be schematized as a branched combination of three harmonic oscillators, as shown in fig. 6.2. Indices 1, 2, 3 are respectively used for the marionette, the mirror and the reaction mass; x is the body position, M is its mass, K is the wire elastic constant and β is its viscous coefficient.

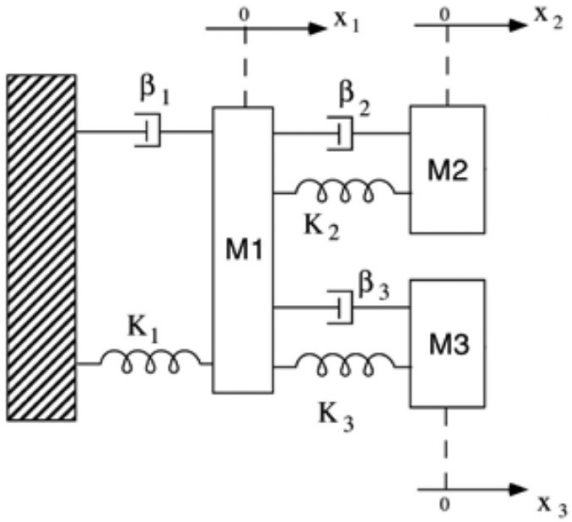

Figure 6.2: schematization of Virgo+ branched system payload: indices 1, 2 and 3 are respectively used for the marionette, the mirror and the reaction mass; x is the body position, M is its mass, K is the wire elastic constant and β is its viscous coefficient.

For the **pendulum mode**, the equation of motion are:

$$\begin{cases} \ddot{x}_1 + \frac{\omega_1}{Q_1}\dot{x}_1 + \mu_{12}\frac{\omega_2}{Q_2}(\dot{x}_1 - \dot{x}_2) + \omega_1^2 x_1 + \mu_{21}\omega_2^2(x_1 - x_2) + \\ \qquad + \mu_{31}\frac{\omega_3}{Q_3}(\dot{x}_1 - \dot{x}_3) + \mu_{31}\omega_3^2(x_1 - x_3) &= \frac{f_1 - f_2 - f_3}{M_1} \\ \ddot{x}_2 + \frac{\omega_2}{Q_2}(\dot{x}_1 - \dot{x}_2) + \omega_2^2(x_1 - x_2) &= \frac{f_2}{M_2} \\ \ddot{x}_3 + \frac{\omega_3}{Q_3}(\dot{x}_1 - \dot{x}_3) + \omega_3^2(x_1 - x_3) &= \frac{f_3}{M_3} \end{cases} \tag{6.1}$$

where $\mu_{12} = M_2/M_1$ and $\mu_{13} = M_3/M_1$ are the mass ratios, ω_i is the i-th body uncoupled resonance frequency, Q_i is the i-th body uncoupled quality factor of the mechanical resonance and f_i is the stochastic uncoupled generalized force.

Taking the Fourier transform of this system, we can write:

$$\hat{D}\begin{pmatrix} \hat{X}_1 \\ \hat{X}_2 \\ \hat{X}_3 \end{pmatrix} = \begin{pmatrix} (\hat{F}_1 - \hat{F}_2 - \hat{F}_3)/M_1 \\ \hat{F}_2/M_2 \\ \hat{F}_3/M_3 \end{pmatrix}$$

where $\hat{X}_i$ is the i-th body position Fourier transform, $\hat{F}_i$ is the i-th body generalized force Fourier transform and $\hat{D}$ is the matrix:

$$\hat{D} = \begin{pmatrix} -\omega^2 + \omega_1^2 + \mu_{12}\omega_2^2 + \mu_{13}\omega_3^2 + i\omega\left(\frac{\omega_1}{Q_1} + \mu_{12}\frac{\omega_2}{Q_2} + \mu_{13}\frac{\omega_3}{Q_3}\right) & -\mu_{12}\omega_2^2 - i\omega\mu_{12}\frac{\omega_2}{Q_2} & \mu_{13}\omega_3^2 - i\omega\mu_{13}\frac{\omega_3}{Q_3} \\ -\omega_2^2 - i\omega\frac{\omega_2}{Q_2} & -\omega + \omega_2^2 + i\omega\frac{\omega_2}{Q_2} & 0 \\ -\omega_3^2 - i\omega\frac{\omega_3}{Q_3} & 0 & -\omega + \omega_3^2 + i\omega\frac{\omega_3}{Q_3} \end{pmatrix}$$

Diagonalizing the matrix $\hat{D}$, i.e. decoupling degrees of freedom in equations of motions eq. 6.1, it is possible to find the coupled quality factors, linked to normal resonance modes of the system, which are measured quantities. The measured pendulum quality factor is the combination of the three uncoupled quality factors of the marionette, the reaction mass and the mirror, as [109]:

$$Q^{pend}_{meas} = \omega_0 M_0 \left[\frac{\omega_1 M_1}{Q_1} \left(1 - \frac{\omega_0^2}{\omega_3^2}\right)^2 + \frac{\omega_3 M_3}{Q_3} \frac{\omega_0^4}{\omega_3^4} - \frac{\omega_2 M_2}{Q_2} \left(\frac{\omega_1^2\omega_3^2 + \omega_0^4 - \omega_0^2(\omega_1^2 + \omega_3^2 + \mu_{13}\omega_3^2)}{\mu_{12}\omega_2^2\omega_3^2} \right) \right]^{-1}$$

where ω_0 is the coupled resonance frequency linked to the mirror pendulum mode (in Virgo+ suspension $\omega_0 = 2\pi\, 0.59Hz$) and M_0 is the pendulum effective mass. Note that each Q_i is the sum of structural and viscous contribution of the i-th uncoupled body suspension wires.

To evaluate thermal noise, the $\hat{D}$ matrix can be expressed in terms of the impedence matrix $\hat{Z}$:

$$\hat{Z} \begin{pmatrix} \hat{X}_1 \\ \hat{X}_2 \\ \hat{X}_3 \end{pmatrix} = \begin{pmatrix} \hat{F}_1 - \hat{F}_2 - \hat{F}_3 \\ \hat{F}_2 \\ \hat{F}_3 \end{pmatrix}$$

where:

$$\hat{Z} = \frac{1}{i\omega} \begin{pmatrix} M_1 D_{11} & M_1 D_{12} & M_1 D_{13} \\ M_2 D_{21} & M_2 D_{22} & M_2 D_{23} \\ M_3 D_{31} & M_3 D_{32} & M_3 D_{33} \end{pmatrix}$$

Once that matrix is found, the pendulum thermal noise is:

$$S_x^{pend}(\omega) = \frac{4k_B T}{\omega^2} \mathcal{R}e\left[\hat{Z}_{22}^{-1}(\omega)\right] \tag{6.2}$$

where we consider only the inverse of the term $\hat{Z}_{22}$ since the mirror is the main contribution.

Vertical modes can be computed in a similar way, substituting conveniently resonance frequencies and elastic constants in equations of motion. There are two resonance frequencies for vertical modes, at $\sim 5.9Hz$ and at $\sim 14.8Hz$. Their quality factors are linked to uncoupled quality factors as:

$$\begin{aligned} Q^{vert}_{meas,0} &= \omega_0 M_0 \left[\frac{\omega_1 M_1}{Q_1} \left(1 - \frac{\omega_0^2}{\omega_3^2}\right)^2 + \frac{\omega_3 M_3}{Q_3} \frac{\omega_0^4}{\omega_3^4} - \frac{\omega_2 M_2}{Q_2} \left(\frac{\omega_1^2\omega_3^2 + \omega_0^4 - \omega_0^2(\omega_1^2 + \omega_3^2 + \mu_{13}\omega_3^2)}{\mu_{12}\omega_2^2\omega_3^2} \right) \right]^{-1} \\ Q^{vert}_{meas,+} &= \omega_+ M_+ \left[\frac{\omega_1 M_1}{Q_1} + \frac{\omega_2 M_2}{Q_2} \left(\frac{\omega_+^2}{\omega_+^2 - \omega_2^2} \right)^2 + \frac{\omega_3 M_3}{Q_3} \left(\frac{\omega_+^2}{\omega_+^2 - \omega_3^2} \right)^2 \right]^{-1} \end{aligned}$$

where $\omega_0 = 2\pi\, 5.9Hz$, $\omega_+ = 2\pi 14.8Hz$ and M_0 and M_+ are vertical mode effective masses.

The steps described for pendulum mode, are still valid for vertical ones. So, thermal noise vertical contribution is (see eq. 3.52):

$$S_X^{vert}(\omega) = \theta_0 \frac{4k_B T}{\omega^2} \mathcal{R}e\left[\hat{Z}_{22}^{-1}(\omega)\right] \tag{6.3}$$

where $\theta_0 \sim 0.24 \mu rad$ (see sec. 3.5.1).

Violin mode thermal noise contribution is computed through the normal mode expansion:

$$S_X^{viol}(\omega) = N \frac{4k_B T}{\omega} \sum_n \frac{\phi_n \omega_n^2}{m_n \left[(\omega^2 - \omega_n^2)^2 + \phi_n^2 \omega_n^4\right]} \tag{6.4}$$

where N is the number of suspending wires, m_n is the effective mass of the n-th order violin (see eq. 3.58), ϕ_n is the loss angle (eq. 3.56), and ω_n is the violin resonance frequency (eq. 3.54).

The overall suspension thermal noise is the sum of the three contributions expressed in eq. 6.2, 6.3 and 6.4; expressing thermal noise in terms of the strain amplitude of gravitational waves $h(\omega)$, we have to divide for the interferometer arm length $L_{arm} = 3km$:

$$h_{TN}(\omega) = \frac{2}{L_{arm}} \sqrt{S_X^{pend} + S_X^{vert} + S_X^{viol}} \tag{6.5}$$

In fig. 6.3 I report the strain amplitude due to thermal noise contribution, estimated with eq. 6.5, with respect to frequency [150].

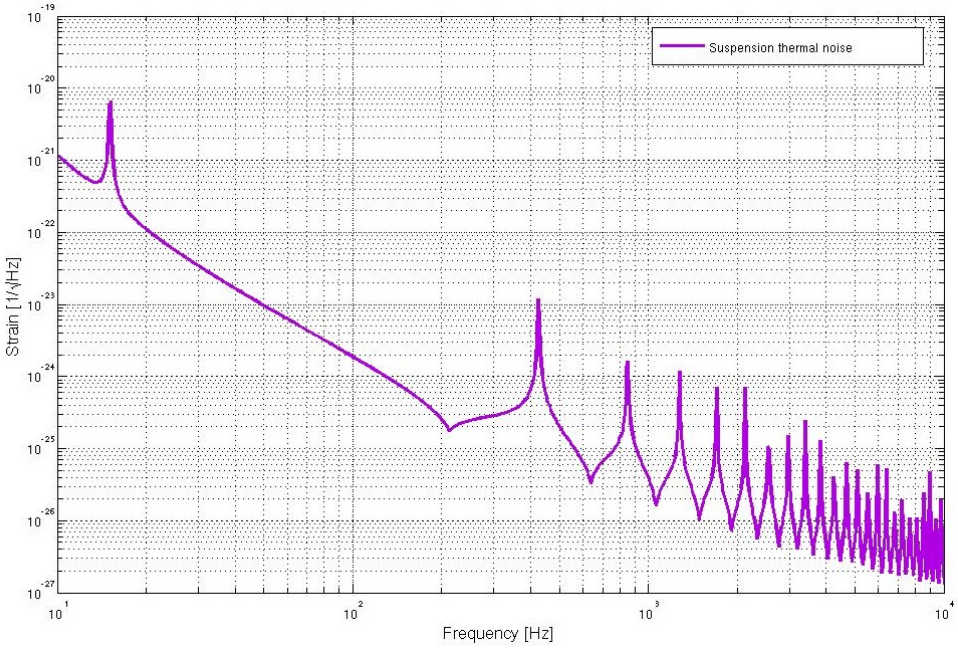

Figure 6.3: Virgo+ suspension thermal noise estimation in terms of strain gravitational wave signal amplitude with respect to frequency: pendulum mode, vertical modes and violin modes are considered.

6.3 Mirror bulk contribution

Bulk thermal noise contribution is evaluated using a finite element model, computed with an Ansys script [149]. In Ansys simulation each mirror is composed by different parts:

- the bulk the main part of the mirror, composed by a fused silica cylinder;
- the coating, which is composed by a two-material multilayer: Ta_5O_2 with a high refractive index, and SiO_2 with a low refractive index; the two-material alternation allows us to achieve the total reflectivity necessary for Virgo+ interferometer;
- the ears, which are fused silica components, attached through silicate bonding to the bulk (see sec. 4.1.2);
- the anchors, which are of the same material of bulk and fibers, glued through water glass to the ears (see sec. 4.1.2).

Since input and end mirrors have different geometrical sizes, we developed two models (see fig. 6.4); mirror nominal parameters are reported in tab. 6.1.

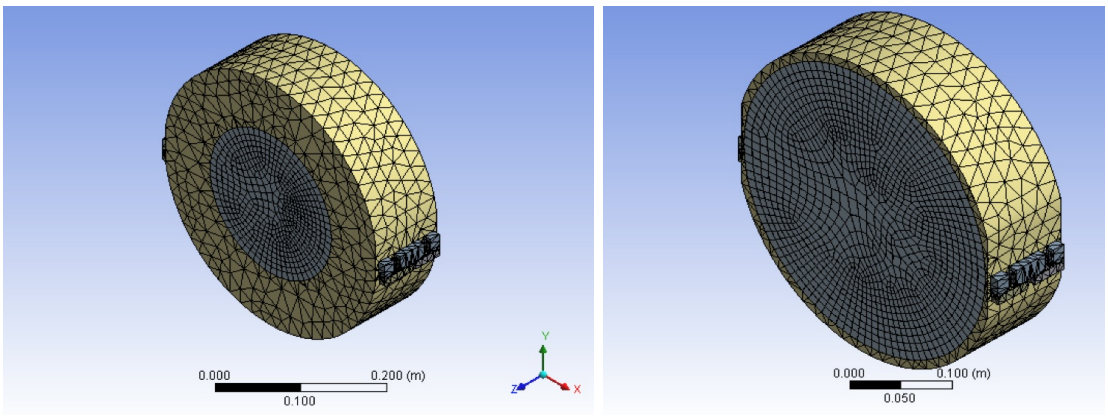

(a) Input mirror model (b) End mirror model

Figure 6.4: finite element models of input and end mirrors: the meshing used for numerical computation is well visible; in grey the mirror coating layers are shown.

To compute mirror thermal noise given by structural losses, we use the Levin's approach (eq. 3.50), supposing frequency independent loss angles:

$$S_X^{struct}(\omega) = \frac{8k_BT}{\omega F_0^2} U_{tot}\phi_{tot}^{struct} = \frac{8k_BT}{\omega F_0^2} U_{tot} \left(\sum_i \phi_i \frac{U_i}{U_{tot}} \right)_{struct} \tag{6.6}$$

where F_0 is the oscillating force amplitude, U_{tot} is the maximum strain energy stored in all the system, U_i is the maximum strain energy stored in the i-th part of the mirror and ϕ_i is the corresponding loss angle.

The finite element model allows us to compute easily the total structural loss angle, i.e. the term in the brackets of eq. 6.6; in particular we can evaluate the strain

	INPUT	**END**
Bulk		
thickness (m)	0.100	0.100
diameter (m)	0.350	0.350
flat height (m)	0.050	0.100
density (kg/m^3)	2200	
Young's modulus (GPa)	72.3	
Poisson ratio	0.17	
Coating		
diameter (m)	0.200	0.330
Ta_5S_2 thickness (μm)	0.956	2.393
SiO_2 thickness (μm)	2.388	4.1086
Ta_5S_2 loss angle	$5 \cdot 10^{-5}$	
SiO_2 loss angle	$2 \cdot 10^{-4}$	
Ta_5S_2 density (kg/m^3)	8200	
SiO_2 density (kg/m^3)	2200	
Ta_5S_2 Young's modulus (GPa)	140	
SiO_2 Young's modulus (GPa)	72.7	
Ta_5S_2 Poisson ratio	0.26	
SiO_2 Poisson ratio	0.167	
Silicate bonding		
thickness (nm)	60	
area (cm^2)	$2 \cdot 18$	
density (kg/m^3)	2200	
Young's modulus (GPa)	72.9	
Poisson ratio	0.17	
loss angle	0.1	
Water glass		
area (cm^2)	$4 \cdot 3$	
density (kg/m^3)	2200	
Young's modulus (GPa)	72.9	
Poisson ratio	0.17	
loss angle $\cdot$ thickness (μm)	0.5	

Table 6.1: Input and End mirrors nominal geometrical and physical parameters used in finite element simulation: I distinguish between bulk, coating, silicate bonding and water glass material.

energy per part and per layer dU_i/ds, so that the total loss angle can be re-written as:

$$\phi_i^{struct} = \frac{s_i}{U_{tot}} \frac{dU_i}{ds} \phi_i \tag{6.7}$$

where s_i is the layer thickness. So, knowing the layer thickness and loss angle from measurements and computing the strain energy from the finite element model, we can apply that expression to evaluate total loss angles ϕ_i^{struct} for the Virgo+ coatings, silicate bonding and water glass.

In tab. 6.1, I report the typical coating layer thickness [151], and the typical silicate bonding thickness [152]. On the contrary, there is no evidence about the water glass typical thickness: so, we decide to vary the product $\phi_{WG} \cdot s_{WG}$, until the measured quality factors are fitted. We find that the value $\phi_{WG} \cdot s_{WG} = 0.5 \mu m$ well fits the experimental results (see fig. 6.5).

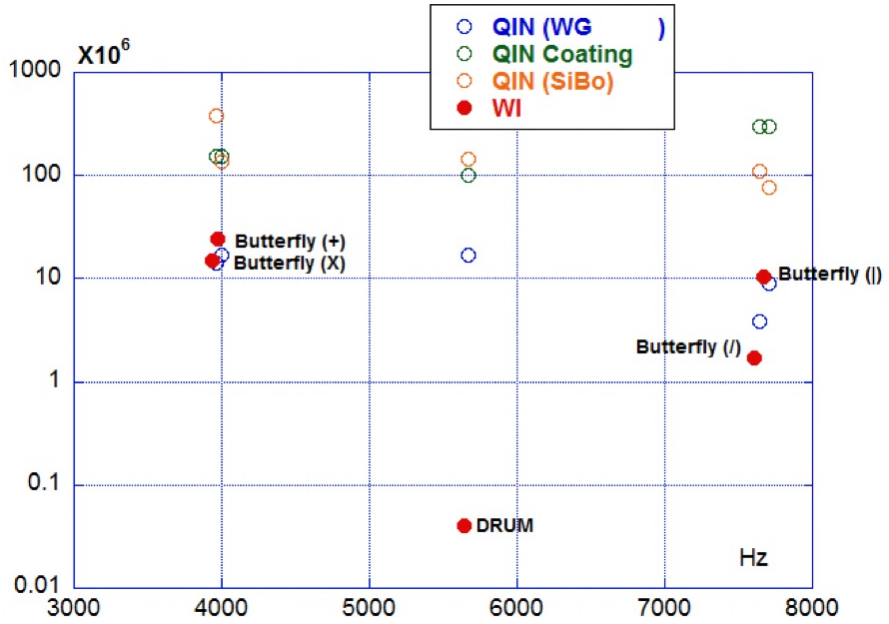

Figure 6.5: West-Input measured quality factors of the first five internal modes (in red) compared with upper limits set by different loss mechanisms: water glass (in blue), mirror coating (in green) and silicate bonding (in orange).

In fig. 6.5 I report the comparison between West-Input measured quality factors and upper limit quality factor computed for different loss mechanisms (coatings, silicate bonding and water glass with $\phi_{WG} \cdot s_{WG} = 0.5 \mu m$). For the butterfly modes there is a good agreement between measured and simulated data, while it is not true for the drum mode. The same behavior it is found for all monolithic payloads.

Probably, drum modes are affected by further loss mechanisms that lower quality factors. In fact:

- for the North-Input, there is a coupling between the drum mode and the XIII order violin mode (see sec. 4.6.3): that coupling lowers drum mode quality factor, but not affects the off-resonance thermal noise;

- for the West-Input, the drum mode has the lowest quality factor among bulk modes ($Q_{WI}^{drum} \approx 40000$): we consider that value is given by a viscous damping, even if its nature is not sure. In fact, considering the same viscous process acting on overall drum modes of the West-Input payload, we can derive the viscous coefficient β from eq. 3.9:

$$Q_{visc}^{D1} = \frac{\omega_{D1} m_{D1}}{\beta} \tag{6.8}$$

  where ω_{D1} is the first drum resonance frequency and m_{D1} is its effective mass. Then, we compute the limit quality factor Q_{visc}^{D2} of the second drum mode using the same viscous coefficient, finding a quality factor smaller than the measured one ($Q_{visc}^{D2} = 42000 \ll 192000 = Q_{meas}^{D2}$). So, even if there is no clue of its viscous nature, we take the worst possible case, considering the first drum mode as viscous;

- for the End mirrors, drum modes have low quality factor, but not so low to be explained in term of viscous loss mechanism.

To take into account possible viscous effects on drum modes in thermal noise estimation, we sum to the Levin formula (eq. 6.6) a term given by the normal expansion contribution of the West-Input payload, which is the dominant one:

$$S_X^{visc}(\omega) = \frac{4k_B T}{\omega} \frac{\phi_{visc}}{m_{D1}\omega_{D1}^2} \tag{6.9}$$

where m_{D1} is the first drum effective mass, ω_{D1} is its frequency and ϕ_{visc} is the drum loss angle, depending on the measure quality factor as:

$$\phi_{visc}(\omega) = \frac{\omega}{\omega_{D1}} \frac{1}{Q_{D1}^{meas}} \tag{6.10}$$

Finally, the mirror thermal noise estimation is the sum of two contribution, structural (eq. 6.6) and viscous (eq. 6.9):

$$S_X^{bulk}(\omega) = S_X^{struct}(\phi_{struct}) + S_X^{visc}(\phi_{visc}(\omega))$$

The result of that computation is shown in fig. 6.6 with all thermal noise contributions: the red solid line corresponds to suspension thermal noise, the black solid line is the bulk contribution, while the green solid line is the quadratic sum of overall terms, considering suspensions, structural and viscous mirror bulk modes.

6.4 Virgo+ thermal noise

The Virgo+ thermal noise estimation includes suspensions and bulk contributions, considering both structural and viscous losses. Actually, it is not sure that the lower measured quality factors are due to viscous losses: maybe there could be some mode couplings which cause an energy leak at resonance without spoiling thermal noise in off-resonance region. Anyway, we consider the worst possible case, that is done by the viscous mechanism, to estimate thermal noise upper limit.

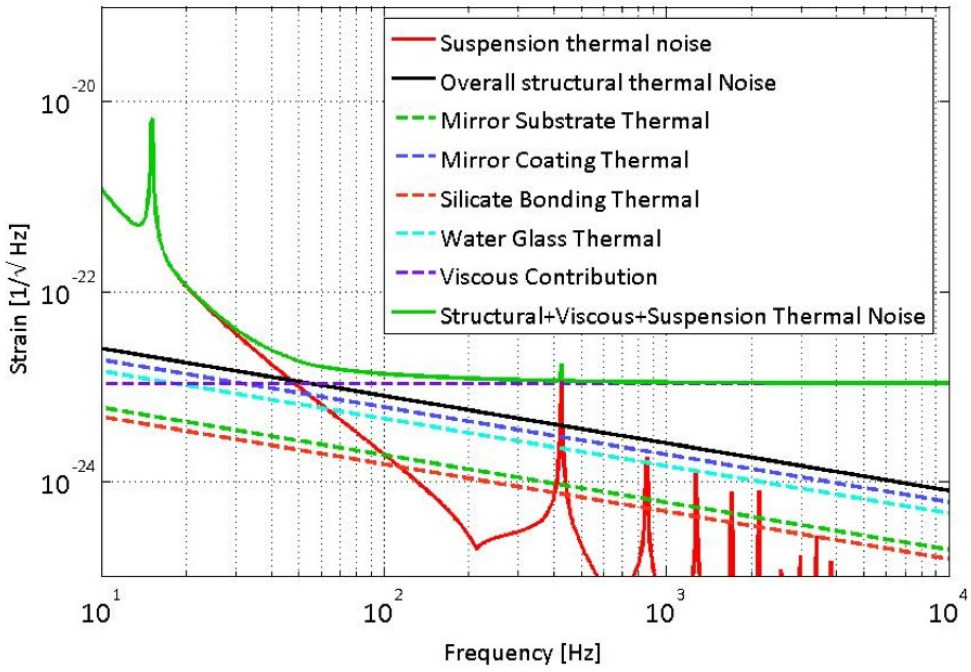

Figure 6.6: Virgo+ thermal noise curve estimated from analytical and numerical models: suspension contribution is the red solid line, the black solid line is the bulk contribution, while the green solid line is the quadratic sum of overall terms, considering suspensions, structural and viscous losses of mirror bulk mode.

In fig. 6.7 I compare Virgo+ measured sensitivity curve (in black), with thermal noise design curve (in red) and with thermal noise curve estimated from measurements and models (in green). The design and the estimated thermal noise curves are very close in the low frequency region; on the contrary they have different slope in the high frequency region, due to the viscous contribution to the estimated curve. Anyway, even in the worst possible case, the estimated curve is at least one order of magnitude lower than the measured sensitivity curve.

In order to better compare estimated thermal noise curve to the measured sensitivity curve, we sum estimated thermal noise contribution to the Virgo+ *noise budget curve* that is the quadratic sum of all noise sources (in that case, except thermal noise) affecting the interferometer: there are both fundamental noises (as shot noise, radiation pressure, seismic noise) and technical noises (as stray light, electronic noise, control noise, frequency noise). In fig. 6.8 it is evident that thermal noise does not explain the high noise level in Virgo+ sensitivity curve: in fact the noise budget is lower of a factor 2 than the measured sensitivity curve in the low frequency region. On the contrary at high frequency region the dominant noise source is the shot noise and the noise budget justifies the measured sensitivity curve.

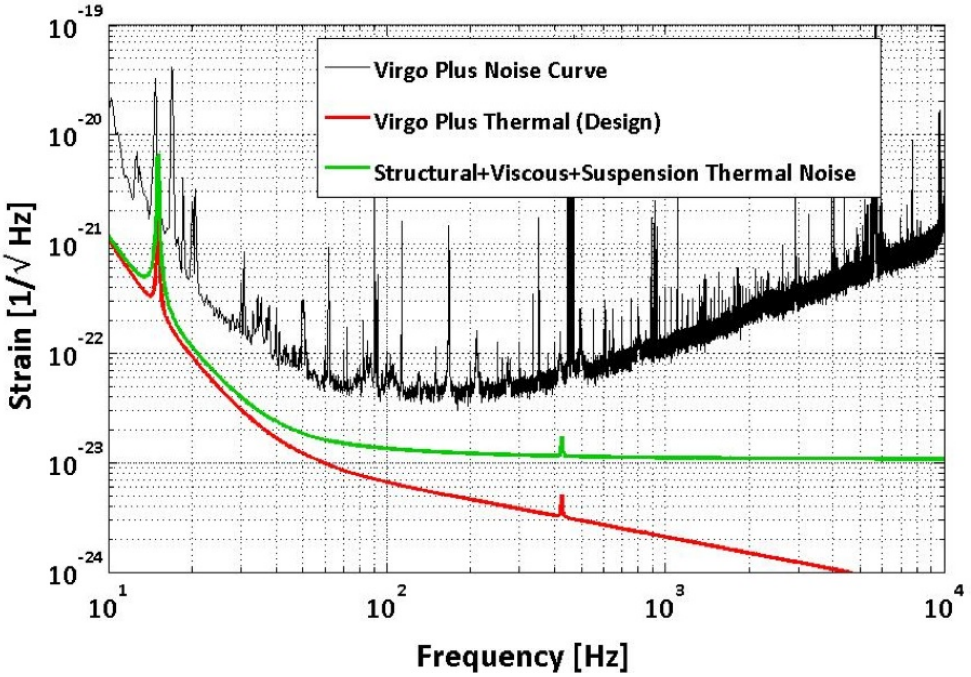

Figure 6.7: comparison between Virgo+ sensitivity curve (in black), thermal noise curve estimated by measurements and models (in green) and the design thermal noise curve (in red).

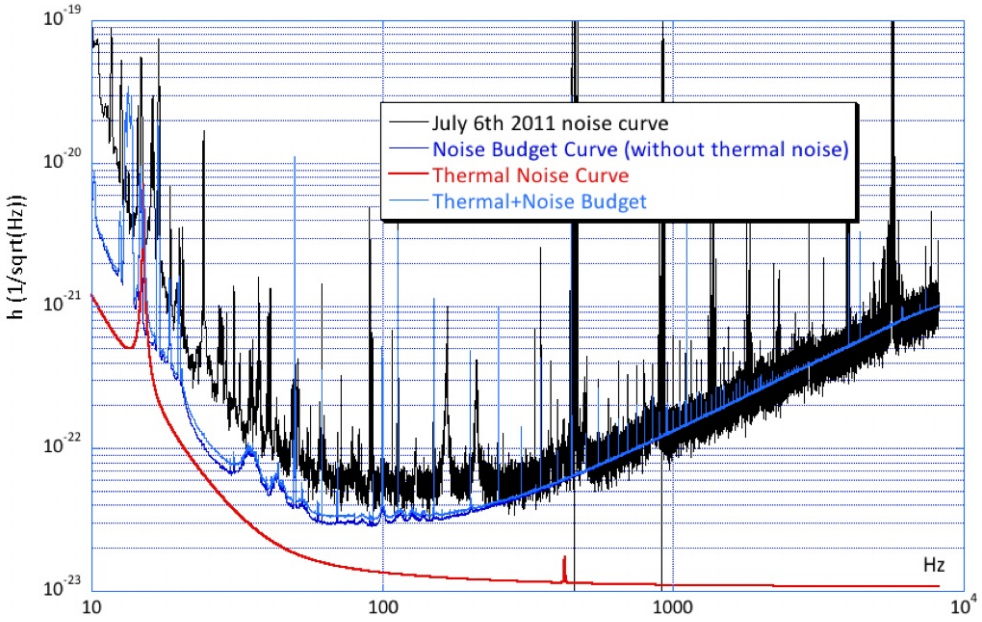

Figure 6.8: comparison between Virgo+ sensitivity curve (in black), estimated thermal noise (in red), noise budget without thermal noise (in blue) and noise budget with estimated thermal noise curve (in pale blue).

Conclusion

Virgo+, the first upgrade of the gravitational wave interferometer Virgo, aimed to improve the sensitivity curve of one order of magnitude in the frequency band between $10Hz$ and $300Hz$, by reducing the thermal noise contribution.

That reduction is possible by replacing the last suspension stages of the test masses (called payloads) with new monolithic suspensions. In the new system, fibers, clamps and mirrors are made of a same material, which has a low intrinsic dissipation: fused silica. Using that material to build the payload, energy losses due to internal friction and damping processes are reduced.

However, as Virgo+ was operated, the sensitivity improvement turned out to be smaller than the expected one (see fig. 2). Hence, an expensive campaign of mechanical quality factor measurements, using the overall interferometer, started in order to check if the sensitivity was limited by mechanical dissipations or by other noise sources as, for example, the diffused light.

From quality factor measurements we can estimate thermal noise using an analytical or numerical model of the physical system and dissipative processes. Moreover, for some resonances, we know the loss mechanisms and the regions where there is the larger deformation during the vibrational motion. In that case, the knowledge of quality factors allows us to identify further damping processes acting on a system component and improve next payload designs, a mandatory target for Advanced Virgo.

To study mechanical resonance quality factors, at first, it is necessary to identify the fused silica fiber internal modes (as pendulum mode, vertical modes and violin modes) and mirror bulk modes. In particular, in order to distinguish mirror bulk modes from the violin ones that lie in the same frequency region, I studied the modal frequency dependence with respect to temperature during the 3-months-long data-set of VSR3, the third Virgo Scientific Run.

After the line identification, I performed mechanical quality factor measurements, exciting payload resonances and then following their amplitude oscillation ring-down. The quality factor results are reported in appendix C. From these measurements, it is evident that the Q-values are one order of magnitude lower than expected. Furthermore, there is a great dispersion between values of the same cathegory of mode, which can vary as much as two orders of magnitude. As an example, for mirror bulk modes, the highest ($Q_{max} = 24 \cdot 10^6$) and the lowest ($Q_{min} = 4 \cdot 10^5$) values have been found in the same payload, West-Input Fabry-Perot mirror.

Since violin modes present the same behavior, further analysis was performed. In fact studying violin and pendulum modes is useful to evaluate the intrinsic losses of fused silica fibers; but violin mode study has the advantage to be extended over a

large frequency band, allowing us to perform quality factor studies with respect to frequency.

In order to point out the excess loss source, an experimental apparatus to measure quality factors of a single-fiber suspension has been set up. In that configuration it was possible to modify the applied tension and to change the regulation of the upper clamp system, which is identical to the Virgo+ one. From the measurements it is evident that changing even a bit the stress on the upper clamp, the quality factor values and frequency dependence of violin modes significantly vary. That explains the low values and the high dispersion of Virgo+ data. Moreover, the overall quality factor of violin modes turns out to be worse than the nominal value for fused silica. Thus, for Advanced Virgo, it was decided to modify the upper clamp system of the new monolithic suspensions. The new upper clamp will not have any regulation screw and probably it will be similar to the present lower clamp.

Finally, through quality factor data, a thermal noise estimation has been done. The experimental results have been used to optimize simulation parameters and so to understand the dissipative processes going on. From that computation, it follows that, even if thermal noise is higher than expected, its contribution is not sufficient to explain the measured sensitivity curve of Virgo+, which is at least a factor 3 above estimates.

This result is evident in fig. 6.9, where the Virgo+ measured sensitivity curve (in black) with the thermal noise curve estimated from measurements (in red) are shown. In the same plot the noise budget curve (i.e. the sum of the projections of the interferometer fundamental and technical noise sources) without thermal noise (in blue) and with the thermal noise estimated from measurements (in pale blue) is reported as reference.

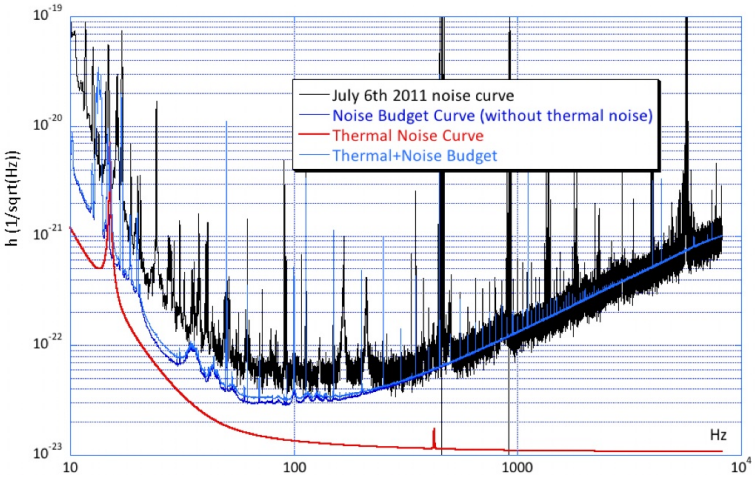

Figure 6.9: comparison between the Virgo+ measured sensitivity curve (in black), the estimated thermal noise curve (in red), the noise budget without thermal noise contribution (in blue) and the noise budget with the estimated thermal noise curve (in pale blue).

Conclusioni

Con Virgo+, il potenziamento dell'interferometro per onde gravitazionali Virgo, era previsto un miglioramento della curva di sensibilità di un ordine di grandezza nella banda di frequenze compresa tra $10Hz$ e $300Hz$, grazie all'abbassamento del livello di rumore termico. Questa riduzione è possibile sostituendo gli ultimi stadi di sospensione delle masse di test (chiamati *payload*) con le nuove sospensioni monolitiche, in cui i fili che sostengono lo specchio, gli attacchi e lo specchio stesso sono costituiti di un unico materiale, intrinsicamente poco dissipativo: la silice fusa. Utilizzando questo materiale per costruire il *payload* si riducono le perdite di energia dovute alle frizioni interne e ai processi dissipativi.

Dopo aver montato le sospensioni monolitiche in Virgo+, è stato osservato un miglioramento della curva di sensibilità minore di quello aspettato (fig. 1). Quindi è iniziata una serie di misure sui fattori di merito delle risonanze interne delle sospensioni monolitiche, al fine di verificare se la sensibilità è limitata dalle dissipazioni meccaniche o da altre forme di rumore, come ad esempio la luce diffusa.

Dalle misure dei fattori di merito è possibile stimare il rumore termico tramite un modello teorico (sia esso analitico o numerico) del sistema fisico e dei processi dissipativi in atto. Inoltre esistono alcuni modi di risonanza per cui sono ben noti i meccanismi dissipativi presenti e le regioni dove si ha la maggiore deformazione durante il modo di vibrazione. In questi casi, la conoscenza dei fattori di merito permette di comprendere se un particolare componente del sistema è soggetto ad ulteriori fenomeni dissipativi, consentendo quindi di modificarne il disegno tecnico e la sua realizzazione al fine di migliorarne le prestazioni. Quest'ultima fase è fondamentale per evitare che le stesse problematiche siano presenti anche nelle sospensioni di Advanced Virgo.

Per eseguire al meglio lo studio dei fattori di merito delle risonanze meccaniche, per prima cosa è stato necessario riconoscere i modi propri delle fibre di silice fusa (come il modo di pendolo, i modi verticali e i modi di violino) dai modi propri dello specchio. In particolare, per distinguere i modi interni dello specchio dai modi di violino che cadono nella stessa regione di frequenze, è stato necessario studiare come variano le loro frequenze con la temperatura su un arco di tempo pari ai tre mesi della terza presa dati scientifica di Virgo, VSR3.

Una volta identificate le risonanze interne, è stato possibile eseguire le misure dei fattori di merito eccitando le singole risonanze e seguendo il decadimento esponenziale della loro ampiezza nel tempo. Da queste misure è apparso evidente che i fattori di merito misurati sono più bassi di almeno un ordine di grandezza rispetto a quelli aspettati. Inoltre, è presente una dispersione dei valori dei fattori di merito per modi dello stesso tipo, fino a due ordini di grandezza: ad esempio per i modi interni dello

specchio il valore più alto ($Q_{max} = 24 \cdot 10^6$) e quello più basso ($Q_{min} = 4 \cdot 10^5$) sono stati trovati nello stesso *payload* monolitico, il West-Input.

Lo stesso comportamento si osserva per i modi di violino, su cui ho portato avanti delle ulteriori analisi. Lo studio dei violini, come del modo di pendolo, è utile per comprendere le perdite a cui sono soggette le fibre di silice fusa; inoltre permette di compiere analisi sulla dipendenza dei fattori di merito dalla frequenza, essendo posizionati in una larga banda di frequenze.

Al fine di individuare la fonte delle perdite in eccesso, ho messo a punto un apparato per misurare i fattori di merito di una sola fibra di silice fusa sospesa. In questa configurazione è stato possibile variare la regolazione del sistema di ancoraggio superiore della fibra, identico al sistema montato in Virgo+, e modificare la tensione a cui la fibra è sottoposta. Da queste misure è risultato che variando di poco la regolazione delle viti del sistema di ancoraggio superiore della fibra, è possibile cambiare significativamente il valore e l'andamento in frequenza dei fattori di merito dei modi di violino. Questo spiega sia il basso valore, sia l'alta dispersione dei fattori di merito misurati in Virgo+. In conseguenza di ciò, è stato decisa una modifica del sistema di ancoraggio in vista della nuova sospensione monolitica di Advanced Virgo, al fine di non abbassare le prestazioni delle fibre di silice fusa. Il nuovo sistema di ancoraggio superiore sarà privo di viti di regolazione.

Infine tramite le misure dei fattori di merito effettuate, è stato possibile stimare la curva di rumore termico in Virgo+, definendo un modello analitico (per le sospensioni) ed uno numerico (per lo specchio) del *payload* monolitico. I dati sperimentali sono stati utilizzati per ottimizzare i parametri inseriti nelle simulazioni e così risalire ai meccanismi di dissipazione presenti nel sistema. Ne è risultato che il rumore termico stimato, seppure più elevato di quello previsto nel progetto di Virgo+, non è in grado di giustificare l'alto livello della curva di sensibilità misurata, almeno un fattore 3 sopra le stime. Questo è evidente in fig. 6.9 dove confronto la curva di sensibilità misurata in Virgo+ (in nero) con la curva di rumore termico stimata tramite le misure effettuate sui fattori di merito (in rosso). Nel grafico sono riportate anche le curve del *noise budget* (ovvero la somma quadratica delle proiezioni dei rumori presenti in Virgo+, sia quelli fondamentali, sia quelli di natura tecnica) senza contributo del rumore termico (in blu) e con il contributo di rumore termico stimato dalle misure (in azzurro).

Appendix A

Anelasticity models

We examine three models of anelasticity in solids. None of them gives a full description of a real material behavior, but neverthless they are a useful approximation [84, 85]:

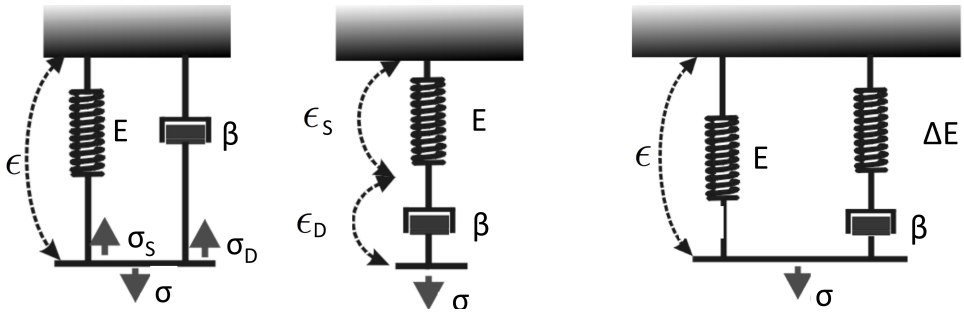

(a) Kelvin Voigt (b) Maxwell (c) Standard Anelastic Solid

Figure A.1: schemes of the solid models describing the different dissipation behaviors.

In the following descriptions, we link macroscopic variables to their microscopic counterparts: the spring constant k is linked to the Young's modulus E, the displacement x to the strain ϵ and the applied force F to the stress σ.

Kelvin-Voigt solid Suppose to take a lossless spring, done of a material with Young's modulus E and to apply a sudden constant stress σ. If there is no dissipation, the strain reaches "immediately" the Hooke law value $\epsilon_0 = \sigma/E$. But, if there is a viscous dissipation within the body, it could be described with a dashpot in parallel to the spring (see fig. A.1(a)): the dashpot causes a lag in the strain ϵ, which exhibits an exponential approach to the Hooke law value with a decay time τ_ϵ. This relaxation is strictly correlated to the dissipation process.

If the dashpot is described by a viscous constant β:

$$\beta = \tau_\epsilon E$$

we can write the constitutive equation for such a material as the sum of two stress contributions σ_S and σ_D, coming from the spring and the dashpot respectively:

$$\sigma = \sigma_S + \sigma_D = E\epsilon + \tau_\epsilon E\dot{\epsilon} \tag{A.1}$$

This is a good description for materials like cork, but it is not suitable for metals.

It is important not to confuse the relaxation time τ_ϵ with the characteristic decay time τ_0 defined for a harmonic damped oscillator with equation of motion $m\ddot{x} + \frac{m}{\tau_0}\dot{x} + m\omega_0^2 x = f$. To find the relation between τ_ϵ and τ_0 we compare this equation with eq. A.1; in particular we are interested in the term in $\dot{x}$, which is the counterpart of the term in $\dot{\epsilon}$:

$$\frac{m}{\tau_0}\dot{x} \to \tau_\epsilon E\dot{\epsilon}$$

Considering that $\epsilon = x/l_0$, we have $\dot{\epsilon} = \dot{x}/l_0$; then, remembering that the stress is a force per unit area, we obtain:

$$\frac{m}{\tau_0} = \frac{S}{l_0}E\tau_\epsilon = m\omega_0^2\tau_\epsilon \Rightarrow \tau_0 = \frac{1}{\omega_0^2\tau_\epsilon}$$

The time τ_ϵ comes out from the relaxation processes acting in a real solid. Since a potential barrier should be exceeded to reach the new equilibrium condition, these processes are not instantaneous.

Maxwell solid Consider a lossless spring and modify suddenly its length, through a constant strain: that means we are applying an instantaneous force. In that case, the corresponding mechanical model is a spring arranged in series with a dashpot (see fig. A.1(b)). The equation for such a material is the sum of two strain contributions $\dot{\epsilon}_S$ for the spring and $\dot{\epsilon}_D$ for the dashpot:

$$\dot{\epsilon} = \dot{\epsilon}_S + \dot{\epsilon}_D = \frac{\dot{\sigma}}{E} + \frac{\sigma}{\tau_\sigma E}$$

where we used the relation $\sigma_D = \tau_\sigma E\dot{\epsilon}$ for the dashpot, with the relaxation time τ_σ appearing in the stress.

This equation shows that, for a constant strain, stress decays exponentially. On the other hand, for a constant stress, it predicts a linear increasing of the strain, which is a very wrong description for crystalline solids.

Standard Anelastic Solid A large number of materials show both a relaxation time τ_σ for the stress and a relaxation time τ_ϵ for the strain. The mechanical model is a lossless spring with Young's modulus E in parallel with a Maxwell solid: the dashpot is described with its viscous coefficient β and the in-series spring with a Young's modulus ΔE (see fig. A.1(c)). Then, the stress and the strain are related as:

$$\frac{\Delta E}{\beta}\sigma + \dot{\sigma} = \frac{E\Delta E}{\beta}\epsilon + (E + \Delta E)\dot{\epsilon}$$

For a constant strain ϵ_0, stress decays exponentially from its initial value σ_0 to the equilibrium Hooke value $E\epsilon_0$:

$$\sigma(t) = E\epsilon_0 + (\sigma_0 - E\epsilon_0)e^{-t/\tau_\sigma}$$

where $\tau_\sigma = \frac{\beta}{\Delta E}$. Analogously, for a constant stress σ_0, strain decays exponentially from its initial value ϵ_0 to the Hooke value σ_0/E:

$$\epsilon(t) = \frac{\sigma_0}{E} + (\epsilon_0 - \frac{\sigma_0}{E})e^{-t/\tau_\epsilon}$$

where $\tau_\epsilon = \frac{E+\Delta E}{E\Delta E}\beta$.

It can be shown with a bit of algebra that the constitutive law is:

$$\sigma + \tau_\sigma \dot{\sigma} = E_r(\epsilon + \tau_\epsilon \dot{\epsilon})$$

where $E_r \equiv E$ is called relaxed Young's modulus, while the unrelaxed Young's modulus is $E_u = E + \Delta E$. In the frequency domain we obtain:

$$\sigma(\omega)(1 + i\omega\tau_\sigma) = E_r(1 + i\omega\tau_\epsilon)\epsilon(\omega)$$

From this equation it is possible to derive the associated loss angle, using the expression of the complex Young's modulus (eq. 3.11):

$$E(\omega) = E_r \frac{1 + i\omega\tau_\epsilon}{1 + i\omega\tau_\sigma}$$

Since the loss angle is the phase of the complex Young's modulus $\phi(\omega) = \mathcal{I}m[E]/\mathcal{R}e[E]$:

$$\phi(\omega) = \Delta \frac{\omega\bar{\tau}}{1 + \omega^2\bar{\tau}^2} \tag{A.2}$$

where:

$$\begin{aligned} \bar{\tau} &= \sqrt{\tau_\sigma \tau_\epsilon} \\ \Delta &= \frac{\tau_\epsilon - \tau_\sigma}{\sqrt{\tau_\sigma \tau_\epsilon}} \end{aligned} \tag{A.3}$$

It is easy to see that $\phi \propto \omega$ for $\omega\bar{\tau} \ll 1$ and $\phi \propto \omega^{-1}$ for $\omega\bar{\tau} \gg 1$. The loss angle has its maximum $\phi_{max} = \Delta/2$ at $\omega = \bar{\tau}^{-1}$. This is called *Debye's peak* (see fig. A.2). This model fits with those dissipative processes which are characterized by two parameters, as two time constants: it gives a correct description for most of the practical cases. Anyway, it can be generalized with more Maxwell units, involving three or more parameters.

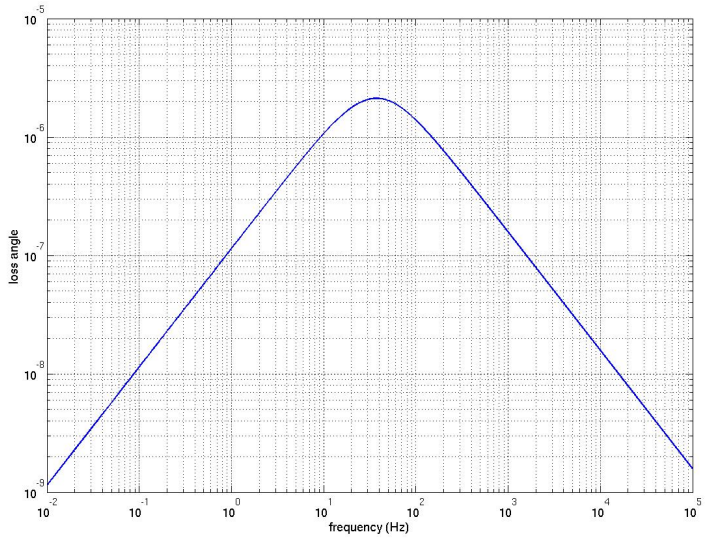

Figure A.2: loss angle Debye's peak with respect to frequency.

Appendix B

The flexural equation of a thin beam

Consider a thin beam of length L, as shown in fig. B.1. The x-axis is the vertical dirction, while the y-axis is the horizontal. When we transversally apply a force F, the beam deflects of a quantity δ.

The equation of motion describing the horizontal wire displacement y from the vertical position along the x-axis is [83]:

$$EI\frac{d^4y}{dx^4} - \mathcal{T}\frac{d^2y}{dx^2} = \rho_L\frac{d^2y}{dt^2} \tag{B.1}$$

where E is the Young's modulus, I is the cross section moment, $\mathcal{T}$ is the tension in the beam and ρ_L is the linear mass density of the beam.

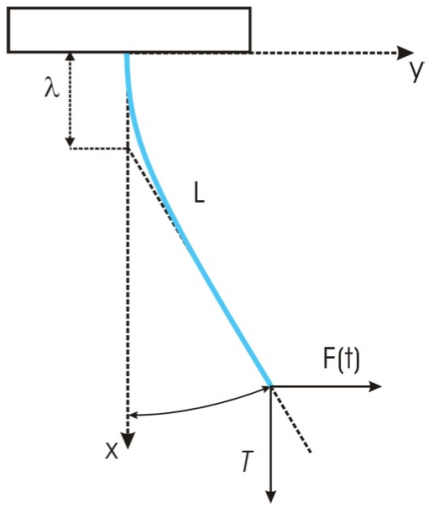

Figure B.1: scheme of the deformation of a fibre once it is pulled apart by a force $F(t)$; the pendulum mass is supposed pointlike. The pendulum swings with an effective length smaller than the real length L by the amount λ.

The general solution is:

$$y(x) = Ae^{-k_e x} + Be^{-k_e(L-x)} + Cx + D \tag{B.2}$$

where A, B, C and D are four constant to be determined from the boundary conditions; k_e is the flexural stiffness which is the inverse of the *bending point*, i.e. the characteristic elastic distance over which the wire bends:

$$k_e = \frac{1}{\lambda} = \sqrt{\frac{\mathcal{T}}{EI}} \tag{B.3}$$

In the static case, as boundary conditions, we can impose that the upper extremity is clamped and that the torque is zero at the free end:

$$\begin{aligned} y(0) &= 0 \\ y'(0) &= 0 \\ y(L) &= \delta \\ y''(L) &= 0 \end{aligned}$$

obtaining:

$$\begin{aligned} A + Be^{-k_e L} + D &= 0 \\ -Ak_e + Bk_e e^{-k_e L} + C &= 0 \\ Ae^{-k_e L} + B + CL + D &= \delta \\ Ak_e^2 e^{-k_e L} + Bk_e^2 &= 0 \end{aligned}$$

Since $k_e L \gg 1$ we can approximate:

$$\begin{aligned} A + D &= 0 \\ -Ak_e + C &= 0 \\ B + CL + D &= \delta \\ B &= 0 \end{aligned}$$

so, eq. B.2 can be written as:

$$y(x) = \frac{\delta e^{-k_e x}}{k_e L - 1} + \frac{\delta k_e x}{k_e L - 1} - \frac{\delta}{k_e L - 1}$$

The stored elastic energy is [83]:

$$V_{el} = \frac{1}{2} EI \int_0^L \left(\frac{d^2 y(x)}{dx^2} \right)^2 dx$$

In that case we obtain:

$$V_{el} = -\frac{1}{4} EI \frac{\delta^2 k_e^3}{(k_e L - 1)^2} \left(e^{-2k_e L - 1} \right)$$

Since we can write the elastic energy in the form:

$$V_{el} = \frac{1}{2} k_{el} \delta^2$$

in the approximation $k_e L \gg 1$ the elastic constant k_{el} is:

$$k_{el} = \frac{EIk_e}{2L^2} = \frac{\sqrt{\mathcal{T} EI}}{2L^2} \tag{B.4}$$

Appendix C

Virgo+ mechanical quality factors

I report the Quality factor measurements: in the tables there are the name of each resonance, its frequency f, its decay time τ, the decay time error σ_τ, the quality factor Q, the quality factor error σ_Q and the relative error ϵ_{rel}.

NI						
mode	$f(Hz)$	$\bar{\tau}(s)$	$\sigma_\tau(s)$	Q	σ_Q	ϵ_{rel}
pendulum z	0.59	255000	25500	4.73 E+05	4.7 E+04	0.10
pendulum x	0.59	235000	23500	4.36 E+05	4.4 E+04	0.10
vertical y	5.972	8300	2000	1.56 E+05	3.7 E+04	0.24
roll tz	8.31	7500	790	1.96 E+05	2.1 E+04	0.11
vertical y	14.86	103.0	1.2	4.808 E+03	5.4 E+01	0.01
roll tz	20.07	85.2	1.2	5.372 E+03	7.6 E+01	0.01
I viol	443.34	17300	2000	2.41 E+07	2.9 E+06	0.12
I viol	452.6	10240	360	1.456 E+07	5.2 E+05	0.04
I viol	462.74	18200	300	2.640 E+07	4.3 E+05	0.02
I viol	463.89	14200	2500	2.07 E+07	3.7 E+06	0.18
II viol	884.84	9700	1000	2.69 E+07	2.8 E+06	0.11
II viol	904.54	4770	570	1.36 E+07	1.6 E+06	0.12
II viol	925.47	16730	490	4.86 E+07	1.4 E+06	0.03
II viol	927.61	6800	1400	1.97 E+07	4.2 E+06	0.21
III viol	1325.93	3100	370	1.29 E+07	1.5 E+06	0.12
III viol	1355.38	2570	47	1.094 E+07	2.0 E+05	0.02
III viol	1387.41	8630	380	3.76 E+07	1.7 E+06	0.04
III viol	1389.02	3880	690	1.69 E+07	3.0 E+06	0.18
IV viol	1766.29	3650	910	2.03 E+07	5.1 E+06	0.25
IV viol	1802.2	1530	96	8.66 E+06	5.5 E+05	0.06
IV viol	1845.97	2480	620	1.44 E+07	3.6 E+06	0.25
IV viol	1847.25	4200	970	2.44 E+07	5.6 E+06	0.23

NI						
mode	$f(Hz)$	$\bar{\tau}(s)$	$\epsilon_\tau(s)$	Q	ϵ_Q	ϵ_{rel}
V viol	2205.6	1470	55	1.019 E+07	3.8 E+05	0.04
V viol	2249.63	322	19	2.28 E+06	1.4 E+05	0.06
V viol	2305.85	1500	87	1.087 E+07	6.3 E+05	0.06
V viol	2309.07	633.0	9.5	4.592 E+06	6.9 E+04	0.02
VI viol	2644.3	1160	37	9.64 E+06	3.1 E+05	0.03
VI viol	2698.67	373.0	3.0	3.162 E+06	2.5 E+04	0.01
VI viol	2761.31	730	81	6.33 E+06	7.0 E+05	0.11
VI viol	2768.28	453.0	4.6	3.940 E+06	4.0 E+04	0.01
VII viol	3075.08	288	58	2.78 E+06	5.6 E+05	0.20
VII viol	3145.5	104.0	9.0	1.028 E+06	8.9 E+04	0.09
VII viol	3210	286.0	4.6	2.884 E+06	4.6 E+04	0.02
VII viol	3223.5	117.0	4.0	1.185 E+06	4.1 E+04	0.03
VIII viol	3510.57	41.0	1.7	4.52 E+05	1.9 E+04	0.04
VIII viol	3653.12	87.0	2.5	9.98 E+05	2.9 E+04	0.03
VIII viol	3670.41	103.0	5.5	1.188 E+06	6.3 E+04	0.05
IX viol	3930.72	16.0	0.6	1.976 E+05	7.5 E+03	0.04
butterfly × (0,2) bulk	3964.3	46.60	0.87	5.80 E+05	1.1 E+04	0.02
butterfly + (0,2) bulk	3996.67	1011	47	1.269 E+07	5.9 E+05	0.05
IX viol	4091.65	44.60	0.87	5.73 E+05	1.1 E+04	0.02
IX viol	4113.22	43.6	1.0	5.63 E+05	1.3 E+04	0.02
X viol	4350.64	12.00	0.31	1.640 E+05	4.2 E+03	0.03
X viol	4390.33	21.40	0.81	2.95 E+05	1.1 E+04	0.04
X viol	4433.46	11.400	0.058	1.5878 E+05	8.0 E+02	0.01
X viol	4545.41	63.30	0.12	9.039 E+05	1.6 E+03	0.00
XI viol	4751.29	6.9	0	1.03 E+05	0.0 E+00	0.00
XI viol	4954.41	24.0	1.5	3.74 E+05	2.4 E+04	0.06
XI viol	4955.5	24.0	1.5	3.74 E+05	2.4 E+04	0.06
XII viol	5253.57	7.60	0.35	1.254 E+05	5.8 E+03	0.05
XII viol	5321.75	11.60	0.29	1.939 E+05	4.8 E+03	0.02
XIII viol	5602.81	7.00	0.23	1.232 E+05	4.1 E+03	0.03
?	5666.04	616	12	1.097 E+07	2.1 E+05	0.02
XIII viol/drum (1,0)	5671.54	19.10	0.46	3.403 E+05	8.2 E+03	0.02
XIII viol	5674.3	8.40	0.26	1.497 E+05	4.7 E+03	0.03
XIII viol/drum (1,0)	5675.92	19.5	1.7	3.48 E+05	3.0 E+04	0.09
?	6623.24	11.80	0.31	2.455 E+05	6.4 E+03	0.03
?	7192.82	22.80	0.51	5.15 E+05	1.2 E+04	0.02
butterfly – (0,3) bulk	7641.47	23.0	3.9	5.52 E+05	9.3 E+04	0.17
butterfly | (0,3) bulk	7710.49	222	11	5.38 E+06	2.8 E+05	0.05
egg × bulk	7992.64	49.4	9.1	1.24 E+06	2.3 E+05	0.18
egg + bulk	8022	306	31	7.71 E+06	7.7 E+05	0.10
ears – bulk	8926.14	58.5	5.9	1.64 E+06	1.6 E+05	0.10
ears | bulk	8984.7	91.1	9.1	2.57 E+06	2.6 E+05	0.10

NI						
mode	$f(Hz)$	$\bar{\tau}(s)$	$\epsilon_\tau(s)$	Q	ϵ_Q	ϵ_{rel}
drum (1,1) bulk	10191	24.9	2.5	7.98 E+05	8.0 E+04	0.10
drum (1,1) bulk	10323	18.3	1.8	5.93 E+05	5.9 E+04	0.10
butterfly (4,0) bulk	11367	13.2	1.3	4.72 E+05	4.7 E+04	0.10
drum (2,1) bulk	14524	< 0.5		< 2 E+04		
drum (2,1) bulk	14684	< 0.5		< 2 E+04		
butterfly (5,0) bulk	15066	< 0.5		< 2 E+04		
butterfly (5,0) bulk	15223	4.88	0.49	2.34 E+05	2.3 E+04	0.10
drum (0,2) bulk	15673	4.14	4.1	2.04 E+05	2.0 E+04	0.10
cloverleaf	15791	1.65	0.17	8.21 E+04	8.2 E+03	0.10
cloverleaf	15898	< 0.5		< 2 E+04		
?	18189	2.76	0.28	1.57 E+05	1.6 E+04	0.10
?	18250	0.700	0.070	4.03 E+04	4.0 E+03	0.10
?	18551	7.95	0.80	4.63 E+05	4.6 E+04	0.10
?	18741	1.82	0.18	1.07 E+05	1.1 E+04	0.10
?	18793	4.75	0.48	2.80 E+05	2.8 E+04	0.10
?	18905	6.08	0.61	3.61 E+05	3.6 E+04	0.10
?	20564	0.640	0.064	4.13 E+04	4.1 E+03	0.10
?	20598	0.620	0.062	3.98 E+04	4.0 E+03	0.10

WI						
mode	$f(Hz)$	$\bar{\tau}(s)$	$\sigma_\tau(s)$	Q	σ_Q	ϵ_{rel}
pendulum z	0.59	574000	57000	1.06 E+06	1.1 E+05	0.10
pendulum x	0.59	681000	68000	1.26 E+06	1.3 E+05	0.10
vertical y	5.91	1570	160	2.91 E+04	2.9 E+03	0.10
roll tz	8.21	16300	1600	4.20 E+05	4.2 E+04	0.10
vertical y	14.78	104.9	2.6	4.87 E+03	1.2 E+02	0.02
roll tz	20.04	103	11	6.47 E+03	7.0 E+02	0.11
I viol	452.01	26100	3400	3.71 E+07	4.8 E+06	0.13
I viol	458.71	11900	1500	1.71 E+07	2.1 E+06	0.12
I viol	459.73	8380	57	1.2103 E+07	8.2 E+04	0.01
I viol	460.92	47500	4500	6.88 E+07	6.6 E+06	0.10
II viol	904.64	8740	110	2.48 E+07	3.2 E+05	0.01
II viol	917.4	3820	140	1.101 E+07	4.0 E+05	0.04
II viol	919.79	3720	21	1.0749 E+07	6.0 E+04	0.01
II viol	921.57	17900	770	5.18 E+07	2.2 E+06	0.04
III viol	1352.57	5100	70	2.17 E+07	3.0 E+05	0.01
III viol	1374.13	2650	160	1.144 E+07	6.9 E+05	0.06
III viol	1377.29	2210	130	9.56 E+06	5.5 E+05	0.06
III viol	1379.93	10600	1400	4.58 E+07	6.1 E+06	0.13
IV viol	1801.36	2070	30	1.171 E+07	1.7 E+05	0.01
IV viol	1826.42	705	48	4.05 E+06	2.7 E+05	0.07
IV viol	1836.15	823.0	8.5	4.747 E+06	4.9 E+04	0.01
IV viol	1838.18	4000	2100	2.3 E+07	1.2 E+07	0.52
V viol	2250.93	790	20	5.59 E+06	1.4 E+05	0.03
V viol	2285.28	460	190	3.3 E+06	1.4 E+06	0.41
V viol	2290.93	340	17	2.45 E+06	1.2 E+05	0.05
V viol	2294.1	590	10	4.252 E+06	7.2 E+04	0.02
VI viol	2703.63	211.0	6.4	1.792 E+06	5.4 E+04	0.03
VI viol	2737.05	294	17	2.53 E+06	1.5 E+05	0.06
VI viol	2741.01	70.50	0.74	6.071 E+05	6.3 E+03	0.01
VI viol	2749.94	306.0	8.1	2.644 E+06	7.0 E+04	0.03
VII viol	3146.58	280	86	2.77 E+06	8.5 E+05	0.31
VII viol	3187	42.5	1.2	4.26 E+05	1.2 E+04	0.03
VII viol	3193.3	87.6	1.9	8.79 E+05	1.9 E+04	0.02
VII viol	3200.59	92.0	1.3	9.25 E+05	1.3 E+04	0.01
VIII viol	3585.2	100.0	9.0	1.13 E+06	1.0 E+05	0.09
VIII viol	3634.08	13.90	0.26	1.587 E+05	3.0 E+03	0.02
VIII viol	3642.51	12.90	0.93	1.48 E+05	1.1 E+04	0.07
VIII viol	3647.71	36.80	0.60	4.217 E+05	6.9 E+03	0.02
butterfly × (0,2) bulk	3939.45	1290	31	1.597 E+07	3.8 E+05	0.02
butterfly + (0,2) bulk	3971.54	1960	32	2.445 E+07	4.0 E+05	0.02

WI						
mode	$f(Hz)$	$\bar{\tau}(s)$	$\sigma_\tau(s)$	Q	σ_Q	ϵ_{rel}
IX viol	4018.17	6.90	0.70	8.71 E+04	8.7 E+03	0.10
IX viol	4077.31	11.30	0.47	1.447 E+05	6.1 E+03	0.04
IX viol	4083.6	81	41	1.04 E+06	5.2 E+05	0.51
IX viol	4088.33	82.5	1.8	1.060 E+06	2.3 E+04	0.02
X viol	4502.28	17.30	0.67	2.447 E+05	9.4 E+03	0.04
X viol	4503.05	95	49	1.35 E+06	7.0 E+05	0.52
X viol	4513.19	95	44	1.35 E+06	6.3 E+05	0.47
X viol	4519.18	96.2	4.5	1.366 E+06	6.4 E+04	0.05
XI viol	4868.26	14.40	0.32	2.202 E+05	4.9 E+03	0.02
XI viol	4927.66	121	58	1.87 E+06	8.9 E+05	0.48
XI viol	4929.88	138.0	9.9	2.14 E+06	1.5 E+05	0.07
XI viol	4930.39	138	10	2.14 E+06	1.6 E+05	0.07
XII viol	5295.92	9.30	0.39	1.547 E+05	6.5 E+03	0.04
XII viol	5307.64	32.0	5.5	5.34 E+05	9.1 E+04	0.17
XII viol	5315.45	23.7	4.3	3.96 E+05	7.1 E+04	0.18
XIII viol	5612.7	15.50	0.95	2.73 E+05	1.7 E+04	0.06
?	5630.22	878.0	4.2	1.5530 E+07	7.5 E+04	0.00
?	5631.69	1120	160	1.98 E+07	2.8 E+06	0.14
?	5638.65	352.0	3.6	6.235 E+06	6.4 E+04	0.01
drum (1,0) bulk	5642.5	1.73	0.17	3.07 E+04	3.1 E+03	0.10
XIII viol	5651.6	32	15	5.6 E+05	2.6 E+05	0.47
XIII viol	5659.7	33.8	1.8	6.01 E+05	3.3 E+04	0.05
XIII viol	5679.78	175	97	3.1 E+06	1.7 E+06	0.55
XIV viol	5955.5	4.330	0.035	8.101 E+04	6.6 E+02	0.01
XIV viol	6001.78	28.1	1.5	5.30 E+05	2.7 E+04	0.05
XV viol	6307.68	4.10	0.41	8.12 E+04	8.1 E+03	0.10
XV viol	6349.11	9.71	0.44	1.94 E+05	8.8 E+03	0.05
XV viol	6379.98	28.40	0.40	5.69 E+05	8.1 E+03	0.01
XVI viol	6751.91	7.97	0.62	1.69 E+05	1.3 E+04	0.08
butterfly – (3,0) bulk	7605.68	80.7	5.2	1.93 E+06	1.2 E+05	0.06
?	7613.4	16.90	0.64	4.04 E+05	1.5 E+04	0.04
butterfly | (3,0) bulk	7673.81	1020	400	2.46 E+07	9.7 E+06	0.40
egg × bulk	7999.55	155	48	3.9 E+06	1.2 E+06	0.31
egg + bulk	8028.91	4500	2400	1.15 E+08	6.2 E+07	0.54
?	8492.6	45.4	8.4	1.21 E+06	2.2 E+05	0.19
?	8934.07	98	11	2.75 E+06	3.0 E+05	0.11
ears – bulk	8944.52	24.8	1.1	6.97 E+05	3.2 E+04	0.05
ears | bulk	8992.26	250.0	3.5	7.06 E+06	1.0 E+05	0.01
?	9231.75	39	12	1.12 E+06	3.6 E+05	0.32
?	9385.19	48.9	7.2	1.44 E+06	2.1 E+05	0.15

WI						
mode	$f(Hz)$	$\bar{\tau}(s)$	$\sigma_\tau(s)$	Q	σ_Q	ϵ_{rel}
drum (1,1) bulk	10165	49.0	4.9	1.57 E+06	1.6 E+05	0.10
drum (1,1) bulk	10335	55.2	5.5	1.79 E+06	1.8 E+05	0.10
butterfly (4,0) bulk	11328	49.3	4.9	1.76 E+06	1.8 E+05	0.10
butterfly (4,0) bulk	11442	114	11	4.12 E+06	4.1 E+05	0.10
drum (2,1) bulk	14362	< 0.5		< 2 E+04		
drum (2,1) bulk	14511	4.68	0.47	2.13 E+05	2.1 E+04	0.10
?	15007	30.9	3.1	1.46 E+06	1.5 E+05	0.10
butterfly (5,0) bulk	15056	< 0.5		< 2 E+04		
butterfly (5,0) bulk	15178	3.08	0.31	1.47 E+05	1.5 E+04	0.10
drum (0,2) bulk	15659	3.90	0.39	1.92 E+05	1.9 E+04	0.10
?	18084	3.42	0.34	1.94 E+05	1.9 E+04	0.10
?	18093	1.27	0.13	7.20 E+04	7.2 E+03	0.10
?	18418	15.8	1.6	9.13 E+05	9.1 E+04	0.10
?	18617	4.53	0.45	2.65 E+05	2.7 E+04	0.10
?	18825	6.30	0.63	3.73 E+05	3.7 E+04	0.10
?	18908	12.70	0.13	7.56 E+05	7.6 E+04	0.10
?	19006	23.1	2.3	1.38 E+06	1.4 E+05	0.10
?	19075	3.33	0.33	2.00 E+05	2.0 E+04	0.10
?	20743	8.66	0.87	5.64 E+05	5.6 E+04	0.10
?	21849	3.43	0.34	2.35 E+05	2.4 E+04	0.10
?	21857	18.9	0.19	1.30 E+06	1.3 E+05	0.10
?	22042	1.32	0.13	9.15 E+04	9.2 E+03	0.10
?	21849	3.43	0.34	2.35 E+05	2.4 E+04	0.10

NE						
mode	$f(Hz)$	$\bar{\tau}(s)$	$\sigma_\tau(s)$	Q	σ_Q	ϵ_{rel}
pendulum z	0.59	105000	11000	1.95 E+05	2.0 E+04	0.10
pendulum x	0.59	169000	17000	3.13 E+05	3.1 E+04	0.10
vertical y	5.97	560.0	8.5	1.051 E+04	1.6 E+02	0.02
roll tz	80.9	610	130	1.55 E+05	3.3 E+04	0.21
vertical y	14.88	109	25	5.1 E+03	1.2 E+03	0.23
roll tz	20.03	101	14	6.36 E+03	8.7 E+02	0.14
I viol	447.82	42000	6900	5.91 E+07	9.7 E+06	0.16
I viol	458.25	35700	1800	5.14 E+07	2.5 E+06	0.05
I viol	460.78	28500	150	4.126 E+07	2.2 E+05	0.01
I viol	469.14	30600	2100	4.51 E+07	3.1 E+06	0.07
II viol	893.32	13400	420	3.76 E+07	1.2 E+06	0.03
II viol	913.62	14000	5400	4.0 E+07	1.6 E+07	0.39
II viol	918.95	11400	200	3.291 E+07	5.8 E+05	0.02
II viol	934.35	13800	380	4.05 E+07	1.1 E+06	0.03
III viol	1338.74	6510	150	2.738 E+07	6.4 E+05	0.02
III viol	1369.01	4820	150	2.073 E+07	6.6 E+05	0.03
III viol	1377.04	3920	65	1.696 E+07	2.8 E+05	0.02
III viol	1400.56	9370	750	4.12 E+07	3.3 E+06	0.08
IV viol	1783.49	2930	480	1.64 E+07	2.7 E+06	0.16
IV viol	1825.33	2290	53	1.313 E+07	3.0 E+05	0.02
IV viol	1834.43	1340	15	7.722 E+06	8.8 E+04	0.01
IV viol	1865.06	768	29	4.50 E+06	1.7 E+05	0.04
V viol	2225.58	1850	35	1.293 E+07	2.2 E+05	0.02
V viol	2272.39	888	40	6.34 E+06	2.8 E+05	0.04
V viol	2288.49	2360	61	1.697 E+07	4.4 E+05	0.03
V viol	2328.71	2890	120	2.114 E+07	8.7 E+05	0.04
VI viol	2669.23	768	35	6.44 E+06	3.0 E+05	0.05
VI viol	2723.44	38.5	7.2	3.29 E+05	6.2 E+04	0.19
VI viol	2744.27	319	64	2.75 E+06	5.5 E+05	0.20
VI viol	2788.03	316	70	2.77 E+06	6.1 E+05	0.22
VII viol	3104.35	282.0	9.5	2.750 E+06	9.2 E+04	0.03
VII viol	3168.7	107	17	1.07 E+06	1.7 E+05	0.16
VII viol	3192.62	120.0	6.4	1.204 E+06	6.4 E+04	0.05
VII viol	3236.73	185	66	1.88 E+06	6.7 E+05	0.36
VIII viol	3532.93	51.9	3.6	5.76 E+05	4.1 E+04	0.07
VIII viol	3556.83	193	19	2.16 E+06	2.2 E+05	0.10
VIII viol	3565.2	198	20	2.22 E+06	2.2 E+05	0.10
VIII viol	3567.72	220	22	2.47 E+06	2.5 E+05	0.10
VIII viol	3578.16	181	18	2.03 E+06	2.0 E+05	0.10
butterfly + (0,2) bulk	3980.03	710	25	8.87 E+06	3.1 E+05	0.04
butterfly × (0,2) bulk	4025.97	163	23	2.06 E+06	2.8 E+05	0.14
IX viol	4070.93	92	24	1.17 E+06	3.0 E+05	0.26
IX viol	4126.58	13.80	0.28	1.789 E+05	3.7 E+03	0.02

NE						
mode	$f(Hz)$	$\bar{\tau}(s)$	$\sigma_\tau(s)$	Q	σ_Q	ϵ_{rel}
X viol	4473.8	185.0	8.1	2.60 E+06	1.1 E+05	0.04
X viol	4484.23	188	19	2.65 E+06	2.7 E+05	0.10
X viol	4486.75	200	20	2.82 E+06	2.8 E+05	0.10
X viol	4495.11	206	21	2.91 E+06	2.9 E+05	0.10
X viol	4501.22	44.6	1.7	6.31 E+05	2.4 E+04	0.04
X viol	4551.46	18.90	0.49	2.702 E+05	7.1 E+03	0.03
XI viol	4779.48	132	13	1.98 E+06	2.0 E+05	0.10
XI viol	4789.91	166	17	2.50 E+06	2.5 E+05	0.10
XI viol	4800.8	211	21	3.18 E+06	3.2 E+05	0.10
XI viol	4813.55	274	27	4.14 E+06	4.1 E+05	0.10
XII viol	5237.73	166	17	2.73 E+06	2.7 E+05	0.10
XII viol	5246.09	168	17	2.77 E+06	2.8 E+05	0.10
XII viol	5248.62	180	18	2.97 E+06	3.0 E+05	0.10
XII viol	5255.05	191	19	3.15 E+06	3.1 E+05	0.10
drum (1,0) bulk	5706.87	172.0	2.5	3.084 E+06	4.5 E+04	0.01
XIII viol	6154.69	179	18	3.46 E+06	3.5 E+05	0.10
XIII viol	6165.12	162	16	3.14 E+06	3.1 E+05	0.10
XIII viol	6167.65	169	17	3.27 E+06	3.3 E+05	0.10
XIII viol	6176.01	168	17	3.26 E+06	3.3 E+05	0.10
butterfly | (3,0) bulk	7667.45	275	16	6.62 E+06	3.9 E+05	0.06
butterfly – (3,0) bulk	7761.16	96.80	0.64	2.360 E+06	1.6 E+04	0.01
egg + bulk	8031.89	456	16	1.151 E+07	4.1 E+05	0.04
egg × bulk	9077.96	188	16	5.36 E+06	4.4 E+05	0.08
ears | bulk	9746.66	420.0	6.4	1.286 E+07	1.9 E+05	0.02

NE						
mode	$f(Hz)$	$\bar{\tau}(s)$	$\sigma_\tau(s)$	Q	σ_Q	ϵ_{rel}
drum (1,1) bulk	10274	348	35	1.12 E+07	1.1 E+06	0.10
drum (1,1) bulk	10331	26.4	2.6	8.58 E+05	8.6 E+04	0.10
radial bulk ?	10387	22.8	2.3	7.44 E+05	7.4 E+04	0.10
butterfly (4,0) bulk	11443	81.1	8.1	2.91 E+06	2.9 E+05	0.10
butterfly (4,0) bulk	11547	17.3	1.7	6.27 E+05	6.3 E+04	0.10
drum (2,1) bulk	14541	2.86	0.29	1.31 E+05	1.3 E+04	0.10
drum (2,1) bulk	14677	2.23	0.22	1.03 E+05	1.0 E+04	0.10
butterfly (5,0) bulk	15200	30.8	0.31	1.47 E+06	1.5 E+05	0.10
butterfly (5,0) bulk	15250	4.75	0.48	2.28 E+05	2.3 E+04	0.10
drum (0,2) bulk	15773	1.71	0.17	8.48 E+04	8.5 E+03	0.10
cloverleaf bulk	15888	5.87	0.59	2.93 E+05	2.9 E+04	0.10
cloverleaf bulk	15949	1.01	0.10	5.07 E+04	5.1 E+03	0.10
?	18460	1.52	0.15	8.79 E+04	8.8 E+03	0.10
?	18589	15.8	1.6	9.13 E+05	9.1 E+04	0.10
?	18608	2.36	0.24	1.38 E+05	1.4 E+04	0.10
?	18690	1.76	0.18	1.03 E+05	1.0 E+04	0.10
?	18787	3.05	0.31	1.80 E+05	1.8 E+04	0.10
?	18842	37.5	0.38	2.22 E+06	2.2 E+05	0.10
?	18883	0.76	0.08	4.53 E+04	4.5 E+03	0.10
?	20616	3.52	0.35	2.28 E+05	2.3 E+04	0.10
?	21818	35.1	3.5	2.41 E+06	2.4 E+05	0.10
?	21920	0.67	0.07	4.63 E+04	4.6 E+03	0.10
?	22280	116	12	8.15 E+06	8.2 E+05	0.10
?	22558	3.41	0.34	2.42 E+05	2,4 E+04	0.10
?	22692	2.18	0.21	1.56 E+05	1.6 E+04	0.10
?	22774	0.70	0.07	5.04 E+04	5.0 E+03	0.10
?	23051	3.13	0.31	2.27 E+05	2.3 E+04	0.10
?	23066	0.63	0.06	4.59 E+04	4.6 E+03	0.10
?	23312	1.42	0.14	1.04 E+05	1.0 E+04	0.10
?	23598	2.66	0.27	1.97 E+05	2.0 E+04	0.10
?	24965	0.77	0.08	6.06 E+04	6.1 E+03	0.10

WE						
mode	$f(Hz)$	$\bar{\tau}(s)$	$\sigma_\tau(s)$	Q	σ_Q	ϵ_{rel}
pendulum z	0.59	717000	72000	1.33 E+06	1.3 E+05	0.10
pendulum x	0.59	377000	38000	6.99 E+05	7.0 E+04	0.10
vertical y	5.92	134	13	2.49 E+03	2.5 E+02	0.10
roll tz	8.01	810	180	2.04 E+04	4.4 E+03	0.22
vertical y	14.78	63.1	6.3	2.93 E+03	2.9 E+02	0.10
roll tz	20.06	80.1	8.0	5.05 E+03	5.1 E+02	0.10
I viol	457.94	10100	2800	1.45 E+07	4.0 E+06	0.28
I viol	461	17900	6000	2.59 E+07	8.7 E+06	0.33
I viol	463.65	1800	62	2.622 E+06	9.1 E+04	0.03
I viol	463.71	1940	60	2.826 E+06	8.7 E+04	0.03
II viol	913.26	8100	990	2.32 E+07	2.8 E+06	0.12
II viol	919.53	12200	2200	3.52 E+07	6.3 E+06	0.18
II viol	924.58	4630	390	1.34 E+07	1.1 E+06	0.09
II viol	925.2	2790	140	8.11 E+06	4.1 E+05	0.05
III viol	1365.96	549	39	2.36 E+06	1.7 E+05	0.07
III viol	1372.62	1850	93	7.98 E+06	4.0 E+05	0.05
III viol	1385.92	1860	110	8.08 E+06	4.7 E+05	0.06
III viol	1386.17	1370	110	5.97 E+06	4.9 E+05	0.08
IV viol	1821.28	1890	100	1.081 E+07	5.7 E+05	0.05
IV viol	1830.73	3650	350	2.10 E+07	2.0 E+06	0.10
IV viol	1844.12	867	87	5.02 E+06	5.0 E+05	0.10
IV viol	1844.17	332	33	1.92 E+06	1.9 E+05	0.10
V viol	2272.57	423	160	3.0 E+06	1.1 E+06	0.38
V viol	2288.87	469	19	3.37 E+06	1.4 E+05	0.04
V viol	2303.74	21.1	2.1	1.53 E+05	1.5 E+04	0.10
V viol	2304.49	187.0	2.1	1.354 E+06	1.5 E+04	0.01
VI viol	2722.87	424	21	3.63 E+06	1.8 E+05	0.05
VI viol	2739.71	642	29	5.53 E+06	2.5 E+05	0.05
VI viol	2759.97	32.9	3.3	2.85 E+05	2.9 E+04	0.10
VI viol	2761.95	64.2	6.4	5.57 E+05	5.6 E+04	0.10
VII viol	3168.1	133	13	1.32 E+06	1.3 E+05	0.10
VII viol	3188.98	32.1	3.2	3.22 E+05	3.2 E+04	0.10
VIII viol	3608.98	46.2	4.6	5.24 E+05	5.2 E+04	0.10
VIII viol	3630.68	38.0	3.8	4.33 E+05	4.3 E+04	0.10
VIII viol	3661.48	12.9	1.3	1.48 E+05	1.5 E+04	0.10
butterfly + (0,2) bulk	3969.13	1090	78	1.359 E+07	9.7 E+05	0.07
butterfly × (0,2) bulk	4014.61	318	18	4.01 E+06	2.3 E+05	0.06
IX viol	4065.13	60.6	6.1	7.74 E+05	7.7 E+04	0.10
X viol	4460.22	68.2	6.8	9.56 E+05	9.6 E+04	0.10
X viol	4488.66	29.2	2.9	4.12 E+05	4.1 E+04	0.10
X viol	4489.14	29.2	2.9	4.12 E+05	4.1 E+04	0.10
X viol	4537.17	21.3	2.1	3.04 E+05	3.0 E+04	0.10

WE						
mode	$f(Hz)$	$\bar{\tau}(s)$	$\sigma_\tau(s)$	Q	σ_Q	ϵ_{rel}
XI viol	4858.09	27.0	2.7	4.12 E+05	4.1 E+04	0.10
XII viol	5209.8	25.6	2.6	4.19 E+05	4.2 E+04	0.10
?	5693.43	96.3	9.6	1.72 E+06	1.7 E+05	0.10
drum (1,0) bulk	5701.33	893	49	1.599 E+07	8.7 E+05	0.05
?	7561	–	–	–	–	–
butterfly | (3,0) bulk	7653	1.94	0.19	4.66 E+04	4.7 E+03	0.10
butterfly – (3,0) bulk	7745	–	–	–	–	–
egg + bulk	8058.59	37.3	3.7	9.44 E+05	9.4 E+04	0.10
egg × bulk	8895.5	120	12	3.35 E+06	3.4 E+05	0.10
ears | bulk	9081.69	127	13	3.62 E+06	3.6 E+05	0.10
ears – bulk	9699.22	80.2	8.0	2.44 E+06	2.4 E+05	0.10
drum (1,1) bulk	10245	2.35	0.24	7.58 E+04	7.6 E+03	0.10
drum (1,1) bulk	10313	50.6	5.1	1.64 E+06	1.6 E+05	0.10
XXV violin ?	11394	82.1	8.2	2.94 E+06	2.9 E+05	0.10
XXV violin ?	11402	116	12	4.16 E+06	4.2 E+05	0.10
XXV violin ?	11410	102	10	3.66 E+06	3.7 E+05	0.10
XXV violin ?	11422	68.4	6.8	2.46 E+06	2.5 E+05	0.10
butterfly (4,0) bulk	11525	35.0	3.5	1.27 E+06	1.3 E+05	0.10
egg bulk ?	12288	93.1	9.3	3.59 E+06	3.6 E+05	0.10
ears bulk ?	13639	101	10	4.37 E+06	4.4 E+05	0.10
violin ?	13990	35.5	3.6	1.57 E+06	1.6 E+05	0.10
drum (2,1) bulk	14524	152	15	6.94 E+06	6.9 E+05	0.10
drum (2,1) bulk	14585					
butterfly (5,0) bulk	15183	4.56	0.46	2.17 E+06	2.2 E+05	0.10
butterfly (5,0) bulk	15226					
	15624	8.68	0.87	4.26 E+05	4.3 E+04	0.10
drum (0,2) bulk	15763	30.0	3.0	1.49 E+06	1.5 E+05	0.10
cloverleaf	15889					
cloverleaf	15898					
?	18425	0.81	0.08	4.70 E+04	4.7 E+03	0.10
?	18603	2.24	0.22	1.31 E+05	1.3 E+04	0.10
?	18669	8.70	0.87	5.10 E+05	5.1 E+04	0.10
?	18730	16.3	1.6	9.59 E+05	9.6 E+04	0.10
?	18790	3.24	0.32	1.91 E+05	1.9 E+04	0.10
?	18874	10.8	1.1	6.41 E+05	6.4 E+04	0.10
?	19060	5.17	0.52	3.10 E+05	3.1 E+04	0.10
?	19302	3.79	0.38	2.30 E+05	2.3 E+04	0.10
?	20692	1.36	0.14	8.81 E+04	8.8 E+03	0.10
?	21848	12.6	1.3	8.63 E+05	8.6 E+04	0.10
?	23078	5.38	0.54	3.90 E+05	3.9 E+04	0.10
?	23083	4.28	0.43	3.10 E+05	3.1 E+04	0.10
?	23373	3.20	0.32	2.35 E+05	2.4 E+04	0.10

Appendix D

Single fiber violin mode quality factors

I report the Quality factor measurements: in the tables there are the name of each resonance, its frequency f, the quality factor Q, the quality factor error σ_Q and the relative error ϵ_{rel}.

Aged fiber: $m = 2kg$, standard screw regulation				
order	$f(Hz)$	Q_x	σ_x	ϵ_{rel}
I	274.65	3.46 E+06	3.5 E+05	0.10
II	547.88	4.00 E+06	4.0 E+05	0.10
III	823.57	2.15 E+06	2.1 E+05	0.10
IV	1095.86	1.39 E+06	5.8 E+04	0.04
V	1369.93	5.85 E+05	3.2 E+04	0.05
VI	1641.49	2.02 E+05	1.5 E+04	0.08
VII	1913.74	1.57 E+06	1.6 E+05	0.10
VIII	2188.21	2.49 E+06	3.0 E+05	0.12
IX	2461.22	1.25 E+06	5.0 E+04	0.04
X	2733.19	9.43 E+05	3.8 E+04	0.04
XI	3002.17	6.67 E+05	3.7 E+04	0.06
XII	3273.18	5.52 E+05	1.1 E+04	0.02
XIII	3543.1	4.74 E+05	2.4 E+04	0.05
XIV	3809.15	2.68 E+05	9.8 E+03	0.04

Table D.1: aged fiber quality factor data: direction x, suspended mass $m = 2kg$, standard screw regulation.

Aged fiber: $m = 5kg$, standard screw regulation							
order	$f(Hz)$	Q_x	σ_x	ϵ^x_{rel}	Q_z	σ_z	ϵ^z_{rel}
I	438.36	1.62 E+06	5.6 E+03	0.00	8.77 E+05	8.7 E+04	0.1
II	874.30	1.62 E+06	3.1 E+05	0.19	7.25 E+05	4.5 E+04	0.06
III	1313.75	1.16 E+05	7.1 E+03	0.06	3.42 E+05	2.5 E+03	0.01
IV	1747.66	8.93 E+05	4.8 E+04	0.05	2.99 E+05	2.2 E+04	0.07
V	2183.13	1.06 E+06	9.6 E+03	0.01	3.00 E+05	1.1 E+04	0.04
VI	2613.81	2.10 E+05	1.4 E+04	0.07	1.81 E+05	3.1 E+04	0.17
VII	3044.89	6.29 E+05	1.4 E+04	0.02	1.34 E+05	1.9 E+04	0.14
VIII	3477.80	1.97 E+05	4.8 E+03	0.02	–	–	–
IX	3904.02	9.43 E+04	4.7 E+03	0.05	–	–	–
X	4322.09	8.85 E+04	6.4 E+03	0.07	–	–	–
XI	4730.24	4.31 E+04	1.0 E+04	0.24	–	–	–

Table D.2: aged fiber quality factor data: direction x and z, suspended mass $m = 5kg$, standard screw regulation.

Aged fiber: $m = 5kg$, tight lateral screws							
order	$f(Hz)$	Q_x	σ_x	ϵ^x_{rel}	Q_z	σ_z	ϵ^z_{rel}
I	438.36	1.28 E+06	1.9 E+04	0.01	1.32 E+06	1.3 E+05	0.1
II	874.30	1.09 E+06	8.4 E+03	0.01	1.09 E+06	2.2 E+04	0.02
III	1313.75	9.09 E+05	5.8 E+04	0.06	8.93 E+05	2.3 E+05	0.26
IV	1747.66	3.76 E+05	4.5 E+04	0.12	3.47 E+05	5.5 E+04	0.16
V	2183.13	4.27 E+05	7.7 E+04	0.18	2.92 E+05	1.3 E+04	0.04
VI	2613.81	8.13 E+05	8.1 E+04	0.10	6.25 E+04	8.3 E+02	0.01
VII	3044.89	–	–	–	3.32 E+05	1.4 E+04	0.04
VIII	3477.80	9.90 E+04	1.7 E+04	0.18	2.39 E+05	1.6 E+05	0.69
IX	3904.02	5.32 E+04	8.0 E+02	0.02	2.16 E+05	1.6 E+03	0.01

Table D.3: aged fiber quality factor data: direction x and z, suspended mass $m = 5kg$, tight lateral screws.

Aged fiber: $m = 5kg$, tight upper screws							
order	$f(Hz)$	Q_x	σ_x	ϵ^x_{rel}	Q_z	σ_z	ϵ^z_{rel}
I	438.36	1.39 E+06	5.6 E+04	0.04	1.25 E+06	1.7 E+04	0.01
II	874.30	1.01 E+06	1.1 E+05	0.11	9.09 E+05	8.8 E+04	0.1
III	1313.75	6.99 E+05	7.0 E+04	0.10	5.95 E+05	1.8 E+04	0.03
IV	1747.66	3.02 E+05	3.0 E+04	0.10	2.71 E+05	2.7 E+04	0.1

Table D.4: aged fiber quality factor data: direction x and z, suspended mass $m = 5kg$, tight upper screws.

Aged fiber: $m = 5kg$, loose upper screws							
order	$f(Hz)$	Q_x	σ_x	ϵ^x_{rel}	Q_z	σ_z	ϵ^z_{rel}
I	438.36	6.41 E+05	1.5 E+05	0.23	3.24 E+05	6.7 E+03	0.02
II	874.3	5.78 E+05	2.7 E+04	0.05	3.44 E+05	3.4 E+04	0.1
III	1313.75	5.75 E+05	9.9 E+04	0.17	5.56 E+05	5.6 E+04	0.1
IV	1747.66	6.62 E+04	1.2 E+03	0.02	9.09 E+04	9.1 E+03	0.1

Table D.5: aged fiber quality factor data: direction x and z, suspended mass $m = 5kg$, loose upper screws.

New fiber: $m = 5kg$, standard screw regulation							
order	$f(Hz)$	Q_x	σ_x	ϵ^x_{rel}	Q_z	σ_z	ϵ^z_{rel}
I	458.5	1.62 E+07	4.1 E+05	0.03	7.04 E+06	1.2 E+05	0.02
II	917.3	1.21 E+07	4.1 E+04	0.00	3.58 E+06	1.5 E+05	0.04
III	1373.63	9.26 E+06	1.8 E+05	0.02	3.28 E+06	3.8 E+04	0.01
IV	1829.95	6.45 E+06	1.2 E+05	0.02	3.19 E+06	2.9 E+04	0.01
V	2285.02	6.49 E+06	6.4 E+05	0.10	2.16 E+06	1.3 E+04	0.01
VI	2736.65	6.80 E+06	5.3 E+04	0.01	1.42 E+06	8.6 E+03	0.01
VII	3189.92	1.37 E+06	1.3 E+04	0.01	6.94 E+05	1.4 E+04	0.02
VIII	3641.43	2.56 E+06	1.7 E+04	0.01	1.54 E+05	1.1 E+03	0.01
IX	4081.28	4.39 E+06	3.2 E+05	0.07	–	–	–
X	4528.74	4.72 E+05	3.5 E+04	0.07	–	–	–
XI	4951.95	5.95 E+05	5.5 E+04	0.09	–	–	–

Table D.6: new fiber quality factor data: direction x and z, suspended mass $m = 5kg$, standard screw regulation.

New fiber: $m = 5kg$, standard screw regulation							
order	$f(Hz)$	Q_x	σ_x	ϵ^x_{rel}	Q_z	σ_z	ϵ^z_{rel}
I	458.5	2.45 E+07	1.9 E+06	0.08	4.10 E+06	5.7 E+05	0.14
II	917.3	1.57 E+07	5.2 E+04	0.00	3.64 E+06	4.1 E+05	0.11
III	1373.63	4.98 E+06	8.8 E+04	0.02	2.58 E+06	3.3 E+04	0.01
IV	1829.95	4.76 E+06	1.0 E+05	0.02	8.55 E+06	2.6 E+06	0.31
V	2285.02	2.72 E+06	1.1 E+05	0.04	1.93 E+06	1.3 E+05	0.07
VI	2736.65	1.04 E+06	1.5 E+05	0.14	2.23 E+06	5.3 E+04	0.02
VII	3189.92	8.85 E+05	1.2 E+05	0.14	–	–	–
VIII	3641.43	6.02 E+05	7.5 E+04	0.12	–	–	–
IX	4081.28	1.96 E+05	1.6 E+03	0.01	–	–	–

Table D.7: new fiber quality factor data: direction x and z, suspended mass $m = 5kg$, tight upper screws.

Bibliography

[1] Schutz B. F., *A first course in general relativity*, Cambridge University Press, Cambridge, 1985.

[2] Camp J. B., Cornish N. J., *Gravitational Wave Astronomy*, Annual Review Nuclear and Particles Science, vol. 54, p. 525, 2004

[3] Thorne K. S., Misner C. W., Wheeler J. A., *Gravitation*, W. H. Freeman publisher, 1973

[4] Thorne, K.S., *Multipole expansions of gravitational radiation*, Review of Modern Physics, vol. 52, p. 299, 1980

[5] Jaranowski P., Krolak A., Schutz B. F., *Data analysis of gravitational-wave signals from spinning neutron stars: the signal and its detection*, Physical Review D, vol. 58, p. 063001, 1998

[6] McDonald G., *A Review of Pulsar Glitch Mechanisms*, Ph.D. thesis, University of Johannesburg, South Africa, 2007

[7] Andersson N., Comer G., Prix R., *The Superfluid two - stream instability and pulsar glitches*, MNRAS, 2002

[8] Link B. K., Epstein R. I., *Thermally driven neutron star glitches*, Astrophysical Journal, vol. 457, p. 844, 1996

[9] Chandrasekhar S., *Ellipsoidal Figures of Equilibrium*, Yale Univ. Press, 1969

[10] Friedman J. L., Schutz B. F., *Secular Instabilities of rotating newtonian stars*, Astrophysical Journal, vol. 222, p. 281, 1978

[11] Roberts P. H., Stewartson K., *On the Stability of a Maclaurin Spheroid of Small Viscosity*, Astrophysical Journal, vol. 137, p. 777, 1963

[12] Chandrasekhar S., *Solutions of Two Problems in the Theory of Gravitational Radiation*, Physical Review Letters, vol. 24, p. 611, 1970

[13] Lindblom L., Owen B. J., Ushomirsky G., *Effect of a neutron-star crust on the r -mode instability*, Physical Review D, vol. 62, p. 084030, 2000

[14] Andersson N., *A new class of unstable modes of rotating relativistic stars*, Astrophysical Journal, vol. 502, p.708, 1998

[15] Blanchet L., *Gravitational radiation from post-newtonian sources and inspiralling compact binaries*, Living Review in Relativity, 9, 2006

[16] Grishchuk L. P., *Update on gravitational-waves research*, Astrophysical Update, 281-310, 2004

[17] Hannam M., *Status of black-hole-binary simulations for gravitational-wave detection*, arXiv:0901.2931 [gr-qc], 2009

[18] Abadie J. et al, *Predictions for the rates of compact binary coalescences observable by ground-based gravitational-wave detectors*, Classical and Quantum Gravity, vol. 27, p. 173001, 2010

[19] Weisberg J.M., Taylor J.H., *The relativistic binary pulsar B1913+16: thirty years of observations and analysis*, Astronomical Society of the Pacific Conference Series, vol. 328, p. 25, 2005

[20] Fryer C. L., New K. C. B., *Gravitational Waves from Gravitational Collapse*, Living Review in Relativity, 14, 2011

[21] Ott C. D., *TOPICAL REVIEW: The gravitational-wave signature of core-collapse supernovae*, Classical Quantum Gravity, vol. 26, p. 063001, 2009

[22] Abernathy M. et al, *Einstein gravitational wave Telescope conceptual design study*, ET-0106C-10, 2010

[23] Dimmelmeier H., Ott C. D., Marek A., Janka H.T., *Gravitational wave burst signal from core collapse of rotating stars*, Physical Review D, vol. 78(6), p. 064056, 2008

[24] Atteia J., Boer M., *Observing the prompt emission of gamma-ray bursts*, Comptes Rendus Physique, vol. 12, p. 255, 2011

[25] Bloom J. S., Perley D. A., Li W., Butler N. R., Miller A.A., et al, *Observations of the Naked-Eye GRB 080319B: Implications of Nature's Brightest Explosion*, Astrophysical Journal, vol. 691, p. 723, 2009

[26] Kouveliotou C. et al, *Identification of two classes of gamma-ray bursts*, Astrophysical Journal Letters, vol. 413, p. L101, 1993

[27] Kochanek C. S., Piran T., *Gravitational waves and gamma-ray bursts*, Astrophysical Journal Letters, vol. 417, p. L17, 1993

[28] Zhang B., Kobayashi S., Meszaros P., *GRB early optical afterglow: implications for the initial Lorentz factor and the central engine*, Astrophysical Journal, vol. 589, p. 861, 2003

[29] Abbott B. P. et al, *Search for gravitational-wave bursts associated with gamma-ray bursts using data from LIGO science run 5 and Virgo science run 1*, Astrophysical Journal, vol. 715, p. 1438, 2010

[30] Abadie J. et al, *Search for gravitational-wave bursts associated with gamma-ray bursts using data from LIGO science run 6 and Virgo science run 2 and 3*, under review

[31] Allen B., *The stochastic gravity-wave background: sources and detection*, Proceedings of the Les Houches School on Astrophysical Sources of Gravitational Waves, Cambridge University Press,1996

[32] Allen B., *Stochastic gravity-wave background in inflationary-universe models*, Physical Review D, vol. 37, p. 2078, 1988

[33] Kamionkowski M., Kosowsky A., Turner M. S., *Gravitational radiation from first-order phase transitions*, Physical Review D, vol. 49, p. 2837, 1994

[34] Regimbau T., Mandic V., *Astrophysical sources of a stochastic gravitational-wave background*, Classical and Quantum Gravity, vol. 25, p. 184018, 2008

[35] Marassi S., Schneider R., Ferrari V., *Gravitational wave backgrounds and the cosmic transition from Population III to Population II stars*, Monthly Notices of the Royal Astronomical Society, vol. 398-1, p. 293, 2009

[36] Ferrari V., Matarrese S., Schneider R., *Stochastic background of gravitational waves generated by a cosmological population of young, rapidly rotating neutron stars*, Monthly Notices of the Royal Astronomical Society, vol. 303, p. 258, 1999

[37] Abbott B. P. et al, *An upper limit on the stochastic gravitational-wave background of cosmological origin*, Nature, vol. 460, p. 990, 2009

[38] Shawhan P. S., *Rapid alerts for following up gravitational wave event candidates*, Proceedings of SPIE conference, 2012

[39] Abramovici A. et al., *LIGO: The Laser Interferometer Gravitational-Wave Observatory*, Science, vol. 256, p. 325, 1992, [http://www.ligo.caltech.edu]

[40] Giazotto A., *Interferometric detection of gravitational waves*, Physics Report C, vol. 182, p. 365, 1989, [http://www.virgo.infn.it]

[41] Danzmann K. et al., *GEO600: Proposal for a 600 m Laser Interferometric Gravitational Wave Antenna*, Max-Planck Institut für Quantenoptik Report 190, Garching, Germany, 1990, [http://www.geo600.uni-hannover.de]

[42] Miyoki S., et al., *The CLIO project*, Classical and Quantum Gravity, vol. 23, p. S231, 2006 [http://www.icrr.u-tokyo.ac.jp/gr/home/gre.html] [http://gwcenter.icrr.u-tokyo.ac.jp/en/]

[43] Saulson P. S., *Fundamentals of interferometric gravitational wave detectors*, World Scientific Publishing, 1994

[44] Bondu F., *Dark fringe shot noise sensitivity*, Virgo internal note, VIR-NOT-OCA-1390-243, 2003

[45] Caves C. M., *Quantum-mechanical noise in a interferometer*, Physical Review D, vol. 23, p. 1693, 1981

[46] Meers B. J., Strain K. A., *Modulation, signal, and quantum noise in interferometers*, Physical Review A, vol. 44, p. 4693, 1991

[47] Buonanno A., Chen Y., *Quantum noise in second generation, signal-recycled laser interferometric gravitational-wave detectors*, Physical Review D, vol. 64, p. 042006, 2001

[48] Corbitt T., Mavalvala N., *Review: Quantum noise in gravitational-wave interferometers*, Journal of Optics B, vol. 8, p. S675, 2005

[49] Saulson P. R. ,*Terrestrial gravitational noise on a gravitational wave antenna*, Physical Review D, vol. 30, p. 732, 1984

[50] Cella G. et al. *Relevance of Newtonian seismic noise for the Virgo interferometer sensitivity*, Classical Quantum Gravity, vol. 15, p. 3339, 1998

[51] Vinet J. Y. et al, *Scattered light noise in gravitational wave interferometric detectors: A statistical approach*, Physical Review D, vol. 56, p. 6085,1997

[52] Tournefier E., *Back-scattering by the optical benches: results for Virgo and constraints for Advanced Virgo*, Virgo internal note, VIR-NOT-070A-08, 2008

[53] Fiori I, Tournefier E., Canuel B, Marque J., *Diffused light mitigation in Virgo and constraints for Virgo+ and Advanced Virgo*, Virgo internal note, VIR-0792A-09, 2009

[54] Vinet J. Y. et al, *The Virgo physics book, vol. II*, 2004, [http://wwwcascina.virgo.infn.it/vpb/]

[55] Vajente G. *Analysis of sensitivity and noise sources for the Virgo gravitational wave interferometer*, PhD thesis, Universiy of Pisa, 2008

[56] Vinet J.Y. et al, *Optimization of long-baseline optical interferometers for gravitational-wave detection*, Physical Review D, vol. 38, p. 433, 1988

[57] Punturo M. *The Virgo sensitivity curve*, Virgo internal note, VIR-NOT-PER-1390-51, 2004

[58] Kogelnik H., Li T., *Laser beams and resonators*, Applied Optics, vol. 5, p. 1550, 1966

[59] Ruggi P., *L'attenuazione del rumore sismico nel rivelatore di onde gravitazionali Virgo*, Master thesis (in italian), Università degli studi di Pisa, 2003

[60] Braccini S. et al, *Measurement of the Virgo superattenuator performance for seismic noise suppression*, Review Scientific Instrument, vol. 72, p. 3643, 2001

[61] Bernardini A., Majorana E., Puppo P., Rapagnani P., Ricci F., Testi G., *Suspension last stages for the mirrors of the Virgo interferometric gravitational wave antenna*, Review Scientific Instruments, vol. 70, p. 3463, 1999

[62] Fowles G. R., *Introduction to modern optics*, Dover Pubblication, Inc., New York, 1989.

[63] Lorenzini M., *Suspension Thermal noise issues for Advanced gravitational wave interferometric detectors*, PhD thesis, University of Firenze, 2007

[64] Pound R. V., *Electronic Frequency Stabilization of Microwave Oscillators*, Review Scientific Instrument, vol. 17, p. 490, 1946

[65] Drever R. W. et al., *Laser phase and frequency stabilization using an optical resonator*, Applied Physics B, vol. 31, p. 97, 1983

[66] Cavalier F. et al., *The Global control of the Virgo experiment*, Nuclear Instruments and Methods in Physics Research, vol. 550, p. 467, 2005

[67] Barsotti L., *The control of the Virgo interferometer for gravitational wave detection*, PhD thesis, University of Pisa, 2006

[68] Morrison E., MeersB. J., Robertson D. I., Ward H., *Experimental demonstration of an automatic alignment system for optical interferometers*, Applied Optics, vol. 33, p. 5037, 1994

[69] Anderson D. Z., *Alignment of resonant optical cavities*, Applied Optics, vol. 23, p. 2944, 1984

[70] Acernese F. et al, *Automatic Alignment for the first science run of the Virgo interferometer*, Astroparticle Physics, vol. 33 p. 131, 2010

[71] Smith M., Willems P., *Auxiliary Optics Support System Conceptual Design Document*, vol. 1, Thermal Compensation System, LIGO-T060083-01-D

[72] Day R., Marque J., *Central Heating Radius of Curvature Correction (CHRoCC)*, Virgo internal note, VIR-0695A-10, 2010

[73] Puppo P., *Virgo+MS sensitivity curve*, Virgo internal note, VIR-0639B-09, 2009

[74] Hild S., Losurdo G., *Advanced Virgo design: Comparison of the Advanced Virgo sensitivity from Bench 4 and GWINC (v1)*, Virgo internal note, VIR-055A-08, 2008

http://lhocds.ligo-wa.caltech.edu:8000/advligo/GWINC

[75] Punturo M. *Advanced Virgo sensitivity document*, Virgo internal note, VIR-0073B-12, 2012

[76] Accadia T. et al, *Advanced Virgo Technical Design Report*, Virgo internal note, VIR-0128A-12, 2012

[77] Callen H. B., Welton T. A., *Irreversibility and generalized noise*, Physical Review, vol. 83, p. 34, 1951

[78] Greene R. F., Callen H. B., *On the formalism of the thermodynamic fluctuation theory*, Physical Review, vol. 83, p. 1231, 1951

[79] Callen H. B., Greene R. F., *Onthe theorem of irreversible thermodynamics*, Physical Review, vol. 86, p. 702, 1952

[80] Greene R. F., Callen H. B., *On the theorem of irreversible thermodynamics II*, Physical Review, vol. 88, p. 1387, 1952

[81] Callen H. B., Barasch M. L., Jackson J. L.,*Statistical mechanics of irreversibility*, Physical Review, vol. 88, p. 1382, 1952

[82] Saulson P. R., *Thermal noise in mechanical experiments*, Physical Review D, vol. 42, p. 2437, 1990

[83] Landau L. D., Lifshitz E. M., *Theory of Elasticity*, Addison-Wesley, 1959

[84] Ferreirinho J., *Internal friction in high Q materials*, in "The Detection of Gravitational Waves", D. G. Blair ed., Cambridge University press, first reprint, p. 116, 1991

[85] Brif C., *Notes on anelastic effects and thermal noise in suspensions of test masses in interferometric gravitational-wave detectors*, LIGO technical note, LIGO-T990041-00-R, 1999

[86] Marchesoni F., Cagnoli G., Gammaitoni L., *Damping in low-frequency mechanical pendulums*, Physical Letters A, vol. 187, p. 359, 1994

[87] Cagnoli G. et al, *Suspension losses in low-frequency mechanical pendulums*, Physical Letters A, vol. 213, p. 245, 1996

[88] Saulson P. R., Stebbins R. T., Dumont F. D., Mock S. E., *The inverted pendulum as a probe of anelasticity*, Review Scientific Instrument, vol. 65, p. 182, 1994

[89] Nowick A. S., Berry B. S., *Anelastic relaxation in crystalline solids*, Academic Press, New York, 1972

[90] Zener C., *Theory of internal friction in reeds*, Physical Review, vol. 52, p. 230, 1937

[91] Zener C., *General theory of thermoelastic internal friction*, Physical Review, vol. 53, p. 90, 1938

[92] Cagnoli G. et al, *Low-frequency internal friction in clamped-free thin wires*, Physical Letters A, vol. 255, p. 230, 1999

[93] Lifshitz R., Roukes M. L., *Thermoelastic damping in micro and nanomechanical systems*, Physical Review B, vol. 61, p. 5600, 2000

[94] Gretarsson A. M., Harry G. M., *Dissipation of mechanical energy in fused silica fibers*, Review Scientific Instruments, vol. 70, p. 4081, 1999

[95] Huang Y. L., Saulson P. R., *Dissipation mechanisms in pendulums and their implications for gravitational wave interferometers*, Review Scientific Instruments, vol. 69, p. 544, 1997

[96] Cagnoli G. et al, *Very high Q measurements on a fused silica monolithic pendulum for use in enhanced gravity wave detectors*, Physical Review Letters, vol. 85, p. 2442, 2000

[97] Rapagnani P, *Development and test at $T = 4.2K$ of a capacitive resonant transducer for cryogenic gravitational wave antenna*, Nuovo Cimento, vol. 5, p. 385, 1982

[98] Ohishi N., Otsuka S., Kawabe K., Tsubono K., *Estimation of thermal noise by a direct measurement of the mechanical conductance*, Physics Letters A, vol. 266, p. 228, 2000

[99] Numata K., Ando M., Yamamoto K., Otsuka S., Tsubono K., *Wide-band direct measurement of thermal fluctuations in a interferometer*, Physical Review Letters, vol. 91, p. 260602, 2003

[100] Yamamoto K., *Study of thermal noise caused by inhomogeneously distributed loss*, PhD thesis, University of Tokyo, 2000

[101] Gillespie A., Raab F., *Thermally excited vibrations of the mirrors of laser interferometer gravitational wave detectors*, Physical Review D, vol. 52, p. 577, 1995

[102] Levin Y., *Internal thermal noise in the LIGO test masses: a direct approach*, Physical Review D, vol. 57, p. 659, 1998

[103] Logan J. E., Robertson N. A., Hough J., Veitch P. J.,*An investigation of coupled resonances in materials suitable for test masses in gravitational wave detectors*, Physics Letters A, vol. 161, p. 101, 1991

[104] Majorana E., Ogawa Y., *Mechanical thermal noise in cupled oscillators*, Physics Letters A, vol. 233, p. 162, 1997

[105] Numata K., *Direct measurement of mirror thermal noise*, PhD thesis, University of Tokyo, 2002

[106] Logan J. E., Hough J., Robertson N. A., *An investigation of limitation to quality factor measurements of suspended masses due to resonances in suspension wires*, Physics Letters A, vol. 170, p. 352, 1992

[107] Logan J. E., Hough J., Robertson N. A., *Aspects of the thermal motion of a mass suspended as a pendulum by wires*, Physics Letters A, vol. 183, p. 145, 1993

[108] Cagnoli G., et al., *Damping diluition factor for a pendulum in an interferometric gravitational waves detector*, Physics Letters A, vol. 272, p. 39, 2000

[109] Piergiovanni F., Punturo M., Puppo P., *The thermal noise of the Virgo+ and Virgo Advanced last stage suspension (The PPP effect)*, Virgo internal note, VIR-015E-09, 2009

[110] Black E., *Thermal noise in coupled harmonic oscillators*, LIGO internal note, LIGO-T990045, 1999

[111] Black E., Cameron R., *Modal Q's, loss angles, and thermal noise in coupled harmonic oscillators*, LIGO internal note, LIGO-T010059-00-R, 2001

[112] Gonzalez G. I., Saulson P. R., *Brownian motion of a mass suspended by an anelastic wire*, Journal Acoustic Society American, vol. 96, p. 207, 1994

[113] Gillespie A., Raab F., *Thermal noise in the test mass suspensions of a laser interferometer gravitational wave detector prototype*, Physics Letters A, vol. 178, p, 357, 1993

[114] Brif C., *Optimization of thermal noise in multi-loop pendulum suspensions for use in interferometric gravitational wave detectors*, LIGO internal note, LIGO-P990028, 1999

[115] Campagna E., *Modeling some sources of thermal noise through Finite Element Analysis: application to the Virgo interferometric antenna*, PhD thesis, University of Pisa, 2004

[116] Hutchinson J. R., *Vibrations of solid cylinders*, Journal Applied Mechanics, vol. 47, p. 901, 1980

[117] Bondu F., Vinet J. Y., *Mirror thermal noise in interferometric gravitational wave detectors*, Physics Letters A, vol. 198, p. 74, 1995

[118] Yamamoto K., et al., *Experimental study of thermal noise caused by an inhomogeneously distributed losses*, Physics Letters A, vol. 280, p.289, 2001

[119] Yamamoto K., et al., *A theoretical approach to the thermal noise caused by an inhomogeneously distributed loss - Physical insight by the advanced modal expansion*, arXiv:gr-qc/0612044v2, 2007

[120] Bondu F., Hello P., Vinet J. Y., *Thermal noise in mirrors of interferomtric gravitational wave antenna*, Physics Letters A, vol. 246, p. 227, 1998

[121] Liu Y. T., Thorne K. S., *Thermoelastic noise and homogeneous thermal noise in finite sized gravitational-wave test masses*, Physical Review D, vol. 62, p. 122002, 2000

[122] Rowan S., et al, textitThe quality factor of natural fused quartz ribbons over a frequency range from 6 to $160Hz$, Physics Letters A, vol. 227, p. 153, 1997

[123] Vocca H., *Studio del rumore termico in regime di stazionarietà e di non-stazionarietà per l'interferomtero Virgo*, PhD thesis (in italian), University of Perugia, 2003.

[124] Willems P., *Dumbbell-shaped fibers for gravitational wave detectors*, Physics Letters A, vol. 300, p. 162, 2002

[125] Cumming A., et al., *Finite element modelling of the mechanical loss of silica suspension fibres for advanced gravitational wave detectors*, Classical Quantum Gravity, vol. 25, p. 215012, 2009

[126] Elliffe E. J., et al., *Hydroxide-catalysis bonding for stable optical systems for space*, Classical Quantum Gravity, vol. 22, p. S257, 2005

[127] Gwo D. H., *Ultra precision and reliable bonding method*, United States Patent n.US 6 284 085 B1

[128] Gwo D. H., *Ultra-Precision Bonding for Cryogenic Fused Silica Optics*, Proceedings of SPIE, p. 3435, 1998

[129] Sneddon P. H., Bull S., Cagnoli G. , Crooks D. R. M., Elliffe E. J., Faller J. E., Fejer M. M., Hough J. and Rowan S., *The intrinsic mechanical loss factor of hydroxide-catalysis bonds for use in the mirror suspensions of gravitational wave detectors*, Classical Quantum Gravity, vol. 20, p. 5025, 2003

[130] Reid S., Cagnoli G., Elliffe E. J., Faller J., Hough J., Martin I., Rowan S., *Influence of temperature and hydroxide concentration on the setting time of hydroxy-catalysis bonds*, Physics Letters A, vol. 363, p. 341, 2007

[131] Rowan S., Twyford S. M., Hough J., Gwo D. H., Route R., *Mechanical losses associated with the technique of hydroxide-catalysis bondng of fused silica*, Physics Letters A, vol. 246, p. 471, 1998

[132] Smith J. R., Cagnoli G., Crooks D. R. M., Fejer M. M., Goßler S., H. Luck, S. Rowan, J. Hough and K. Danzmann Class. Quantum Grav., vol. 21, pp. S1091-S1098, 2004.

[133] Colombini M., et al., *Q measurements on monolithic suspensions*, Virgo internal note, VIR-0622A-10

[134] Kolsky H., *Stress waves in solids*, Dover ed., New York, 1963

[135] Love A. E. H., *A treatise on the mathematical theory of elasticity*, Cambridge university press, Cambridge, 1920

[136] Cagnoli G., Willems P. A., *Effects on nonlinear damping in highly stressed fibers*, Physical Review B., vol. 65, p. 174111, 2002

[137] Willems P., Sannibale V., Weel J., Mitrofanov V., *Investigations of the dynamics and mechanical dissipation of fused silica suspension*, Physics Letters A, vol. 297, p. 37, 2002

[138] Puppo P., *A finite element model of the Virgo mirrors*, Virgo internal note, VIR-NOT-ROM-1390-262, 2004

[139] McSkimin H. J.,*Measurement of elastic constant at low temperatures by means of ultrasonic waves-data for silicon and germanium single crystals, and for fused silica*, Journal Applied Physics, vol. 24, p. 988, 1953

[140] Piergiovanni F., *Elastic behavior of silica fibres in Virgo+ suspensions*, Virgo internal note, VIR-0218B-11, 2011

[141] Colla A., et al., *Update on NoEMi and the lines database*, Virgo internal note, VIR-0091A-11, 2011

[142] Accadia T., et al., *The NoEMI (Noise Frequency Event Miner) framework*, Journal of Physics: Conferences Series, vol. 363, p. 012037, 2012

[143] Punturo M., *Mechanical simulation of the Virgo+ mirrors*, Virgo internal note, VIR-0556A-10, 2010

[144] Nardecchia I., *Rumore termico delle sospensioni in Advanced Virgo*, Master thesis (in italian), University of Rome "La Sapienza", 2012

[145] Punturo M., *Violin modes characterization*, Virgo logbook entry 24094, 2009

[146] Piergiovanni F., Lorenzini M., Cagnoli G., Campagna E., Cesarini E., Losurdo G., Martelli F., Vetrano F., Vicerè A., *The dynamics of monolithic suspensions for advanced detectors: a 3-segment model*, Journal of Physics: Conference Series, vol. 228, p. 012017, 2010

[147] Piergiovanni F., *Monolithic Suspensions (fibres and clamping) in Virgo+*, presentation at Thermal Noise Workshop, Cascina 2012

[148] Gretarsson A. M., Harry G. M., Penn S. D., Saulson P. R., Startin W. J., Rowan S., Cagnoli G., Hough J., *Pendulum mode thermal noise in advanced interferometers: a comparison between fused silica fibers and ribbons in the presence of surface losses*, Physical Letters A, vol. 270, p. 108, 2000

[149] Colombini M., Nardecchia I., Puppo P., Majorana E., Rapagnani P., Ricci F., *Virgo+ thermal noise study*, Virgo internal note, VIR-0074A-12, 2012

[150] Di Pace S., *Studio del rumore termico degli specchi di Virgo con sospensioni monolitiche*, Master thesis (in italian), University of Rome "La Sapienza", 2011

[151] Penn S., et al., *Mechanical loss in tantala/silica dielectric mirror coatings*, Classical Quantum Gravity, vol. 20, p. 2917, 2003

[152] Cunningham L., et al., *Re-evaluation of the mechanical loss factor of hydroxide-catalysis bonds and its significance for the net generation of gravitational wave detectors*, Physics Letters A, vol. 374, p. 3993, 2010